



Provided by the author(s) and University of Galway in accordance with publisher policies. Please cite the published version when available.

Title	Optical variability in Late-M and Early-L dwarfs
Author(s)	Dulaimi, Salam E. Hammeed
Publication Date	2021-05-05
Publisher	NUI Galway
Item record	http://hdl.handle.net/10379/16739

Downloaded 2024-04-25T06:58:55Z

Some rights reserved. For more information, please see the item record link above.





Optical Variability in Late-M and Early-L Dwarfs

by

Salam E. Hammeed Dulaimi B.Sc. M.Sc.

A thesis submitted in partial fulfilment for the degree of Doctor of Philosophy

in the



Centre for Astronomy

School of Physics

National University of Ireland Galway

Under the supervision of:

Dr. Ray F. Butler

Dr. Aaron Golden

September 2020

Contents

List of Tables:	V
List of Figures:.....	VI
Nomenclatures.....	XII
Author’s Novel Contributions.....	XVI
DEDICATION.....	XVII
Publications.....	XIX
Presentations (talks and posters).....	XX
Declarations.....	XXII
Abstract	XXIII
Thesis Motivation	XXVI
Chapter 1	1
1.1 Introduction	2
1.2 Ultracool Dwarf Stars	2
1.3 Interior physics of ultracool dwarf stars	5
1.4 Thermonuclear Processes within Ultracool Dwarfs	7
1.5 Evolution of Ultracool Dwarfs	9
1.6 Atmosphere and Spectral Classification of Late-M, L and T-type Dwarf Stars	14
1.7 Radio Emission Processes from Stellar and Substellar Regions	17
1.8 Periodic Photometric Variability of Ultracool Dwarfs	27
1.8.1 Optical Variability due to Magnetically Induced Spots	30
1.8.2 Optical Variability due to Dust Clouds	32
1.8.3 Optical Variability due to Auroral Hot Spots	33
1.9 Thesis Overview	37
Chapter 2	40
2.1 Introduction	41
2.2 Optical Setup – Vatican Advanced Technology Telescope (VATT)	41
2.3 Galway Ultra-Fast Imager (GUFI)	43
2.4 Factors affecting CCD photometric precision	52
2.5 Low Light Level CCD (L3-CCD) Technology and Astronomical Usage Considerations	56

2.6 Atmospheric noise effects	62
2.6.1 Atmospheric Extinction	63
2.6.2 Atmospheric Scintillation and Seeing	64
2.7 The Low Light Level (L3) GUFi Pipeline	67
2.7.1 L3_group()	68
2.7.2 L3_calib()	72
2.7.3 L3_work()	76
2.8 Fringing effects	83
2.9 Summary	85
Chapter 3	86
3.1 Introduction	87
3.2 GUFi pipeline photometry	88
3.3 Differential Photometry	90
3.4 Optimum Aperture (O.A.) & Lucky Photometry (LuckyPhot)	93
3.5 Post-Photometry Assessment of Lightcurves	103
3.6 Photometric Error Model	106
3.7 Detecting Periodic Variability of Photometric Datasets	109
3.7.1 The Lomb-Scargle (LS) Periodogram	109
3.7.2 Phase Dispersion Minimization (PDM)	113
3.7.3 Phase Folding	116
3.7.4 Markov chain Monte Carlo (MCMC)	118
3.7.5 Light Curve Fitter (LCF)	121
3.8 Summary	129
Chapter 4	130
4.1 Introduction	131
4.2 Target Selection	132
4.2.1 BRI 0021+0214	132
4.2.2 2MASS J00361617+18211:	134
4.3 Photometric Observations and Analysis	138
4.4 Results	141
4.4.1 BRI 0021+0214	141
4.4.2 2MASS J00361617+18211	151
4.4.3 Optimum Aperture vs. Fixed Aperture	161

4.5 Summary	166
Chapter 5	169
5.1 Introduction	170
5.2 Targets	172
5.2.1 2MASSW J0746425+200032AB	172
5.2.2 2MASS J1314203+132001AB	175
5.3 Optical Observation and Outline of Data Analysis	179
5.4 Results	182
5.4.1 2M J0746+20AB	182
5.4.2 2M J1314+13AB	207
5.5 Spin-Orbit Alignment Of the two binary systems: 2M J0746+20AB and 2M J1314+13AB	236
5.5.1 Introduction	236
5.5.2 2M J0746+20AB	238
5.5.3 2M J1314+13AB	241
5.6 Summary	244
Chapter 6	247
6.1 Discussion and Conclusions	248
6.2 Future Work	253
6.2.1 LuckyPhot Development	253
6.2.2 Upgrading the Galway Ultra Fast Imager (GUFU mk. III)	254
Bibliography	256

List of Tables:

2.1 VATT Specifications.....	42
2.2 GUFI Photometer characteristics.....	51
2.3 Measured Readnoise ($e^- \text{ pixel}^{-1} \text{ readout}^{-1}$).....	58
3.1 Calculations during of the LuckyPhot technique.....	99
4.1 A summary of the physical properties of the two targets in our campaign.....	137
4.2 Observation details for BRI 0021.....	138
4.3 Observation details for 2M J0036.....	139
4.4 Amplitude variability and photometric error analysis of BRI 0021.....	149
4.5 Amplitude variability and photometric error analysis of 2M J0036.....	151
5.1 A summary of properties of 2M J0746+20AB.....	174
5.2 A summary of properties of 2M J1314+13AB.....	177
5.3 Observation Details of 2M J0746+20AB.....	180
5.4 Observation Details of 2M J1314+13AB.....	181
5.5 Amplitude variability and photometric error analysis of 2M J0746+20A & 2M J0746+20B.....	184
5.6 Preview of 2M J0746+20AB results from this work.....	203
5.7 Amplitude variability of 2M J1314+13A.....	208
5.8 Amplitude variability of 2M J1314+13B.....	209
5.9 Photometric error analysis of 2M J1314+13AB.....	214
5.10 Preview of 2M J0746+20AB results from this work.....	231

List of Figures:

1.1 Plots of central temperature T_c (in K), density ρ_c (in g cm^{-3}), and degeneracy parameter ψ_c against $\log M/M_\odot$ from Chabrier and Baraffe (2000).....	6
1.2 Effective temperature T_{eff} against time ($\log t$, years) from Chabrier and Baraffe (2000).....	10
1.3 The evolution of the luminosity (L/L_\odot) against time (in yr) from Burrows et al. (1997).....	11
1.4 The evolution of radius (R) against effective temperature (T_{eff}) from Burrows et al. (1997).....	12
1.5 The evolution of \log_{10} gravity (in cgs units) against effective temperature (T_{eff}) from Burrows et al. (1997).....	13
1.6 Spectra of a late-M (M9), early- to mid-L (L3), and late-L dwarf (L8) for comparison from Kirkpatrick et al. (1999).....	15
1.7 Near-infrared spectra of a mid-L (2MASS J0850359+105716), a late-L (2MASS J1632291+190441) and a T dwarf (Gl 229B) for comparison from Kirkpatrick et al. (1999).....	17
1.8 Series of processes called the $\alpha\Omega$ -dynamo.....	20
1.9 Plot radio against X-ray luminosity for magnetically active stars including the Sun from Berger et al. (2008).....	23
1.10 Three samples of radio lightcurves from ultracool dwarfs from Hallinan et al. (2007), Berger et al. (2009b) and McLean et al. (2011).....	25
2.1 An analogy for the operation of a CCD from Howell (2006).....	45
2.2 The DV887 iXon camera.....	46
2.3 Schematic of an EMCCD.....	47
2.4 Comparison of simplified back-illuminated and front-illuminated pixel crosssections from Sheehan (2008).....	48
2.5 Quantum efficiency (QE) of the Andor iXon DV887 back-illuminated EMCCD camera.....	49

2.6	GUFI photometer mounted at the Cassegrain focus of VATT.....	50
2.7	A comparison between the performance of an L3CCD.....	60
2.8	The effect of atmospheric extinction from Collins (2014).....	63
2.9	Atmospheric turbulence effect from Collins (2014).....	65
2.10	The L3-GUFI pipeline start-up screen.....	67
2.11	Flow-chart of modules within L3_groups ().....	68
2.12	The make_lists GUI to manage all data acquired from the GUFI photometer.....	68
2.13	Example of the folders created for a given night via the make_lists routine.....	69
2.14	The hdr_fix GUI for amending the FITS image header information.....	70
2.15	The check_data GUI for detecting and trimming any damaged datacubes.....	71
2.16	The make_groups GUI for grouping the common frames.....	72
2.17	Flow-chart of modules within L3_calib ().....	73
2.18	Bias frame acquired by taking a zero second frame from the GUFI L3-CCD camera with a closed shutter.....	74
2.19	Flat-field frame from GUFI.....	75
2.20	The sci_data GUI used for the reduction of science frames.....	76
2.21	The data_ops GUI used for the breaking up of FITS datacubes, binning, registering and co-addition of FITS files.....	77
2.22	The starlist GUI used for finding stars and numbering them with their coordinates in the output file.....	79
2.23	The app_size GUI used to test a number of photometric aperture sizes and find the one that provides the highest SNR.....	80
2.24	The ref_stars GUI used to locate appropriate reference stars, which will be used later for differential photometry.....	81
2.25	The data_analysis GUI which allows the user to perform photometric analyses such as differential photometry.....	82
2.26	One of the three PSET windows for the data_analysis GUI.....	83
3.1	A plot of SNR versus aperture size (pixels) to determine the optimum aperture radius as from in the app size routine.....	92
3.2	The process of O.A. selection technique from Collins (2014).....	95

3.3 A summary of the Lucky Photometry (LuckyPhot) technique from Collins (2014)	96
3.4 Figures A and B illustrate LuckyPhot selection method from Collins (2014)	98
3.5 Example of the format of the file for one frame for input to LuckyPhot	101
3.6 Shows the user settings for the RUN OVAR routine	102
3.7 The user settings for the RUN SELPHOT routine	103
3.8 Procedure of the post-photometry routines	105
3.9 The final error model fit for the six reference stars used for the analysis of 2MASS J0746+2000AB on March 04, 2017 UT	107
3.10 Shows adjacent frequencies powers, f (e.g. $f \sim$ between 10 - 20 Day ⁻¹) that result from the effect of spectral leakage	110
3.11 Simulated data showing the undersampled true period	111
3.12 Shows the LS periodogram constructed from the February and March 2017 combined lightcurve of 2M J1314+13A	112
3.13 Outputs from the LS periodogram technique and the PDM technique for 2M J0746+20AB for the November 2017 epoch	115
3.14 Phase folded photometric lightcurves of the M7 dwarf 2M J1314+13A from the May 2018 epoch	117
3.15 The same phased lightcurve of 2M J1314+13A from Figure 3.14A	118
3.16 Posterior probability distributions obtained from applying the MCMC algorithm to the BRI 0021 lightcurve on October 10 2017	119
3.17 Lightcurve of the very low mass binary 2M J0746+20AB on March 20, 2017	122
3.18 Show the March 04 2017 night from 2M J0746+20AB. The red model sinusoid overplotted is the best fit using the Least Square Fit LSF from LCF routine	124
3.19 The operational flowchart for the lightcurve Fitter LCF application illustrated in Figure 3.20	125
3.20 GUI outlining sequence of steps to calculate and plot the LSF for data	126

3.21 Output based on the sequence of events in Figure 3.20.....	128
4.1 BRI 0021 was monitored for a total of six nights, over two separate epochs.....	142
4.2 Lomb-Scargle periodogram and bootstrapping distribution of all BRI 0021 epochs, calculated from the combined data set in Figure 4.1.....	143
4.3 Phase dispersion minimization plot of all of the BRI 0021 data	144
4.4 Plots A and B are the fitted sinusoidal model (red curve) of BRI 0021 on December 22 2017 and posterior probability distributions for the model parameters.....	146
4.5 Phase-folded lightcurve of all epochs in the BRI 0021 observation Campaign.....	147
4.6 Equatorial rotational velocity vs. the inclination angle for the rotation axis of BRI 0021 relative to our line of sight.....	148
4.7 Lightcurves of 2M J0036 taken in VATT I-band over three nights.....	154
4.8 Lomb-Scargle Periodogram analysis of F.A. with No LuckyPhot (GUF1 photometry), O.A. with LuckyPhot and bootstrapping distribution on 2M J0036 for the entire 2017 epoch.....	155
4.9 Plots A and B compare the results obtained from PDM using F.A. with No LuckyPhot (GUF1 photometry) and O.A. with LuckyPhot on 2M J0036 for the entire 2017 epoch.....	157
4.10 Plots A and B are the fitted sinusoidal model (red curve) of 2M J0036 on November 25 2017 and posterior probability distributions for the model parameters.....	158
4.11 Plots A, B, C and D are unbinned and binned phase-folded lightcurves of all data for 2M J0036.....	159
4.12 Overplotted sinusoidal model of ~ 3.1 hrs on a randomly selected night (15 th Dec 2017)	160
4.13 Equatorial rotational velocity vs. the inclination angle for the rotation axis of 2M J0036 relative to our line of sight.....	161
4.14 Present the 2M J0036 differential lightcurves using the entire data set of 25 and 26 November 2017 and 15 December 2017.....	163
4.15 The errors from the lightcurves (shown in Figure 4.14).....	164
4.16 The number of points within each data bin before and after the LuckyPhot process for the 2M J0036 data set.....	165

4.17 Comparison of techniques to determine which one has a lower spread.....	166
5.1 I-band images of the 2M J0746+20AB and 2M J1314+13AB fields.....	181
5.2 I-band lightcurves of 2M J0746+20AB.....	185
5.3 I-band lightcurves of 2M J0746+20A.....	188
5.4 I-band lightcurves of 2M J0746+20B.....	190
5.5 Lomb-Scargle (LS) periodogram and bootstrapping distributions of all three epochs of the I-band GUF1 photometric data of 2M J0746+20A.....	193
5.6 Phase dispersion minimization (PDM) plot of all epochs of 2M J0746+20A.....	194
5.7 Plots A and B are the fitted sinusoidal model (red curve) of 2M J0746+20A on November 24 2017 (O.A.+LuckyPhot) and posterior probability for the model parameters.....	195
5.8 Lomb Scargle (LS) Periodogram and bootstrapping distributions of all epochs of 2M J0746+20B.....	196
5.9 Phase dispersion minimization plot for all three epochs of 2MJ0746+20B.....	197
5.10 Plots A and B are the fitted sinusoidal model (red curve) of 2M J0746+20B on December 27 2017 (O.A.+LuckyPhot) and posterior probability for the model parameters.....	198
5.11 Plots A and B are unbinned and binned phase-folded lightcurve of 2M J0747+20A from all three epochs.....	199
5.12 Plots A and B are unbinned and binned phase-folded lightcurve of 2M J0746+20B from all epochs combined.....	200
5.13 Lomb-Scargle (LS) periodogram of all epochs combined of I-band GUF1 photometric data of 2M J0746+20AB.....	202
5.14 Plots A and B are unbinned and binned phase-folded lightcurves of 2M J0746+20AB from all epochs combined.....	205
5.15 Plots A and B are Lightcurves of 2M J0746+20AB from two nights (17 th and 20 th March), selected randomly from the 2017 March epoch.....	206
5.16 The I-band lightcurves of 2M J1314+13AB using a Fixed Aperture (F.A.) without LuckyPhot.....	211

5.17 The same data of 2M J1314+13AB as Figure 5.14 using an Optimum Aperture (O.A.) with LuckyPhot	213
5.18 2M J1314+13A: Comparison of the results from utilizing F.A.+No LuckyPhot and O.A.+LuckyPhot	215
5.19 2M J1314+13B: The results obtained from using F.A. with no LuckyPhot (GUF1 photometry) and O.A. with LuckyPhot.....	218
5.20 Lomb-Scargle (LS) periodogram and bootstrapping distributions of all epochs of the I band GUF1 photometric data of 2M J1314+13A & 2M J1314+13B.....	221
5.21 PDM of all epochs of the I-band datasets of 2M J1314+13A & 2M J1314+13B	225
5.22 Plots A, B, C and D are the fitted sinusoidal model of 2M J1314+13A and 2M J1314+13B on February 24 2017 (O.A.+LuckyPhot) and posterior probability distributions of the model parameters for the A and B components.....	226
5.23 Plots A, B, C, D, E, F, G and H are unbinned and binned phase-folded photometric lightcurves of 2M J1314+13A & 2M J1314+13B.....	229
5.24 Lomb-Scargle (LS) periodogram of all epochs combined of I-band GUF1 data of 2M J1314 13AB.....	230
5.25 Comparison of the differential lightcurves for the night of 24 Feb 2017, obtained from using O.A. with LuckyPhot and a F.A. with no LuckyPhot.....	232
5.26 Equatorial rotational velocity vs. inclination angle of the orbital plane of 2M J0746+20A	239
5.27 Equatorial rotational velocity vs. inclination angle of the orbital plane of 2M J0746+20B	240
5.28 Equatorial rotational velocity vs. inclination angle of the orbital plane of 2M J1314+13A	242
5.29 Equatorial rotational velocity vs. inclination angle of the orbital plane of 2M J1314+13B	243
6.1 I-band image of the BRI 0021 field, obtained at the 1.8m VATT using our GUF1 photometer	254

Nomenclatures

$\alpha\Omega$	– dynamo	Alpha-Omega dynamo
ADU		Analogue to Digital Unit
ω		Angular Frequency
AU		Astronomical Unit
CO		Carbon Monoxide
CCD		Charge-Coupled Device
χ^2		Chi-Squared
σ_{Dark}		Dark Current
ψ		Degeneracy Parameter
m_{Diff}		Differential Magnitude
DFT		Discrete Fourier Transform
T_{eff}		Effective Temperature
ECM		Electron Cyclotron Maser
EM		Electron Multiplication
EMSSG	Environmental Monitoring and Space Science Group	
T_F		Fermi Temperature
FOV		Field of View
F.A.		Fixed Aperture
F_T		Flux of the Target Star
fps		Frame per second
FWHM		Full Width at Half Maximum
GUFI		Galway Ultra Fast Imager
GOF		Goodness of fit

GUI	Graphical User Interface
HJD	Heliocentric Julian Day
H-R	Hertzsprung-Russell (diagram)
HBMM	Hydrogen Burning Minimum Mass
IRAF	Image Reduction and Analysis Facility
JD	Julian Day
M_{jup}	Jupiter Mass
R_J	Jupiter Radius
kG	Kilogauss Magnetic Fields
LSF	Least Square Fitting
LCF	Light Curve Fitter
LDR	Line Depth Ratio
Li	Lithium
LS	Lomb-Scargle Periodogram
L3	Low Light Level
LuckyPhot	Lucky Photometry Technique
m_T	Magnitude of the Target Star
Z_{\odot}	Solar Metallicity
CH_4	Methane
MHJD	Modified Heliocentric Julian Date
MJD	Modified Julian Day
MGIO	Mount Graham International Observatory
OVAR	Optical VARIability Technique
O.A.	Optimum Aperture
pc	Parsec
PDM	Phase Dispersion Minimization

PRNU	Pixel Response Non-Uniformity
PSF	Point Spread Function
P	Polytropic Index
ρ	Pressure
QE	Quantum Efficiency
QVAR	Quasar Variability
R	Radius
$v \sin i$	Rotational Velocity
SNR	Signal to Noise Ratio
L_{\odot}	Solar Luminosity
M_{\odot}	Solar Mass
g	Gravity
TB	Terabytes
σ_{IRAF}	The formal photometric error in the instrumental magnitude in the photometric aperture
F_{ref}	The mean fluxes of the all selected reference stars
MCMC	Markov chain Monte Carlo
m_{ref}	The mean magnitudes of the all selected reference stars
M_{sky}	The mean per pixel estimation of the sky background within the sky annulus
N_{sky}	The number of sky pixels in the annulus around the star
STD	Standard Deviation
TiO	Titanium (II) Oxide
2MASS	Two Micron All Sky Survey

UCD	Ultracool Dwarf
UT	Universal Time
VO	Vanadium (II) Oxide
VATT	Vatican Advanced Technology Telescope
VLA	Very Large Array
VLBA	Very Long Baseline Array
VLT	Very Large Telescope
VLM	Very Low Mass
ZDI	Zeeman–Doppler Imaging
Z_{Mag}	Zero Point Magnitude

Author's Novel Contributions

Dulaimi et al. 2020a, submitted.

- Discovered optical variability in the M7 dwarf BRI 0021-0214 (Ch 4).
- Discovered the inclination angle for the rotation axis of BRI 0021 and 2M J0036 relative to our line of sight (Ch 4).
- Improvement of fringe correction routine.
- Applied of two photometric analysis tools, GUF1 pipeline with Fixed Aperture photometry (F.A.) and Optimum Aperture (O.A.) with LuckyPhot to test which system produces the best lightcurves (Ch 3, Ch 4 & Ch 5)
- Development of results comparison tool to quantify which technique produced higher precision lightcurves with lower spread photometric scatter (Ch 4).
- Development of routines for updating timestamp (UT & JD) of the FITS files, photometric error and binning the lightcurves (Ch 2 & Ch 3).

Dulaimi et al. 2020b, in prep.

- Discovered optical variability in the secondary components of ultracool dwarf binary 2MASS J1314+13AB and 2MASS J0746+20AB (Ch 5).
- Investigated the orbital coplanarity of ultracool dwarf binary 2MASS J1314+13AB and 2MASS J0746+20AB (Ch 5).
- Applied our novel tool, Light Curve Fitter (LCF), designed to deconvolve two component signals within a combined binary optical time series (Ch 3 & Ch 5).

DEDICATION

I firstly wish to express my gratitude to my supervisors Dr. Ray Butler and Dr. Aaron Golden for their instructions and guidance throughout this work. Their enthusiasm and knowledge have been instrumental in driving my work to where it is today. I'd also like to thank Dr. Éamonn Harvey and Dr. Eoin O'Connor for their constant support and words of encouragement, and for reading this thesis. I've appreciated the coffee breaks and moments of rest during my PhD years, so thanks to Alison, Mohammed, Nevenoe, Eoin, Amy and the friends who've dropped by from time to time. A special thanks to Rebecca in the Physics office, I will not forget your help over the years with Agresso. A special acknowledgment and thanks to Karol Fitzgerald for the code help and for your cherished friendship, and encouragement. To Richard P. Boyle and all staff of the VATT telescope, it was an incredible experience for me to visit such a facility at 10,427 feet. Special thanks to Adrian, Alan and Niall at the Blackrock Castle Observatory, for their assistance with the Lucky Photometry codes which were essential to the research performed within this thesis. To my children who shared their hugs of encouragement, and my wife Nada who gave me understanding, space and time to complete this thesis, which was no small sacrifice. Finally but certainly not least, I'd like to express my deepest gratitude to my parents who initially set me on the path to higher education. I will endeavour to pass the same values on to my own children.

Acknowledgements

I gratefully acknowledge the support of the Ministry of higher education in Iraq and Nahrain University who funded my research.



Publications

- S. Dulaimi, R. P Boyle, A. Golden and R. F Butler. **Optical Variability, Rotation Period and Inclination Angle of the M9.5 dwarf BRI 0021-0214.** Submitted to Monthly Notices of the Royal Astronomical Society.
- S. Dulaimi, R. P Boyle, K. Fitzgerald, A. Golden and R. F Butler. **Deconvolving the optical light curves of the tight dwarf binaries 2MASS J0746425+200032AB and 2MASS J1314203+132001AB.** Submitted to Monthly Notices of the Royal Astronomical Society.
- S. Dulaimi, R. P Boyle, A. Collins, N. Smith, A. Giltinan, A. Golden and R. F Butler. **Comparison between Lucky photometry and GUF1 photometry techniques.** In preparation.
- K. Fitzgerald, S. Dulaimi, R. P Boyle, A. Golden and R. F Butler. **The Light Curve Fitter: A novel application for deconvolving two superimposed sinusoidal waves developed using the Agile Software Development Lifecycle.** Submitted to Astronomy and Computing.
- Harvey, E.J., Redman, M.P., Boumis, P., Akras, S., Fitzgerald, K., Dulaimi, S., Williams, S.C., Darnley, M.J., Lam, M.C., Kopsacheilli, M. and Derlopa, S., 2020. **Two New Nova Shells associated with V4362 Sagittarii and DO Aquilae.** Monthly Notices of the Royal Astronomical Society (Published).

Presentations (talks and posters)

- Speaker for Journal Club session at the Centre for Astronomy, NUI Galway. Title: **“Magnetically driven optical and radio aurorae at the end of the stellar main sequence”**. Date: 10th March 2016.
- Speaker at the Postgraduate Physics seminar, Physics Department, Title: **“Ultracool dwarfs –characteristics and phenomena”**. Date: 13th May 2016.
- Poster presentation at INAM conference (Irish National Astronomy Meeting), Dublin, Ireland. Title: **“Lightcurve analysis of radio detected ultracool dwarfs”**. Date: 07th - 09th Sep 2016.
- Speaker for Journal Club session at the Centre for Astronomy, NUI Galway. Title: **“Spin-orbit alignment in the very low mass binary regime the L dwarf tight binary 2MASS J07464+20AB”**. Date: 27th Oct 2016.
- Speaker for Journal Club session at the Centre for Astronomy, NUI Galway. Title: **“Ultracool dwarfs in open clusters and star-forming regions”**. Date: 02nd March 2017.
- Poster presentation at the IOP Ireland Spring Meeting held in Limerick. Title: **“Discovery the optical period of the secondary member 2MASS J0746+20B”**. Date: 12th of May 2018.

- Poster presentation at Cool Stars 20 conference held in Boston / Cambridge, USA. Title: **"Untangling the light-curves of the brown dwarf binary 2MASS J0746+20AB"**. Date: July 29th - Aug 3rd, 2018
- Poster presentation at the INAM conference (Irish National Astronomy Meeting) held in Birr. Title: **"Spin-orbit alignment in the M7 binary 2MASS J1314+13AB"**. Date: 08th of Sep 2018.
- Speaker at the INAM conference (Irish National Astronomy Meeting) held in Armagh Observatory and Planetarium. Title: **"Deconvolving the light-curves of the M7 dwarf binary 2MASS J1314+13AB"**. Date: 05th of Sep 2019.
- Speaker at the INAM conference (Irish National Astronomy Meeting) hosted by the Centre for Astrophysics & Relativity of Dublin City University (Virtual Conference). Title: **"Determining the rotation period of the M9.5 dwarf BRI 0021-0214 via photometric observation"**. Date: 03rd of Sep 2020.
- Poster presentation at the Royal Astronomical Society (Virtual Conference). Title: **"A Search for the optical counterpart to the radio emissions detected from the M9.5 dwarf BRI 0021-0214"**. Date: 14 - 28th of Sep 2020.
- Poster presentation at the Astronomical Data Analysis Software and Systems (online). Title: **"Deconvolving two superimposed sinusoidal waves via Light Curve Fitter application"**. Date: 08 - 12th of Nov 2020.
- Poster presentation at Cool Stars 20.5 conference (Virtual Conference). Title: **"The Light Curve Fitter: A novel application for deconvolving two superimposed sinusoidal waves developed using the Agile Software Development Lifecycle"**. Date: 02 - 04th of March 2021.

Declarations

The work in this thesis is based on research carried out at the Centre for Astronomy, School of Physics, National University of Ireland, Galway.

The thesis describes work which is entirely my own except where otherwise accredited. No part of this thesis has been submitted elsewhere for any other degree or qualification at any other institution.



"Equipped with his five senses, man explores the universe around him and calls the adventure Science."

Edwin Hubble

Abstract

Brown dwarfs and low-mass stars together comprise the group of galactic objects known as ultracool dwarfs. A number have been detected as radio sources – in some cases, emitting periodic radio pulses synchronised to the dwarf's known rotational period. Detections of optical variability in ultracool dwarfs have been primarily attributed to stellar rotation, with the modulations observed a consequence of either magnetic spots on the surface, the presence of atmospheric dust, or auroral emission. A combination of these mechanisms may be required to explain some dwarf lightcurves. Rotational estimates of ultracool dwarfs are typically obtained spectroscopically; however accurate estimates of true rotation velocities require knowledge of the dwarf's rotational inclination axes. Direct measurement of a rotational signature in photometric data however provides an unambiguous rotational period, and this information can be used to constrain dwarf inclination geometries.

In this thesis, we report on over ~ 160 hrs monitoring in I-band of multiple epochs from four ultracool dwarfs, spanning M tight binary dwarf 2MASS J1314203+132001A and L tight binary dwarf 2MASS J0746425+200032AB, the M9.5 dwarf BRI 0021-0214, and the L3.5 dwarf 2MASS J00361617+18211. This photometric campaign was carried out using the Galway Ultra-Fast Imager (GUFI) on the 1.8m Vatican Advanced Technology Telescope (VATT), on Mt. Graham, Arizona. All selected dwarfs exhibit periodic optical

variability, where periods of both secondary components for our binary samples were newly discovered.

This thesis discusses the use of two photometric analysis tools with the explicit aim of improving the quality of ground-based photometric measurements. Each data set was used to test the performance of the two systems. We find the LuckyPhot technique has obvious benefits to high precision photometry by reducing photometric errors, where the mean RMS error was reduced by $\sim 47\%$ with respect to the errors produced by the more standard GUF1 pipeline method.

This thesis also outlines a novel tool, Light Curve Fitter, which we apply to the binaries to investigate the presence of periodic photometric modulation in both binary members: refining the dominant member variability parameters, and searching for an elusive period of the weaker member. Light Curve Fitter is a python-based program, capable of detecting superposition of two sinusoidal waves to untangle the weaker components variability signature from that of the dominant source variability.

We identify a newly discovered optical variability in the primary and secondary components of ultracool dwarf binary 2MASS J1314203+132001AB and 2MASS J0746425+200032AB, respectively. The optical data presented for both systems shows strongly correlated emissions in terms of phase and temporal variability. We have also shown the A and B variability signals of both dwarf binaries 2MASS J0746425+200032AB and 2MASS J1314203+132001AB, respectively, to be extremely consistent and stable over multiple epochs. This stability had seen in both radio and spectroscopic data, and the mechanism driving these processes in different parts of the electromagnetic spectrum could perhaps be fundamentally linked.

We also investigate the orbital coplanarity of both binary dwarfs. Here the ability to deconvolve the inclination angle from the spectroscopic radial velocities, using direct estimates of the dwarf rotational periods, allows us to constrain the spin-orbit coupling of

the binary system. In the case of the L dwarf binary 2MASS J0746425+200032AB, we calculate the equatorial inclination angle of the binary rotation axes are in alignment with the orbital plane of the system to within 10 degrees, consistent with solar-type binary formation mechanisms. For the M7 dwarf binary 2MASS J1314203+132001AB, due to missing parameters for the primary component, we investigate a tentative alignment of the spin-orbital axes of the A component. We find that the equatorial inclination angle of the secondary member spin axes is largely consistent with being aligned perpendicularly to the orbital plane. Finally, we find the rotation axes of the two single dwarfs are not perpendicular to our line of sight.

"It is clear to everyone that astronomy at all events compels the soul to look upwards and draws it from the things of this world to the other."

Plato

Thesis Motivation

This work commenced in February, 2016 and initially started as an investigation of periodic photometric variability of four ultracool dwarfs spanning the \sim M7 - L3.5 spectral range - the M tight binary dwarf 2MASS J1314203+132001AB and L tight binary dwarf 2MASS J0746425+200032AB, the M9.5 dwarf BRI 0021-0214, and the L3.5 dwarf 2MASS J00361617+18211. Although all four targets have high spectroscopically derived rotation rates, we were motivated to conduct I-band optical observations in order to confirm photometric variability for 2MASS J00361617+1821, 2MASS J1314203+132001AB and 2MASS J0746425+200032AB, and to determine whether the optical periodicity in these objects existed and was stable over the years. In addition, we were motivated to remove the uncertainty around the possible periodicity of BRI 0021-0214, and to investigate the presence of optical modulation in the 2MASS J1314203+132001B and 2MASS J1314203+132001A, since no periodic optical variability had been detected from both so far. Knowledge of these rotation periods for both components of the binary dwarfs would allow us to investigate the orbital coplanarity of each system, and provide further insight into the astrophysics of these targets.

Another goal in this work was to investigate the performance of optimum aperture vs. standard (fixed) differential aperture photometry, aiming to produce more precise lightcurves with lower photometric scatter. This would allow us to improve lightcurve fits and to investigate secular stability of the rotation periods, amplitudes and phase of these dwarfs.

"Astronomy is useful because it raises us above ourselves; it is useful because it is grand... It shows us how small is man's body, how great his mind, since his intelligence can embrace the whole of this dazzling immensity, where his body is only an obscure point, and enjoy its silent harmony."

Henri Poincaré

Chapter I

Background to Ultracool Dwarf Stars

1.1 Introduction

For many years, brown dwarfs were considered to be the missing link between the massive gas planets and the lowest mass stars. The existence of brown dwarfs was predicted more than 30 years before they were first observed (Kumar, 1963; Hayashi and Nakano, 1963). The first study that confirmed the discovery of a brown dwarf was by Nakajima et al. (1995), who observed the cool brown dwarf Gliese 229B (Gl229B). The category of ultracool dwarfs consists of brown dwarfs and low mass stars, which together represent most of the stellar mass in the Milky Way Galaxy. Based on an extensive accumulation of theoretical and observational studies of their stellar properties, four spectral groups (late-M, L, T and Y) have been assigned to these stellar or sub-stellar objects.

This chapter is structured as follows: Section 1.2 is an overview of ultracool dwarf stars and their properties. Section 1.3 presents a summary of the physics of ultracool dwarf stars. We outline the thermonuclear processes of ultracool dwarfs in Section 1.4. In Section 1.5, we summarise the evolutionary models for sub-stellar objects that are adopted to predict temperature, luminosity, mass, gravity and other parameters. In Section 1.6, we briefly outline the spectral and atmospheric properties of late-M, L and T-type dwarfs. Section 1.7 outlines the magnetic activity in stellar and sub-stellar objects, and the mechanism that is responsible for generating radio emissions in both cases. Lastly, in Section 1.8, we discuss the various causes responsible for periodic optical modulation from ultracool dwarfs.

1.2 Ultracool Dwarf Stars

As already noted, ultracool dwarfs (UCDs) encompass brown dwarfs and low mass stars together. These very faint, dense and cool objects are very difficult to

detect and very hard to classify (Basri, 2000). These objects are found at, or below, the stellar-substellar boundary (end of the Hertzsprung-Russell (H-R) diagram), with a spectral class range of M7 and later (Kirkpatrick et al., 1997). UCDs are fully convective objects, with an effective temperature below 2500 K, which makes their atmospheres increasingly cool and neutral (Harding, 2012). Unlike the main sequence stars, these objects are not large enough to sustain thermonuclear fusion, and therefore have very low temperatures and luminosities. Indeed, it is extremely difficult to monitor UCDs more distant than 100 pc, even with the latest generation of large terrestrial telescopes. Today, about 15% of the known objects in the solar neighborhood are UCDs (Cantrell et al., 2013; Bartlett et al., 2017; Fernandes et al., 2019). The brown dwarf categories have hazy boundaries, they are too large to be planets and too small to be stars. Brown dwarfs have masses between ~ 13 and $75 - 80$ times the mass of Jupiter or ~ 0.0125 to 0.077 the mass of the Sun (Saumon et al., 1995, Basri, 2000). Objects with mass less than $\sim 0.07 - 0.08 M_{\odot}$ can never sustain thermonuclear hydrogen-burning (fusing H – He) in their core, like our Sun (Basri, 2000). Theory predicted that the presence of electron degeneracy before hydrogen-burning occurred could hinder the gravitational collapse of a star (Kumar, 1963). While this description can be considered to be a rough definition of a brown dwarf, it is not rigorous enough, considering that some higher mass brown dwarfs can accommodate some hydrogen fusion (Basri, 2000, Lane, 2008). Many evolutionary models (e.g., Burrows et al., 1993, Burrows et al., 1997, Baraffe et al., 1998, Chabrier et al., 2000, Burrows et al., 2001, Baraffe et al., 2003, Saumon and Marley, 2008, Dieterich et al., 2014, Baraffe et al., 2015, Dupuy and Liu, 2017) predicted a hydrogen-burning minimum mass limit of $70 - 80 M_{Jup}$ ($0.07 - 0.08 M_{\odot}$) for an object of solar metallicity, and $\sim 98 M_{Jup}$ for an object of zero metallicity. The central temperature for an object of solar metallicity is roughly 3×10^6 K, and the surface temperature is in the range of $\sim 1600 - 1750$ K with a luminosity of $6 \times 10^{-5} L_{\odot}$ (Ushomirsky et al., 1998). Several studies (e.g., Burrows et al., 1993; Reiners and Basri, 2009), showed that mid-M dwarfs ($\sim M3.5$) are

probably fully convective objects, believed to harbour high-pressure environments, and gradually losing their luminosity, gravitational energy and temperature over long timescales.

As already noted, brown dwarfs are not massive enough to ignite hydrogen steadfastly in their cores, but deuterium fusion can occur in brown dwarfs that are as little as $\sim 13 M_{Jup}$ ($\sim 0.012 M_{\odot}$), as it requires a lower temperature of initiation (Basri, 2000, Joergens, 2005). Also, dwarfs of mass heavier than $\sim 65 M_{Jup}$ ($\sim 0.06 M_{\odot}$) can fuse lithium (Basri, 2000). By the early 1990s, the so-called 'Li test' was used to distinguish between substellar and stellar objects, by detecting the Li absorption line at 6708 \AA in their atmosphere (Rebolo et al., 1992). The principle behind the lithium test is relatively simple, as stars cannot retain their lithium beyond $\sim 100 \text{ Myr}$ at most, because of the associated central temperature (Basri, 2000). This never happens in most brown dwarfs. Dantona and Mazzitelli (1985) found that objects whose mass is less than $\sim 60 M_{Jup}$ ($\sim 0.06 M_{\odot}$) never attain the minimum lithium burning temperature in their cores due to core degeneracy. However, this test is not a perfect indicator, since lithium is also detected in young stellar objects, which have not yet had enough time to deplete fully. Conversely, high-mass dwarfs can deplete their lithium if they are old enough (Lane, 2008; Harding, 2012). In the mid to late-T dwarfs, Li is in molecular form and therefore cannot be identified by the 6708 \AA absorption line, although it can be detected as a band near $\sim 15.5 \mu\text{m}$ (Burrows et al., 2001).

There is still some debate about the boundary between brown dwarfs and giant planets. Although the mass threshold for deuterium fusion is roughly $13 M_{Jup}$ (the lower mass limit of brown dwarfs), it has been revealed that planets can also burn deuterium at roughly $0.0012 M_{\odot}$ ($\sim 1.25 M_{Jup}$) (Hoxie, 1970; Joergens, 2005; Mollière and Mordasini, 2012; Bodenheimer et al., 2013). Brown dwarfs begin forming the same as ordinary stars, by gravitational collapse, whereas protoplanetary disks form giant planets (Burrows et al., 2001). The main

difference between these processes of formation is the need for giant planets to form a rocky core first, which for stars and brown dwarfs is not the case.

1.3 Interior physics of ultracool dwarf stars

This section is mainly based on Burrows et al. (1997), Basri (2000), Reid et al. (2000), Chabrier and Baraffe (2000) and Burrows et al. (2001).

The relation between pressure and other locally-varying parameters such as mass and temperature is known as the equation of state for stellar objects. While it is a challenge to calculate the equation of state for ultracool dwarfs, it necessitates taking partial pressure ionization, polarized and partially degenerate classical and quantum plasmas into consideration. The interior models of brown dwarfs exhibit typical conditions in the core involving densities of $10 \text{ g cm}^{-3} \lesssim \rho_c \lesssim 10^3 \text{ g cm}^{-3}$, temperatures T_c as low as $\sim 3 \times 10^6 \text{ K}$, and pressures of $P_c \sim 10^5 \text{ Mbar}$ (Burrows et al., 2001). The physics of low-mass stars relies on their masses. Studies have emphasized that stars $< 0.4 M_\odot$ (later than spectral type M3 – 3.5) are fully convective but still behave classically (Wright and Drake, 2016), whereas hydrogen-burning minimum mass stars are partially degenerate. This degeneracy is identified by the degeneracy parameter, $\psi = \frac{kT}{kT_F}$ where T_F is the electron Fermi temperature, which will indicate the degree of degeneracy ($\psi \rightarrow 0$ corresponds to full degeneracy (defined by Fermi-Dirac statistics)), while $\psi \rightarrow +\infty$ corresponds to the classical limit (Maxwell-Boltzmann). It should be noted that the degeneracy parameter ψ is of order unity and the temperature is the order of the electron Fermi temperature T_F . See Figure 1.1, which illustrates the relationships between the mass of ultracool dwarfs and substellar objects and their central temperatures, densities and degeneracy parameter.

It is important to calculate the polytropic index, which features in the Lane–Emden equation where the pressure is related to the density in the form:

$$P_c = K\rho_c^{(n+1)/n} \dots \dots \dots (1.1)$$

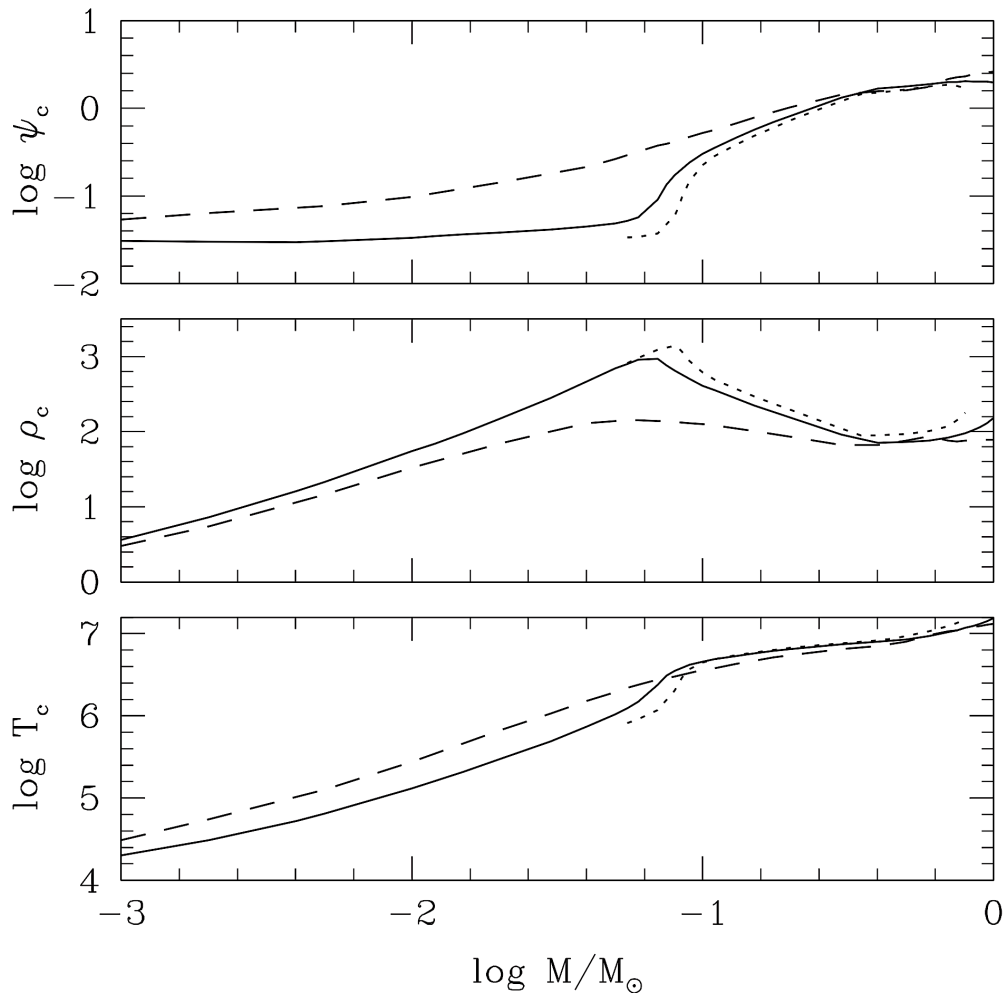


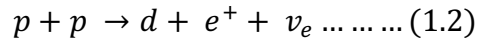
Figure 1.1 Plots of central temperature T_c (in K), density ρ_c (in g cm^{-3}), and degeneracy parameter ψ_c against the mass range of ultracool dwarf stars for objects with solar metallicity Z_\odot at 5 Gyr (solid line) and 10^8 yr (dashed line), and with a metallicity $Z = 10^{-2} Z_\odot$ at 5 Gyr (dotted-line). This was adapted from Chabrier and Baraffe (2000).

where n is a constant and known as the polytropic index, P_c and ρ_c are the central pressure and density, respectively, and K is a constant. For stars greater than $\sim 0.4 M_\odot$, the polytropic index changes slowly from $n = 3/2$ to $n = 3$ as the mass increases, due to the growing radiative core. Based on the standard stellar structure model, main sequence stars like our Sun have an index $n = 3$ polytrope (Pols, 2011), and P_c and ρ_c increase with increasing mass. In contrast, main sequence stars below $0.4 M_\odot$ become fully convective (with an index $n = 3/2$ polytrope) and so cannot possess a tachocline layer like our Sun. In these stars, radius (R) is proportional to mass (M), and central density increases with decreasing mass ($\rho_c \propto M^{-2}$), since the gas is still within the classical regime. For objects below the hydrogen-burning minimum mass, the electron degeneracy parameter, ψ , is nearly zero (full degeneracy). Because of this, the properties change, where the mass-radius relationship turns into $M \propto R^{-3}$, and the central density begins to decrease with decreasing mass $\rho_c \propto M^2$, yielding non-monotonic behavior of ρ_c and P_c with M . These relationships between mass and radius do not apply to objects that are subjected to partial degeneracy such as Jupiter or brown dwarfs, which all have similar radii.

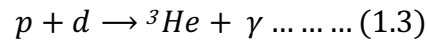
1.4 Thermonuclear Processes within Ultracool Dwarfs

Ultracool dwarfs begin just like their main-sequence siblings, as their formation follows the traditional theory of formation through the first stages of star evolution (Bodenheimer, 1978; Shu et al., 1987). This involves the collapse of an interstellar cloud of dust and gas, gravity tightly gathering the components and forming a very young star (protostar) at its centre. When gravitational contraction heats a protostar of mass greater than the hydrogen-burning minimum mass limit, when the core reaches a temperature and pressure high enough to trigger

thermonuclear fusion reactions in the core and ignite the proton-proton chain (pp – I):



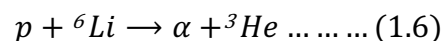
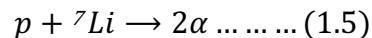
Equation 1.2 describes the thermonuclear fusion process of ultracool dwarfs (Burrows et al., 1993; Chabrier and Baraffe, 1997) , where p are free protons, d are deuterium ions, e^+ are positrons and ν_e are electron neutrinos. The deuterium generated in the first branch in the proton-proton chain (pp – I) can combine with another free proton to produce the light isotope of Helium, 3He .



Research by Hoxie (1970) predicted that objects greater than $\sim 0.0012 M_{\odot}$ ($\sim 1.25 M_{Jup}$) burn all their deuterium in a short time (between $0.1 < \tau < 10$ Myr) due to low deuterium abundance. About 95% of the total luminosity emits from the object during the deuterium-fusion process.



These reactions in Equations 1.3 and 1.4 are the chief source of the energy (more than $\sim 99\%$) for substellar objects ($\leq 0.07 M_{\odot}$), while pp – II reactions detailed below provide only $\sim 1\%$. For objects greater than $65 M_{Jup}$ ($\sim 0.06 M_{\odot}$) lithium isotopes Li are fused according to the following equations which form part of the pp-II branch:



As we mentioned before, the lithium depletion point occurs at ~ 100 Myr (Chabrier et al., 2000). Objects of mass $\geq 0.06 M_{\odot}$ burn their lithium, in contrast

to the hydrogen-burning minimum mass of $\sim 0.07 M_{\odot}$. It was thus because of the close proximity of the lithium burning point to the hydrogen-burning minimum mass point, the Li test was initially used to differentiate between substellar and stellar objects.

1.5 Evolution of Ultracool Dwarfs

There has been numerous research, e.g. Chabrier et al. (2000), Burrows et al. (2001) and Baraffe et al. (2015) to study the evolution of brown dwarfs, which relied largely on empirical spectra and evolutionary models. There is a considerable departure in the atmospheric conditions of ultracool dwarfs compared to the M-type dwarfs down to type M6. In comparison to stars like the Sun, the atmosphere of brown dwarfs and low-mass stars is cool enough to form neutral atoms, to have collisional excitation (absorbers and emitters) and many chemical molecular species, depending on factors such as temperature and gravity. In fact, the temperature and luminosity for sub-stellar bodies are unstable since the nuclear reactions described in Section 1.4 cannot be sustained for long and hence their radiative losses evolve. As shown in Figure 1.2, the temperature profile T_{eff} of sub-stellar objects decreases steadily after the initial protostellar contraction stage. While brown dwarfs of $\sim 79 M_{Jup}$ ($\sim 0.075 M_{\odot}$) can maintain temperatures of a few thousand Kelvin (for up to about 300 Myr), brown dwarf temperatures never stabilize after this time and gradually decrease over their lifetime.

As noted in Section 1.2, the hydrogen-burning minimum mass point is approximately $0.070 - 0.075 M_{\odot}$. The central temperature for solar-type metallicities at the hydrogen-burning minimum mass is as low as $\sim 3 \times 10^6$ K, the surface temperature range is $\sim 1600 - 1750$ K (Ushomirsky et al., 1998), and the luminosity is $\sim 6 \times 10^{-5} L_{\odot}$ (Ushomirsky et al., 1998; Burrows et al., 2001). The

essential evolutionary quantities in the formation of substellar-mass objects can be adequately estimated, using the relationships below that follow approximate power-laws (Burrows et al., 2001):

$$L \sim 4 \times 10^{-5} L_{\odot} \left(\frac{10^9 \text{ yr}}{t}\right)^{1.3} \left(\frac{M}{0.05 M_{\odot}}\right)^{-2.64} \left(\frac{k_R}{10^{-2} \text{ cm}^2 \text{ gm}^{-1}}\right)^{0.35} \dots \dots \dots (1.7)$$

$$T_{\text{eff}} \sim 1550 \text{ K} \left(\frac{10^9 \text{ yr}}{t}\right)^{0.32} \left(\frac{M}{0.05 M_{\odot}}\right)^{0.83} \left(\frac{k_R}{10^{-2} \text{ cm}^2 \text{ gm}^{-1}}\right)^{0.088} \dots \dots \dots (1.8)$$

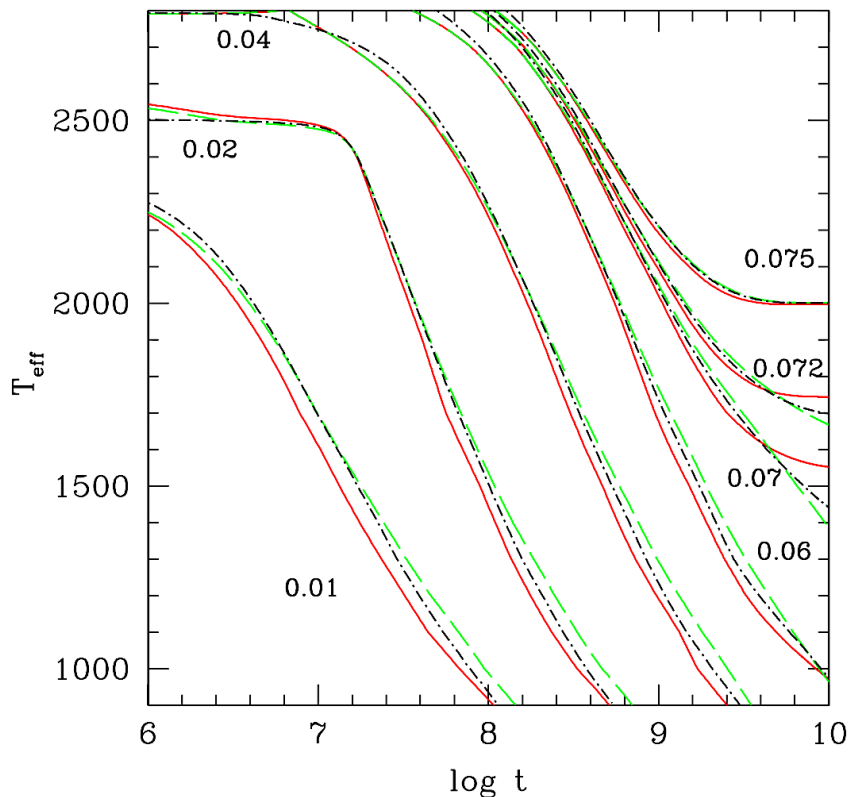


Figure 1.2 Effective temperature T_{eff} vs. time ($\log t$, years) for different masses (in M_{\odot}) and sets of atmospheric models. The solid red lines represent DUSTY models (with dust opacity), which takes into account turbulent mixing in atmospheric areas. The dotted green lines correspond to COND models (no dust opacity), which relates to inefficient atmospheric mixing. The black dashed-dotted lines show the NextGen models (no dust formation), which are based on dust-free environments (Allard et al., 1996; Hauschildt et al., 1999). This plot was taken from Chabrier and Baraffe (2000).

where k_R represents the mean opacity. Note that these relationships are valid for solar-type metallicities, whereas, for other atmospheric opacity prescriptions (such as for silicate clouds) different solutions to the above equations will be obtained (Burrows et al., 2001).

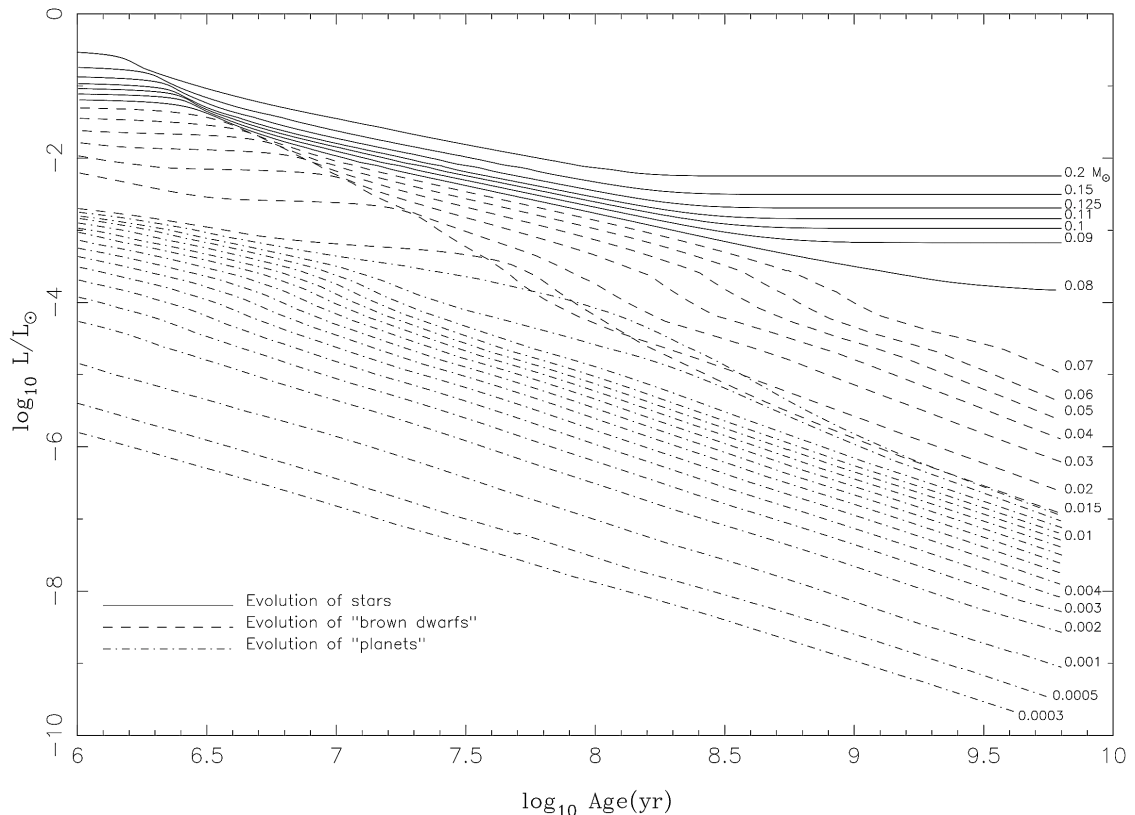


Figure 1.3 The evolution of the luminosity (L/L_{\odot}) of M dwarfs and sub-stellar objects vs. time (in yr). The solid, dashed and dot-dashed lines correspond to stars, brown dwarfs and planets, respectively, whose masses are marked (in M_{\odot}). This figure was taken from Burrows et al. (1997), who designate brown dwarfs as objects that can have deuterium fusion (above $\sim 0.0012 M_{\odot}$), whereas they define planets as objects that do not have enough mass to burn deuterium - although, as noted in Section 1.2, the non-deuterium-burning basis of the planet definition has since been questioned. The lowest three curves in this plot correspond to Saturn ($\sim 0.3 M_{Jup}$), half the mass of Jupiter and one Jupiter mass. As can be seen from the curves, there are luminosity bumps between 10^8 and 10^9 yrs for stars and brown dwarfs, due to the formation of silicate and iron grain.

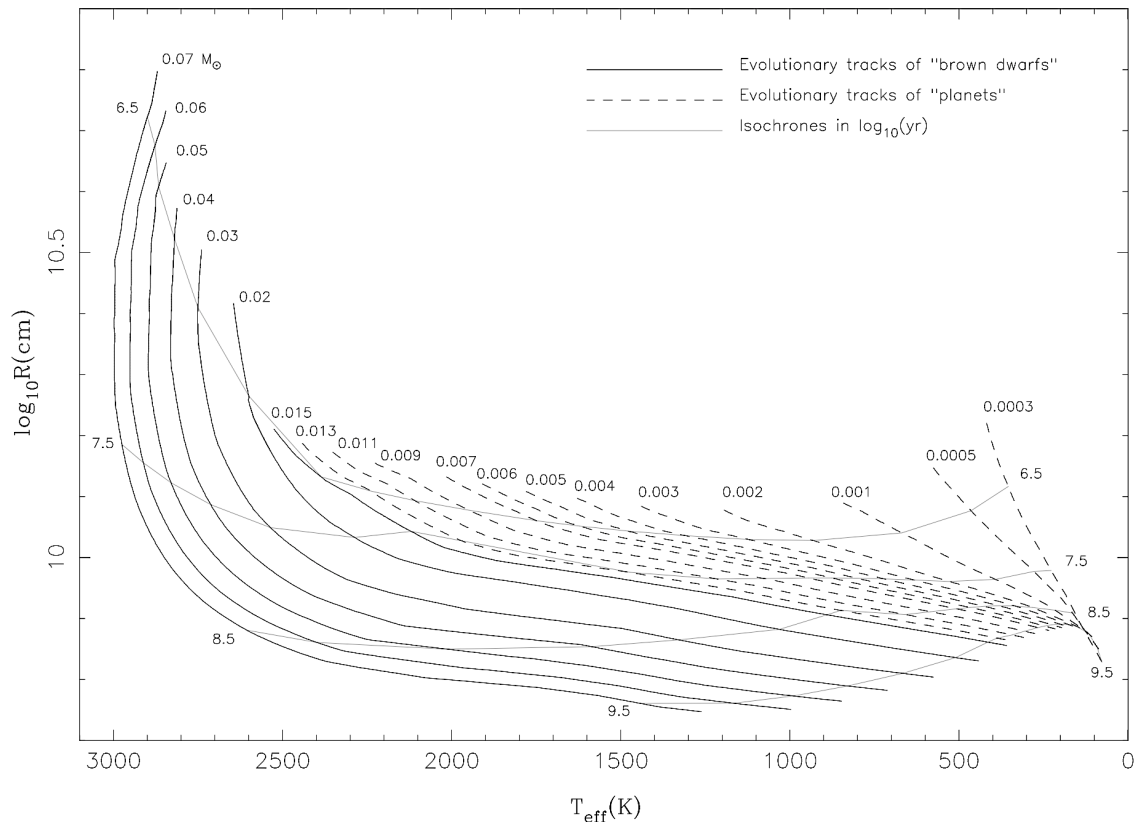


Figure 1.4 The evolution of radius (R) with effective temperature (T_{eff}), for different masses (from Saturn mass ($0.0003 M_{\odot}$) to the hydrogen-burning minimum mass ($0.07M_{\odot}$)). The brown dwarfs and planets are shown as solid and dashed curves, respectively. This evolutionary model is shown for a range of 6.5 - 9.5 log years (~ 300 Myr - 3 Gyr). As is clear from the plot, the radius of brown dwarfs decreases steadily with time, possibly due to compression factor due to increasing degeneracy pressure over their lifetime (Burrows et al., 1993). This plot was taken from Burrows et al. (1997).

Evolutionary models by Burrows et al. (1997) and Chabrier et al. (2000) predict that the temperatures and luminosities of brown dwarfs change dramatically with time (Figure 1.2 & 1.3). Because of their low temperatures and extremely low luminosities, this makes them very difficult to detect. On the other hand, the radius of the brown dwarf has a steady evolution over its lifetime as the models predict (Burrows et al., 1997; Figure 1.4).

The mass and radius relationships for low mass stars were obtained by Burrows et al. (1993), Marley et al. (1996) and Burrows et al. (2001), where g represents the surface gravity:

$$M \sim 35M_{Jup} \left(\frac{10^5}{g}\right)^{-0.64} \left(\frac{T_{eff}}{1000K}\right)^{0.23} \dots \dots \dots (1.9)$$

$$R \sim 6.7 \times 10^4 km \left(\frac{10^5}{g}\right)^{0.18} \left(\frac{T_{eff}}{1000K}\right)^{0.11} \dots \dots \dots (1.10)$$

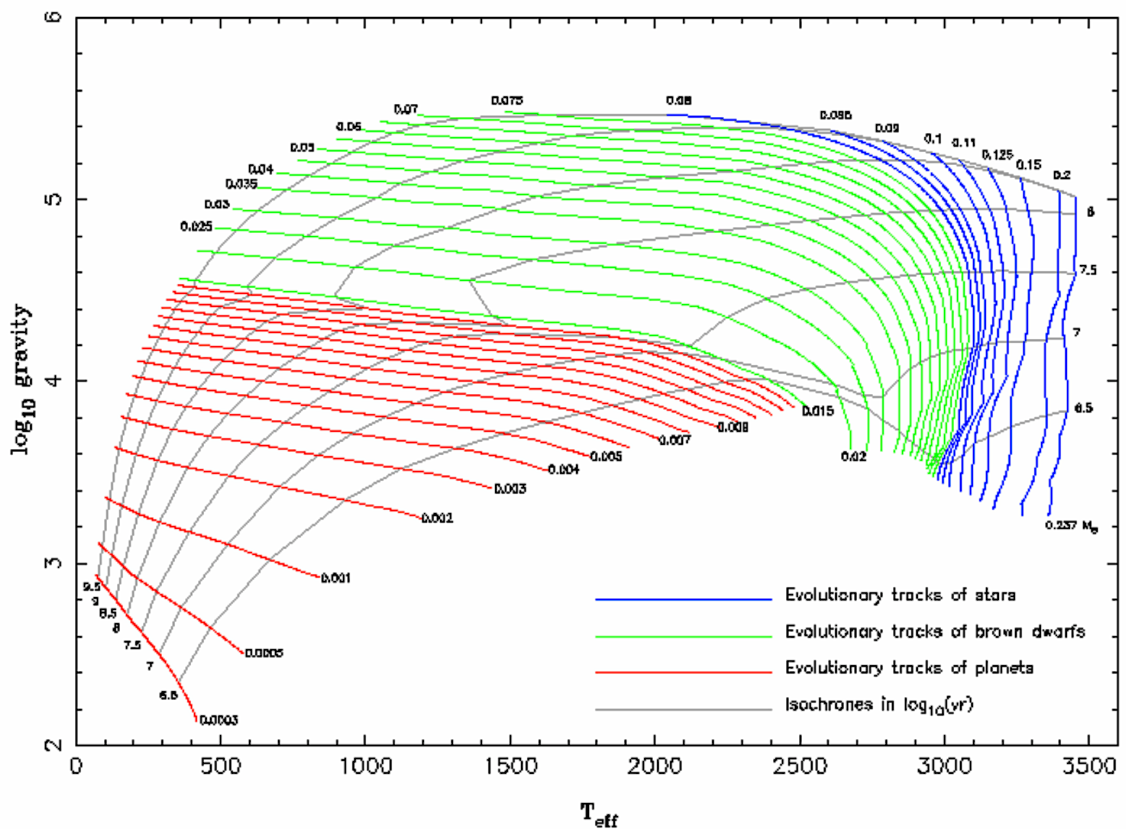


Figure 1.5 The evolution of \log_{10} gravity (in cgs units) vs. effective temperature T_{eff} (in K), for M-dwarfs, sub-stellar and planetary objects. These evolutionary tracks are shown for a range of \log 6.5 - 9.5 years. The evolutionary tracks of brown dwarfs, planets and stars are shown as solid green, red and blue lines, respectively. This plot was taken from Burrows et al. (1997).

The surface gravity which depends only on radius and mass ranges from $\log g \approx 4.4$ at $\sim 1 M_{\odot}$ (like our Sun), $\log g \approx 5.5$ for $0.070 M_{\odot}$ (the hydrogen-burning minimum mass) and $\log g \approx 3.4$ for objects at the deuterium-fusion minimum mass ($\leq 0.0012 M_{\odot}$). Figure 1.5 shows the variation of $\log g$ with T_{eff} , as the gravity increases with time in all cases. Note that in the case of massive brown dwarfs, the temperature remains stable or increases slightly due to gravitational contraction, before irresistibly decreasing in later times.

1.6 Atmosphere and Spectral Classification of Late-M, L and T-type Dwarf Stars

The atmosphere of an ultracool dwarf plays a key role in determining the evolution and appearance of the object, despite being a small fraction of the total mass (Marley and Robinson, 2015). The relatively cool, dense atmosphere of ultracool dwarfs is regarded as a good environment for molecular particulates formation and hence atmospheric chemistry (Visscher et al., 2006). The atmosphere regulates the object's spectral signature, as it imprints on the thermal radiation emitted the different signatures of gases, condensates, gravity, and temperature profiles. For this reason, our ability to understand the atmospheres of ultracool dwarfs depends on our understanding of the spectrum and evolution over time of these cool objects (Marley and Robinson, 2015). It has now been well established that the transition from partially convective configurations to fully convective interiors (not possessing a tachocline layer) occurs in the mid-M stars ($\sim M3$ spectral type) around a mass of $\sim 0.35 M_{\odot}$ (Reiners and Basri, 2009; Harding, 2012; Wright and Drake, 2016).

At T_{eff} about 3500 K (spectral class $\sim M3$), hydrogen and carbon are present in the form of H_2 and CO respectively, while excess oxygen is bound in titanium(II) oxide (TiO), vanadium(II) oxide (VO) and H_2O , and less so in the form of OH and

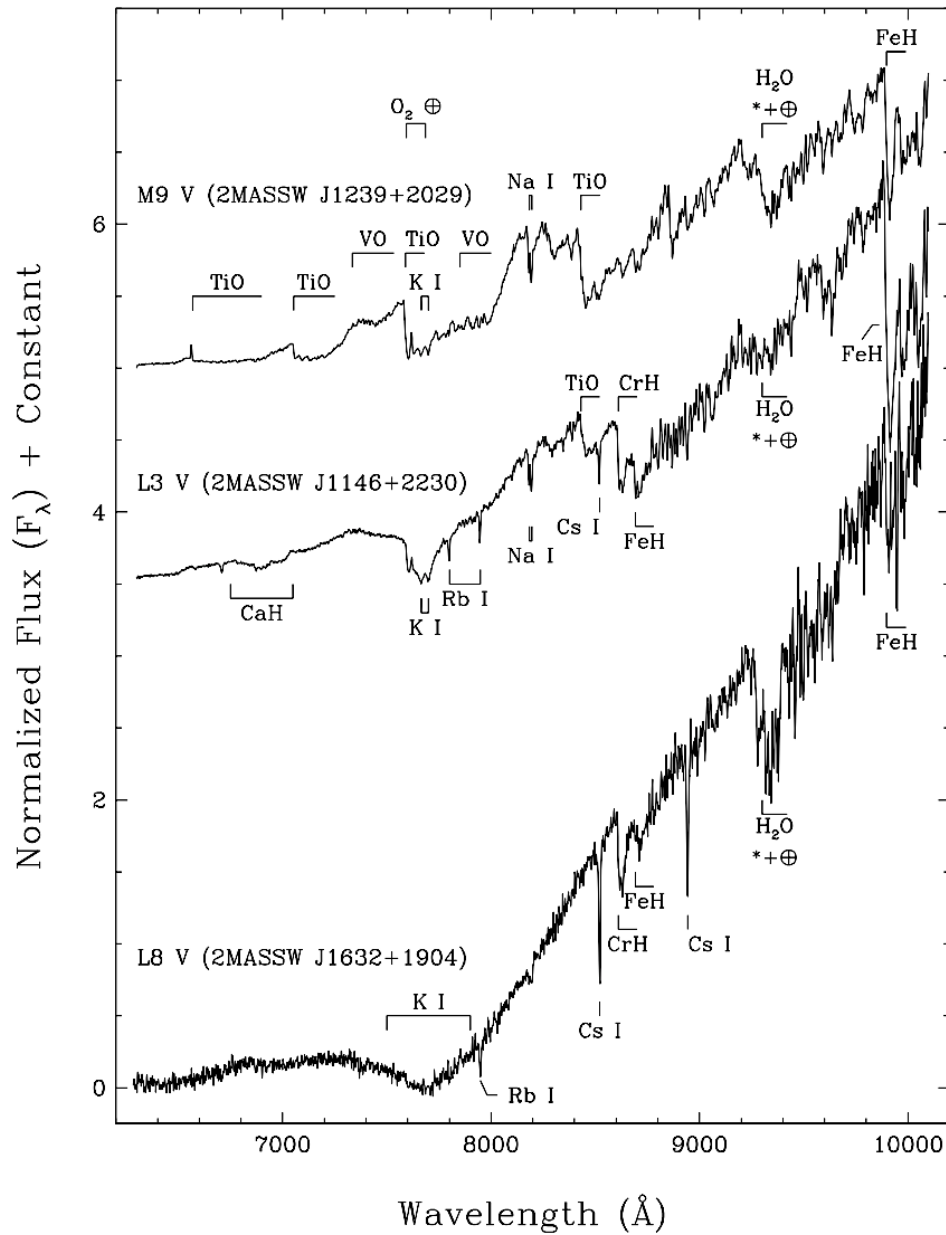


Figure 1.6 Spectra of late-M (M9), early- to mid-L (L3), and late-L (L8) dwarfs for comparison. Prominent features in the spectra such as hydride bands (FeH , CrH , CaH , and MgH), metal hydrides (FeH , CaH , and MgH), strong absorption lines (TiO , VO , and H_2O) and alkali lines (K , Na , Rb , Cs) are indicated. There is an obvious weakening/disappearance of oxide absorption (TiO) features in the L dwarfs spectrum, while features such as alkali and hydride bands (e.g. FeH and CrH) are prominent. The $Na I$ line becomes gradually weaker as we move down the spectral sequence. In addition, the slope after $\sim 7600 \text{ \AA}$ is increasing due to the exceptional broadening of the $K I$ resonance doublet, which contributes to the color. This plot is adapted from Kirkpatrick et al. (1999).

O molecules (Fegley Jr and Lodders, 1996). Signatures of metal oxides and metal hydrides such as (*FeH*, *CaH*, and *MgH*) are found in the spectrum at the temperature of this regime, and absorption lines are prominent for *TiO* and *VO* at optical wavelengths and in the infrared for *H₂O* and *CO* (Figure 1.6). Thus, the strong presence of *TiO* and *VO* absorption lines in the spectra are characteristic of the M dwarf spectral class (Kirkpatrick et al., 1991; Kirkpatrick et al., 2000). However, the *TiO* and *VO* bands become much less prominent at $T_{eff} \sim 2000$ K or so, with a small amount of *TiO* remaining in the spectrum (Kirkpatrick et al., 1999).

Based on spectroscopic observations, the subsequent spectral class, the L dwarfs, have been shown to be cooler than type M dwarfs, with an effective temperature in the range 2000 ~ 1300 K (Kirkpatrick et al., 1999). They are defined by spectroscopic signatures in the optical region of the spectrum, where metallic oxides absorption (*TiO* and *VO*) lines are replaced by metallic hydride emission bands (*FeH*, *CrH*, *MgH*, and *CaH*) and the dominance of neutral alkali metal lines such as *Li*, *Na*, *K*, *Cs*, and *Rb* and *H₂O* and *CO* molecular absorption lines (Figure 1.6 & Figure 1.7) (Kirkpatrick et al., 1999). Due to the presence of chemical particulates (such as *Ca*, *Al*, *Fe*, *Si*, and *Mg*), the opacity level changes (Kirkpatrick et al., 1999; Martín et al., 1999).

At T_{eff} about 1300 - 1500 K, a slow transition takes place in the equilibrium form of carbon monoxide (*CO*) molecules to become methane (*CH₄*). This 1300K boundary led to the definition of a new spectral type of UCD, initially dubbed 'methane dwarfs', and later the T-dwarfs (Figure 1.7). Gl 229B (which orbits the red dwarf Gl 229A) became the prototype of the T dwarfs, after methane absorption features were revealed in its spectrum (Oppenheimer et al., 1995). The T dwarf optical spectrum is characterized by a lack of metal hydrides, a greater *H₂O* absorption compared to L dwarfs and a steeper spectral slope, in addition to methane absorption bands that dominate in their spectra (Figure 1.7).

For an in-depth discussion of spectral type L and T dwarfs, we refer the reader to Burgasser (2001); Burgasser et al. (2002); Kirkpatrick (2005).

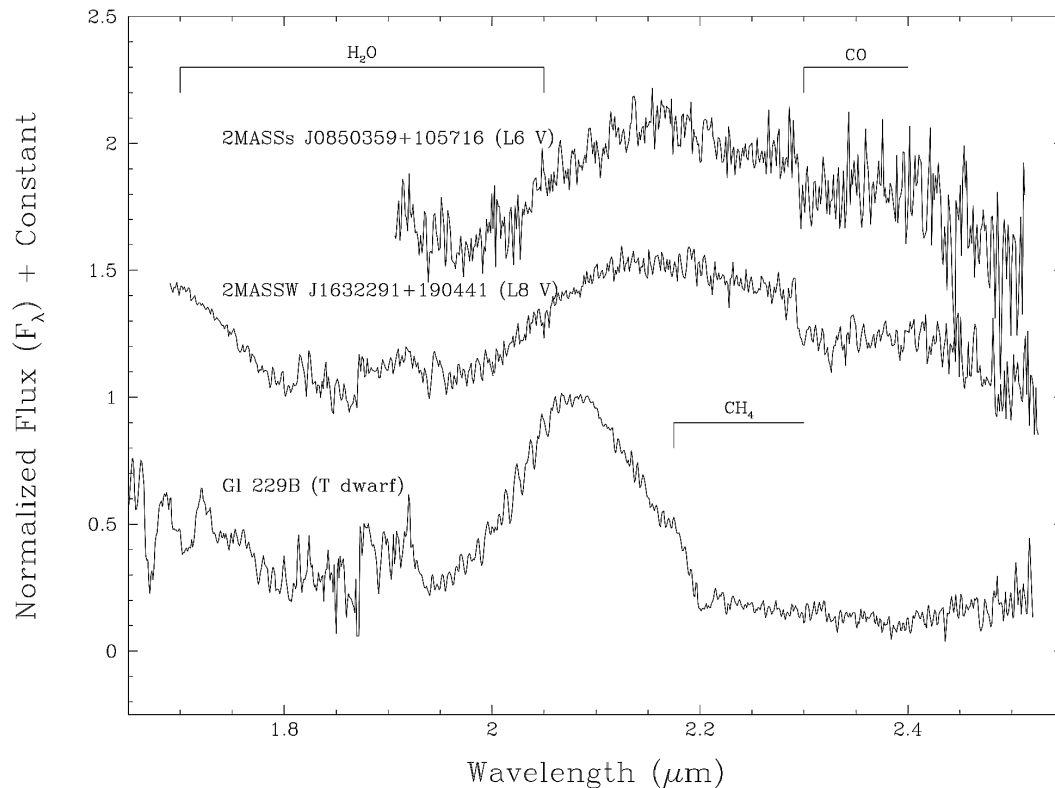


Figure 1.7 Near-infrared spectra of a mid-L (2MASS J0850359+105716), a late-L (2MASS J1632291+190441) and a T dwarf (Gl 229B) for comparison. In the spectrum of the late-L dwarfs, we note the presence of a CO absorption band and the absence of methane (CH_4) absorption features. We also point out that in the infrared, H_2O and CH_4 absorption bands dominate. This Figure was taken from Kirkpatrick et al. (1999).

1.7 Radio Emission Processes from Stellar and Substellar Regions

In this section, we present an overview of the different radiation mechanisms that are thought to play a role in radio emissions from stellar and sub-stellar objects.

Radio observations from the most massive O-type stars down to the very low mass dwarf stars play a fundamental role in understanding the outer atmospheres of stars. Radio emissions from the sun and stars arise from several different phenomena, and their characteristics may vary depending on the amount of energy associated with the event (Dulk, 1985; Seaquist, 1993). It has now been well established that there are a number of mechanisms that may be responsible for non-flaring, steady and quiescent emissions (usually caused by incoherent radiation processes), in addition to intense and extremely energetic events such as solar flares activity (usually caused by coherent radiation processes) (Dulk, 1985).

Much of the radio radiation observed is caused by the collision excitation as electrons accelerate or deflect when they travel through Coulomb fields and collide with ions, causing deceleration or braking, or charged particles. Electrons may collide with the nucleus, so electrons are either slowed down or entirely stopped by the force of any atoms they encounter. The kinetic energy of electrons is converted into photons. This process is referred to as thermal bremsstrahlung or 'free-free' emission (Dulk, 1985; Shu, 1991; Seaquist, 1993; Güdel, 2002; Rybicki and Lightman, 2008). For electrons that are mildly relativistic ($\gamma < 2$ or 3), gyrosynchrotron radiation arises from considerable acceleration due to spiralling around magnetic field lines (Dulk, 1985; Seaquist, 1993; Güdel, 2002; Wu et al., 2019). These emission processes are known as incoherent radiation processes. Two other incoherent emission processes, synchrotron emission and gyroresonance emission (the alternative name is cyclotron), are also present in many systems, but for electrons with highly relativistic energies ($\gamma \gg 1$) and nonrelativistic particles ($\gamma \approx 1$), respectively (Dulk, 1985; Seaquist, 1993; Güdel, 2002).

One form of coherent radio-emitting process is the plasma emission, which can occur at the plasma frequency. However, other observed kinds of coherent

emissions are believed to occur when there is instability in the plasma, such as electron cyclotron maser (ECM) emission. It is believed that these particle – wave plasma instabilities could be caused by gyrating electrons in the magnetic field lines oscillating in resonance with the electric field lines of electromagnetic waves at a particular frequency (Dulk, 1985; Seaquist, 1993). This emission is produced near the electron cyclotron frequency:

$$\nu_c \approx 2.8 \times 10^6 B \text{ Hz} \dots\dots\dots (1.11)$$

where ν is frequency in Hz and B is field strength in Gauss. These two types of emission have gained increasing attention both for solar and stellar bursts; for details see Dulk (1985); Seaquist (1993); Güdel (2002); Benz (2002). The ECM mechanism was theoretically predicted by Twiss (1958); Gaponov (1959a); Gaponov (1959b); Schneider (1959), then experimentally by Pantell (1959). This mechanism could be responsible for the excessively high-energy radiation generated in magnetized plasma environments (Treumann, 2006). The necessary condition for this plasma to host the maser (Microwave Amplification by Stimulated Emission of Radiation), is instability in the plasma along with a strong magnetic field (Dulk, 1985; Treumann, 2006).

Over the past two decades, the ECM instability mechanism has gained increasing attention as a source of radio emission bursts in ultracool dwarfs magnetospheres, although it is possible to detect other radiation processes that may be a source of the non-varying quiescent component of the radio emission (for details, see Hallinan et al. (2008); Harding (2012)). Maser activity is thought to be the cause of certain spectral types of solar and stellar radio bursts (e.g., Twiss, 1958; Mangeney and Veltri, 1976; Dulk and Marsh, 1982; Bingham et al., 2001; Kellett et al., 2002; Treumann, 2006). Other studies (e.g., Melrose, 1976; Hewitt et al., 1981; Zarka, 1998) pointed out that the ECM mechanism is likely to dominate in magnetospheres of planets such as Jupiter, as it explains the observation of Jovian decametric emissions. Also, the ECM mechanism has been

suggested to be responsible for other intense radio emissions, such as the auroral kilometric radiation of the Earth (Wu and Lee, 1979; Pritchett, 1984a; Pritchett, 1984b).

It is widely believed that the magnetic field of high mass stars is generated by so-called the $\alpha\Omega$ – dynamo (Parker, 1975). Magnetic fields are predominately produced by the rotation of a conductive charged fluid, which induces an electric field across the magnetic field. The production of more electric field can drive electric current and thereby produce a magnetic field, and so the magnetic field loop continues. Poloidal and toroidal magnetic fields (in the case of Sun-like stars) are widely believed to be generated when the outer convective zone meets the inner radiative zone. Between these two zones, there is the transition region kno-

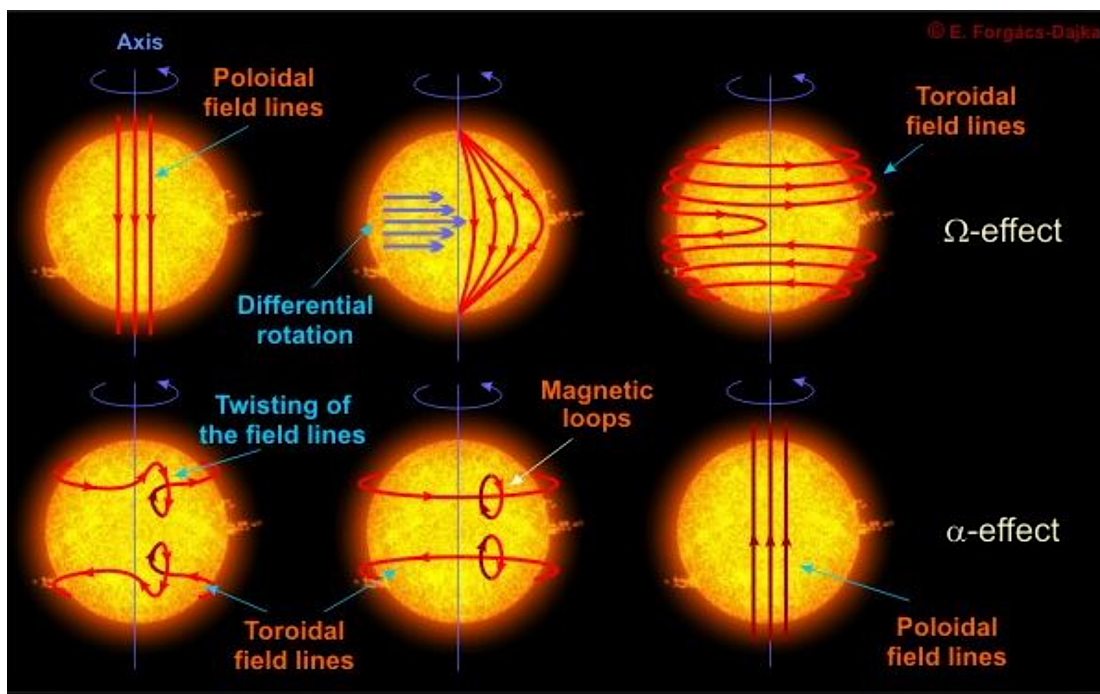


Figure 1.8 This series of processes called the $\alpha\Omega$ -dynamo (Ω -effect and α -effect) can produce a self-reinforcing magnetic field. This Figure is adopted from: <https://www.crediblehulk.org/index.php/2017/01/12/the-solar-dynamo-the-physical-basis-of-the-solar-cycle-and-the-suns-magnetic-field/>.

-wn as a 'tachocline', which contains a strong differential rotation at the base of the solar convective zone that converts the weaker poloidal (meridional) magnetic fields into stronger toroidal (azimuthal) magnetic fields, and vice versa (e.g., Ossendrijver, 2003; Howe, 2009). These magnetic fields are brought through magnetic buoyancy to the stellar surface. However to sustain the dynamo cycle, the process begins again when the rotation of the star once again produces poloidal magnetic fields that are moved to the transition region (tachocline), and so on.

Stellar differential rotation stretches out and winds the magnetic field lines around the Sun, which results in transforming poloidal magnetic fields into toroidal magnetic fields: this phenomenon is called the Ω -effect (Figure 1.8) (Bushby and Mason, 2004). In contrast, the α effect is that magnetic field lines are reversed and twisted into loops of field, due to the upthrust of flux tubes of magnetic fields from the surface of a star which converts toroidal magnetic fields to poloidal magnetic fields. Together, these two effects comprise the $\alpha\Omega$ dynamo (Figure 1.8) (Bushby and Mason, 2004; Harding, 2012). Therefore, strong stellar fluid motions generate magnetic stresses by dragging magnetic field lines (Harding, 2012). In fact, the energy needed to maintain a corona and chromosphere can be provided by releasing magnetic stresses. Indicators like the CaII K absorption line, chromospheric and coronal X-ray emission and H_{α} emission are often used as reliable tracer tools to indicate the presence of magnetic fields in main sequence stars (Schrijver et al., 1989; Pevtsov et al., 2003).

The $\alpha\Omega$ -dynamo is widely believed to hold with spectral classes ranging from F to early-M, while the dynamo breaks down around spectral class M3/M4 (around a mass of 0.3 - 0.4 M_{\odot}), where stars transition from partially convective (Sun-like) and develop fully convective interiors. Despite this, previous studies have shown that magnetic activity is prevalent in stars that are cooler than M4, where stars can produce kilogauss magnetic field strengths without the help of tachocline

shear (Saar and Linsky, 1985; Johns-Krull and Valenti, 1996; Donati et al., 2006; Reiners and Basri, 2007; Browning, 2008). Moreover, given that atmospheres of ultracool dwarfs become increasingly neutral and cool, and therefore have a higher electrical resistivity, dynamo theory originally suggested that these dwarfs could potentially generate small-scale fields, with a turbulent dynamo, or alternatively generate large-scale, non-axisymmetric fields. Observational studies have, however, revealed a large-scale axisymmetric magnetic field in the M4 dwarf V374 Peg via spectroscopic magnetic mapping of its surface (Donati et al., 2006). In addition, Zeeman Doppler Imaging of M type stars shows a shift in the geometry of the magnetic field from toroidal and non-axisymmetric fields in M0 - M3 dwarfs to poloidal axisymmetric fields in M4 stars. This shift coincides with the migration from partially convective to fully convective interiors and may provide further evidence of a change in the dynamo mechanism (Donati et al., 2008; Morin et al., 2008).

Alternative dynamos have been proposed for magnetic field generation in fully convective dwarfs, such as the α^2 -dynamo, which is based on 3-dimensional magnetohydrodynamic simulations that would produce large-scale magnetic fields for low-mass stars, brown dwarfs, and probably gaseous planets (Chabrier and Küker, 2006). Indeed, many studies indicated that the underlying magnetic dynamos could be very similar in brown dwarfs, low-mass stars and giant planets (Christensen et al. 2009; Morin et al. 2011); however, this approach is currently under study (see Kao et al. 2016). The α^2 effect in magnetic field generation indicates the effects of stratification and rotation of fluid, assuming no differential rotation. Chabrier and Küker (2006) found that this model dynamo efficiently generates large-scale, non-axisymmetric magnetic fields, in which the α^2 effect produced several kiloGauss field strengths for fully convective stars such as very late-type stars and brown dwarfs, where larger magnetic field strengths can be generated from faster rotating bodies.

Cooler than spectral type $\sim M7$, there is a distinct change in magnetic activity. A number of initial studies have shown that the magnetic activity traced in H_α and coronal X-ray emission decreases sharply, while H_α and X-ray flares were detected in a small number of objects, despite an apparent decline in quiescent emission (Reid et al., 1999; Liebert et al., 1999; Gizis et al., 2000; Rutledge et al., 2000; Liebert et al., 2003; Fuhrmeister and Schmitt, 2004; Rockenfeller et al., 2006; Robrade et al., 2010). Indeed, this detection of H_α and X-ray flares effectively supports the presence of chromospheric and coronal activity. It is beli-

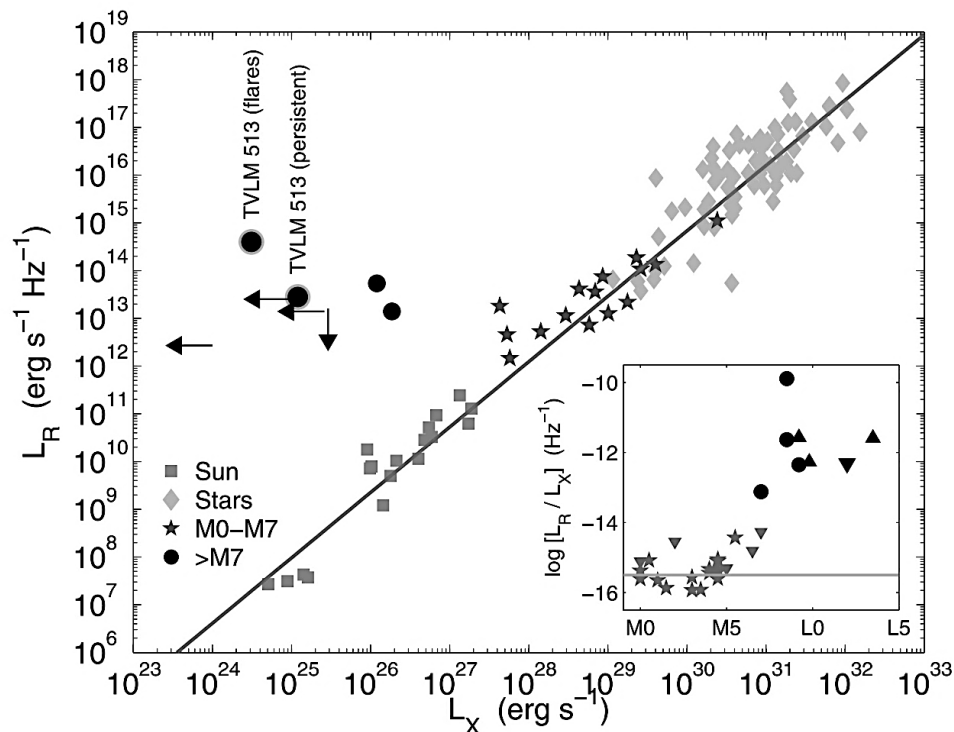


Figure 1.9 Plot of radio against X-ray luminosity for magnetically active stars including the Sun. The tight correlation between L_R and L_X is unambiguous, but this correlation begins to breakdown beyond spectral type M7. The observational data for late-M and L dwarfs are taken from Rutledge et al. (2000), Berger et al. (2001), Berger et al. (2002), Berger (2005), Berger et al. (2006), Burgasser & Putman (2005), and Audard et al. (2007), while other data are adapted from Güdel (2002). The inset plot confirms the departure from a constant ratio of radio to X-ray luminosity, for late M and L spectral types. This Figure is taken from Berger et al. (2008).

-eved that the overall decline in magnetic activity is due to reducing atmospheric ionization levels with spectral type (below 2300 K) or probably a change in the nature of the magnetic dynamo (Berger, 2002; Mohanty et al., 2002). The magnetic fields become decoupled in these atmospheric conditions, reducing the necessary injection of the magnetic field energy needed to heat the plasma. Furthermore, as a result of declining conductivity, it becomes difficult to generate current, which would indicate that it is not possible to maintain large-scale configurations (Mohanty et al., 2002).

Since the rotation of the stars plays an important role in the magnetic dynamos, the relationship between the magnetic activity and the rotational period can provide a unique window for understanding the dynamo mechanism. In the case of solar-type stars, higher levels of H_{α} and coronal X-ray emissions are emitted by more rapidly rotating stars. But the rotation - magnetic activity relationship has been shown to break down for objects beyond spectral type $\sim M8$, as there is no indication of these activity markers in many rapid rotators (Neuhaeuser et al., 1998; Gizis et al., 2000; Mohanty and Basri, 2003; West et al., 2004; Berger et al., 2009a; Reiners et al., 2010; Konopacky et al., 2010; Williams et al., 2013).

There is a tight correlation between the radio and the peak X-ray luminosities of a wide range of magnetically active stars up to spectral type M7, known as the Güdel–Benz relations (Guedel and Benz, 1993; Benz and Güdel, 1994). However, the radio emission from the M9 brown dwarf LP 944-20 observed by Berger et al. (2001) diverged from the Güdel–Benz relations by several orders of magnitude, and subsequent detections have proved that this divergence is not uncommon e.g. Berger et al. (2008) and Berger et al. (2009a) (Figure 1.9). Recently, a study carried out by Williams et al. (2013) revealed that differences in radio activity and other activity indicators (which are inconsistent with the Güdel–Benz relations) may be possible for later spectral types and faster rotational velocities ($v \sin i$) $> 20 \text{ km s}^{-1}$.

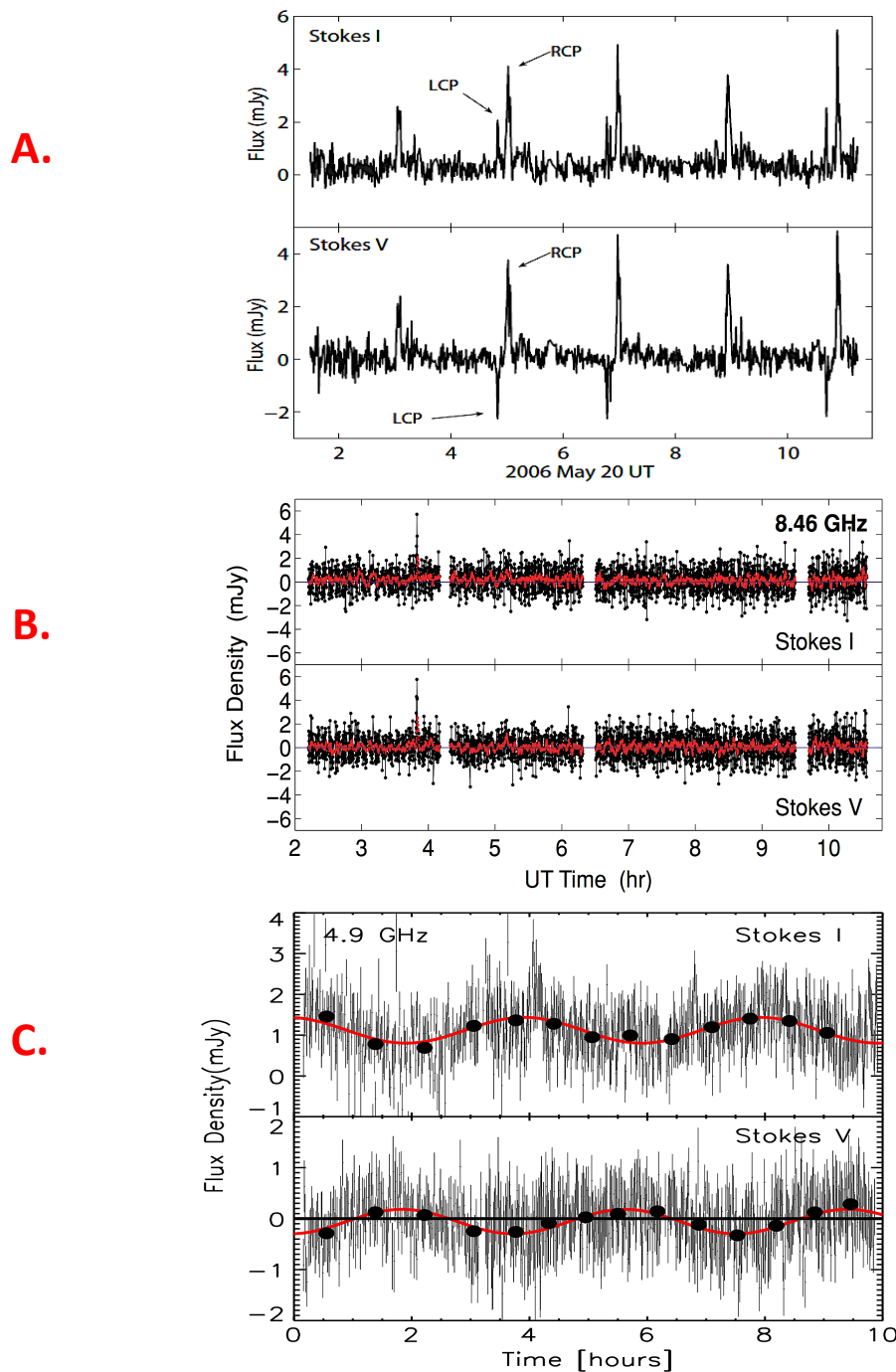


Figure 1.10 Three samples of radio lightcurves from ultracool dwarfs. For each example of lightcurves, the top plot displays the total intensity (Stokes I) while the bottom plot contains the circularly polarized emission (Stokes V). **(A)** TVLM 513-46 at 8.46 GHz showing significant periodic double pulses (100% right and left circularly polarized emission), occurring every ~ 1.96 hrs, and weak quiescent emission. This Figure is adopted from (Hallinan et al., 2007). **(B)** L dwarf binary 2M J0746+20 at 8.46 GHz show-

Caption of Figure 1.10 continued from previous page

-ing a strong single short-duration burst, right circularly polarized, that occurs at ~ 4 UT, and quiescent non-variable emission. This Figure is taken from (Berger et al., 2009b). (C) 2M J1314+13AB at 4.86 GHz showing that the radio emission is varying sinusoidally at 4.86 GHz. This Figure is adopted from (McLean et al., 2011).

In the case of ultracool dwarfs, the decline in magnetic activity seen in $H\alpha$ or coronal X-ray emissions does not indicate a decrease in field strength or filling factor (Lynch, 2014). Indeed, past observations have revealed quiescent and flaring non-thermal radio emissions from some dwarfs (late M type dwarfs, L dwarfs, and T dwarfs), confirming that some ultracool dwarfs are still capable of producing intense magnetic fields (Berger et al., 2001; Berger, 2002; Berger et al., 2005; Burgasser and Putman, 2005; Osten et al., 2006; Hallinan et al., 2006; Berger, 2006; Antonova et al., 2007; Hallinan et al., 2007; Berger et al., 2009b; Route and Wolszczan, 2012; McLean et al., 2012; Williams et al., 2013; Hallinan et al., 2015; Kao et al., 2016).

It has been well established that ultracool dwarfs with detectable radio emissions can exhibit a wide range of behaviors (Figure 1.10). A few surveys (e.g., Berger et al., 2008; Ravi et al., 2011) have reported quiescent radio emission of ultracool dwarfs, where this emission is broadband, does not vary detectably, and has low levels of circular polarization. Several dwarfs have lightcurves that exhibit variation in agreement with the rotation period. Either these lightcurves show smooth variations (e.g., McLean et al., 2011) or have short highly circularly polarized flare peaks ($\sim 100\%$) of very short duration (e.g., Burgasser and Putman, 2005; Hallinan et al., 2007). It appears that the underlying mechanisms that give rise to this radio emission are both incoherent and coherent. Berger (2002) proposed that incoherent gyrosynchrotron emission from a non-thermal distribution of mildly relativistic electrons could be a cause of the

persistent and flared emission from TVLM 513-46. The electron cyclotron maser ECM instability is an alternative mechanism accepted to be responsible for the pulsed emission from ultracool dwarfs such as TVLM 513-46546, 2MASS J0036+18 and LSR J1835+3259 (Hallinan et al., 2006; Hallinan et al., 2007; Hallinan et al., 2008; Berger et al., 2009; Williams & Berger 2015). This emission is responsible for the detected 100% circularly polarized periodic burst (Figure 1.10, panel A). Equation 1.11 implies the presence of kilogauss magnetic fields of ~ 3 kG in a large-scale stable magnetic field configuration, which is consistent with the typical average magnetic field strengths > 3.9 kG measured from Zeeman broadening of magnetically sensitive FeH lines for several samples of M dwarfs ranging from M2 down to M9 spectral type (Reiners and Basri, 2007). In fact, a number ultracool dwarfs spanning the spectral type range M8 to T6.5 have been observed to exhibit similar radio pulsing behavior (Route and Wolszczan, 2012).

1.8 Periodic Photometric Variability of Ultracool Dwarfs

Over the past decade, many photometric surveys have revealed that brown dwarfs and very-low mass stars are optically variable. The reason behind these surveys is also to study the physical nature of their atmospheres; for instance, to investigate if the features that are the most likely cause of variability rapidly form and disappear or are stable over long timescales. Various surveys have found variation at the predicted rotation period for an object (e.g., Clarke et al., 2002; Koen, 2006; Lane et al., 2007; Littlefair et al., 2008). Ultracool dwarfs have also shown non-periodic variability, or periodic variability of time scales not correlating with the rotation of these very cool objects (e.g., Gelino et al., 2002; Lane et al., 2007; Maiti, 2007).

There are three plausible sources for producing optical variability as the star rotates: magnetic-induced spots, atmospheric dust, and auroral hot spots, or alternatively a mix of them (Martín et al., 2001; Gelino et al., 2002; Rockenfeller et al., 2006; McLean et al., 2011; Harding, 2012; Harding et al., 2013a; Hallinan et al., 2015; Croll et al., 2016; Pineda et al., 2017).

Optical studies have indicated the major influence of the presence of atmospheric dust in the photosphere of ultracool dwarfs. It has now been well established that the presence of photospheric dust is a consequence of some elements being absorbed from the gas phase, altering the metallicity or opacity of the atmosphere. After the M/L transition, the formation of dust grains initiates under the cool and dense conditions in the photosphere of ultracool dwarfs, and becomes more prominent in such environments; the presence of photospheric dust thus defines the L spectral classification (Littlefair et al., 2008). Previous studies have shown the potential for turbulent conditions in the atmospheres of ultracool dwarfs, together with rapid rotation and the existence of chemical and other atmospheric dynamics, all of which are likely to be parameters in the classification of stellar lightcurves (Allard et al., 2001). Furthermore, It is believed that the presence of photospheric dust can affect the magnetic properties of ultracool dwarfs (e.g., Marley & Robinson 2015). As was mentioned in Section 1.7, a largely neutral and cool atmosphere, coupled with persistent collisions in the dense atmosphere between dust grains and charged particles, results in more electrically resistive atmospheres in L- dwarfs (Mohanty et al., 2002; Gelino et al., 2002). Variability due to dust clouds is more fully explored in Section 1.8.2.

Magnetic spots are more common in solar-type stars, where the magnetic activity is generally attributed to the $\alpha\Omega$ -dynamo, but while this mechanism apparently cannot operate in ultracool dwarfs, the α^2 or turbulent dynamos (outlined in Section 1.7) may (Rädler et al., 1990; Durney et al., 1993; Browning, 2008; Christensen et al. 2009; Yadav et al. 2015). A number of campaigns have

observed optical modulation of brown dwarfs and low mass stars (attributed to e.g. magnetically induced spots after radio emission detection); however, the transitional effective temperatures after the M/L transition presented another cause of this modulation in L spectral type, due to the prominent presence of photospheric dust clouds for these objects (Artigau et al., 2009; Radigan et al., 2012; Gillon et al., 2013; Radigan et al., 2014; Buenzli et al., 2014; Crossfield et al., 2014b). In support of this conclusion, previous studies found that magnetic activity, as signaled by H_{α} , decreased rapidly in the M/L transition, approaching negligible levels in the spectral type L3 (West et al., 2004). While the detection of radio emission flares from a T6.5 dwarf (~ 900 K) (Route and Wolszczan, 2012), confirms that magnetic activity (~ 1.7 kG) persists beyond the observed drop-off in chromospheric/coronal activity detected across early-to-mid L spectral classes (Schmidt et al., 2015; Pineda et al., 2016; Gizis et al., 2017), a mixture of stellar magnetic and atmospheric features is likely to be the cause of modulation in these cool objects (Harding, 2012). Variability due to magnetic spots is more fully explored in Section 1.8.1. As a result, up until 2015, variability was largely attributed to magnetic cool spots, or to the presence of dust clouds, or both. Chromospheric and magnetospheric emissions have also been considered a plausible candidate as a cause of variability in ultracool dwarfs (Littlefair et al., 2008).

In recent years, another favoured scenario for producing variability in ultracool dwarfs has arisen: auroral activity (Hallinan et al. 2015; Kao et al. 2016; Pineda et al. 2017), very similar to that responsible for polar aurorae on the magnetized planets in our Solar System including the Earth (e.g., Clarke et al., 1980). For a more in-depth discussion of this fascinating alternative possibility, see Section 1.8.3.

1.8.1 Optical Variability due to Magnetically Induced Spots

Lower temperature regions formed on the photosphere of a star and produced by the presence of powerful magnetic activity, which in turn suppresses convection in these regions, are dubbed magnetic spots. Visibility of this surface feature is constrained by the inclination angle for the rotation axis of the object relative to the line of sight of the observer, and may be responsible for optical variability as the object rotates. Several techniques may be employed for assessing variations in the emitted light of cool stars, such as:

- Zeeman–Doppler Imaging (ZDI), which is used to study the magnetic fields of fully convective stars, also measures the properties of the surface field of these objects. Moreover, periodic modulation of Zeeman signatures can be identified during the rotation of the star. However, the use of the ZDI technique is much more challenging for late-M dwarfs (M7-M9) or later spectral types ($\lesssim 2000$ K), as these objects become much fainter and therefore increasingly hard to measure via spectroscopic techniques with regard to the assessment of the stellar rotation period.
- Another diagnosis known as Line Depth Ratios (LDRs) may be employed where temperature-sensitive lines can be measured. The temperature contrast between the starspot and the surrounding photosphere causes the temperature-sensitive lines to change their intrinsic depth (Catalano et al., 2002). Based on some test observations, this technique has been found to be effective for slowly rotating stars.
- Photometry is of course a technique widely used to study the flux variations that are being emitted from an object (Howell, 2006). With the advent of the latest CCD technologies, this method has proven its effectiveness and

has been employed in variability studies for the majority of brown dwarfs and low-mass stars.

As noted earlier in Section 1.7, the photometric studies of ultracool dwarfs that were initiated as a result of radio studies showed that magnetic activity and optical variability could be associated. Until recently, there was no reason to doubt that the existence of starspots and other activity is a likely cause of variability that is relatively common in late-M and early-L dwarfs (Rockenfeller et al., 2006; Lane et al., 2007; Croll et al., 2016). McLean et al. (2011) reported periodic photometric modulation from the M7 dwarf 2M J1314+13AB in the g and i optical bands with a period of 3.79 hours. This period of rotation was in good agreement with the 3.89 ± 0.05 hrs period obtained via multi-epoch radio observations. They reported that the g- and i-optical band variations are correlated. Since they found that g- and i- band variations are in phase, this correlation is compatible with models of star spots induced variability (McLean et al., 2011). For comparison, the M8.5 dwarf TVLM 513-46 exhibits quasi-sinusoidal periodic photometric modulation with the same ~ 2 hours period seen in the radio and H_{α} emission (Lane et al., 2007; Hallinan et al., 2007; Hallinan et al., 2008; Harding, 2012; Harding et al., 2013a). Most intriguingly, however, Littlefair et al. (2008) reported anti-correlated variations in the Sloan g' and i' bands for TVLM 513-46. They referred to dust clouds coupled with stellar rotation rather than cool spots as a plausible cause of optical variability. However, they recognized that this interpretation was problematic when considering the fairly warm atmosphere of this type of dwarf. In addition, high-resolution Doppler images of the M9 dwarf LP 944-20 showed magnetic spots at high latitude (Barnes et al., 2015). They proposed that the optical variability generated by this type of feature could be attributed to auroral activity.

1.8.2 Optical Variability due to Dust Clouds

In section 1.6, we mentioned the characteristics of M, L and T dwarfs' optical spectra which are of fundamental importance to this section. Atmospheric dust clouds are considered to be a significant parameter, and could affect the shape of the photometric lightcurves of ultracool dwarfs.

Once the effective temperatures of low mass stars and brown dwarfs drop after the M/L transition, the magnetic activity is expected to decline sharply (as signaled by a lack of H α or X-rays) (Neuhaeuser et al., 1998; Gizis et al., 2000; West et al., 2004); therefore, atmospheric dust clouds are likely responsible for the large amplitude modulation that has been detected in these objects (Bailer-Jones and Mundt, 2001; Gelino et al., 2002; Enoch et al., 2003; Maiti, 2007; Littlefair et al., 2008; Goldman et al., 2008; Clarke et al., 2008; Artigau et al., 2009; Radigan et al., 2012; Gillon et al., 2013; Radigan et al., 2014; Buenzli et al., 2014; Crossfield et al., 2014a). Indeed, multi-wavelength photometry of such objects suggests that the observed variability is thought to be driven by the presence of dust cloud cover coupled with stellar rotation, which may result in periodic and nonperiodic time variability of these dwarfs. Most intriguingly, atmospheric dust clouds may not be confined only to the M/L transition. Spitzer / IRAC observations pointed out that almost all L-dwarfs are likely variable objects (Metchev et al., 2015). Also, we have already mentioned that anti-correlated lightcurves have been discovered in Sloan g' and i' bands of the M8.5 TVLM 513-46 (Littlefair et al., 2008). They indicated that the Sloan- g' and Sloan i' bands are dominated by continuum opacity and molecular absorption, respectively. Consequently, the formation of a dust cloud in the dwarf's atmosphere can either decrease or increase the flux of these color bands. They attributed the cause to atmospheric dust clouds as a likely explanation for the periodic variability.

A number of studies have emphasized the presence of kG fields for M, L, and T dwarfs (Hallinan et al., 2006; Hallinan et al., 2007; Reiners and Basri, 2007; Hallinan et al., 2008; Reiners and Basri, 2009; Morin et al., 2010; Route and Wolszczan, 2012; Route and Wolszczan, 2016; Kao et al., 2016; Shulyak et al., 2017). We have already mentioned in Section 1.8.1, there have been numerous studies of late-M and early L-dwarfs concluding that magnetically induced spots on the surface of the dwarfs are a likely source of the periodicity due to magnetic activity in these objects (Rockenfeller et al., 2006; Lane et al., 2007; Croll et al., 2016). A wide range of ultracool dwarf spectral types have been shown to exhibit magnetic activity, even in a regime where dust clouds are believed to dominate, where early/late L and even T dwarfs still exhibit H_{α} emission (Schmidt et al., 2015; Pineda et al., 2016). Therefore, for all spectral types, both the aforementioned astrophysical causes (starspots and dust clouds) might be responsible for the periodic modulation.

1.8.3 Optical Variability due to Auroral Hot Spots

All planets within our solar system, including Earth that possess magnetic fields with atmospheres/magnetospheres, exhibit aurorae. Traditionally, there are three dynamo mechanisms that produce auroral currents in our solar system. The first mechanism governs Earth's and Saturn's auroras (e.g. Cowley et al., 2004), as these arise from magnetospheric disturbances caused by the solar wind. Such disturbances are sometimes sufficiently powerful to alter the paths of charged particles in both magnetospheric plasma and solar winds. The charged particles, in particular electrons, accelerate along magnetic field lines that lead to the precipitation of these electrically energetic particles into the high-latitude regions of the upper atmosphere, where they collide with gas atoms, causing the atoms to glow colourfully. The second mechanism is that auroras arise from electrical

currents along magnetic field lines produced by the relative motion between the rotating planet and an orbiting satellite. This mechanism is responsible for the auroral emission associated with the moons Enceladus and Io of Saturn and Jupiter, respectively (e.g. Saur et al., 2004). Finally, a co-rotation breakdown between an orbiting plasma disk and the magnetosphere of the planet can result in a shearing layer that induces auroral currents. This mechanism dominates the main Jovian auroral oval (e.g. Cowley and Bunce, 2001).

Several studies have recently found that all three kinds of auroral activity, but much more powerful, may extend from magnetized planets to the ultracool dwarf regime. A large multi-wavelength monitoring of the M8.5 dwarf TVLM 513-46 revealed lightcurves that are highly correlated in phase between all signals (Yu et al., 2012; Harding, 2012; Harding et al., 2013a). This high degree of phase stability has not been previously detected in the ultracool dwarf regime. This supported the new idea that the variability could be due to an auroral hot spot on the surface of the dwarf rather than clouds of dust (Harding, 2012; Harding et al., 2013a). The contradictory results of TVLM 513-46 between the Littlefair et al. (2008) study and the newer studies are attributed to the possibility that atmospheric dust cover being more active when observations were taken by Littlefair et al. (2008) and therefore have a significant effect on the dwarf. In addition, Harding et al. (2013a) reported stability over ~ 5 years in both amplitude and phase of the optical period, implying the persistence of features that made it possible to rule out dust cloud features. This activity in TVLM 513-46 is similar to the aurorae seen on planets that have magnetic fields in our own solar system, including the Earth (Clarke et al., 1980).

More recently, a study by Hallinan et al. (2015) reinforced the argument that "the detected variability of ultracool dwarfs may be due to auroral behaviour". Simultaneous optical spectroscopic and radio monitoring of the late M-dwarf LSR J1835 + 13 was performed, and the findings in some optical wavelengths revealed

variability that was anti-correlated in phase to other wavelengths. In fact, the multi-wavelength observations of LSR J1835 + 13 showed that the object supported auroral activity that is significantly more powerful than any aurora previously discovered from magnetised-planets in our solar system, as a result of interaction between charged particles and hydrogen in the atmosphere of the dwarf. They reported that LSR J1835 + 32 is variable with the same periodicity in pulsed radio emission, optical, and Balmer lines (Hallinan et al., 2015). They proposed that the same population of electrons in the dwarf's magnetosphere is causally responsible for radio and optical emissions (Yu et al., 2012; Harding, 2012; Hallinan et al., 2015). Hallinan et al. (2015) postulated that such an auroral feature could also explain the anti-correlated lightcurves of TVLM 513-46, that was previously thought to be due to cloud phenomena (Littlefair et al., 2008).

A series of recent studies have indicated that auroral activity may be present at detectable levels on cooler objects of spectral classes late L, T and even Y. Notably, the radio emission observed from dwarfs of spectral types such as T2.5 (Kao et al., 2016) and T6.5 (Route and Wolszczan, 2012; Williams et al., 2015) indicated auroral activity. Therefore, auroral activity could be the cause for some of the periodic optical modulations across L and T spectral types (Artigau et al., 2009; Radigan et al., 2012).

As outlined in Section 1.7, multi-wavelength observations of TVLM 513-46 revealed electron cyclotron maser (ECM) instability as the underlying mechanism responsible for the detected highly circularly polarized periodic radio bursts (Hallinan et al., 2006; Hallinan et al., 2008). The discovery of ECM emission at 4 – 8 GHz bandwidth (Hallinan et al., 2006; Hallinan et al., 2008), suggested that such an emission process would be similar to that driving the auroral radio emissions in the giant magnetized solar system planets (Zarka, 1998). Recent studies have shown that ECM emissions have been widely observed in all radio-emitting dwarfs (e.g., Treumann, 2006; Hallinan et al., 2007; Hallinan et al., 2008;

Berger et al., 2009b), and therefore this process is likely to be able to produce sustainable particle bombardment to the surface of the dwarf. Moreover, in the case of TVLM 513-46, many studies have reported the stability of ECM emissions on timescales of years (Hallinan et al., 2006; Hallinan et al., 2007; Hallinan et al., 2008; Yu et al., 2012; Harding, 2012; Harding et al., 2013a), which speaks to the stability of the hot spot observed in the ultracool dwarf regime. Although a number of studies (e.g., Treumann, 2006; Hallinan et al., 2007; Hallinan et al., 2008) have shown that the ECM instability mechanism must be behind the aurorae in ultracool dwarfs, the physical conditions that cause the aurorae remain a debatable point. Pineda et al. (2017) discussed potential auroral scenarios in the ultracool dwarf regimes. They expected that the three auroral dynamo mechanisms that are responsible for polar aurorae on the magnetized planets in our solar system would perform slightly differently, in the case of ultracool dwarfs. Pineda et al. (2017) assumed that ultracool dwarfs in binary systems rotating around much larger stars interact with the stellar wind of the companion, much as planets do around our Sun. Verifying this observationally would be difficult, because while on the one hand, the production of powerful aurorae is not preferred for those ultracool dwarfs with larger separations (about 10 AU) (Zarka, 2007), on the other hand, dwarfs with very close separation are very difficult to observe, demanding adaptive optics technology and/or using astronomical interferometry such as very long VLBI baseline interferometry. And of course, some known aurora-emitting dwarfs like TVLM 513-46 and LSR J1835+13 have no stellar or dwarf companions. Several authors have suggested that both co-rotation breakdown and satellite interaction scenarios could generate enough energy to power the auroral activity (Schrijver, 2009; Nichols et al., 2012; Hallinan et al., 2015). Pineda et al. (2017) pointed out that there is no need for an external star to power an auroral electrodynamic engine, as ultracool dwarfs could produce the aurora internally due to large magnetosphere currents. Although the underlying physical conditions are ambiguous, ultracool dwarf systems need “strong magnetic field strengths, fast rotation rates, large-scale magnetic field

topologies, and the presence of powerful magnetospheric plasma”. They believed that co-rotation breakdown is the dominant underlying mechanism in UCD regimes for the generation of auroral activity and may involve the existence of close-in planetary companions to these cool objects (Pineda et al., 2017).

1.9 Thesis Overview

Chapter 1 In this introductory chapter, we outline the background theory of ultracool dwarfs. We review the search for these objects, the subsequent spectral classification and the evolutionary models for sub-stellar objects that are adopted to predict temperature, luminosities, mass, gravity and other local parameters. We also discuss the magnetic activity in stellar and sub-stellar objects, and the mechanism that is responsible for generating radio emissions in both cases. Finally, we highlight the various causes responsible for periodic optical modulation from ultracool dwarfs, and the associated photometric variability observations that helped to distinguish these causes.

Chapter 2 This chapter concentrates on the optical instrument (the GUF1 photometer) that was designed explicitly for our ultracool dwarf campaign, and used on the 1.8m VATT telescope, on Mt. Graham, Arizona. We discuss also the use of automated data calibration/reduction techniques implemented in the Low Light Level (L3) GUF1 Pipeline, that was applied to the large datasets acquired from the GUF1 photometer.

Chapter 3 This chapter addresses the photometric time-series analysis methods employed in the thesis. It outlines time-resolved optical differential photometry with a standard fixed aperture. It also describes a new technique called Lucky Photometry (LuckyPhot) that can increase the differential photometric precision by selecting the best frames from a dataset and also finding

an optimum aperture for each frame. It then highlights the use of the statistical tools in this thesis including the Lomb-Scargle (LS) periodogram, Markov Chain Monte Carlo (MCMC), Phase Dispersion Minimization (PDM), the Chi-squared test, model-fitting and phase-folding data. These were all used to detect and evaluate periodic variability and the associated period and amplitude errors. A special focus of this chapter is on our Light Curve Fitter routine, that was scripted in Python and used during this work to disentangle a weaker source variability signature from that of a dominant source of variability.

Chapter 4 This chapter reports on the findings of our I-band observations for two radio-detected objects - the L3.5 dwarf 2MASS J00361617+18211 and the M9.5 dwarf BRI 0021 - to determine whether optical periodicity was present over a scale of years and examine the correlation, if any, between the optical and radio regimes. This chapter also calculates the inclination angles relative to our line of sight of these two single dwarfs. Also, it compares the two photometric methods employed: Lucky Photometry with optimum aperture (O.A.) vs. fixed aperture (F.A.) with no Lucky Photometry. Finally, it discusses the proposed source of the periodicity.

Chapter 5 This chapter describes our multi-epoch I-band observations and results for 2MASS J0746425+200032AB and 2MASS J1314203+132001AB. A particular focus of this chapter is the use of Light Curve Fitter, as we were unable to monitor each component of these binary systems as a single point source due to their close separations. By subtracting the period of each component out, we successfully deconvolved the optical behaviour of each component of the two binary systems. This chapter also presents an analysis of the orbital properties of the two binaries helps to investigate whether a scaled-down version of the formation mechanism for solar-type binary systems still holds in the regime of very low mass binary stars.

Chapter 6 Thesis summary and conclusions. We conclude with an overview of this work, and the possibilities for future projects and improvements.

*" Man must rise above the Earth—to the top of the atmosphere and beyond—
for only thus will he fully understand the world in which he lives."*

Socrates

Chapter 2

Optical Instrumentation and Image Reduction / Calibration

2.1 Introduction

This chapter contains two parts. The first part outlines the optical instrumentation that facilitated this research, which was designed and used explicitly for the ultracool dwarf campaign, commissioned on the 1.8m VATT telescope, on Mt. Graham, Arizona. The second part describes the data calibration/reduction suite called Low Light Level (L3) Pipeline that was applied to the data obtained from the GUF1 photometer.

2.2 Optical Setup – Vatican Advanced Technology Telescope (VATT)

The largest enabling factor in this work was the optical observations that were analysed and carried out using GUF1 (Galway Ultra Fast Imager), a photometric camera currently in-situ at the 1.83m Vatican Advanced Technology Telescope (VATT) on Mount Graham in southeast Arizona, United States. VATT is part of the Mount Graham International Observatory (MGIO) and is operated by the Vatican Observatory, in partnership with the University of Arizona. MGIO is considered as one of the best sites in the world, where typical values of seeing range from 0.8" to 1.7" during the majority of observation runs. The 1.83 m is a Gregorian telescope designed for observations in the optical and infrared. It achieved "first light" in 1993. The telescope has an f/1.0 'honeycombed' borosilicate primary mirror which was manufactured at the University of Arizona. Borosilicate glass has low thermal expansion (coefficient of thermal expansion $\approx 3 \times 10^{-6} \text{ K}^{-1}$ at 20 °C), and impressive chemical durability. The telescope has a 16.48 m focal length, and offers the full Sloan and Johnson photometric filter sets, a H_{α} filter, and others. Due to the red nature of UCDs, we observed only in the

Location Specifications	
Longitude	109 53' 31.25" W
Latitude	32 42' 04.69" N
Elevation	3191 m
Telescope Specifications	
Optical System	Aplanatic Gregorian, f/9
Primary Mirror	f/1.0, Diameter 1.83 m
Secondary Mirror	f/0.9, Diameter 0.38 m
Focal Length	16.48 m
Back Focal Distance	50.80 mm
Vignetting-Free Field	72 mm diameter (15 arcmin)
Image Scale	12.52 arcsec/mm
Image quality	0.1 arcsec throughout 6.8 arcmin
Guide Camera sensitivity	18th magnitude in one second
Mount	Altitude/Azimuth
Instruments	
VATT 4K	VATT CCD Imager
GUF	Galway Ultra Fast Imager
VATT Spec	VATT CCD Spectrograph

Table 2.1 VATT Specifications. Values are adapted from: <https://www.vovatt.org/the-telescope-instruments/vatt-specifications> and <https://www.as.arizona.edu/vatican-advanced-technology-telescope>.

VATT I-Arizona ($\sim 7200 - 9100 \text{ \AA}$) broadband filter. The VATT specifications are in Table 2.1.

2.3 Galway Ultra-Fast Imager (GUFU)

In 1969 the first charge-coupled device (CCD) was invented at AT&T Bell Laboratories by Willard Boyle and George E. Smith (Janesick, 2001), while attempting to design a medium for bubble memory.

A CCD is an electronic detector constituted by many square light-sensitive "pixels" (each of which is a metal-oxide-semiconductor capacitor). When light (photons) falls on each pixel, the incoming photons will be converted into electrons due to the photoelectric effect (which states that electrons or other free carriers are emitted when light hits a material), and the amount of charge stored in each pixel is proportional to the incident photon flux over the duration of the exposure.

The simplest analogy commonly used to picture the mechanism involved in how a CCD works is that of an array of buckets (pixels) being used to measure raindrops (photons) (Howell, 2006). Imagine that a 3 by 3 array of buckets to catch raindrops is neatly distributed in rows and columns over a given area as shown in Figure 2.1. Rain dropping will be collected by the buckets (during the course of the exposure); the depth of the buckets represents the well depth, or how much charge (the accumulated water) each pixel can hold. These buckets are placed on conveyor belts, and when the belts start running, the accumulated water (charge) in each line of buckets (pixels) is transferred one by one to the readout register, which in turn is passed to a large measuring container (amplifier) which measures the amount of charge and converts it into a voltage. These voltages are then sampled, digitized in preparation for a computer to analyse the data.

However, there are a number of features associated with a CCD process that must be considered when performing high precision photometry, e.g. when the charge moves sequentially from one pixel to an adjacent pixel and onto the serial readout register which in turn passes the charge to the amplifier, it will create noise in the output signal associated with the rate of the readout and the quality of the electronics. Whereas, the L3-CCD (low-light-level CCD) technology we used in GUF1 allows to obtain images with much lower effective readout noise levels than previous devices.

We conducted observing campaigns with the Galway Ultra Fast Imager (GUF1) photometer, in February 2017, March 2017, October 2017, November 2017, December 2017 and May 2018. GUF1 is a lightweight high speed photometer system based on the Andor iXon EMCCD DV887-BV camera (Figure 2.2). It was originally designed, assembled and tested in NUI Galway and sky-tested on the 1.5m Loiano telescope in Italy (Sheehan and Butler, 2008). It was later modified by Harding (2012) to be compatible with the 1.8m VATT on Mt. Graham, Arizona: here it is currently deployed and available to all VATT users. GUF1 was designed specifically for long-term observational campaigns to examine variable stars that require second to sub-second timescales such as ultracool dwarfs, with a near-100% exposure duty cycle. This photometer can detect the small variations in visible and near-IR light from ultracool dwarfs, by measuring the brightening and fading that takes place as the star rotates. Furthermore, GUF1 can also be used widely in other astronomical research fields, such as transiting exoplanets, planetary imaging, flare stars, high S/N studies of bright sources and any other transient sources in the sky. The Andor iXon DV887 EMCCD camera contains a CCD97 thinned back-illuminated chip, quantum efficiency greater than 90%. It has a 512×512 pixel format, where each pixel is $16 \mu\text{m} \times 16 \mu\text{m}$, giving a total imaging area of 8 mm^2 . This camera is designed to alleviate the problem of read noise at MHz readout rates, with a readout noise of less than one electron at a $> 17 \text{ MHz}$ pixel readout rate (Figures 2.2 & 2.3, and Table 2.2). The CCD97

technology has the advantage of obtaining data in frame transfer mode. The frame transfer CCD sensor is composed of two distinct portions that can be independently clocked and are located on the same chip. The upper area is the

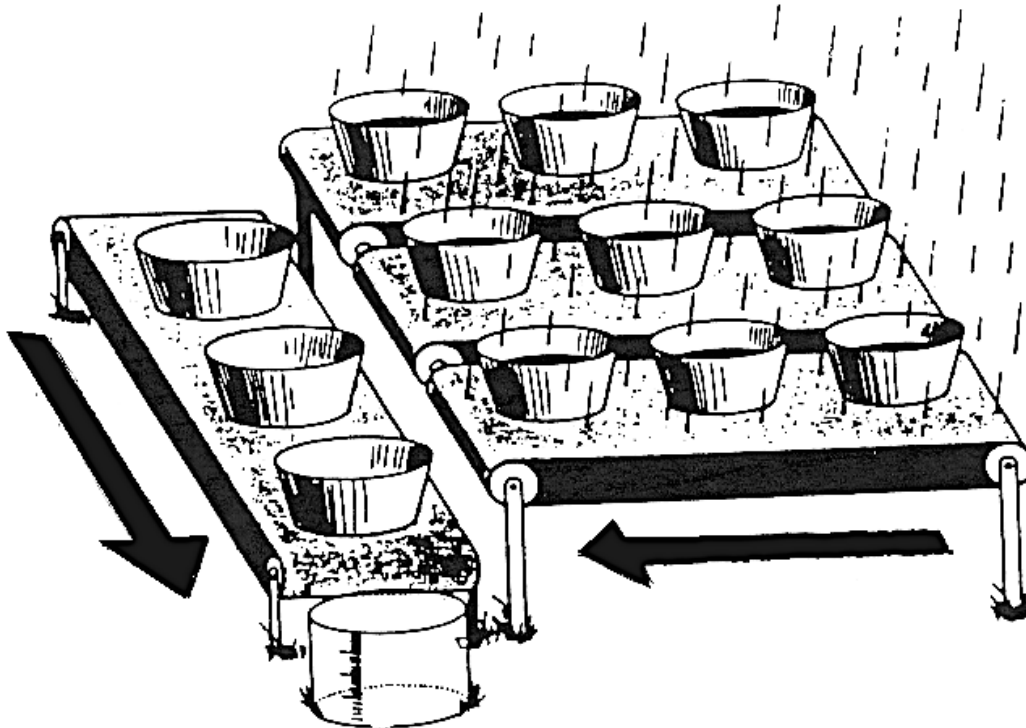


Figure 2.1 An analogy for the operation of a CCD (Image Credit: (Howell, 2006)).

photosensitive region that is allocated to collect and convert photons into electrons and store them, and the other area is the storage region (masked area). The latter is structurally identical to the photosensitive region but is masked off in order to avoid any exposure to light (Figure 2.3). After capturing the image in the photosensitive area, the entire image is quickly transferred (~ 2 ms) to the storage area. After moving the image to the masked storage area, while the photosensitive area is already capturing a new image, line after line is read out through a shift register. These are then amplified and digitized. Therefore, a

mechanical shutter is unnecessary, and the exposure duty cycle jumps to nearly 100%.



Figure 2.2 The DV887 iXon camera (adapted from <https://andor.oxinst.com/products/ixon-emccd-cameras>).

This camera has two different operation modes, electron multiplying and conventional readout, with the latter being used in our case. Traditionally CCDs have been front-illuminated, where the light must pass through the poly-silicon gates before it reaches the bulk silicon, but this structure has a disadvantage in that some of the incoming light can reflect off or be absorbed by the gates, which reduces the signal that is available to be captured. Contrary to the front-illuminated sensor, a back-illuminated sensor (e.g. CCD97) arranges the silicon gates behind the bulk silicon by flipping the silicon wafer during manufacturing and then thinning its reverse side so that light can strike the bulk silicon without passing through the gates (Figure 2.4). This improves the chance of an input photon being captured from about 60% to more than 90%. Therefore, the quantum efficiency of the thinned back-illuminated CCD97 is high over the visible

spectrum (U, B, V and R bands) as well as the near-infrared spectrum (e.g. I band) with a range of ~ 350 - 1000 nm (Figure 2.4 & 2.5).

The system offers 1, 3, 5 and 10 MHz pixel readout rates and produces large data loads by operating at 34 frames per second (fps) in full-frame and up to 526 frames per second in a windowed configuration. The CCD chip is held in a hermetically sealed vacuum head with an anti-reflection coating on the optical window to maximise throughput to the sensor.

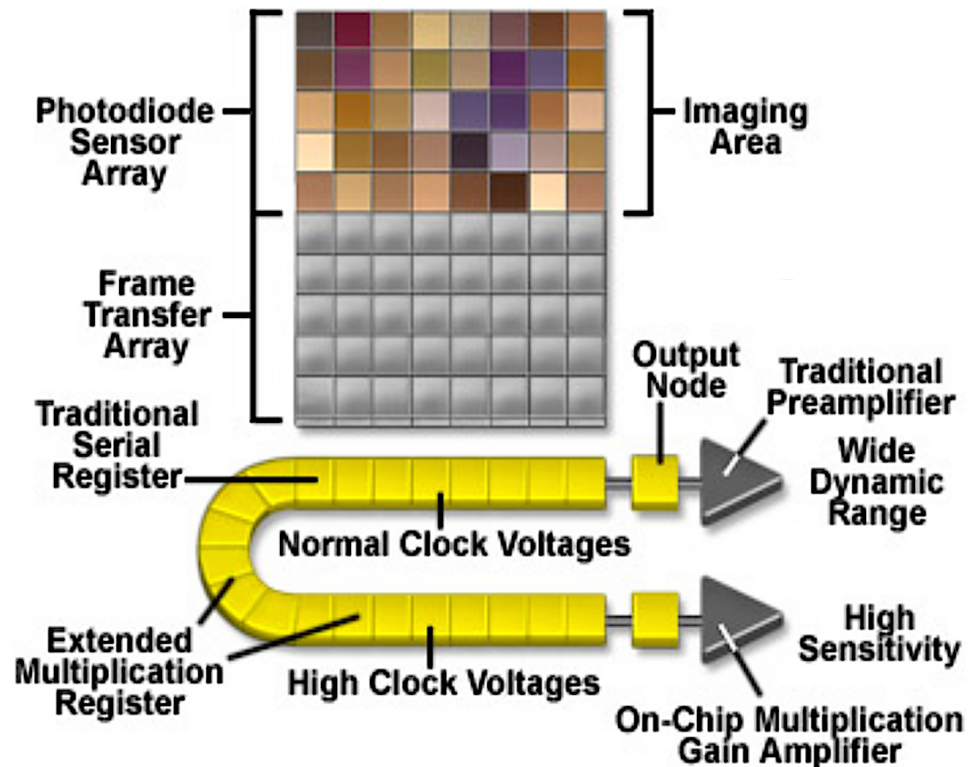


Figure 2.3 Schematic of an EMCCD showing its frame-transfer architecture. (Image credit:<https://www.olympuslifescience.com/en/microscoperesource/primer/digitalimaging/concepts/emccds/>).

Since thermal dark current adds noise in CCD exposures, it is necessary for the CCD chip to be at an extremely low and steady temperature. Therefore, a 3 stage

thermoelectric cooler located in the vacuum head is capable of cooling the chip to -90°C . An additional liquid coolant circulator (Koolance EXT-AO3) improves the performance of the thermoelectric cooler by removing excess heat from the heat sink. The CCD is kept at -80°C for all observations on the VATT telescope.

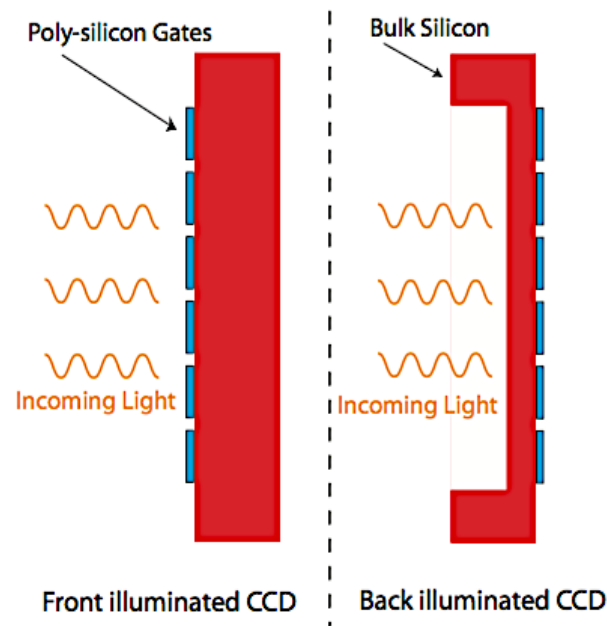


Figure 2.4 Comparison of simplified back-illuminated and front-illuminated pixel cross-sections. This figure is adapted from Sheehan (2008).

The GUF1 photometer (Figure 2.6) offers a native field of view (FOV) at the VATT Cassegrain focus of $\sim 1.7' \times 1.7'$ with a corresponding plate scale of $0.2'' \text{ pixel}^{-1}$. However, GUF1 has options for near-infrared (NIR) and visible-optimised focal reducers; when installed, it offers a FOV of $\sim 3' \times 3'$ and a larger plate scale of $0.35'' \text{ pixel}^{-1}$. The $3' \times 3'$ FOV covers enough of the night sky to typically have a few sufficiently bright photometric comparison stars; between 1 - 6 reference stars in the data reported in this thesis. The iXon camera unit is mounted within an instrument box constructed of 10 mm thick aluminium plates, along with the

focal reducer optics. The liquid coolant circulator is mounted on the outside of the instrument box.

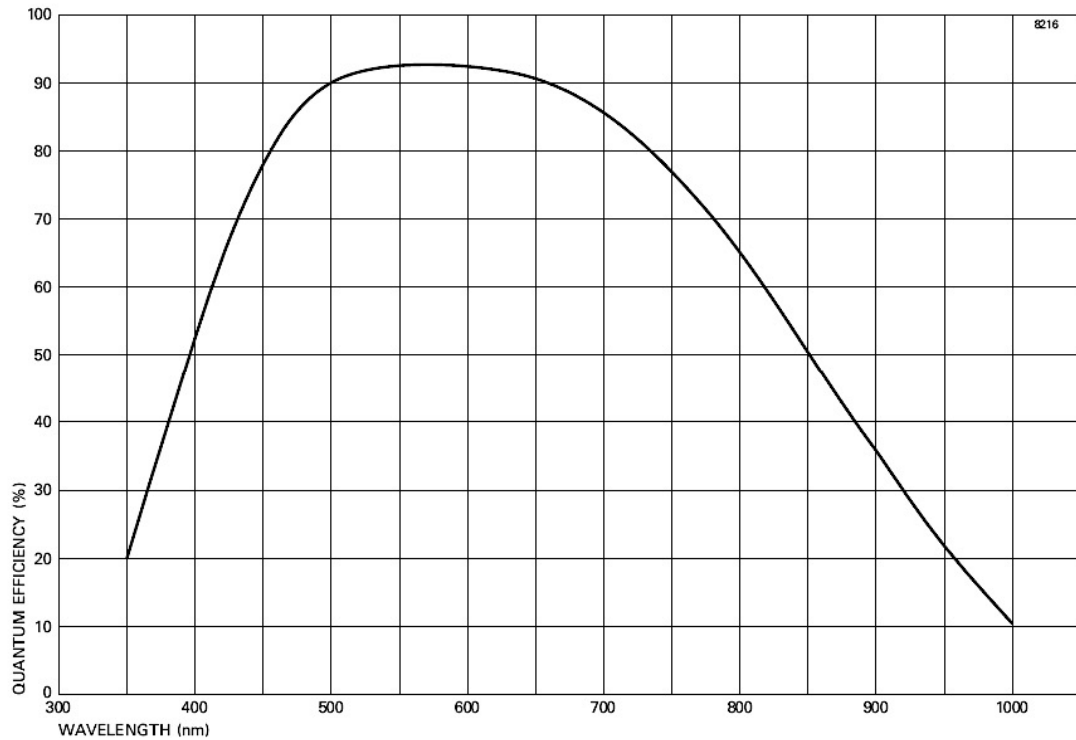


Figure 2.5 Quantum efficiency (QE) of the Andor iXon DV887 back-illuminated EMCCD camera as a function of the photon's wavelength (adapted from Andor specification sheet). The QE peaks at 575 nm with a QE of ~ 92.5%.

A GUF1 system overview is shown in Table 2.2. We refer the reader to Sheehan (2008) and Harding (2012) for an in-depth discussion of L3-CCD technology and the GUF1 photometer.

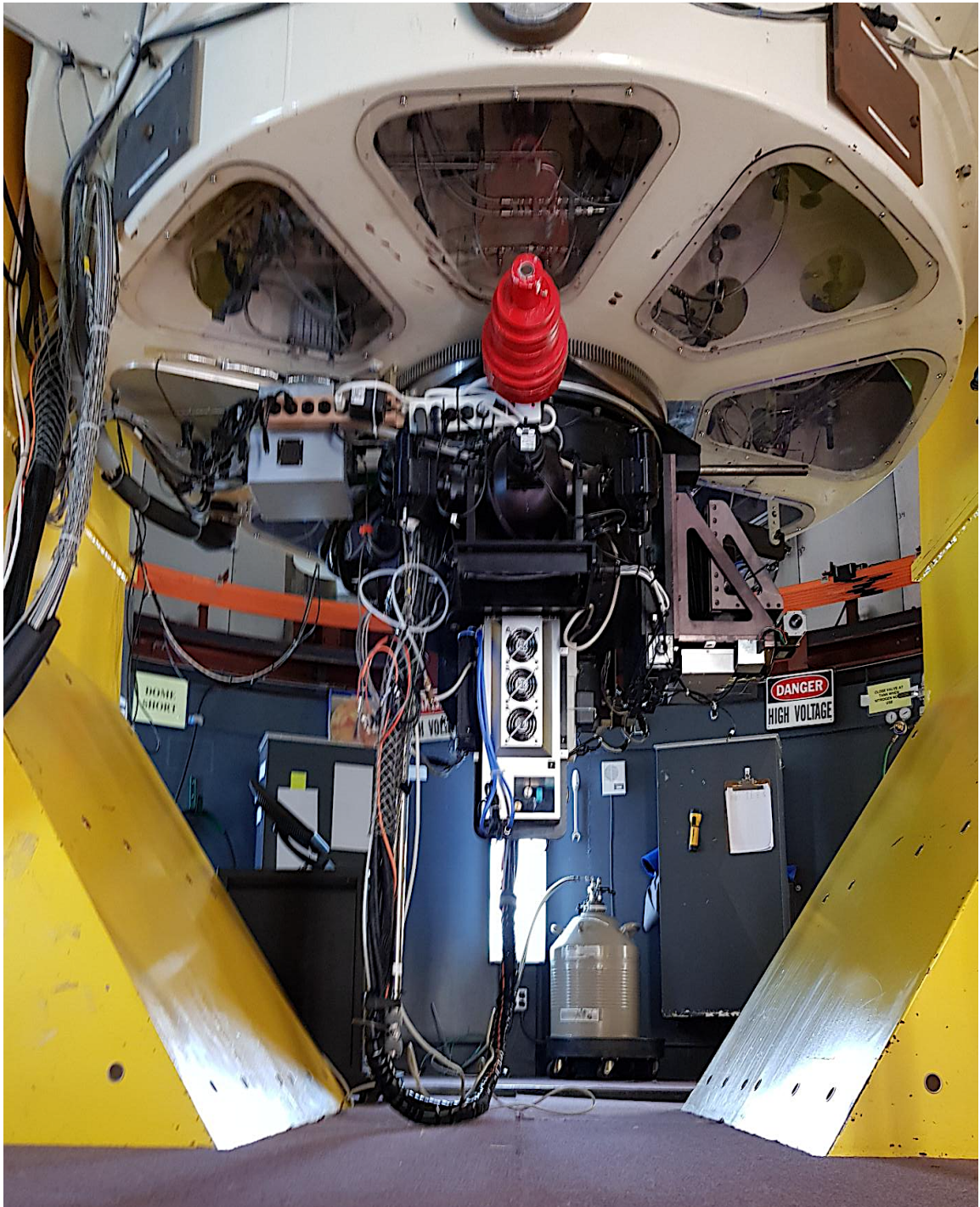


Figure 2.6 GUFI photometer mounted at the Cassegrain focus of VATT. Photo by Salam Dulaimi.

Parameter	Corresponding Value(s)
Active pixels	512 x 512
Pixel size (W x H; μm)	16 x 16
Image area (mm)	8 x 8
Spectral sensitivity (nm)	~350 - 1000
Pixel readout rate (MHz)	10, 5, 3, 1
Digitization @ 10, 5, 3, 1 MHz readout rate	14-bit (16-bit available @ 1 MHz)
Conventional amplifier	3 & 1 MHz
Pre-amplifiers	4.6 \times , 2.4 \times , 1.0 \times
Read noise	< 1 e ⁻ (with EM gain)
Frame transfer time	~ 2 ms
Active area pixel well depth (e ⁻ , typical)	200,000
Linear gain register pixel well depth (e ⁻ , typical)	400,000
Max frames per second	34 (full) - 526 (windowed)
Binning modes	1 \times 1, 2 \times 2, 4 \times 4
Vertical clock speeds (μm)	0.4 to 6.0 (variable)
Peak quantum efficiency (BV 575 nm)	92.5 %
Dark current @ - 70 ° C (e ⁻ pixel ⁻¹ sec ⁻¹)	0.012
Dark current @ -90 ° C (e ⁻ pixel ⁻¹ sec ⁻¹)	0.0035
Field of view (arcminutes)	~ 3 \times 3

Table 2.2 GUF1 Photometer characteristics. We present specifications for the Andor iXon EMCCD DV887 camera. These values are adapted from: Data sheet: iXon DV887 Camera Systems. Andor Technology (2004), and Data Sheet (issue 3): CCD97-00 Back Illuminated 2-Phase IMO Series, Electron Multiplying CCD Sensor, e2v technologies (2004), via <http://www.andor-tech.com/> and <http://www.e2vtechnologies.com/> and Harding (2012)

2.4 Factors affecting CCD photometric precision

A photometric measurement has two primary characteristics; time resolution and photometric accuracy. The time sampling needed to evaluate the physical phenomena of interest will decide the necessary time resolution of the instrument. The photometric accuracy attainable at this time resolution is influenced by the instrument's sensitivity, telescope aperture size, and target's brightness. In variable star work, the magnitude of the variability will determine the necessary photometric accuracy.

A number of major types of noise can affect the quality of the image that can be achieved with a CCD (Banse et al., 1992); (1) Photon Noise, (2) Thermal Noise; (3) Readout Noise, (4) Quantization Noise and (5) Sensitivity Noise; (6) Cosmic rays are also an important factor.

Numbers (2) through (5) of these types of noise emerge from imperfections in the CCD sensor. Although CCD technology has constantly improved since its invention in 1969 (Smith, 2010), some key behaviours and characteristics still need to be taken into account when attempting to produce high accuracy photometry.

- 1- **Photon noise**, also known as shot noise, is related to the nature of the incident photon flux. The amount of photoelectrons collected from a non-variable source by a CCD sensor during a given exposure varies. The typical (1 sigma) variation of the number of photoelectrons collected (photon noise) is found to be equal to the square root of the average number of photons ($\sigma_{\text{photon}} = \sqrt{N_{\text{photon}}}$); therefore, the photon noise is dependent on the number of photons captured. It also depends on the exposure time, since the longer the exposure, the larger the number of photons recorded and the greater the signal to noise ($\frac{N_{\text{photon}}}{\sqrt{N_{\text{photon}}}} = \sqrt{N_{\text{photon}}}$),

but this will affect the time sampling so it is not a fix for all situations. Increasing the aperture size of the telescope plays a role in increasing the photons gathered, thus suppressing the photon noise effects. Noise of this sort is not something inherent to the CCD, but a result of the photon's nature; thus, it is inevitable and ultimately limits the precision of a photometric measurement.

- 2- The second source of noise is the **thermal noise** or dark noise, described as a result of thermal vibration which can liberate electrons from the CCD imager itself, and then, these thermal electrons are gathered within the CCD pixel wells, where they are recorded as an additional signal or otherwise known as dark current. The quantity of "dark electrons" in a pixel increases linearly with exposure time. The noise arising from the dark current (σ_{Dark}) is governed by Poisson statistics as the square root of the average number of dark currents:

$$\sigma_{Dark} = \sqrt{N_{(Dark)}} \dots \dots \dots (2.1)$$

where $N_{(Dark)}$ is the average dark current level ($e^- \text{ pixel}^{-1} \text{ sec}^{-1}$). The L3-CCD detector is designed to substantially decrease the number of thermal electrons within the chip by cooling the CCD chip to below -100° C .

- 3- **Readout noise** is an electronic noise property inherent in all CCDs, a result of the non-ideal operation of physical electronic circuitry. Readout noise is generated in the reading out phase of the CCD, as the electrons present in the pixels are transferred from the CCD chip to the camera output (from a packet of electrons to an analog voltage to a digital number). This transferring and conversion process can add or subtract spurious electrons in the measured signal, which add random scatters to the output value. The amount of noise is independent of the capture time. Relative to photon and thermal/dark noise, the readout noise is more significant for images with short acquisition time and/or very faint background levels.

Remarkable improvements over time have been made in readout noise reduction in CCD imagers, since the readout noise value was $> 500 e^-$ per readout in early CCD cameras, but this value has been effectively lowered to $< 1 e^-$ per pixel readout in the L3-CCD devices.

- 4- **Quantization noise** arises when the analog signal is converted to a digital output by the CCD's A/D converter. This kind of distortion occurs when the division of the analog voltage by the Gain (quantization factor) of the A/D converter leaves a remainder corresponding to 1 or more electrons, and this remainder is then discarded due to rounding to the nearest A/D output value. Quantization noise is usually associated with readout noise as both are evident during the readout stage.

- 5- All pixels across the light-sensitive region of the CCD will not have the same light sensitivity, that is to say, some CCD pixels are more/less sensitive than their neighbours; this variation is termed **sensitivity noise** (or alternatively, pixel response non-uniformity - PRNU). The variations in sensitivity between pixels can be caused by variations in the layer of silicon thickness and other small manufacturing defects. The sensitivity noise is not a big issue for astronomers, as the source of this noise and other variations in the relative amount of light reaching each pixel (due to dust shadows and vignetting) can be mainly eliminated by dividing by a flat-field image. This is possible because it is a systematic and stable form of noise, unlike the previous 4 types described, which are all random noise. It is worth mentioning that the correction process can be more effective, if the colour/spectral type of the flat field image light source and the observation targets, if possible, are approximately the same.

6- Cosmic rays, high-velocity charged particles of celestial origin, can cause 'impact ionization' in the silicon wafer that can significantly boost the number of electrons measured by a CCD pixel. Cosmic ray "hits" are identified on the image as very bright spots or a bright line of pixels. Of course, as the readout electronics cannot distinguish between counts from celestial sources and counts from a cosmic ray, calculations such as star magnitudes, bias pixel values or flat field pixel values can be distorted. The way to get rid of cosmic ray hits in image space is to stack multiple, registered images with statistical rejection of high-valued outliers. Another way to decrease the impact of cosmic rays events dramatically is by using a digital filtering method known as RealPhot, which is an implementation of the extraction method described by Everett and Howell (2001). It involves the analysis of which provides the basis for rejecting the full frame (Collins, 2014). It must be noted, however, that unlike the previous 5 types of noise, cosmic ray hits only affect a tiny minority of pixels in any CCD frame.

Since for our observation campaign, only the Conventional amplifier was used (no EM gain), the total noise $\sigma_{total\ noise}$ can be calculated as follows (Janesick, 2001):

$$\sigma_{total\ noise} = \sqrt{N_* + N_{pixel} (N_s + N_D + \sigma_R^2) } \dots\dots\dots (2.2)$$

where N_* is the total number of photons gathered from an observed object, N_{pixel} is the total number of pixels included in a photometric aperture calculation, N_s is the total number of photons per pixel from the sky background region, N_D is the total number of electrons caused by dark current per pixel and σ_R^2 is the total number of electrons per pixel produced by readout and quantization noise. It is

assumed here that sensitivity noise/PRNU has been removed by flat-fielding, and that pixels affected by cosmic ray hits have been excluded.

2.5 Low Light Level CCD (L3-CCD) Technology and Astronomical Usage Considerations

L3-CCD/EMCCD cameras were first introduced into the scientific imaging community in 2001. The GUF1 photometer used for this project incorporates the CCD97 sensor developed by E2V technologies, which has dual readout amplifiers – Conventional and Electron Multiplication (EM). The L3-CCD operates on a principle similar to ordinary CCDs that generally have one readout amplifier; the only differences are the inclusion of an extra readout register called the gain register, also known as the electron multiplication (EM) register, between the CCD serial shift register and the output gain amplifier. The amplification of charge occurs in the EM register when higher-than-typical clock voltages ($> 40\text{V}$) are applied to the extended multiplication register during the readout operation (Figure 2.3). This high voltage is sufficient to trigger a process known as ‘impact ionization’: when a charge has enough energy to excite and promote from the valence band into the conduction band and create a new electron-hole pair, thereby a free electron charge in the conduction band can create another charge (Sheehan et al., 2006; Hirsch et al., 2013). The depths of the EM register are larger than other serial registers so that the wells have a capacity to accommodate this amplification. The EM gain is highly proportional to the applied voltage; this implies that it can be controlled either by increasing or decreasing the voltage, and has no relation to the pixel readout rate. The EM-gain will increase the signal above the noise floor of the amplifier, hence increasing the

Signal to Noise Ratio (SNR). Consequently, the user can operate at fast frame rates without increasing readout noise.

Each pixel in the gain register represents a multiplication process known as a multiplication stage that has a very low probability of producing gain. In moving the charge from one stage to the next, there is a 1% probability to release another electron as a result of the low probability of impact ionization occurring in a given stage. However, utilizing hundreds of multiplication stages in which impact ionization can occur will yield a high gain of up to thousands, enough to effectively eliminate the relative readout noise and diminish it to zero, as indicated by the following equation:

$$\text{Effective Readout Noise} = \frac{\text{Readout Noise with gain off}}{\text{Applied EM Gain}} \dots \dots \dots (2.3)$$

This allows running at higher frame rates and duty cycles without the usual penalty of higher readout noise (Coates, 2006; Sheehan et al., 2006).

There are other properties influencing the L3-CCD sensitivity that must be considered, such as dark current and clock induced charge. Dark current is one of the major sources of noise in CCD sensors. Physically, some electrons assemble in the CCD pixels even in the absence of light falling on the detector. These dark current electrons are randomly created by thermal agitation within the CCD chip that is sufficient to eject electrons from the silicon lattice, which are then trapped by the CCD's potential well and counted to become part of the signal, indistinguishable from "true" astronomical photo-electrons. The Andor iXon DV887-BV chip at - 90° C, was found to have a very low level of dark current about 0.0035 e⁻ pixel⁻¹ sec⁻¹ (Harding, 2012). Dark current strongly depends on the operating temperature of the CCD, therefore to better improve performance, it is very important to diminish the dark current generated in the pixels of the device to negligible levels through an effective cooling strategy (electronic Peltier, or even better a liquid cooling system) where the CCD is cooled down e.g. to

below -100°C . An effective cooling system can enhance the sensitivity of the CCD camera vastly and permits the acquisition time to be extended up to several hours. Subtracting a dark frame - an exposure of matching duration and temperature, with no light entering the sensor - then reduces the residual dark current in the final frame.

When an electron (charge) is shifted (clocked) during the readout phases, a primary source of noise for L3-CCDs is generated called Clock Induced Charge (CIC), which occurs in any CCD but is normally buried in the readnoise.

Readout Rate, Amplifier	Readout Noise (e^{-} pixel $^{-1}$)		
	Pre-amp 1.0 x	Pre-amp 2.4 x	Pre-amp 4.6 x
1 MHz, Conv	10.88	7.07	6.21
3 MHz, Conv	16.03	10.74	9.45
1 MHz, EM	56.08	31.48	24.38
3 MHz, EM	64.84	40.42	32.98
5 MHz, EM	112.86	63.40	-----
10 MHz, EM	185.24	112.72	-----

Table 2.3 Presented are the matrix of readout rates, Conventional and EM amplifiers as well as pre-amplifier options that available to users of the Andor iXon system, and the associated noise levels in e^{-} pixel $^{-1}$. Despite the fact that EM mode increases nominal readnoise, it decreases effective (actual) readnoise to $<1 e^{-}$. This table is taken from Sheehan et al. (2006).

Unfortunately, the gain multiplication process enhances clock induced charge to significant levels, particularly when it originates early in the readout register. Therefore, at high EM gain, we can see such individual electrons amplified in the image as sharp spikes. This phenomenon is a function of readout rate, and exposure time has no impact on it. However, it is subject to several parameters, including the clocking levels, pulse shape and width, and the operating mode of the CCD (Zhang et al., 2009; Harding, 2012).

Despite all these points of interest when using the option of the EM amplifier, we need to locate the “best” operation mode. We utilised the conventional amplifier (no EM gain) just like a regular CCD during all observation epochs, since we did not need to run the L3-CCD camera exceptionally fast. Instead, exposure times of 5 or 10 sec were used to measure the desired physical phenomena (the exposure time was selected according to how bright the objects are in the star field, and how rapidly their light varies). It can be seen from Table 2.3 that by using a readout rate of 1MHz, we were getting the slowest readout rate, but the least amount of noise. The most common setting we used was a readout rate of 1MHz and a variable pre-amp gain of 2.4x, which collect more e^-/ADU compared to a pre-amp of 4.6x. The conventional amplifier has been configured to have a low readout noise (this is covered by the values in the table 2.3).

One might wonder why we utilized the L3-CCD rather than a standard CCD, since we didn't utilize EM gain? The answer for the most part depends both on the desired frame rate and on flux levels. Figure 2.7 showing SNR vs signal can be instructive in making such decisions. On this basis, we conclude that:

- 1- Under slower frame rates (5 sec exposure time), when we have the option to read out as a ‘conventional CCD’, it tends to be beneficial to do so in terms of decreasing readout noise and accomplishing a better signal to noise. Since employing EM gain reduces the effective CCD well depth, it forces the use of a higher frame rate to avoid saturation. But overall

readout noise increases as the square root of the total number of frames. So a higher frame-rate, producing many more frames in a given observation, can be noisier in net terms - even when EM gain is enabled.

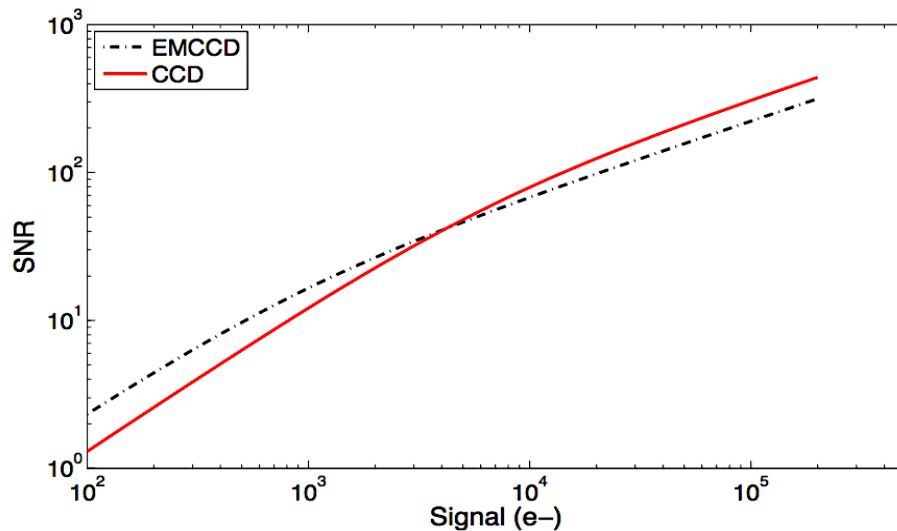


Figure 2.7 A comparison between the performance of an L3CCD (black dashed-dotted line) and a normal CCD (or the Conventional readout channel of an L3-CCD) (red solid line). The readout noise was $8 \text{ e}^- \text{ pixel}^{-1}$ for the regular CCD and $1 \text{ e}^- \text{ pixel}^{-1}$ for the EMCCD. Due to the effect of EM-induced multiplication noise (Excess Noise Factor), we note the reduced SNR values at high signal levels compared to the regular CCD. This figure is taken from Sheehan (2008).

- 2- The EMCCD gain is portrayed as a stochastic process at each stage in the EM register where the final output EM gain cannot be predicted precisely; this is because the avalanche process that stimulates the electron signal before the readout phase is likewise not predictable in nature. We can, however, determine the mean of the EM gain only. The output EM intensity distribution therefore contains an additional photometric uncertainty called the Excess Noise Factor, a.k.a Multiplication Noise. Its impact on an image's signal-to-noise ratio (SNR) is as if the sensor's quantum efficiency was cut in half (as seen at higher signal levels of the dashed line in Figure

2.7). In the event that the EM register enhances our signal by a gain of M , the Excess Noise Factor is defined by the following equation:

$$\text{Excess Noise Factor}^2 = \frac{\sigma_{out}^2}{M_{gain}^2 \sigma_{in}^2} \dots \dots \dots (2.4) \quad \text{where} \quad M_{gain} = (1 + \alpha)^N$$

where σ_{out}^2 and σ_{in}^2 are the variance of the output and input signal for the EM register respectively, α is the probability of multiplication per stage and N is the number of multiplication stages (Robbins and Hadwen, 2003). However, because EM gain $\gg \alpha$, Robbins and Hadwen (2003) found the *Excess Noise Factor*² to be:

$$\text{Excess Noise Factor}^2 = \frac{2}{\alpha + 1} \dots \dots \dots (2.5)$$

As the probability of EM multiplication is between $\sim 0.01 - 1\%$, the acceptable limit for the *Excess Noise Factor*² for large EM gain tends to be $\sqrt{2} \approx 1.414$. Thus, the excess noise factor is equivalent to the reduction in Poissonian signal-to-noise that would occur if the sensor's quantum efficiency was halved (Figure 2.7).

- 3- The frame transfer structure (Figure 2.3) is an important factor to deliver high sensitivity with high speed, which alone is all we need in most situations: to also utilize EM gain would be pointless. As seen before in Table 2.3, the CCD97 has the great advantage of acquiring data in frame transfer mode to improve the duty cycle, since frame transfer mode enables the image to transfer rapidly (transfer times ~ 2 ms) from the captured region to the storage zone situated on the same chip. In this way, a camera shutter is not essential, and the exposure duty cycle - defined as (exposure time / [exposure time + readout dead time]) jumps to nearly 100%.

- 4- The dynamic range of a CCD is an important consideration in the ability to linearly measure suitable comparison stars with the target star. It is defined as the ratio between the brightest regions (full well depth) and the faintest regions (in extrema, equal to the readout noise) of an image which can be captured simultaneously. The dynamic range improves at first with increasing EM gain, until the effective read noise of the system is suppressed by the EM gain to a theoretical minimum of $< 1 e^-$ (the amount of EM-gain scales the read noise by: $\frac{\sigma_{no\ gain}}{\sigma_{applied\ gain}}$), and then, the dynamic range declines due to a continuous decrease in effective well depth of pixels, according to the following equation:

$$Dynamic\ range = \frac{Effective\ well\ depth}{Effective\ readout\ noise} \dots \dots \dots (2.6)$$

Therefore, for applications requiring a large dynamic range, using EM gain is not the most suitable choice. We refer the reader to Sheehan (2008) for a more in-depth explanation of CCD and L3-CCD technology.

2.6 Atmospheric noise effects

One of the big problems astronomers face is terrestrial atmospheric turbulence, which adds noise to ground-based observations. Photometric measurements are therefore subject to atmospheric effects, which have a fundamental influence on the quality of the image. Three atmospheric factors can reduce photometric precisions: **1)** atmospheric extinction, **2)** atmospheric scintillation and **3)** atmospheric seeing (Young et al., 1991).

2.6.1 Atmospheric Extinction

Atmospheric extinction can be characterized as the reduction in brightness of

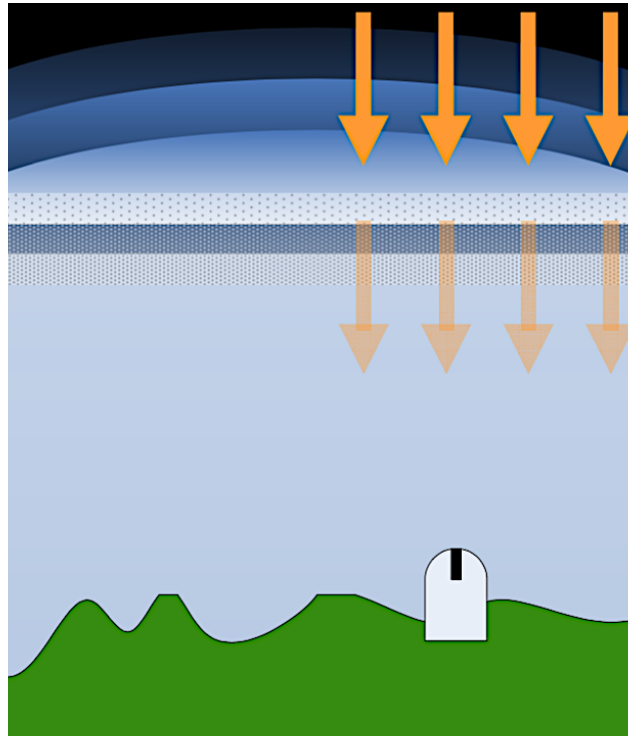


Figure 2.8 The effect of atmospheric extinction: scattering due to the interaction of the light rays from a target star with particles in the atmosphere layer. This Figure is taken from Collins (2014).

the stellar objects as light rays make their way through the Earth's atmosphere. Some photons will collide with atoms, molecules, liquid (water) droplets, dust grains, and other particles in the atmosphere. Therefore, absorption and dispersion of these photons can happen; either way, light rays from the star will be attenuated (Figure 2.8). As a result, the observers capture fewer photons from the celestial body than they would have seen on a planet free of air.

The atmospheric extinction effects are dependent on:

- 1) transparency,
- 2) observer elevation,
- 3) zenith angle,
- 4) wavelength of light observed.

While the cause of atmospheric extinction can be attributed to three factors:

- 1) Molecular absorption caused by atmospheric ozone and water molecules.
- 2) Rayleigh scattering due to air molecules.
- 3) Aerosol scattering due to dust, water and man-made pollutants.

Atmospheric extinction also includes the inhomogeneous variations effect of any cloud structure on photometric accuracy (De Kleer, 2009; Wang et al., 2012).

2.6.2 Atmospheric Scintillation and Seeing

Atmospheric scintillation and atmospheric seeing, are inherently random noises that have a significant influence on astronomical observations. Both are the result of mixing in the atmosphere of Earth. Variations in air density caused by heterogeneous air temperatures lead to fluctuations in atmospheric refractive index, and therefore, the light waves that come from space through the turbulent layers in the atmosphere are refracted in random directions, causing rapid changes in brightness and position, and also intermittently defocusing the light of the telescope aperture (Sheehan and Butler, 2008; Collins, 2014; Osborn et al., 2015); see Figure 2.9.

The effect of turbulence is more apparent near the horizon, as the light waves coming from celestial objects must pass through a more dense atmospheric layer, and therefore have longer paths through the atmosphere before being detected.

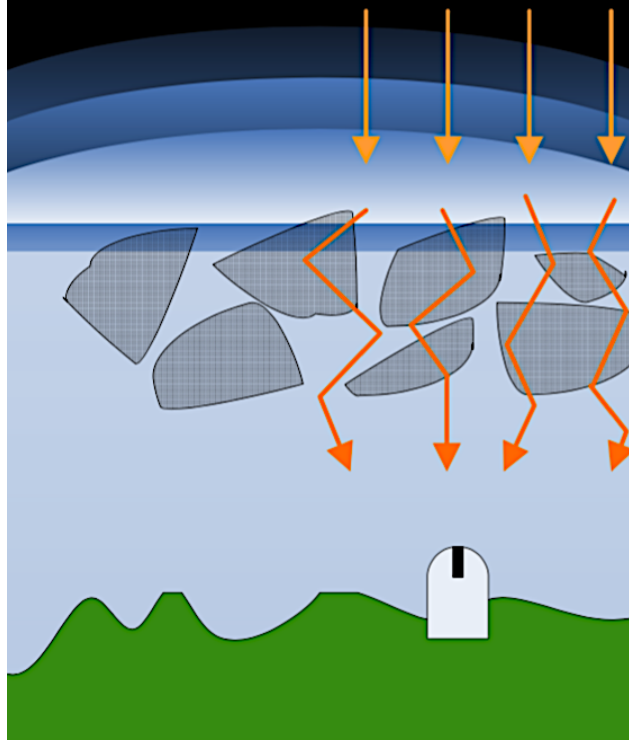


Figure 2.9 Atmospheric turbulence effect: light rays passing through Earth's atmosphere bend differently as they cross through air pockets at different temperatures. This Figure is taken from Collins (2014).

This effect is strongly related to atmospheric seeing; atmospheric scintillation is mostly a result of high-altitude turbulence, whereas seeing is a result of effects arising generally closer to the ground-based telescope (Dravins et al., 1997).

The effects exhibit themselves differently; seeing has a deforming effect on the point spread function (PSF) of the photons incident on the CCD detector, without losing flux. The scintillation process, however, has the effect of flickering reductions in the observed flux from stars (Collins, 2014). Poor seeing is problematic because it widens the PSF out, which has 2 negative impacts:

(1) it forces the use of a larger photometric aperture with greater underlying sky photon noise;

(2) it causes objects at close angular separations to contaminate each other's fluxes.

The effect of the atmosphere is changeable with variations on a timescale of the order of milliseconds (Redfern, 1991; Mackey et al., 2005). Increasing deviation in individual optical measurements increases the uncertainty that limits the photometric accuracy, due to the incoherence in the variations of weather conditions.

Since both effects depend on the wavelength of light, prior studies have shown that using standard colour filter systems, such as the Johnson (Johnson and Morgan, 1953) or Sloan (Fukugita et al., 1996), result in diminishing the effect of the varying atmospheric turbulence on optical measurements. The effect of a variable atmosphere can also be reduced by narrower filter systems, with the caveat of a loss of flux; however, bright objects combined with large telescope apertures can still deliver plenty of flux (Colón et al., 2010).

Observer elevation can also play an important role to reduce the atmospheric effects; in fact, placing observatories at high altitudes and equipping telescopes with adaptive optics is the most preferred option. There is only one way to entirely eliminate the atmosphere: by placing telescopes orbiting outside the atmosphere. The space-based telescope is the optimum solution, such as the Hubble, James Webb and Spitzer space telescopes (Batalha et al., 2013). But, the cost of space telescopes is prohibitively expensive compared to building terrestrial telescopes, and it is also extremely difficult to maintain this kind of telescope.

2.7 The Low Light Level (L3) GUF1 Pipeline

Data gathered with the GUF1 photometer is reduced using our in-house L3 GUF1 Pipeline (Sheehan, 2008). The GUF1 photometer is capable of recording and storing Terabytes (TB) of data in a single night of observations due to its high time-resolution, and so this pipeline is designed to cope with the considerable volumes of datasets generated (Harding, 2012). The L3 GUF1 Pipeline makes use of PyRAF, based on the Python scripting language and capable of calling IRAF tasks, to execute routines as pipeline modules, using IRAF's standard CCD reduction/calibration techniques. This language is used in preference to traditional IRAF CL scripts due to their lack of error analysis tools and debugging capabilities.

The L3-GUF1 Pipeline consists of three main parts (Figure 2.10):

1. L3_group()
2. L3_calib()
3. L3_work()

```

*****
                A Reduction & Analysis pipeline
                for the L3-Photometer

                Written by Brendan Sheehan N.U.I Galway 2007
*****

Pipeline runs as follows:

Part (1)                Part (2)                Part(3)
-----                -----                -----
l3_group()              l3_calib()              L3_work()
- make_lists()          - bias_data()           - isis()
- hdr_fix()             - flat_data()          - data_ops()
- other_hdr_fix()       - sci_data()           - starlist()
- check_data()          -                       - app_size()
- make_groups()         -                       - ref_stars()
                        -                       - l3phot()
                        -                       - data_analysis()

```

Figure 2.10 The L3-GUF1 Pipeline start-up screen.

There is a set of modules / GUIs within each part of the pipeline that can perform multiple tasks on the data files.

2.7.1 L3_group()

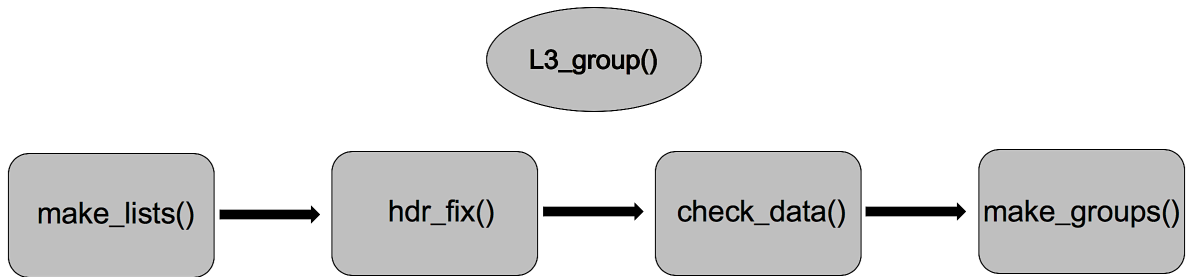


Figure 2.11 Flow-chart of modules within L3_groups().

- ***make_lists()***: This is the first stage for all reductions. It creates look-up files and performs a preliminary checking of the various data folder types:

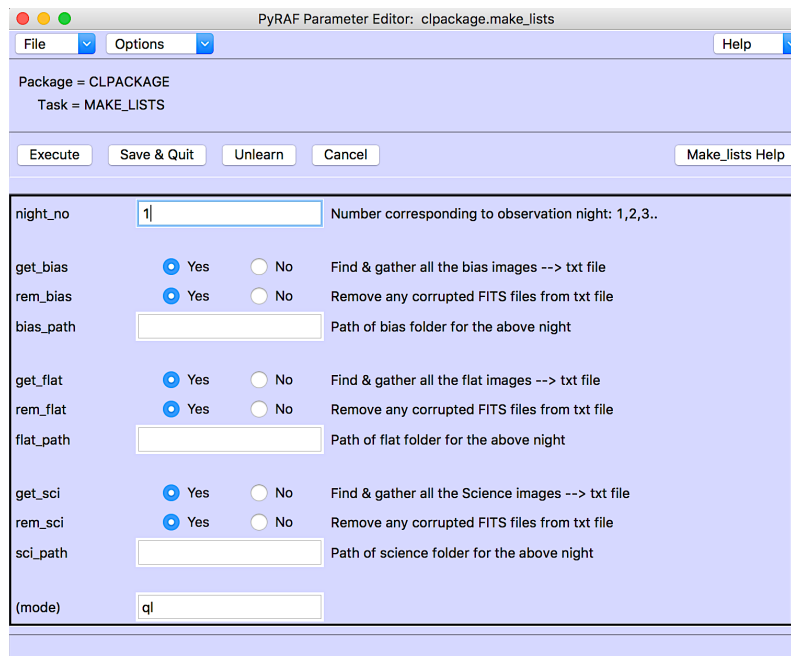


Figure 2.12 The *make_lists* GUI to manage all data acquired from the GUF1 photometer.

bias, flats, science. This routine excludes any corrupted data from all subsequent processing. Night number and directory paths are required from the user to determine where each file is located (Figure 2.12). Consequently, it creates two folders for the given observation night- *filelists_n** to hold the look-up files and *caliblists_n** to store the calibration frames, with '*' referring to the given night number; see Figure 2.13 (Sheehan, 2008).

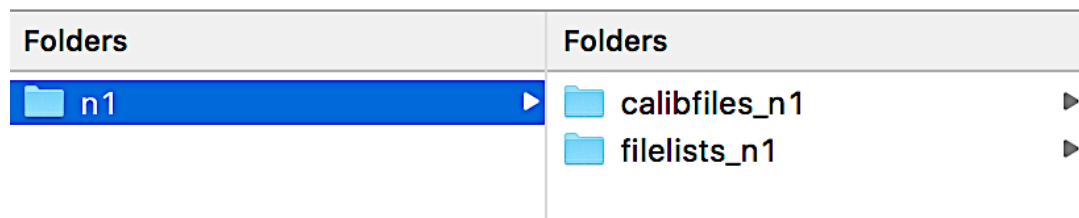


Figure 2.13 Example of the folders created for a given night via the *make_lists* routine.

- hdr_fix()***: Due to possible changes in software control during observations, not all information can be consigned to the FITS headers. This routine allows the user to insert additional essential information to the FITS header such as: general information about the name of observer, the instrument used during the observation, name and coordinates of the target star, telescope information, filter information, readout rates & modes, readnoise of detector, gain values, airmass, and Universal Time (UT) and Julian Day (JD) timestamps (Figure 2.14). Having all the correct header information is important later for the calibration process, because it is used to group frames of the same modes together via the *make_groups()* routine (Sheehan, 2008; Harding, 2012).

- ***other_hdr_fix()***: Our data was taken with the Andor iXon camera, thus it was not necessary to use this module. The `other_hdr_fix` routine allows the L3 pipeline to operate on non-Andor iXon data files.

PyRAF Parameter Editor: clpackage.hdr_fix

File Options Help

Package = CLPACKAGE
Task = HDR_FIX

Execute Save & Quit Unlearn Cancel Hdr_fix Help

night_no Number corresponding to observation night: 1,2,3..

(my_data) Filename(s) or filename list e.g. @list.txt

data_typ Current data type been processed

General Information

observer Name of observer(s)

instrument Name of Instrument

target Name of Object observed, e.g. M15

ra RA for target -> HH:MM:SS

dec DEC for target -> DD:MM:SS

Observatory Information

observat Name of observatory

latitude Latitude for observatory

longitude Longitude for observatory

altitude Observatory - height above sea level (meters)

timezone Timezone of observatory

Optional Keyword correction - (1) or (2)

add_filt Add Filter information

filename (1) Add filter information directly: B,V,R,I,...

filist (2) Input filter lookup list

Extra Keyword correction - will be added if not present

outptamp Select the readout amp type..

(mode)

Figure 2.14 The `hdr_fix` GUI for amending the FITS image header information.

- ***check_data()***: This module investigates datacubes for corrupted image planes (i.e. errors in the data). It was found that corrupted image planes either return a mean count of zero, or else the minimum and maximum counts are identical. The module uses this criterion in order to recognise and find the broken planes and exclude them from new datacubes

generated from the good data which exists before and after the broken image planes, see Figure 2.15 (Sheehan, 2008). The correct timestamp information is preserved for each image plane in the new datacubes. This module is also designed to detect bad bias frames. The threshold boundaries were set such that the lower ADU threshold (*lowthres*) was lowered to 990.0, and the upper threshold (*upthres*) was raised to 1150.0, thus avoiding the removal of good bias frames.

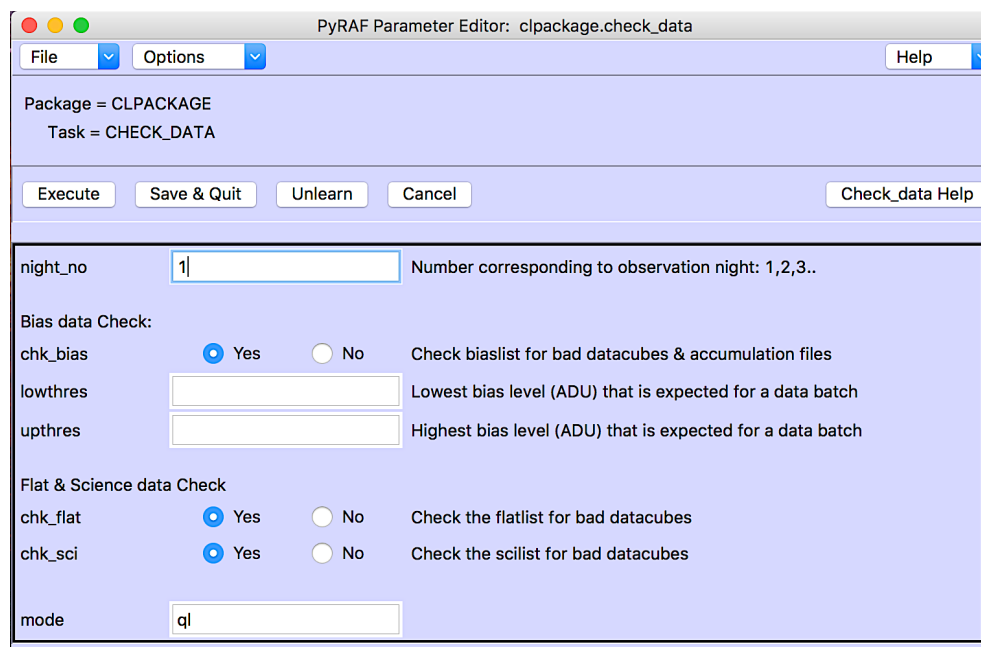


Figure 2.15 The *check_data* GUI for detecting and trimming any damaged datacubes.

- ***make_groups ()***: Once the data has been checked and modified with the correct header information, the data will be ready for the *make_groups* module that creates the final look-up group lists, by sorting the data type based on their acquisition settings; see Figure 2.16 (Sheehan, 2008).
 1. **Bias frames** are grouped by: readout speed, EM-gain and preamp settings and readout mode.

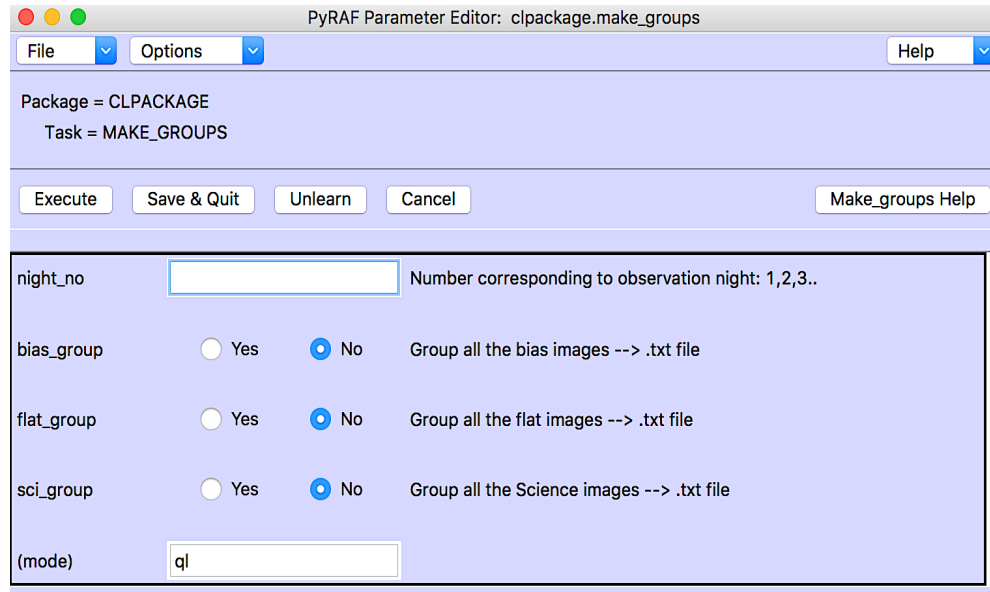


Figure 2.16 The *make_groups* GUI for grouping the common frames.

2. **Flat-field frames** are grouped by: readout speed, EM-gain and pre-amp settings, readout mode and filter type.
3. **Science frames** are grouped by: readout speed, EM-gain and Pre-amp settings, readout mode and filter type

The FITS data is now ready for the reduction / calibration stage, i.e. the standard CCD reduction methods.

2.7.2 L3_calib()

The second part of the L3 pipeline is the image calibration/reduction process that is necessary for producing good quality CCD images by correcting systematic effects in the camera sensor and optical system. It comprises of de-biasing and flat-fielding the science frames; see Figure 2.17.

- ***bias_data()*** : The bias is an inherent systematic from the camera sensor, which represents the offset that is applied when a pixel is read from the

camera sensor. In order to remove this effect, we need to measure the bias by taking the shortest possible exposure with the shutter closed (Figure 2.18). The *bias_data* routine creates a master bias frame for each night and camera setting (according to the groups made earlier by *make_groups()*), through the average combination of multiple bias frames (to reduce effective readout noise). The master bias frames are named as *masterbias *.fits*, where * refers to the group number, and are stored in the '*calibfiles_n**' folder (Lane, 2008; Sheehan, 2008; Harding, 2012).

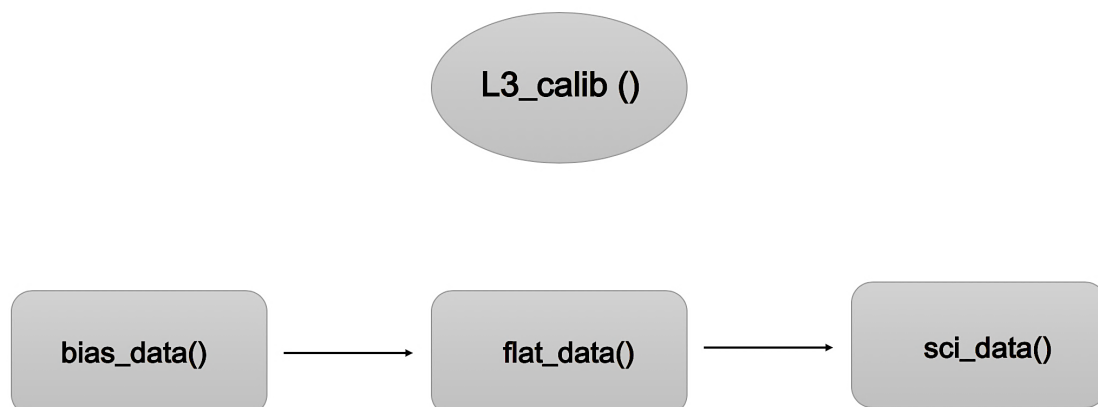


Figure 2.17 Shows flow-chart of modules within *L3_calib()*.

- ***flat_data()***: To remove the sensitivity noise/PRNU described in Section 2.4, we need to capture flat-field frames where the CCD sensor is evenly illuminated by a light source across the entire chip. Usually, we have two options to accomplish this, either using a flat sky at twilight or using in-dome artificial light sources (Romanishin, 2006). Flat-fielding techniques also help to cancel out the dust rings (dark spots) on an image, projected by dust on the camera sensor or a filter just ahead of it; see Figure 2.19. The *flat-data* routine searches for a matching masterbias from the previous *bias_data* step for each group of flats and subtracts it from the

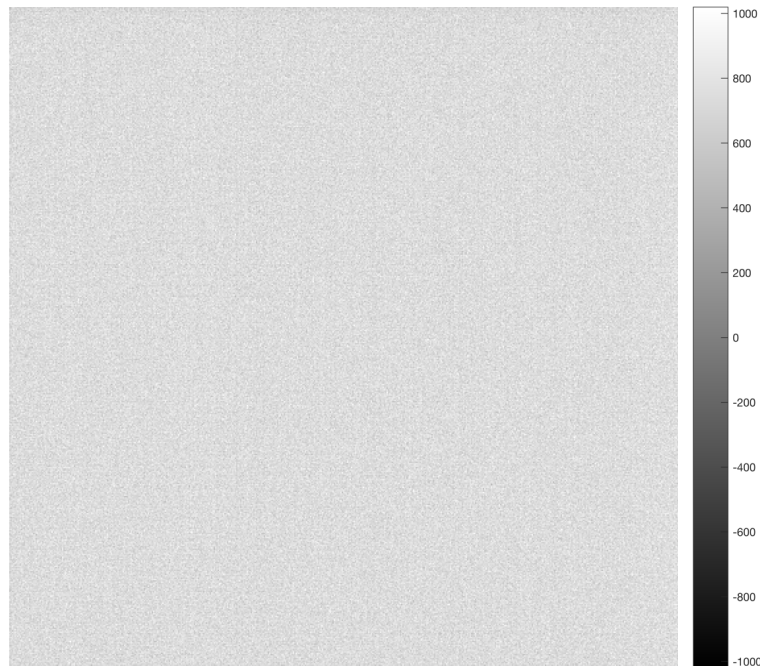


Figure 2.18 Bias frame acquired by taking the shortest possible exposure (milliseconds) with the GUFIL3-CCD camera.

relevant group. Then it coadds the flat-fields and normalizes them to a mean value of 1. The resulting master flats are named as masterflats *.fits. They are stored in the calibration folder. In addition, this routine can locate saturated pixels to generate a Bad Pixel Mask (BPM) so that they can be excluded later (Sheehan, 2008; Harding, 2012; Collins, 2014).

- ***sci_data()***: This is the final step of part II of the L3-GUFI Pipeline. The science frames reduction is performed with this routine (Figure 2.20). This routine automatically finds the correct masterbias.fits and masterflat.fits files in the 'calibfiles_n*' folder by matching them to each corresponding group of science frames (based on modes etc.), though it also allows for the user to manually specify other calibration files. It then performs debiasing and flat fielding of each science frame. At this step, a set of BPM

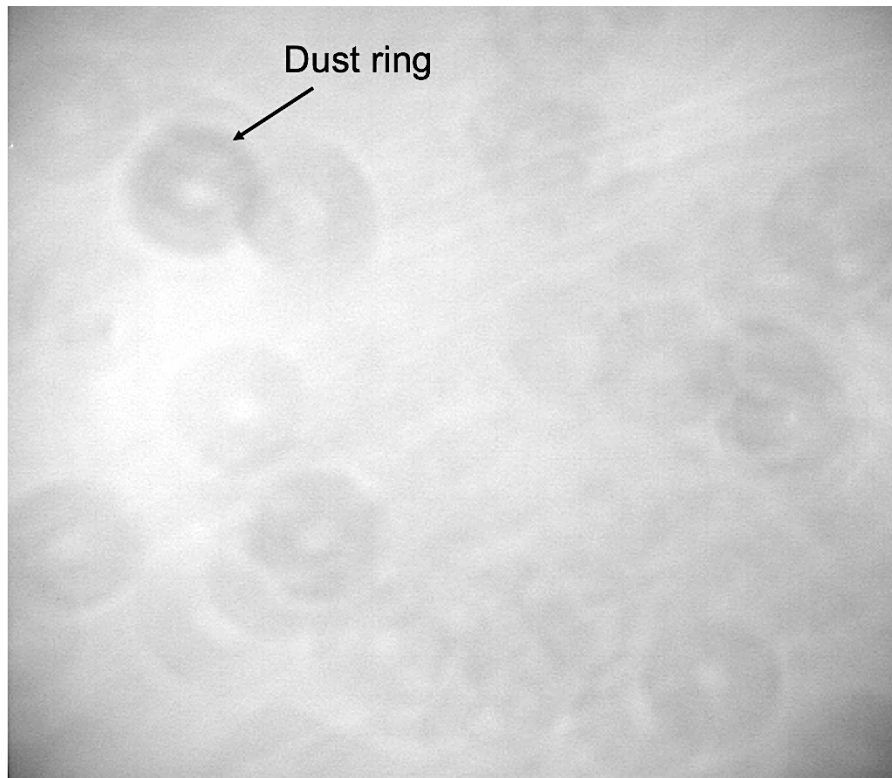


Figure 2.19 Flat-field frame from GUVI. This frame was taken by exposing the CCD to an evenly illuminated source (i.e. the dome).

files can also be created for each science frame (Sheehan, 2008; Harding, 2012).



Figure 2.20 The *sci_data* GUI used for the reduction of science frames.

2.7.3 L3_work()

Once data has been reduced and calibrated, the L3 pipeline offers various modules in part III to set up the science data for photometry analysis, including:

- ***ISIS()***: The L3 pipeline has two options to register images are either utilise the *iraf.xregister* task, or the *ISIS* registration program (Alard & Lupton, 1998; Alard, 2000). We opted to utilised the *iraf.xregister* task on our relatively uncrowded ultracool dwarf fields, as the *ISIS* registration code is not suitable for sparse fields.

- ***data_ops()***: This module breaks up FITS datacubes (which may contain hundreds of FITS frames) into individual FITS frames, before registering

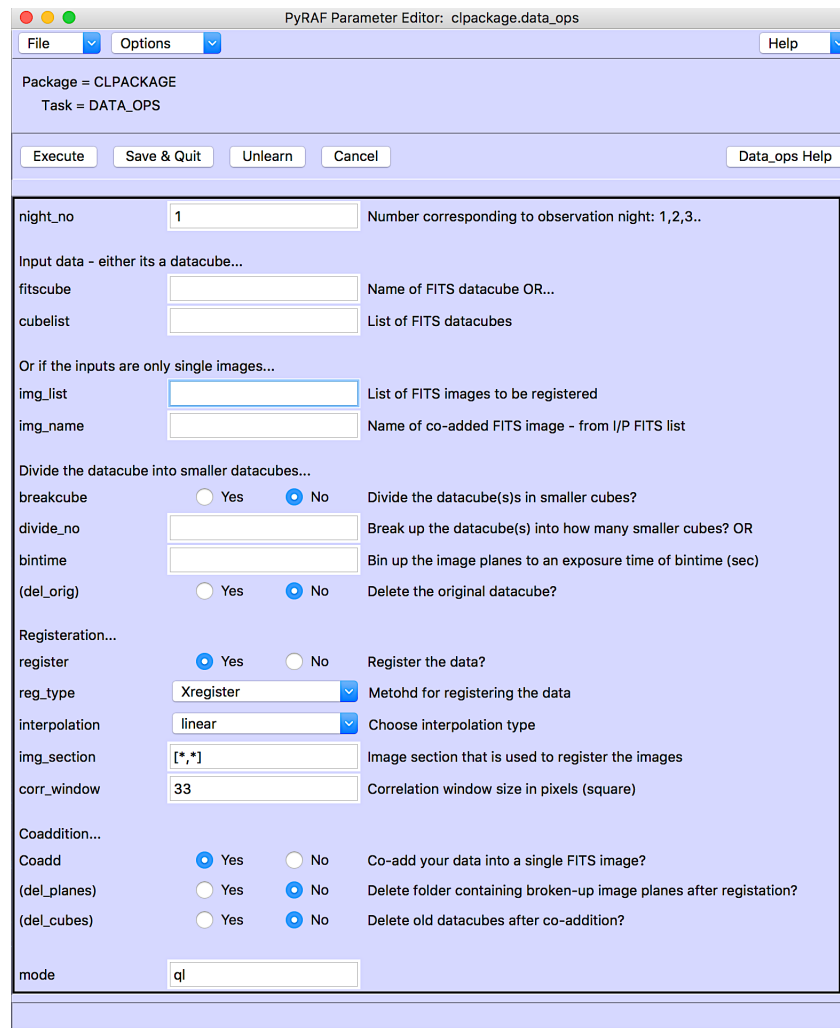


Figure 2.21 The *data_ops()* GUI used for the breaking up of FITS datacubes, binning, registering and co-addition of FITS files.

and co-adding or binning up them into single FITS frames; see Figure 2.21. Co-adding (temporal combination) and binning up (spatial combination) techniques improve the SNR for the final FITS image, and also decrease the number of files that need to be handled individually. The separated FITS frames are then saved (Sheehan, 2008; Harding, 2012).

The registration option within the routine is essential when there is pixel shift or drift between successive frames. This arises only if there has been de-rotation/tracking errors on-sky such as when the VATT telescope, which has ~ 1 arcmin hr^{-1} of tracking errors, was operated without autoguiding. However, if the user intends to perform photometry on each individual frame, they can choose between two approaches:

- (1) Register the frames to one particular reference frame, so that the resulting star list will be common for all frames;
- (2) Do not register the frames to each other, but create an individual star list for each frame (which takes time and resources).

- ***starlist()***: The IRAF/DAOPHOT task `daofind` is utilised to locate stars in the image, and the user identifies any particular star of interest (target) in each frame using SIMBAD. The target and selected reference stars' IDs and coordinates are stored in an output file (this step is very important for subsequent photometry routines). Before utilizing the `starlist` routine, we need to manually examine the (possibly coadded) image by displaying the image in SAOimage ds9 and using the IRAF task `imexamine` to determine the FWHM of the PSF and the standard deviation "STDDEV" of the sky background; these values must be entered into the routine. A 'threshold' value (multiplier of the standard deviation) must also be selected, usually between 5 and 25, as higher values will cause only the brightest stars to be detected; see Figure 2.22 (Sheehan, 2008).
- ***app_size()***: After testing different photometric aperture sizes, this routine finds aperture size with the highest signal noise ratio (SNR) for the target



Figure 2.22 The *starlist* GUI used for finding stars and numbering them with their coordinates in the output file.

stars. This value will be used in the following routines as the photometric radius value; see Figure 2.23 (Sheehan, 2008).

- ***ref_stars()***: This routine finds the ideal (most suitable) differential photometry comparison stars for the target, within a range of +/- 0.5 magnitudes. These comparison stars are utilised for differential photometry: they normalise the target in order to remove systematic flux variations in the field of view, ensuring that variations in the target's flux are inherent in its activity; see Figure 2.24 (Sheehan, 2008; Harding, 2012).

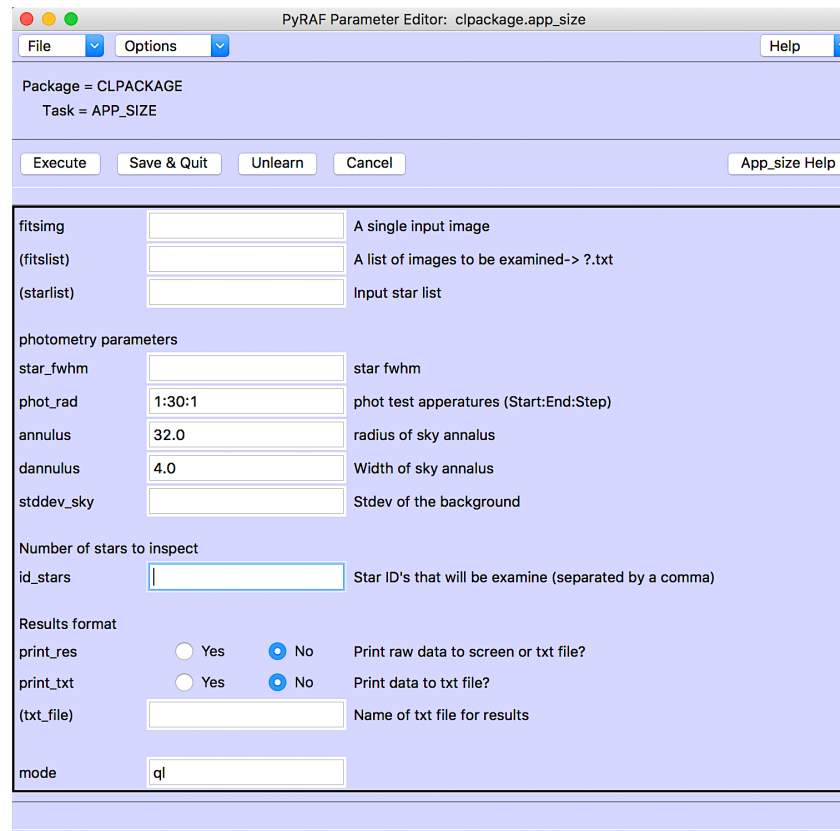


Figure 2.23 The *app_size* GUI used to test a number of photometric aperture sizes and find the one that provides the highest SNR.

- The Andor SOLIS software saves only the initial timestamp of each exposure, and consequently, after a FITS datacube has been broken up, each FITS image will only possess these initial UT and JD values. As a result, we temporarily break out of the pipeline flow, to update timestamps (UT & JD) of the FITS files using our python-script code which adds the cumulative time interval to each FITS frame since the first frame in that broken-up datacube. We then calculate the Modified Julian Date MJD by subtracting 2400000.5 days from the JD of each frame; this modification will facilitate simplified chronological calculations. The regular Julian Date for each frame is also converted to Heliocentric Julian Date (HJD) using an Excel macro (HJD differs from the JD by as much as 8.3 minutes (500

s, 0.0058 days)). We used the HJD correction because there are variations in light arrival times due to the relative positions of the Earth and the target star, as Earth gradually travels around the Sun, altering the star's distance from us.

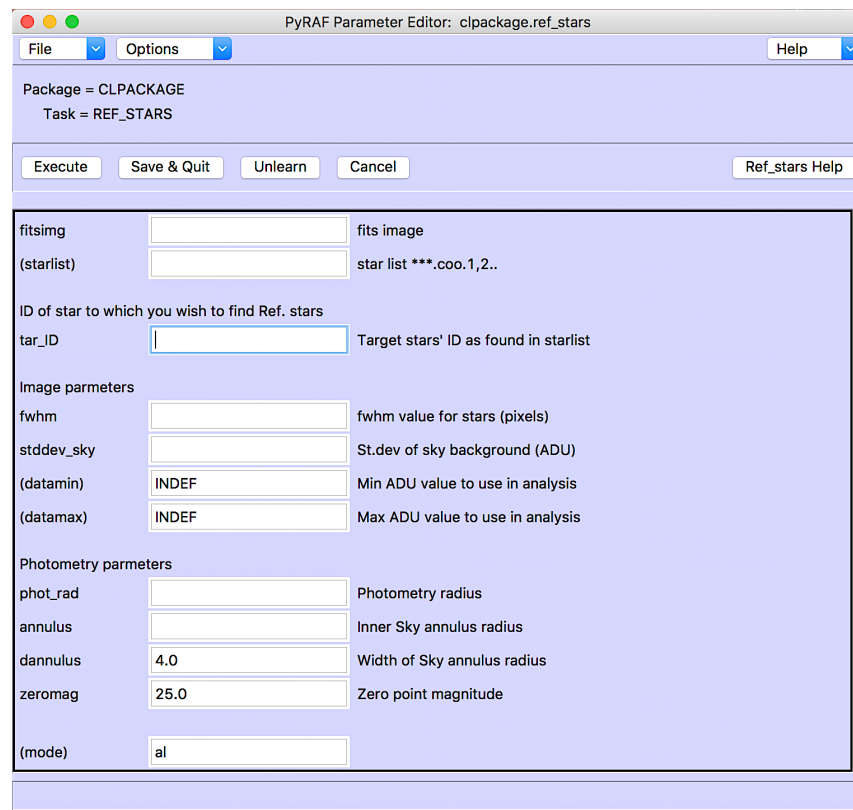


Figure 2.24 The *ref_stars* GUI used to locate appropriate reference stars, which will be used later for differential photometry.

Without HJD correction, our timing measurements of variability in the target would drift out of synchronization with the target's behaviour at source. The difference builds up when analysing data over multiple observation nights, so accounting for this is needed for accuracy. In fact, if we used UT and JD/MJD alone, the target star's inferred rotation period would appear to drift.

- ***data_analysis()***: This routine is the final stage of the L3-GUFI Pipeline. It is capable of performing three different types of photometric analysis (aperture, PSF-fitting, and differential: all three functions based on IRAF/DAOPHOT), although in our case only differential photometry was used to examine the targets' behaviour across time; see Figure 2.25 & 2.26 (Sheehan, 2008).

PyRAF Parameter Editor: clpackage.data_analysis

File Options Help

Package = CLPACKAGE
Task = DATA_ANALYSIS

Execute Save & Quit Unlearn Cancel Data_analysis Help

fitsimg FITS image
(fitslist) FITS image list
(starlist) Input star list ***.coo.1,2..

Image parameters
fwhm Typical FWHM value (in pixels) for the stars
stddev_sky Standard deviation of the sky background
(datamin) INDEF Min ADU value to use in analysis
(datamax) INDEF Max ADU value to use in analysis

Photometry parameters
phot_rad Photometry radius (in pixels)
annulus Sky annulus radius (in pixels)
dannulus Width of Sky annulus radius (in pixels)
zeromag 25.0 Zero point magnitude

Options for crowded field photometry
PSF_fit Yes No Carry out PSF fitting photometry?
it_num Iteration cycle number
psf_phot Setup the crowded field photometry pars ?
CMD_plot Options for plotting a CMD...

Options for differential photometry
differential Yes No Carry out differential photometry?
diff_phot Setup configuration for diff photometry
(resfile) Name of O/P results file ; for list mode only
mode

Figure 2.25 The *data_analysis* GUI which allows the user to perform photometric analyses such as differential photometry.

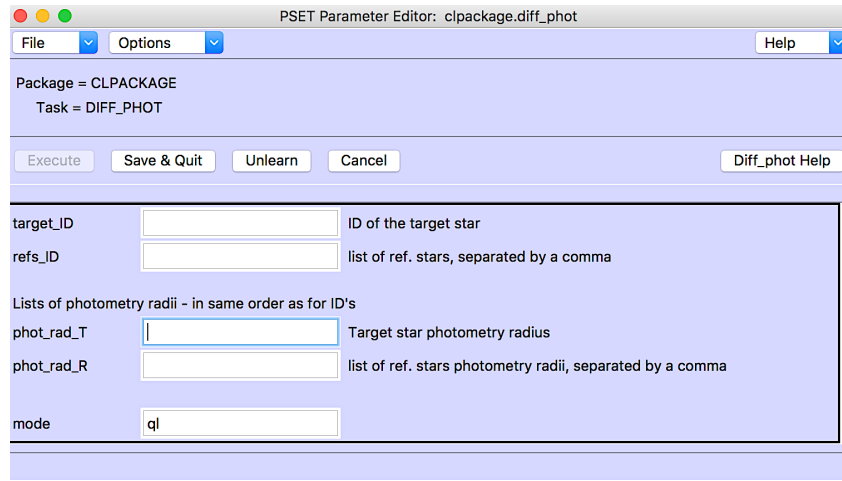


Figure 2.26 One of the three parameter set (PSET) windows for the *data_analysis* GUI, where the user has options to enter the required parameter values for differential photometry.

- Finally, in order to reduce the impacts of minor photometric errors and increase the SNR, we developed python code `bin_lightcurves.py` for binning the lightcurves into one-minute frames.

2.8 Fringing effects

As our I-band optical observations were performed using a CCD97 thinned back-illuminated chip, noticeable interference effects (fringing effects) were present in the science frames as a result of the night sky emission lines (e.g. OH) in the Earth's upper atmosphere. Fringing is not noticeable at shorter wavelengths but grows in amplitude as we expose to red/NIR wavelengths, since CCD silicon material easily absorbs shorter wavelengths. A thinned CCD's substrate becomes transparent for I- band and can cause many internal reflections. The fringing pattern position does not change for a given CCD chip, but the pattern's amplitude

varies depends on sky background, moonlight, and so on (Howell, 2006; Lane, 2008; Harding, 2012). It is an additive effect; essentially some of the sky background offset becomes spatially modulated across the sensor. Since the I-band amplitude variations detected in our selected ultracool dwarf targets amount to $\sim 0.3 - 1.50\%$, these additive effects need to be eliminated if the amplitude variations that result from fringing effects are greater than the target star differential lightcurves.

The fringing pattern is removed from the science frames by creating a fringing template, using fringe frames which are specifically taken for defringing. The observer obtains data on one field on the sky (preferably sparse with few stars), and then moves (or “dithers”) the telescope to another field on the sky, and obtains data. This is repeated many times and if done correctly with properly chosen fields, it ensures that no two pixels on the detector will have the same star or the same value. What this means in the creation of a fringing template, is that we can median combine the dithered data. This process will look at the same pixel in many frames and take the median value of these pixels. So, if we have 100 pixels where only, say, 1% of them are affected by the presence of a star, and 99% contain the sky value, the median value will essentially be the sky value. Bias frames are used to create `master_biasfringe.fits`, in addition to recording and reducing `master_skyflat.fits` (using twilight flats). The fringe frames are debiased and flat fielded; then, all the fringe frames are listed in a text file, stacked and median-combined to create the template `master_fringe.fits`.

To apply the fringing template to the reduced science frames, we adopt `image_list.txt` (which represents the list of all science frames that need remediation) and `master_fringe.fits` as parameters in the python script `mean_defringe_rescale.py` that was developed by Harding (2012). In Harding's code, the fringing template is multiplied by a constant `rescale_constant` to scale it correctly to the background level in the image. We made two improvements to the

algorithm: (1) we changed from mean to mode as the better sky estimator in the presence of stars; (2) we added an additional multiplicative scaling factor for frames where the fringing (OH strength) is a different percentage of the sky mode than it was when the template observations were made.

2.9 Summary

In this chapter, we have described the optical instrument known as Galway Ultra Fast Imager (GUFU) that was used during this campaign, to study variability in visible light from ultracool dwarfs. GUFU is a high speed photometer, based on the Andor iXon DV887-BV camera (Sheehan, 2008, Harding, 2012). This photometer was mounted on the 1.83 m VATT telescope, on Mt. Graham, Arizona.

We also outlined the reasons why we used the L3-CCD (without EM gain) in this work rather than a standard CCD. We introduced approaches to overcome a number of factors and effects that can reduce the photometric precision of CCDs. We described the data flow in the L3-GUFU Pipeline, our data reduction and analysis pipeline (Sheehan, 2008), and explained how its routines use IRAF/PyRAF tasks via the Python software language. We also explained the de-fringing routine `mean_defringe_rescale.py`, that we improved, to remove the fringing effects at NIR wavelengths.

" I look up at the night sky, and I know that, yes, we are part of this Universe, we are in this Universe, but perhaps more important than both of those facts is that the Universe is in us. When I reflect on that fact, I look up—many people feel small, because they're small and the Universe is big, but I feel big, because my atoms came from those stars."

Neil deGrasse Tyson

Chapter 3

Photometric analysis

3.1 Introduction

Astronomical photometry is a method used to measure the flux or intensity of light we receive from celestial bodies such as a star or galaxy. It is therefore very beneficial in assessing the behavior of the emission of an object. The photometric method involves a number of measures that take the raw datasets from the ground-based telescope to the ultimate lightcurve. Acquisition, extraction and analysis are the three distinct parts of the photometric method. The acquisition and the extraction phases were discussed beforehand (Chapter 2). In this chapter, we will discuss the photometric analysis of the astronomical data.

We outline in this chapter, time-resolved optical differential photometry with a fixed aperture and describe a new technique called Lucky Photometry (LuckyPhot) that can increase the differential photometric accuracy by selecting those frames from a dataset having optimal seeing conditions/photometric accuracy (Sheehan, 2008; Collins, 2014). The photometric results of the two tools are discussed in Chapters 4 and 5. We also, discuss the time series analysis tools used in this thesis including the Lomb-Scargle (LS) periodogram, Phase Dispersion Minimization (PDM), Markov Chain Monte Carlo (MCMC), phase folding, the Chi-squared test, and model fitting. These were all used to evaluate the detected periodic variability and the associated period and amplitude errors. Finally, we describe a Light Curve Fitter routine that we scripted in Python and used during this work to untangle the weaker source variability signature from that of the dominant source variability in the photometry of unresolved binary dwarfs.

3.2 GUF1 pipeline photometry

Astronomical photometry was applied in this work to study the optical variability of ultracool dwarfs. We carried out two photometric techniques on our datasets: GUF1 pipeline photometry and Lucky photometry, and we assessed whether the latter technique can reduce the effect of the atmosphere and thus produce a lower photometric scatter in the resulting differential lightcurves.

GUF1 pipeline photometry, also known as aperture photometry is defined as the calculation of flux falling within a specific aperture; generally, a circular aperture of some fixed size. This technique is provided by the *data_analysis* module in the L3-CCD GUF1 pipeline (Section 2.7.3), which is a direct implementation of the *iraf.phot* package (Davis, 1987). Aperture photometry works best when the images contain isolated point sources; such algorithms can handle the profile (point spread function, PSF) of each star individually by sampling the same proportion of the light from each point source, providing an accurate estimation of the relative brightness of stars. Another reason for choosing this technique is that the radius of the aperture selected can be chosen to avoid stray light from the wings of other stars' PSFs (Harding, 2012). The *iraf.phot* package also calculates accurate centers for each star, as well as sky values, which are subsequently adopted in the magnitude calculations. This requires the user to input an approximate FWHM value for the stars, the standard deviation "STDDEV" of the sky background (STDDEV is an IRAF abbreviation), the photometric aperture radius to be used for the target star and reference star(s), the sky annulus inner radius, the width of the sky annulus and ID numbers of the target and reference star (obtained from the pipeline's 'starlist module') (see Figure 2.24). The output photometry file stores the image file name, date of observation, Universal Time (UT), Julian Date (JD), Heliocentric Julian Date (HJD), exposure time (t), gain in e^- ADU, intensity/flux and magnitudes of the target and reference star(s), error calculations in flux and magnitude and a calculation of differential photometry.

The star sits on an offset of sky background, so the phot package calculates and subtracts that background.

$$Flux_{star} = \Sigma - A \times M_{sky} \dots \dots \dots (3.1)$$

$$Mag_{star} = Z_{Mag} - 2.5 \cdot \log_{10} (Flux_{star} + t) \dots \dots \dots (3.2)$$

where M_{sky} is the mean per pixel estimation of the sky background within the sky annulus, Σ is the sum of counts in the aperture, A is the area of the aperture disk, t is the exposure time in seconds and Z_{Mag} is the zero point magnitude - which can have an arbitrary value, as it will cancel out in differential photometry.

The errors in the photometry derived by IRAF:

$$Photometric\ Error = \sqrt{\frac{Flux_{star}}{gain} + A \times \sigma^2 + A^2 \times \frac{\sigma^2}{N_{sky}}} \dots \dots \dots (3.3)$$

$$Mag_{Error} = 1.0857 \times \frac{Photometric\ Error}{Flux_{star}}, Mag_{Error} \ll 1 \dots \dots \dots (3.4)$$

where N_{sky} is the number of sky pixels in the annulus around the star and σ is an estimate of the standard deviation of the sky background.

Ultracool dwarfs are primarily faint and they have small variability amplitudes, so it is essential to obtain the highest SNR for a target's photometry. The correct selection of aperture size is a critical factor in implementing good aperture photometry. As we mentioned previously in (Section 2.7.3), the *app_size* routine in the L3-CCD GUF1 pipeline offers a calculation of the highest value of SNR, for a range of aperture radius values in the phot routine. Equation 3.4 can be modified, since $SNR = \frac{Flux_{star}}{Photometric\ Error}$, to give:

$$SNR = \frac{1.0857}{\sigma_{IRAF}}, \sigma_{IRAF} \ll 1 \dots \dots \dots (3.5)$$

where σ_{IRAF} is the formal photometric error in the instrumental magnitude in the aperture. However, informal photometric errors arising from the image reduction process are neglected in this calculation. The phot task assesses photometric aperture sizes to establish which produces the largest SNR for the star, from which the user can select the most appropriate aperture size for the target star (see Figure 3.1). The diameters of the optimum aperture and sky annulus differ from night to night based on the seeing conditions (Harding, 2012). Using the GUF1 pipeline, the data were binned to one-minute frames in order to determine the optimum aperture, and this single constant aperture size (Fixed Aperture, F.A.) was applied to all stars and across all frames throughout a given observation night, assuming that the fixed aperture size can be applicable as long as astronomical seeing throughout an observation night is comparatively stable. This is a standard approach, and was adopted also by Smith et al. (2004), who developed the QVAR (Quasar Variability) technique. An assessment of GUF1 F.A. performance and another technique (Lucky Phot + Optimum Aperture O.A.) are elaborated on further in Chapter 4 and Chapter 5, and determine which system would deliver the lowest lightcurve scatter.

Before performing GUF1 differential photometry on the target and a selection of reference stars, choosing inherently non-variable reference stars over the timescales of the observation is very important.

3.3 Differential Photometry

Differential photometry is the method performed on all datasets studied in this work, which accurately measures the changes in magnitude/flux of a target object and generates differential lightcurves of the target object with respect to an ensemble of reference stars. This method was selected over absolute photometry, as absolute photometry depends heavily on atmospheric effects and

accurate calibrations for changing airmass. By contrast, with differential photometry, since the target we are studying and the reference stars are relatively close together on the sky and lie in the same frame in CCD images, all stars in the field will be equally affected to first order by changes in conditions. This gives a stability to the photometry that is necessary for time-series observations. Differential extinction corrections must be taken into account in the case of a large field-of-view (FOV), since the reference stars could be observed through different airmasses within the same CCD frame. However, with the 3' x 3' FOV of the GUF1 photometer, the airmasses of all stars in the field are relatively the same and therefore extinction corrections are not required. The *data_analysis* module measures differential magnitude (m_{Diff}), as a function of UT, via the *iraf.phot* routines. Differential photometry is the difference in flux between a target star and an ensemble of selected reference stars:

$$m_{Diff} = m_T - m_{\overline{ref}} = -2.5 \cdot \log_{10} \left(\frac{F_{\overline{ref}}}{F_T} \right) \dots\dots\dots (3.6)$$

where m_{Diff} is differential magnitude, m_T and F_T are the magnitude and flux of the target star for that frame, respectively, and $m_{\overline{ref}}$ and $F_{\overline{ref}}$ are the mean magnitudes and fluxes of the all selected reference stars for that frame, defined as follows:

$$F_{\overline{ref}} = \frac{1}{N} \sum_i^N F_i \dots\dots\dots (3.7)$$

$$m_{\overline{ref}} = -2.5 \cdot \log_{10} \left(F_{\overline{ref}} \right) \dots\dots\dots (3.8)$$

Equations 3.7 and 3.8, which are based on averaging reference star fluxes, were chosen over the alternative of averaging reference star magnitudes directly, since this method provides greater weighting for brighter stars with greater signal to noise ratios and substantially reduced photometric errors.

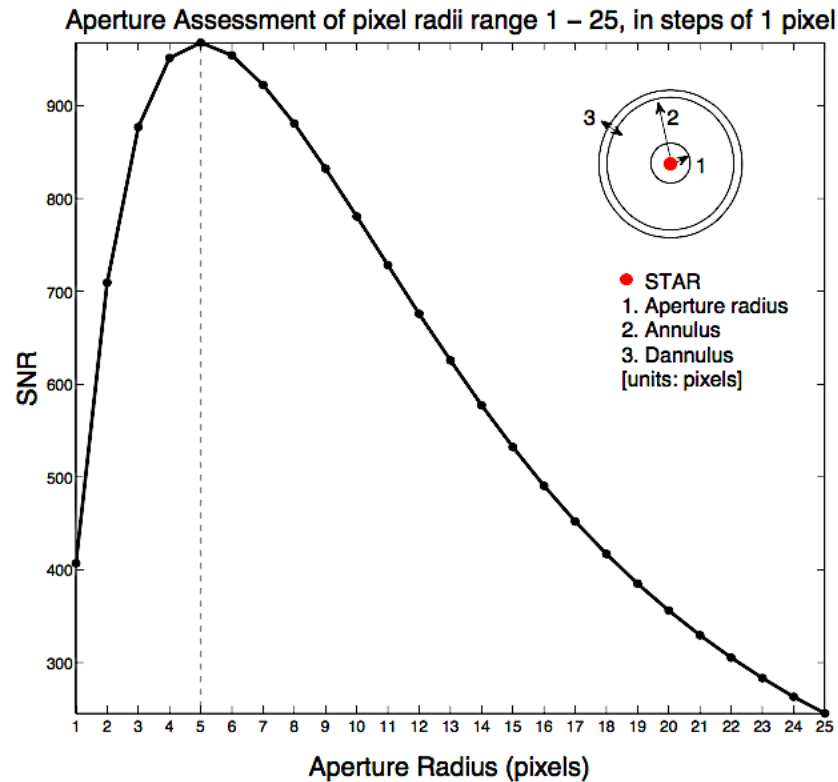


Figure 3.1 A plot of SNR versus aperture size (pixels) to determine the optimum aperture radius in the *app_size* module. As seen from the plot, too large an aperture radius will add more noise from the sky background and then the SNR decreases dramatically. In this example, the most suitable aperture radius is approximately 5 pixels. This plot is taken from (Harding, 2012).

The *ref_stars* module in the L3-CCD pipeline (outlined in Section 2.7.3) allows for selection and rejection of reference stars from the process based on the following selection criteria (Bailer-Jones and Mundt, 2001):

- 1) The selected reference stars must be point sources, with near-Gaussian point spread functions (PSF).
- 2) They must be isolated from other neighbours on the image, to prevent contamination within annuli of other sources, and must not be located near the edge of the frame.

- 3) The selected reference stars must be present on every image to maintain continuity.
- 4) The flux of the selected reference stars must be $\leq 75\%$ of the CCD detector saturation limit, to prevent non-linearity.
- 5) The chosen stars should be within a range of magnitudes (brightness range) of ± 0.5 of the target star.
- 6) If possible, the reference stars and the target should be of the same approximate color/spectral type in order to reduce the telluric extinction effects which would affect photometric accuracy.

Once appropriate reference stars are provided according to the above criteria, the differential photometry would distinguish the inherent variation of the target star from external noise sources. We refer the reader to Lane (2008), Sheehan (2008) and Harding (2012) for an in-depth discussion of GUF1 photometry with a fixed aperture.

3.4 Optimum Aperture (O.A.) & Lucky Photometry (LuckyPhot)

We also used second photometric technique, which is regarded as being capable of reducing photometric errors, allowing better lightcurves to be produced (with lower scatter) from a given data set; this technique is called Lucky Photometry (LuckyPhot), developed by Collins (2014) in the MATLAB environment. The LuckyPhot technique can limit the impact of turbulent weather conditions on photometric measurements through data selection. The photometric scatter imposed by the atmosphere can be considerably decreased by selecting frames that were captured under similar ambient circumstances. We used the same inherently non variable reference stars that were used in GUF1 photometry.

As previously discussed, selecting the appropriate aperture size is a significant choice when extracting flux counts from an image. Photometric apertures that are too small will omit a large fraction of the flux from the star, photometric apertures that are too big will add undesired variations to the signal from the background. We tested a technique which can calculate the optimum aperture (O.A.) (Collins, 2014), modified from a method described by Deeg and Doyle (2001). It was written using the MATLAB environment. Collins (2014) summarized the motivation behind O.A.:

- Due to optical aberrations, all stars cannot have the same width PSF within a frame.
- Variations in atmospheric seeing throughout the observation night can cause variations in the PSF of a star; therefore, it cannot be assumed each star's PSF has the same width between frames.

Previous studies (e.g. Figure 3.1) have determined the method of calculating the optimum aperture for a single star, and the aperture size for each other star can be measured accordingly (Deeg and Doyle, 2001). They assumed that the ratios between aperture sizes of the stars within a frame are constant from frame to frame and assumed that the atmospheric effects that affect seeing are applied equally to all stars. No such assumption is made by the O.A. technique, as it calculates the optimum aperture radius for each star within each frame. It follows the same approach to the fixed aperture method (Section 3.2), determining the most suitable aperture radius by using the SNR of each photometric aperture size (Figure 3.2). Additionally, this technique searches for the zero-crossing point in the SNR derivative for a range of aperture sizes applied to the star. The zero-crossing point indicates a decent assessment of where the star counts dominate and where sky background counts begin to dominate (Figure 3.2).

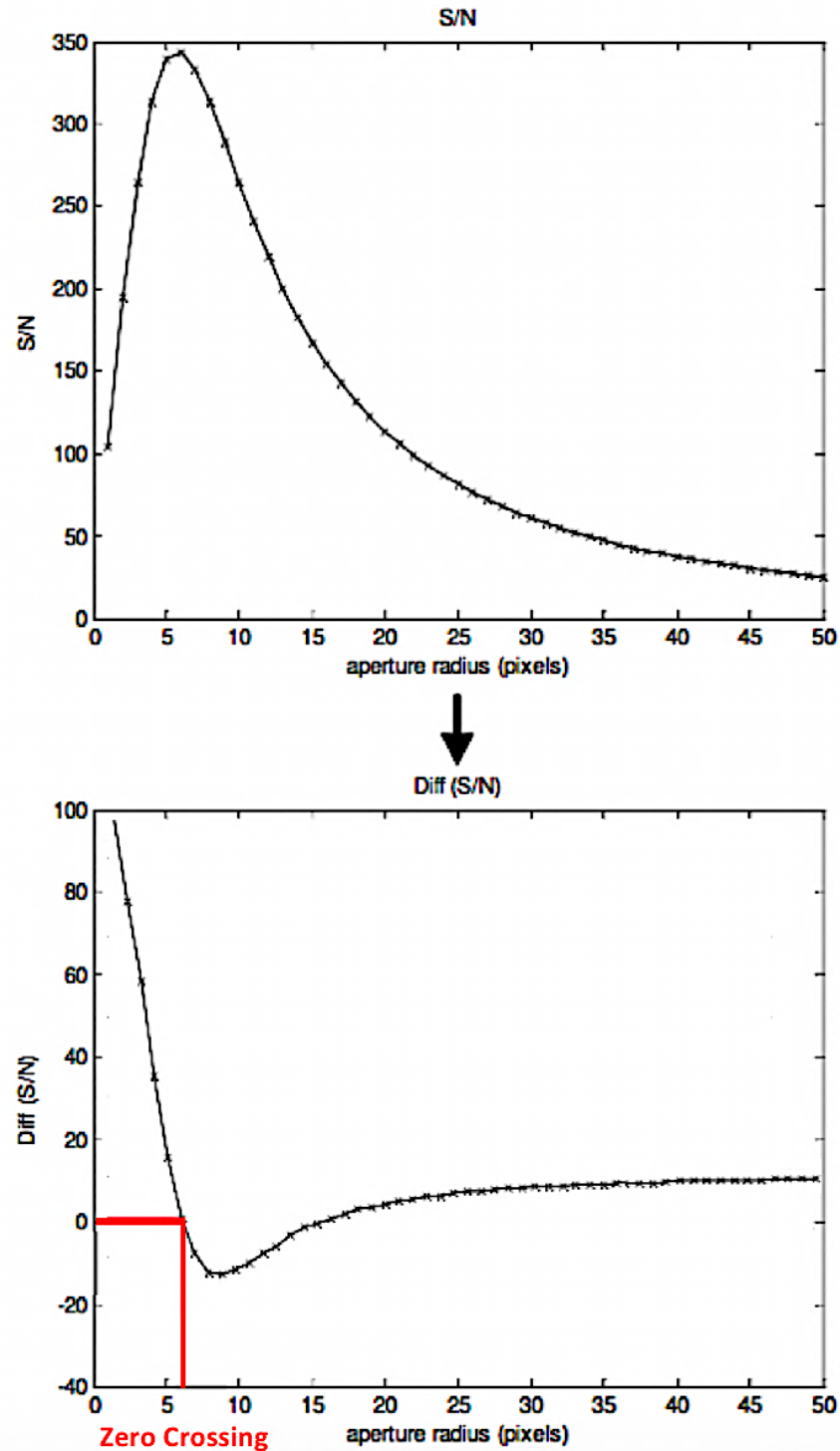


Figure 3.2 The process of O.A. selection. The upper panel shows the SNR plotted against aperture radius. The lower panel shows the zero-crossing point of the derivative of the SNR which represents a good assessment of the optimum aperture (O.A.) size for a given distribution. This figure is taken from Collins (2014).

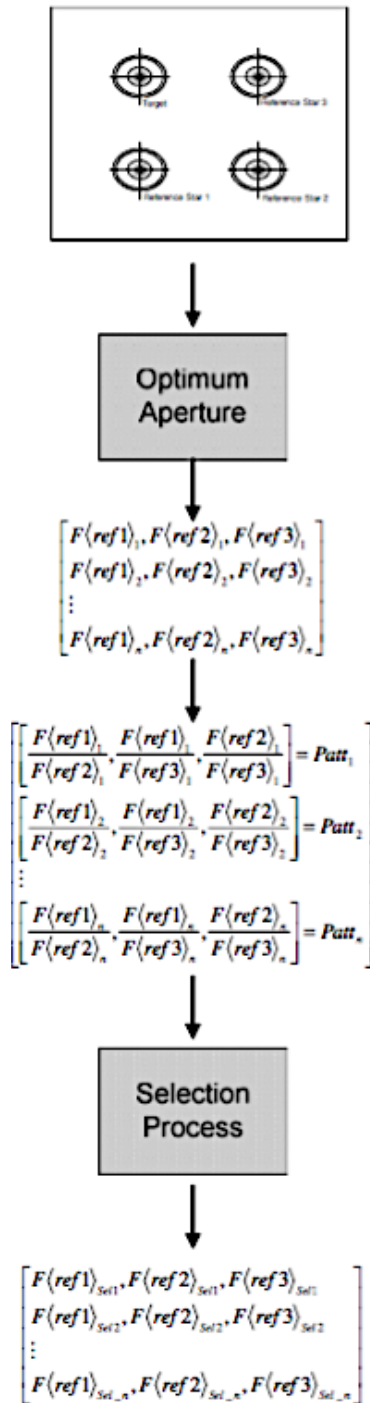


Figure 3.3 A summary of the Lucky Photometry (LuckyPhot) technique. This figure is taken from Collins (2014).

Each step of the LuckyPhot process will be explained, following the flow shown in Figure 3.3. Let us assume that we have a frame (image) with three reference stars and one target. The first step is determining the optimum aperture (O.A.) to extract the flux from each star in each frame as we described before. Then, the ratio of the flux of each reference star to every other reference star (e.g. $R1/R2$, $R1/R3$ and $R2/R3$) within a frame is calculated, to create a measure for the conditions of this frame (Table 3.1). This produces a pattern (array of ratios) which define the atmospheric photometric characteristics in that specific frame, on the basis of which the selection process will identify which frames have common photometric characteristics. As shown in Figure 3.4 & Table 3.1, by performing a sigma-rejection scheme for each reference star ratio calculation across all frames, the most common value for each ratio calculation is identified. The frame selection method is carried out through the application of the pass/fail scheme. The frame is chosen when all ratio combinations lie within their respective σ limits (Figure 3.4). On the other hand, the frame is rejected if any ratio combination does not lie within its σ limits. Frames are then grouped into bins by averaging each star's fluxes in batches of the surviving frames. The time sampling is maintained as not entire data bins are completely rejected - at least 1 frame will be retained per bin, even if, in a worst case scenario, technically it failed the sigma-rejection test.

We used the same output data of the data reduction/calibration process (L3-GUFI pipeline). In addition, we used the same outputs of the *data_ops* module (breaking up FITS datacubes and registration etc), and used the same reference stars that the *starlist* routine (**_fr.fits.coo.1*) had selected for the GUFI/aperture photometry. We wrote a Python script called the *Input_phot* module that takes IRAF phot output files and parses them into the correct format for the LuckyPhot technique. The main output file generated by the *Input_phot* module contains the extracted flux values from each frame. In essence, the data is in blocks of frames. Within each block, we sub-block it into aperture size (as there is a line for each aperture size defined by the start aperture, aperture step and end aperture

sizes), and within this sub-block each star gets a line recording its flux in that aperture (Figure 3.5).

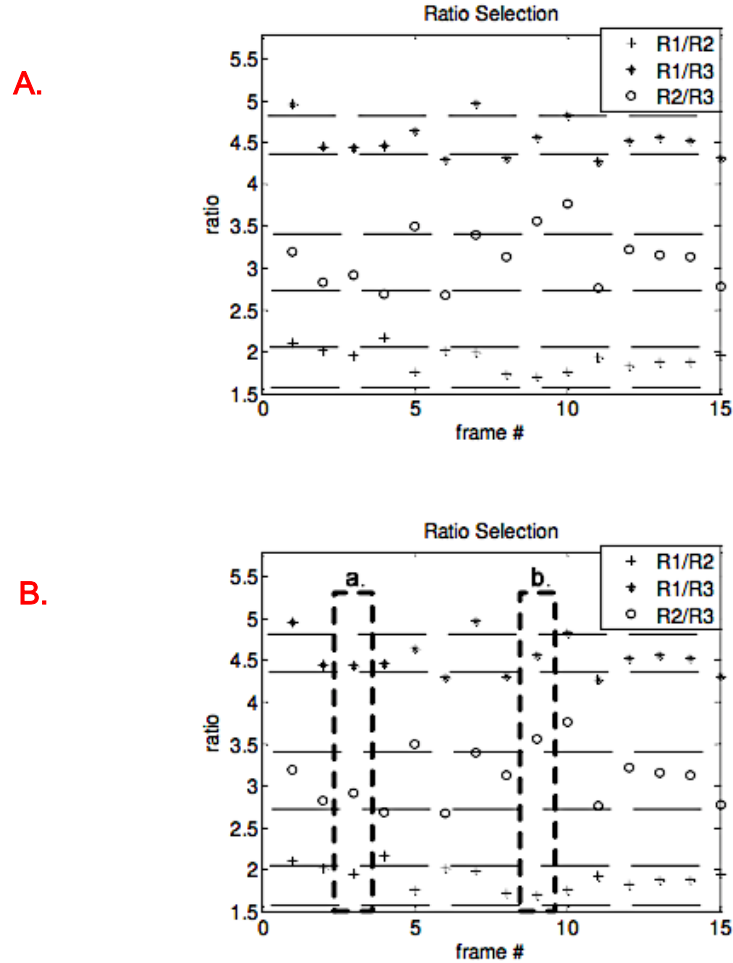


Figure 3.4 Plots **A** and **B** illustrate the LuckyPhot frame selection method. A σ rejection scheme is performed for each reference star ratio calculation across all image frames, the commonest value for each ratio calculation is identified. Horizontal bars represent the σ limit. In plot B, the box "a" shows a frame in which all ratio calculations lie within their respective sigma limits. Therefore, this frame would be chosen for the final differential lightcurve. Whereas the box "b" shows the case where the two ratio calculations (R1/R2 and R1/R3) lie within their respective sigma limits, but (R2/R3) does not. Thus this particular frame would be excluded. The selection process may be repeated a number of times, with fewer improvements. This figure is taken from Collins (2014).

A.

Frame #	R1 Star 1	R2 Star 2	R3 Star 3	R1/R2	R2/R3	R1/R3
1	Flux 1	Flux 2	Flux 3			
2	Flux 1	Flux 2	Flux 3			
3	Flux 1	Flux 2	Flux 3			
n						
				Mean (R1/R2)	Mean (R2/R3)	Mean (R1/R3)

B.

Frame #	Res (R1/R2) = R1/R2 – Mean (R1/R2)	Res (R2/R3) = R2/R3 - Mean(R2/R3)	Res (R1/R3) = R1/R3 – Mean (R1/R3)
1			
2			
3			
n			

C.

Frame #	$\sigma_1 = \text{Res (R1/R2)}^2$	$\sigma_2 = \text{Res (R2/R3)}^2$	$\sigma_3 = \text{Res (R1/R3)}^2$
1			
2			
3			
n			

Table 3.1 Tables that are calculated during the LuckyPhot technique: **A.** creates a pattern that describes the atmospheric photometric characteristics for the frames. **B.** calculates the residuals of the ratio for each pattern. **C.** calculates sigma σ for each ratio. The σ value allows to set optimum rejection level for each ratio.

The basic design of the *Input_phot* output file is as follows - see Figure 3.5 for an example with real values:

Frame 1

Aperture N for star 1 | Uncalibrated Flux | Area | Calibrated Flux | Magnitude | Error |
 Aperture N for star 2 | Uncalibrated Flux | Area | Calibrated Flux | Magnitude | Error |
 Aperture N for star 3 | Uncalibrated Flux | Area | Calibrated Flux | Magnitude | Error |
 Etc.. for all stars

Aperture N+1 for star 1 | Uncalibrated Flux | Area | Calibrated Flux | Magnitude | Error |
 Aperture N+1 for star 2 | Uncalibrated Flux | Area | Calibrated Flux | Magnitude | Error |
 Aperture N+1 for star 3 | Uncalibrated Flux | Area | Calibrated Flux | Magnitude | Error |
 Etc. for all stars

Aperture N+X for star 1 | Uncalibrated Flux | Area | Calibrated Flux | Magnitude | Error |
 Aperture N+X for star 2 | Uncalibrated Flux | Area | Calibrated Flux | Magnitude | Error |
 Aperture N+X for star 3 | Uncalibrated Flux | Area | Calibrated Flux | Magnitude | Error |
 Etc. for all stars where N+X is the final aperture size.

End of frame 1

Frame 2

Aperture N for star 1 | Uncalibrated Flux | Area | Calibrated Flux | Magnitude | Error |
 Aperture N for star 2 | Uncalibrated Flux | Area | Calibrated Flux | Magnitude | Error |
 Aperture N for star 3 | Uncalibrated Flux | Area | Calibrated Flux | Magnitude | Error |
 Etc.. for all stars

Aperture N+1 for star 1 | Uncalibrated Flux | Area | Calibrated Flux | Magnitude | Error |
 Aperture N+1 for star 2 | Uncalibrated Flux | Area | Calibrated Flux | Magnitude | Error |
 Aperture N+1 for star 3 | Uncalibrated Flux | Area | Calibrated Flux | Magnitude | Error |
 Etc. for all stars

Aperture N+X for star 1 | Uncalibrated Flux | Area | Calibrated Flux | Magnitude | Error |
 Aperture N+X for star 2 | Uncalibrated Flux | Area | Calibrated Flux | Magnitude | Error |
 Aperture N+X for star 3 | Uncalibrated Flux | Area | Calibrated Flux | Magnitude | Error |
 Etc. for all stars where N+X is the final aperture size.

End of frame 2

.

.

Frame n

```

1 $ Data
2 140
3 JULIAN DAY: 2457813.973415540
4 FWHMPSF: 2.5
5 1.00 9208.692 3.343015 9088.916 15.104 0.011 0 NoError *\
6 1.00 853.4106 3.485139 727.7294 17.845 0.041 0 NoError *\
7 1.00 8885.294 3.469566 8757.742 15.144 0.012 0 NoError *\
8 1.00 123.073 3.479318 -1.238108 INDEF INDEF 0 NoError *\
9 1.00 325.0781 3.343249 206.2302 19.214 0.081 0 NoError *\
10 1.00 1311.089 3.430356 1185.725 17.315 0.032 0 NoError *\
11 1.00 150.2552 3.395839 26.03526 21.461 0.302 0 NoError *\
12 2.00 31521.71 13.06741 31053.52 13.770 0.006 0 NoError *\
13 2.00 2635.386 12.72935 2176.339 16.656 0.024 0 NoError *\
14 2.00 27323.07 12.75539 26854.14 13.927 0.007 0 NoError *\
15 2.00 463.2187 12.70667 9.227488 22.587 1.218 0 NoError *\
16 2.00 1110.438 12.86611 653.0649 17.963 0.046 0 NoError *\
17 2.00 4166.281 12.83772 3697.12 16.080 0.018 0 NoError *\
18 2.00 550.6941 12.83067 81.34784 20.224 0.180 0 NoError *\
19 3.00 55469.25 28.38016 54452.41 13.160 0.005 0 NoError *\
20 3.00 4753.344 28.59351 3722.203 16.073 0.018 0 NoError *\
21 3.00 47426.69 28.5572 46376.84 13.334 0.005 0 NoError *\
22 3.00 1028.459 28.63227 5.469124 23.155 3.007 0 NoError *\
23 3.00 2110.119 28.46937 1098.072 17.398 0.036 0 NoError *\
24 3.00 7379.237 28.5524 6335.774 15.496 0.014 0 NoError *\
25 3.00 1181.041 28.55256 136.5876 19.661 0.152 0 NoError *\
26 4.00 76797.18 50.58947 74984.61 12.813 0.004 0 NoError *\
27 4.00 6712.1 50.45574 4892.563 15.776 0.016 0 NoError *\
28 4.00 63941.46 50.47615 62085.8 13.018 0.004 0 NoError *\
29 4.00 1808.55 50.5543 2.315909 24.088 9.445 0 NoError *\
30 4.00 3222.397 50.41475 1430.221 17.111 0.033 0 NoError *\
31 4.00 10282.18 50.61153 8432.553 15.185 0.012 0 NoError *\
32 4.00 2044.93 50.5978 194.0605 19.280 0.139 0 NoError *\
33 5.00 92680.49 78.90625 89853.36 12.616 0.004 0 NoError *\
34 5.00 8547.685 78.71066 5709.218 15.609 0.015 0 NoError *\
35 5.00 76339.33 78.76754 73443.59 12.835 0.004 0 NoError *\
36 5.00 2823.548 78.75816 9.630754 22.541 2.884 0 NoError *\
37 5.00 4476.02 78.80433 1674.633 16.940 0.032 0 NoError *\
38 5.00 12774.98 78.77249 9896.2 15.011 0.011 0 NoError *\
39 5.00 3122.176 78.75015 241.4923 19.043 0.136 0 NoError *\
40 6.00 104186.5 113.2373 100129.3 12.499 0.003 0 NoError *\
41 6.00 10340.76 113.6529 6242.2 15.512 0.015 0 NoError *\
42 6.00 85512.32 113.5411 81338.2 12.724 0.004 0 NoError *\
43 6.00 4075.51 113.4642 21.59417 21.664 1.573 0 NoError *\
44 6.00 5894.219 113.3548 1864.611 16.824 0.032 0 NoError *\
45 6.00 15025.55 113.3008 10884.91 14.908 0.011 0 NoError *\
46 6.00 4439.415 113.3834 291.8459 18.837 0.134 0 NoError *\

```

Figure 3.5 Example of the format of the file for one frame for input to LuckyPhot.

There are two main MATLAB scripts to implement LuckyPhot: RUN_OVAR and RUN_SELPHOT, which are run sequentially. The RUN_OVAR routine (Figure 3.6) reads a data file, runs the O.A. technique and plots results. The output from RUN_OVAR is a set of standard differential lightcurves. We used this to appraise our data and fine tune our settings (time bins & reference star selection). When

the user is happy with the data, then it is necessary to save the output of the data using this command: `save ('the_object', 'out_data', 'jd_list')`.

```
%RUN_OVAR
%Adrian Collins
%BCOLabs
%14-4-2009
%%%%%%%%%%%%%%%%%%%%%%%%%%%%%%%%%%%%%%%%%%%%%%%%%%%%%%%%%%%%%%%%%%%%%%%%%%
User Input%%%%%%%%%%%%%%%%%%%%%%%%%%%%%%%%%%%%%%%%%%%%%%%%%%%%%%%%%%%%%%%%%%%%%%%%%%

cd '/Users/salam/Documents/OVAR_package'
in_path = '/Volumes/MyFiles2/Aaron_Data/Combined_Inputs.dat'; %full path to input data file
time_bin_size =5; %seconds
drop_star = []; % drop_star = [2,7,8]; %array with list of dropped stars eg drop_star = [2,3,5];
optimum_aper = 0; %1 - yes 0 - manual
man_aper_array = [10,10,10,10,10,10,10,10,10,10,10,10,10,10,10];%only used if optimum_aper = 0;
plot_final_results = 1; %plot final results 1 = yes 0 = no;
plot_rn_rbar = 1; %plot each rn - rbar
plot_raw_data = 1; %plot raw data from each reference (bg subtracted + aper selected)

%%%%%%%%%%%%%%%%%%%%%%%%%%%%%%%%%%%%%%%%%%%%%%%%%%%%%%%%%%%%%%%%%%%%%%%%%%
```

Figure 3.6 The user settings for the RUN OVAR routine. `in_path` here is the full path to the input file. Data is combined (binned) into intervals of `time_bin_size` seconds. There is an option to drop selected variable reference stars.

Next, the user runs the RUN SELPHOT routine (Figure 3.7). This executes the LuckyPhot technique (selects frames with reference star ratio consistency). The output from this is a set of plots showing magnitude errors (Figure 4.13), number of dropped frames (Figure 4.14), and final differential lightcurves.

```

%RUN_SELPHOT
%Adrian Collins
%BCOlabs
%09-09-2010

clear; close all; clc;

%%%User Input
sig_limits = [7,-0.02,0.1];
num_iters = 1;
t_binning =200; %seconds
data_path = 'C:\Users\salam dulaimi\Documents\MATLAB\';
%%%%%%%%

```

Figure 3.7 The user settings for the RUN SELPHOT routine. `data_path` here is the user saved file from the previous step (RUN_OVAR). The `sig_limits` are sigma limits for how hard the user drives the process. It basically means that the user can limit the number of redundant processes. `num_iters` is the number of times to iterate the LuckyPhot routine.

3.5 Post-Photometry Assessment of Lightcurves

Astronomical observing under poor weather conditions (e.g. intermittent cloud that leads to gaps in the differential lightcurve (data removal), high humidity which affects transparency, and high winds that affect seeing) can affect the quality of the final differential photometric lightcurves. We have rewritten the MATLAB scripts called “post-photometric routines” originally developed by Harding (2012), which aim to assess the stability of reference stars with respect to the target star and to identify areas of poor quality in the final differential lightcurve, based on the detection of increased scatter rms. This assessment detects periods of bad weather conditions and recognizes erroneous data points in the time series. Each step of this assessment can be explained as follows:

- For a given observation night, the ratio of the flux of each reference star compared to the mean of the remaining reference stars is plotted, to

analyse the quality of the reference stars used. We reject as unsuitable any reference star when it has significantly lower SNR than other reference stars in the sample or when its flux has been affected by other impacts in some frames (e.g. hot pixels, isolated cloud, cosmic rays, contamination from other objects in its photometric annulus).

- The mean value of all selected reference stars for each frame, known as the superflux, is calculated. Then, averaging across all the frames, the mean of all the superfluxes, and the mean flux for each reference star, are also calculated.
- The quality factor is calculated using Equation 3.9 (Harding, 2012) for the reference stars numbered $n = 1 \dots N$:

$$Quality\ Factor = std\left(\left(\frac{Flux_{Ref}(n)}{Superflux}\right) - \left(\frac{Mean\ Flux_{Ref}(n)}{Mean\ Superflux}\right)\right) \dots\dots\dots (3.9)$$

where $std()$ is a standard deviation operation over all values of n (all reference stars), $Flux_{Ref}$ is the flux value of each reference star and $Mean\ Flux_{Ref}$ and $Mean\ Superflux$ were calculated in the previous step. This equation compares the instantaneous fractions of the superflux taken by each reference star to their long-term average fractions. We expect the fractions to be very consistent, but in unstable conditions, they can diverge, driving up the quality factor value.

- A quality factor threshold can therefore be set by the user on the basis of the observed quality factor scatter (Figure 3.8). This threshold is utilised as an absolute constraint on data points, since all points with quality factor values above the designated threshold will be removed from the final differential photometry calculation.

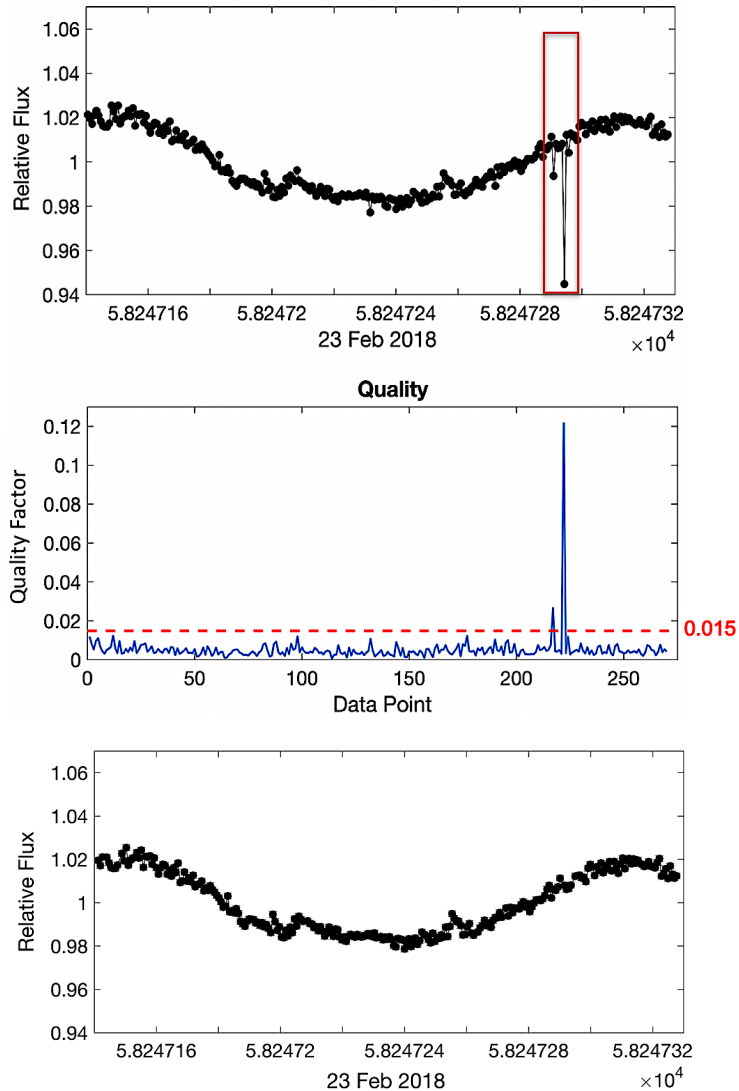


Figure 3.8 Illustration of the post-photometry routines. We selected an observation made on February 23 2018 UT, of 2M J1314+13AB, since the seeing was generally excellent throughout the exposure, but some parts of the night were impacted by intermittent cloud causing deteriorating transparency and seeing conditions, resulting in an increase in the rms scatter for some data points, as shown in the top panel. We assign a quality factor threshold of 0.015 (highlighted with a red dashed horizontal line in the middle panel). All data points above the assigned threshold will be filtered out and will not be used in the final differential calculation. The bottom panel shows the final lightcurve after removing low quality data points automatically.

The outputs of this routine are logged to a file which includes the fluxes of the target and reference stars and their UT time of acquisition. We recalculate superflux from this file and this is then subtracted from the flux of the target star to compute the final differential photometry.

Lastly, we found the STD quality filtering is not necessary when running the LuckyPhot technique, since LuckyPhot already rejects such bad data points automatically. LuckyPhot always keeps *some* point in each binned interval, whereas quality selection can potentially throw away entire bins.

3.6 Photometric Error Model

In order to achieve high precision differential photometry on these faint objects, the photometric errors on each lightcurve data point must be investigated. Magnitude errors in the target and reference star data points were computed using the photometric techniques used in this work; GUF1 photometry (Section 3.2), which is provided by the *data_analysis* module in the L3-CCD GUF1 pipeline (Sheehan, 2008), and the LuckyPhot technique (Collins, 2014), which is provided by the *RUN_OVAR* routine (Section 3.4). In this work, a photometric error model described by Bailer-Jones and Mundt (2001) was used to quantify formal and informal photometric errors. Errors resulting from photon statistics and instrumental readout noise are computed by the IRAF task *phot*, and are regarded as formal photometric errors. Other effects that are hard to estimate accurately, such as residuals after flat fielding and fringe removal, are known as informal photometric errors. This model is based on the fact that reference stars are inherently non-variable objects (this assumption is tested in the process of ratifying reference star selections). We compute the photometric errors of the target object and each reference star by plotting their formal photometric errors (σ_{IRAF}), as calculated by the IRAF task *phot*, versus the standard deviation of

their lightcurves ($\sigma_{rms\ scatter}$). The model assumes a linear relationship between $\sigma_{rms\ scatter}$ and σ_{IRAF} (Figure 3.9), and a simple linear fit of the data can be performed:

$$\sigma_{rms\ scatter} = a + b \cdot \sigma_{IRAF} \dots \dots \dots (3.10)$$

where a & b are coefficients of the first order polynomial to linear fit of the data.

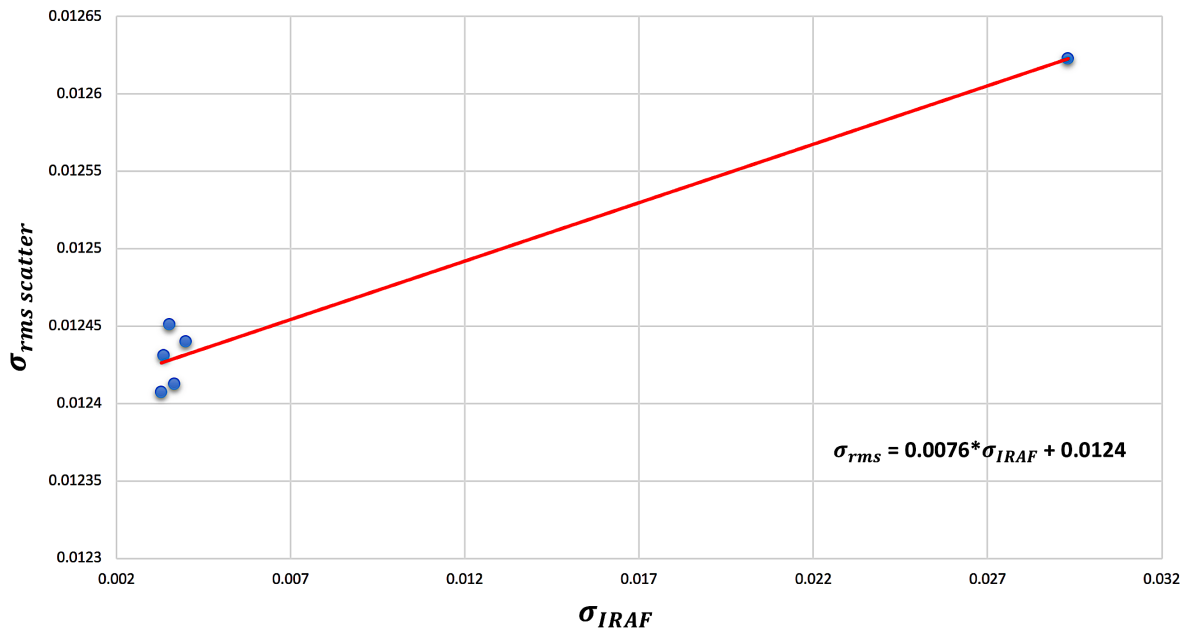


Figure 3.9 The final error model fit for the six reference stars used for the analysis of 2MASS J0746+2000AB on March 04, 2017 UT.

At each point in the target's differential lightcurve, the total photometric error from both the target object and the reference stars can be calculated from Equation 3.11, adopted from Bailer-Jones and Mundt (2001):

$$(\delta M_{total})^2 = (\delta M_{target})^2 + \left(\frac{1}{N \cdot F_r}\right)^2 \sum_i^N F_i^2 (\delta M_i)^2 \dots \dots \dots (3.11)$$

where δM_{target} , δM_i are the magnitude errors in the target object and i^{th} reference star respectively, calculated by applying the a & b fit coefficients from Equation 3.10 to each measurement, N is the number of reference stars used, F_r is the combined flux of reference stars and F_i is the flux of the i^{th} reference star.

To determine the errors in the individual flux data points, let us assume that we have a frame with four reference stars and one target. The magnitude error of the target is known from Equation 3.11. Now, we apply the error in the magnitude of each reference star to their flux and call the resulting flux errors δF_{r1} , δF_{r2} , δF_{r3} , δF_{r4} , δF_{r5} and δF_{r6} . The total flux error of the reference stars can be found:

$$\delta F_{ref\ total} = \sqrt{(\delta F_{r1})^2 + (\delta F_{r2})^2 + (\delta F_{r3})^2 + (\delta F_{r4})^2 + (\delta F_{r5})^2 + (\delta F_{r6})^2} \dots (3.12)$$

Therefore, the magnitude error of all reference stars used is:

$$\delta M_{ref} = \frac{\delta F_{ref\ total}}{F_r} \dots \dots \dots (3.13)$$

Equation 3.13 is valid for $\delta M_{ref} \ll 1$. Lastly, the magnitude error for each lightcurve data point $\delta M_{datapoint}$ is:

$$\delta M_{datapoint} = \sqrt{(\delta M_{target})^2 + (\delta M_{ref})^2} \dots \dots \dots (3.14)$$

Note that $\delta M_{datapoint}$ in Equation 3.14 amount to the same thing as δM_{total} in Equation 3.11, they are both the net error for a single point on the target's differential lightcurve.

These photometric errors are plotted as the error bars in all differential lightcurves in Chapters 4 & 5.

3.7 Detecting Periodic Variability of Photometric Datasets

To identify and evaluate periodic variability in our datasets, a range of statistical techniques were used in this work to measure the validity of the periodic variability detected and the associated errors.

3.7.1 The Lomb-Scargle (LS) Periodogram

The Lomb-Scargle (LS) periodogram, based on the contributions of Lomb (1976) and, independently, Scargle (1982) & Scargle (1989), is one of the statistical tools used in this work. This particular algorithm is ideal for the astronomy community as it was designed to detect and characterize periodic signals in unequally-spaced time-series, and it uses the discrete fourier transform (DFT) which is a periodic function of frequency. Basically, the LS periodogram is a modification of the classical periodogram. There are statistical problems connected with unevenly-spaced data due to the data loss and an increase in aliasing; however, this periodogram can overcome these inherent statistical problems and provide greater statistical stability. The LS periodogram algorithm takes the photometric output file, and returns a power spectrum (signal power vs. temporal frequency) that has been thoroughly examined for significant peaks to investigate the presence of periodic variability. This technique is very significant for limited and patchy lightcurves, since other effects could be present such as spectral leakage, which spreads power into smaller peaks on either side of the true peak frequency, or aliasing, which maps frequencies (f) above half the sampling frequency ($f_s/2$) back to a lower, false aliased frequency ($f_s - f$) (Figure 3.10 & Figure 3.11). Despite the advantages of using the LS periodogram, the power in the periodogram can appear not only with a single frequency, but also at other frequencies in the nearest neighborhood, leading to artificial amplitudes due to

the effect of spectral leakage. The reason for spectral leakage to occur is when a window function which has a finite span is applied to the time function, and therefore frequencies can propagate into adjacent DFT bins (Harding, 2012; Bowdalo et al., 2016). Another issue, known as aliasing or false periods, arises when the data sampling is too slow for the changes in the signal (undersampling), and thus appear as other periods. More data produces more significance at the true frequency, which reduces spectral leakage, but not aliasing: that requires a higher rate of sampling, not a longer span of data. Due to large data gaps between consecutive observations owing to various natural phenomena, (like day/night cycle, weather, moonlight contamination and seasonal cycles, etc.), spectral leakage and aliasing may also occur (Baluev, 2012; Harding et al., 2013a).

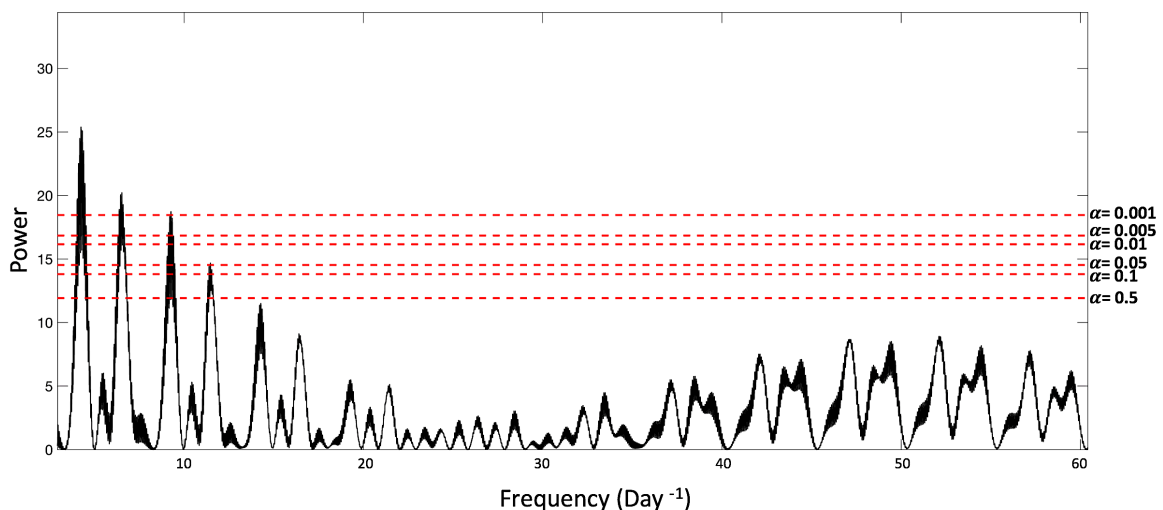


Figure 3.10 We see power peaks at adjacent frequencies, f (e.g. $f \sim$ between 10 - 20 Day⁻¹) that result from the effect of spectral leakage. Whereas, frequencies between 20 - 30 Day⁻¹ look like noise peaks. The red horizontal dashed lines represent the significance of the main peaks ranging from $0.6 - 4\sigma$, as computed by the LS algorithm.

The LS periodogram calculation for an arbitrarily (nonuniformly) sampled data set is given by the following Equation:

$$P_{LS}(\omega) = \frac{1}{2\sigma^2} \left(\frac{[\sum_{i=1}^N (h_i - \bar{h}) \cos \omega(t_i - \tau_{LS})]^2}{\sum_{i=1}^N \cos^2 \omega(t_i - \tau_{LS})} + \frac{[\sum_{i=1}^N (h_i - \bar{h}) \sin \omega(t_i - \tau_{LS})]^2}{\sum_{i=1}^N \sin^2 \omega(t_i - \tau_{LS})} \right) \dots \dots \dots (3.15)$$

where P_{LS} is the power spectrum, h represents each consecutive data point, \bar{h} is the mean of the data points, N is the time series length, t_i represents the sampling time of the i^{th} astronomical observation, σ is the angular frequency defined by $\omega = 2\pi f > 0$ and τ_{LS} is given by :

$$\tau_{LS} = \tan(2\omega t) = \frac{\sum_{i=1}^N \sin 2\omega t_i}{\sum_{i=1}^N \cos 2\omega t_i} \dots \dots \dots (3.16)$$

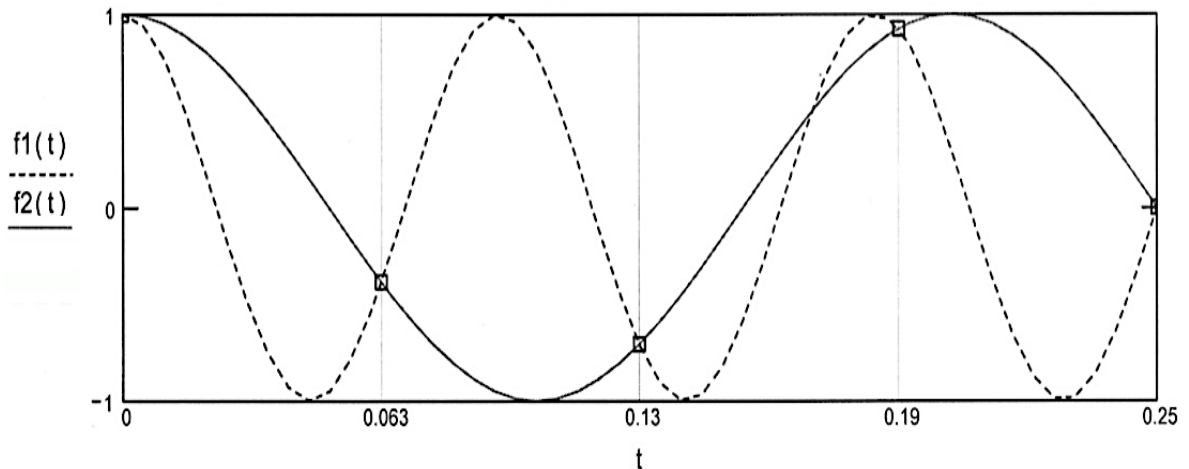


Figure 3.11 Simulated data where a sinusoid at $f_1 = 11$ Hz, when evenly undersampled at $f_s = 16$ Hz [correct sampling would be $f_s = 2 * f_1 = 22$ Hz], is aliased to $f_2 = (f_s - f_1) = 16 - 11 = 5$ Hz.

Based on the LS periodogram analysis, we can estimate the period uncertainty for the potential rotation periods detected for our targets. To do that, we overplotted the LS power spectrum strongest peak period range with a Gaussian profile, and then measured the FWHM, since the width of its FWHM covered a range of possible true periods (Figure 3.12).

The period uncertainty (δP) is calculated as follows:

$$\delta P = \frac{FWHM}{2.35482} \dots \dots \dots (3.17) \quad , \text{since } FWHM = \sqrt{2 \ln 2} \sigma = 2.35482\sigma$$

This gives an estimate of the period uncertainty 1σ . We used this technique with each lightcurve to calculate the uncertainty range for the detected rotation period. Unfortunately, we could not find sufficient periodic precision to allow us to phase lightcurves together between observation epochs for our samples.

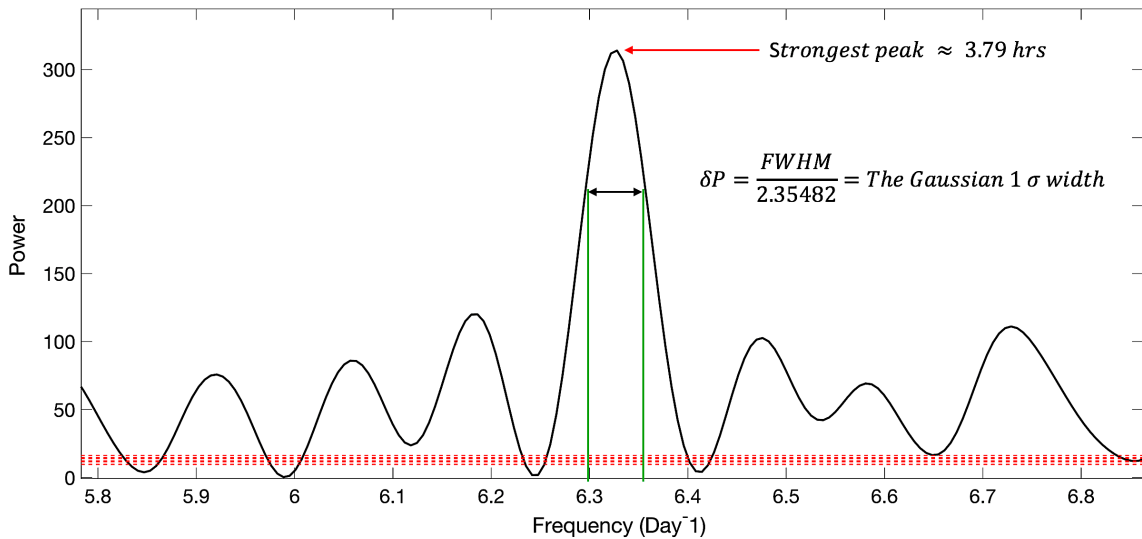


Figure 3.12 Shows the LS periodogram constructed from the February and March 2017 combined lightcurve of the primary component of M7 binary dwarf - 2M J1314+13A. We detected the strongest LS power spectrum peak indicated at a period of ~ 3.79 hrs. Based on this profile, we calculated the period accuracy $\delta P = \frac{FWHM}{2.35482}$, yielding a rotation period and an associated error of 3.79 ± 0.05 hrs - a conservative error estimate where the correct period unquestionably lies inside this allowed boundary.

For the datasets acquired for this project, the span of observations set the upper limit for the maximum possible periodicity of our targets. Therefore, we ran the LS periodogram to search for any periodicity in each separate epoch of our targets, then we investigated which LS power solutions (of significance $> 5\sigma$) were in greatest agreement. In addition, we combined all the observation epochs of the photometry of each target as a single time series to maximize the number of

cycles within the lightcurve. This has a benefit that the time span over which the data are period-searched is also extended and the final error estimates are minimized.

3.7.2 Phase Dispersion Minimization (PDM)

Phase dispersion minimization (PDM), as described by Stellingwerf (1978), is the second data analysis tool employed in this work. The PDM algorithm searches for periodic variation in time series data of variable stars and other celestial bodies. It is an efficient and effective technique for irregularly spaced samples (with gaps), non-sinusoidal signal shapes and any other problems that will render Fourier transform techniques inoperable (Stellingwerf, 1978; Linnell Nemec and Nemec, 1985; Schwarzenberg-Czerny, 1989; Schwarzenberg-Czerny, 1997). Basically, the PDM technique works by phase-folding the data on a trial period, picking the arithmetic mean of the intensities in each phase bin to calculate the mean value of the lightcurve, calculating the scatter within each bin with respect to its mean, and iterating over different trial periods to minimize the variation (dispersion) within the bins of the data points. The period that produces the least possible data point scatter compared to neighbouring periods is most likely the true period.

To describe the PDM approach more rigorously, any discrete set of time series data can be expressed by (F_j, t_j) , where F_j , t_j represent the flux and the observing time of the j^{th} observation. Given N number of data points in all ($j = 1 \dots N$), the variance of F can be defined as:

$$\sigma^2 = \frac{\sum (F_j - \bar{F})^2}{N - 1} \dots \dots \dots (3.18)$$

where \bar{F} is the mean of the flux values; $\bar{F} = \frac{\sum F_j}{N}$. To calculate the variance of the observation sample within each bin v_i^2 , we use an almost identical equation:

$$v_i^2 = \frac{\sum (F_i - \bar{F}_i)^2}{n_i - 1} \dots \dots \dots (3.19)$$

where n_i is the number of data points in the i^{th} bin. The overall variance for all bins, S^2 , is then given by:

$$S^2 = \frac{\sum (n_i - 1) \cdot v_i^2}{\sum n_i - N} \dots \dots \dots (3.20)$$

Through a series of different test periods, the PDM technique looks for the true period in which the scatter of the derived lightcurve is minimized and corresponds to the maximum amplitude of the mean lightcurve (Figure 3.13). This scatter is calculated by the PDM theta statistic $\Theta = S^2 / \sigma^2$ (the ratio of the overall variance for all bins to the variance of the unbinned lightcurve). For a true period in the sample, Θ will be very small, hopefully near-zero. However, for a false period, $S^2 \approx \sigma^2$, and Θ is approximately 1.

We performed a Monte-Carlo test, in order to evaluate the statistical significance of the potential outcomes of the PDM method (Linnell Nemec and Nemec, 1985). Although the PDM algorithm is widely accepted in variable star research, it suffers from some limitations if there are large gaps in the dataset between consecutive observations. This is because the PDM theta statistic can minimize at many different period solutions, when there is aliasing, similar to the LS method in Section 3.7.1. Essentially, a Monte-Carlo numerical test can show the reliability of the identified period by assessing whether the period solution at any minimum Θ level could be due to pure noise. We began the Monte Carlo test by randomizing the dataset's sequences, which removes the original signal component. For these randomized data points, we used the PDM method again

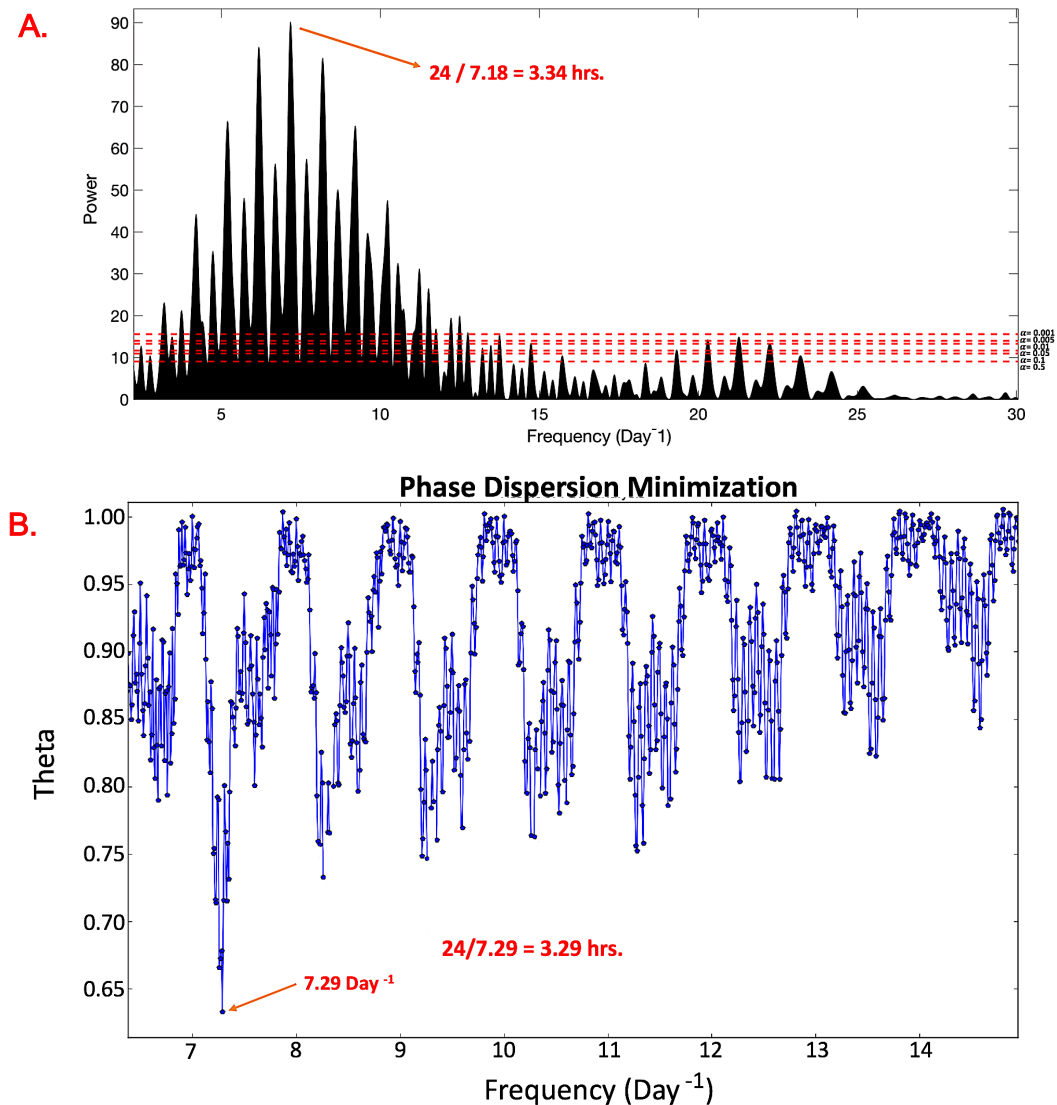


Figure 3.13 Outputs from the LS periodogram technique and the PDM technique for the L binary dwarf 2MASS J0746+2000AB in the November 2017 epoch. In **Panel A**, we indicate the rotation period of 3.34 hours, detected as the most significant peak in the LS periodogram. As determined by the LS periodogram algorithm, we include the red dashed-dotted horizontal lines on the plot which represent a $> 5\sigma$ false-alarm probability of the peaks. **Panel B** Shows the PDM plot of the same epoch, where we plot Theta statistic against frequency (Day⁻¹). We indicate the minimum theta statistic and the corresponding period of 3.29 hrs. We can clearly see that, the LS periodogram findings are directly in line with the PDM findings; then we examine this period with other routines for further confirmation.

using the same parameters as with the actual data. The Monte Carlo tests were iterated for 10^5 trials until the full distribution of the noise-generated Θ values was covered. This distribution was then used to estimate the statistical significance of a given period solution.

3.7.3 Phase Folding

In the case that a period solution can be detected using e.g. the LS method or the PDM method described in the previous sections, the lightcurve data are then folded to the known rotation period (P) in such a way that all the discrete time series data are plotted together as a single rotation period (Figure 3.14A), in order to give us an accurate picture of what the repetitive pattern of object variability looks like. This means plotting relative flux (F) as a function of phase (ϕ), rather than plotting relative flux (F) as a function of time (t). We applied the following equation to compute the phase (ϕ) of each time point t with respect to epoch time (t_o) and period P :

$$\phi = \frac{t - t_o}{P} \dots \dots \dots (3.21)$$

By discarding the integer part of phase ϕ , all data points can be plotted in a single composite cycle. The phase folding method proved to be highly useful, as visual inspection shows whether the phased period is reasonable. More importantly, this method is a test of the measured period: If the data is phased to a false period, the lightcurve's shape becomes less coherent and shows a large scatter in each phase bin without a clear trend (Figure 3.14, Panel B). Whereas, if the sample is phased to a true period, the lightcurve's shape will be smooth and the data points will lie near this curve, and the scatter in the raw lightcurve is nearly the same as the scatter in the phased curve (Figure 3.14, Panel A).

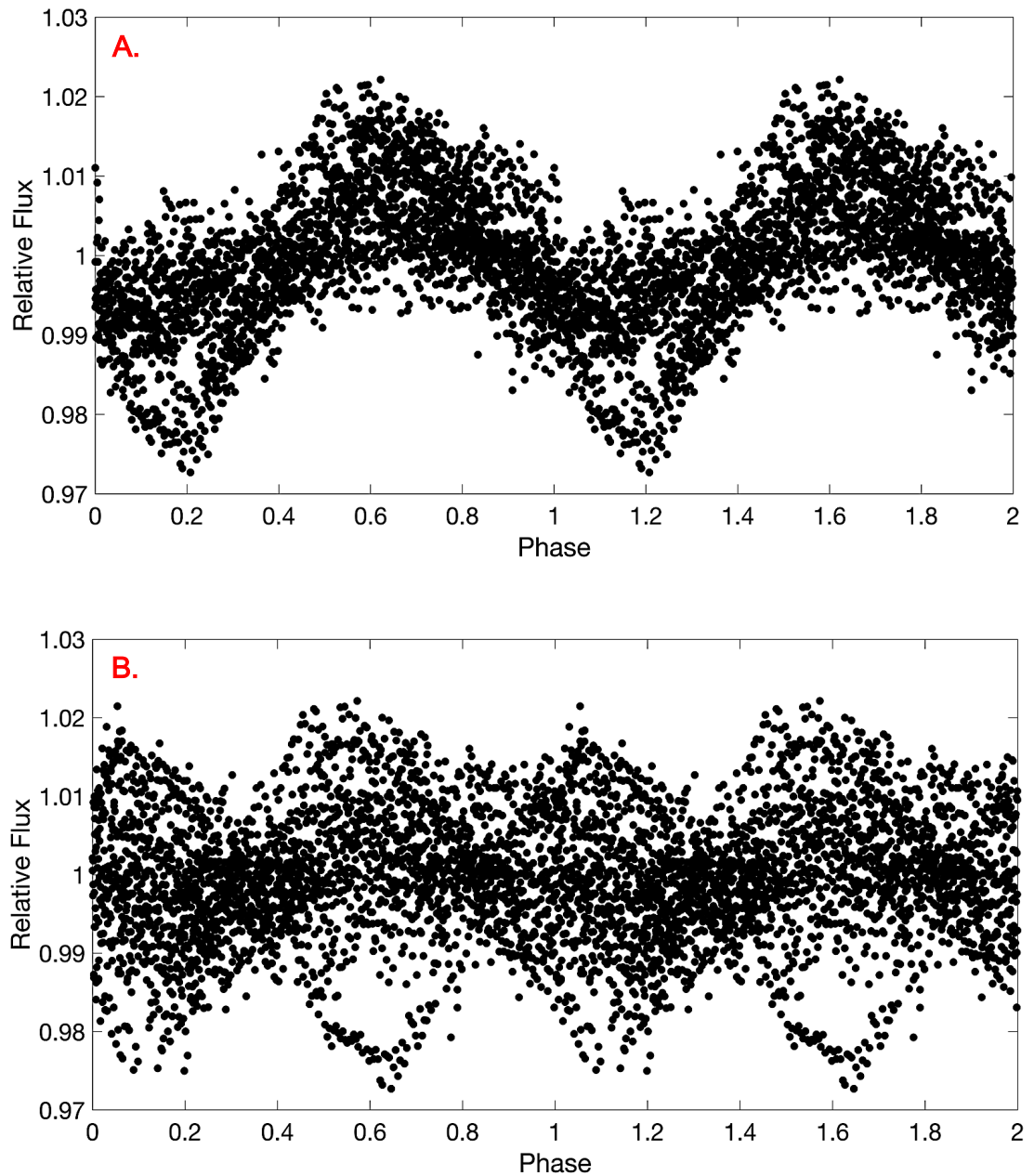


Figure 3.14 Phase folded photometric lightcurves of the M7 dwarf 2M J1314+13A from the May 2018 epoch, after using Light Curve Fitter (Section 3.7.4) to subtract out the period we discovered for the secondary component. **Panel A** has been phase folded to the detected 3.79 hours period from the LS method. Whereas, **Panel B** has been folded to a false period of 3.7 hrs. It is clear that Panel A is a smooth lightcurve showing a clear trend for the data points, conversely, Panel B shows no trend for the data points and the scatter in each phase interval is greater than in Panel A.

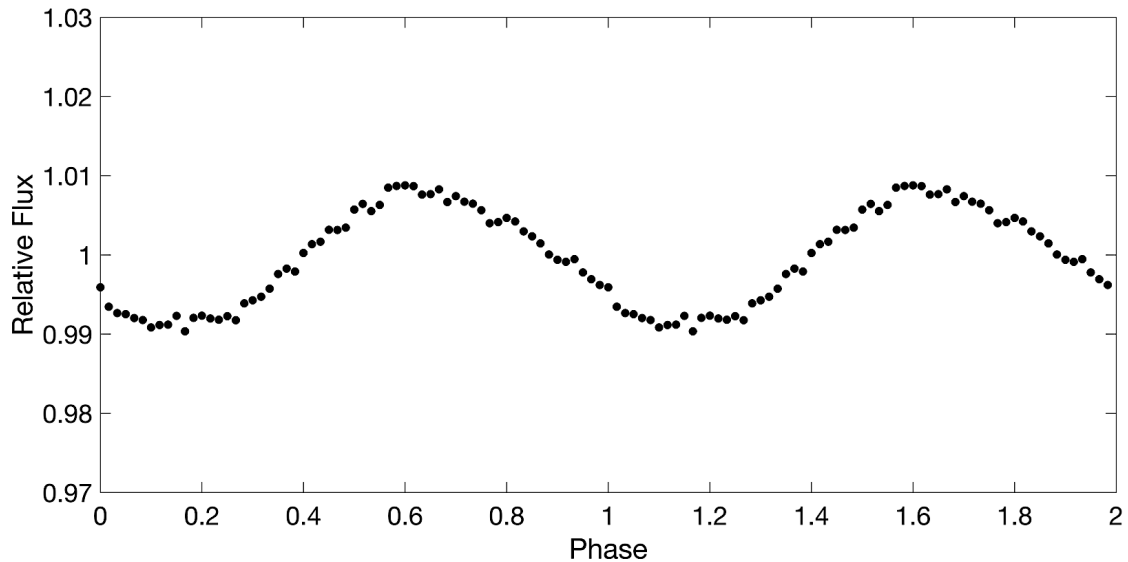


Figure 3.15 The same phased lightcurve of the M7 dwarf 2M J1314+13A from Figure 3.14, Panel A. This data has been binned by a factor of 10, to reduce the effect of random variation. The trend for the data points is now extremely clear.

In Figure 3.14, Panel A, on a visual inspection, we can see the general trend iterated in the data points with a lot of irregular variation. This variation could be mainly due to random observation errors. We can reduce this variation about the overall pattern by performing binning on the data points, i.e. by averaging out the data in phase intervals (Figure 3.15).

3.7.4 Markov chain Monte Carlo (MCMC)

Another analysis tool we used was Markov Chain Monte Carlo (MCMC), to estimate the period by fitting a sinusoidal model to the lightcurve of our targets. MCMC is a Bayesian statistics method that comprises a class of algorithms for a sampling of the posterior probability distribution function. MCMC sampling generates a chain of positions in parameter space, each of which is an approximation of the posterior probability distribution function. Using an MCMC

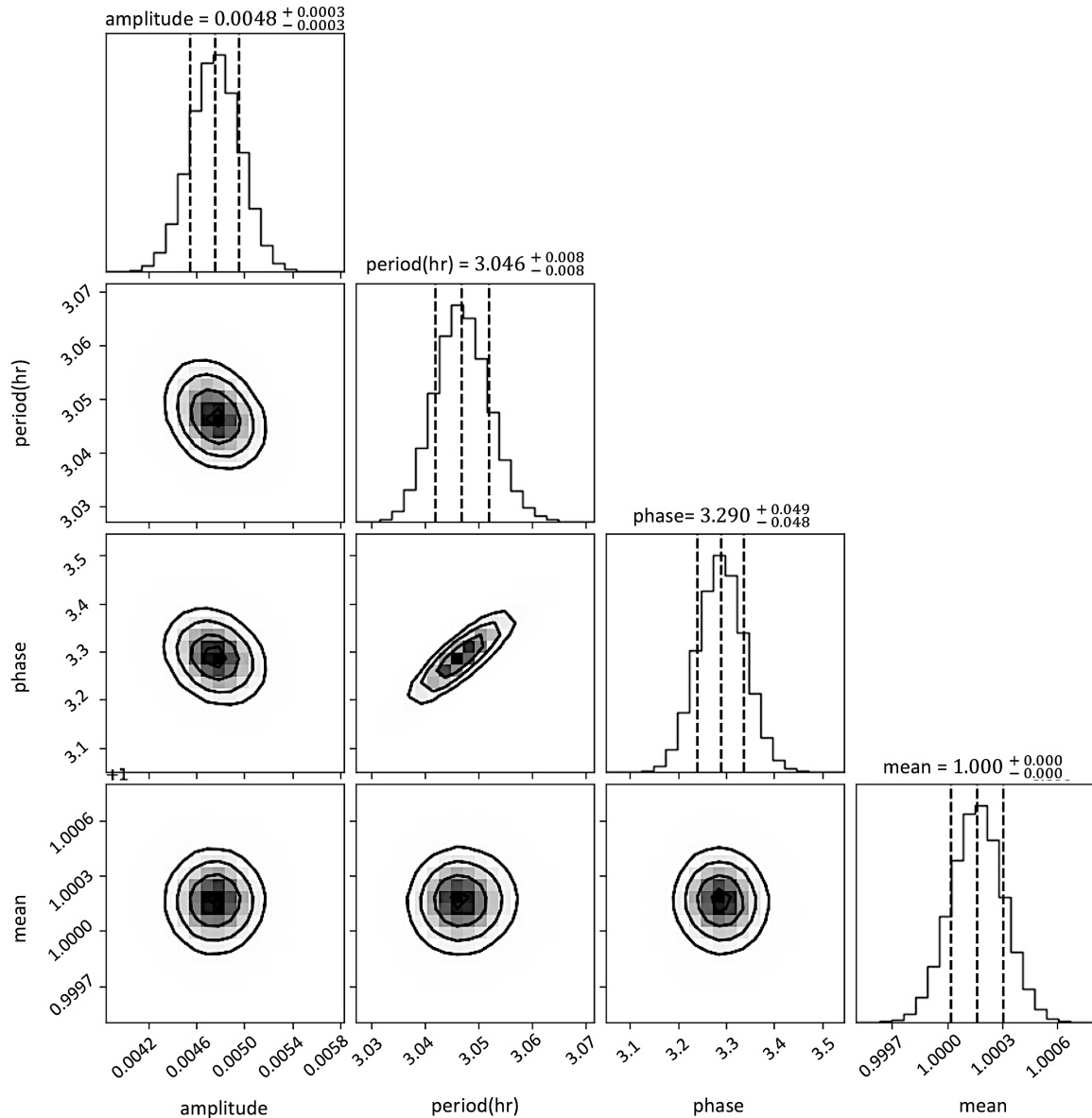


Figure 3.11 Posterior probability distributions obtained from applying the MCMC algorithm to the BRI 0021 lightcurve on October 10 2017. Vertical dashed lines show the median and 1σ uncertainties on the best-fitting model parameters, which are defined by the 16 % and 84 % quantiles of each distribution. Contours show the 0.5, 1.0, 1.5, and 2.0 σ uncertainties of the posterior probabilities in each two-dimensional parameter.

algorithm to fit the lightcurves will naturally provide uncertainties and covariances on the parameters via the posterior probability distribution.

Several algorithms exist for constructing such Markov chains, but the MCMC algorithm we used was the widely used the Metropolis-Hastings algorithm (MacKay, 2003). Putting together the ideas of the MCMC algorithm, it is a repeated process that results in a single chain of parameter sets used to estimate the posterior probability distribution function. MCMC begins with an initial guess to draw samples from the posterior. A proposal step is made by adding random noise, which calculates the probability functions of the initial and proposal step. The probability function ratio indicates whether the proposal step (the random values) provides a better fit to the data. If the proposal step is more probable, the algorithm retains the values proposed and the process is repeated. If the proposal step is less probable, the proposal step is retained with a probability determined by the probability ratio. If the random values do not agree with the data, then the last chain position is simply repeated (MacKay, 2003). Once the maximum probability parameters are found, the Metropolis-Hastings algorithm converges to a stationary set of samples. During the initial "burn-in" stage, a number of steps are skipped so that the algorithm can start with unbiased parameters.

An affine-invariant sampling algorithm has been proposed by Goodman and Weare (2010), which has better performance than standard Metropolis-Hastings algorithms by generating independent samples with much shorter autocorrelation times (i.e. with fewer chain's steps). This process includes the concurrent evolution of a group of chains known as "walkers," in which the proposal distribution for one walker is based on the current positions of the group of walkers (Foreman-Mackey et al., 2013).

In order to obtain the full posterior probability distributions for each parameter of the sinusoidal model, we use `sin_emcee.py` developed by Vos (2019). An example of using this code appears in Allers et al. (2020). They used an open-source implementation of the affine-invariant MCMC ensemble sample (Goodman & Weare, 2010), and the `emcee` package (Foreman-Mackey et al.,

2013). We explored the 4-dimension parameter space to model the lightcurve using 500 walkers with 20000 steps and discarding an initial burn-in sample of 1000 steps. Figure 3.16 shows the posterior probability distributions of the amplitude, period, phase and the fitting model parameters. For observational data taken of BRI 0021 obtained on Oct 10 2017, using the same methodology as originally applied by Allers et al. (2020). Each parameter is constrained, and the MCMC algorithm determines a period of 3.046 ± 0.008 hrs.

3.7.5 Light Curve Fitter (LCF)

Two binary system samples were selected for this project: the M7 dwarf tight binary 2MASS J1314203+132001AB, and the L dwarf tight binary 2MASS J0746+2000AB. In each case, differential photometry was performed with a chosen photometric aperture that enclosed the combined flux of these components. GUF1 could not image each component of both binary systems as a point source: they cannot be spatially resolved with a ground-based telescope limited by atmospheric turbulence, due to ~ 2.7 AU ($\sim 0''.23$) and ~ 1.6 AU ($\sim 0''.130$) separation between the A and B components for 2MASS J1314203+132001AB and 2MASS J0746+2000AB, respectively. Due to the likely presence of two sources periodically varying, a complex combined lightcurve shape was produced with superimposed variability (Figure 3.17).

The binary nature of the targets posed the question: if we subtract the dominant period out, do we see another weaker signal? And can we characterize it?

A software package, titled Light Curve Fitter (LCF), was developed to address these questions. This application was written in Python. LCF can deconvolve two superimposed sinusoidal waves and discriminate the weaker variability signature

from that of the dominant variability. This was accomplished using a combination of Least Square Fitting (LSF) and chi-squared χ^2 techniques.

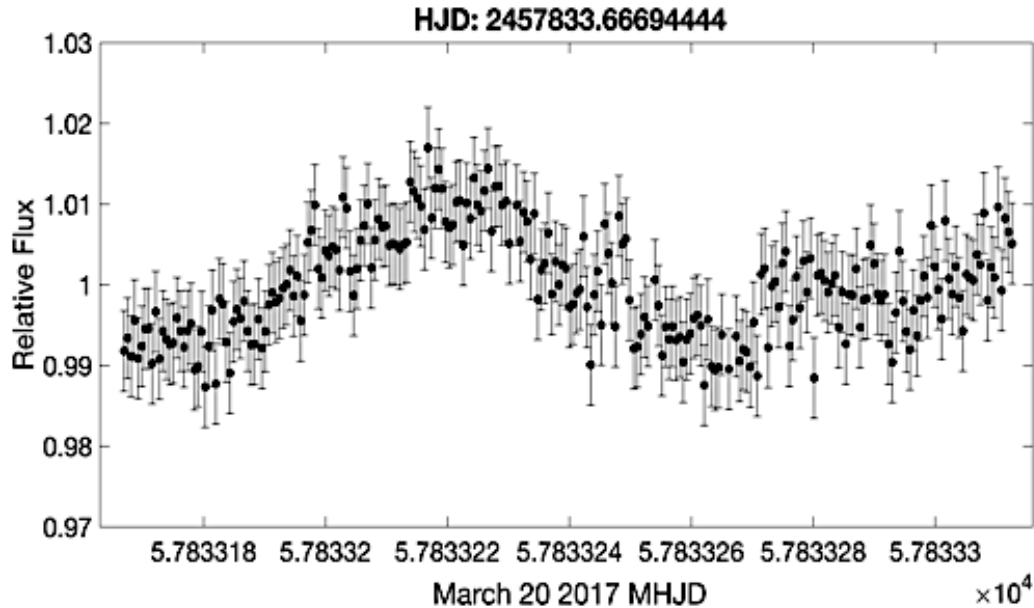


Figure 3.17 Lightcurve of the binary 2MASS J0746+2000AB on March 20, 2017. Both members contribute to the optical variability, resulting in superimposed variability and a complex lightcurve shape.

The LSF technique finds the best fit for a data set which occurs when the sum of the squared residuals, S , is at the minimum:

$$S = \sum_{k=1}^n (F_k - x(t_k, \beta))^2 \dots \dots \dots (3.22)$$

where the data set consists of flux F (the dependent variable) and time t (the independent variable), for $k = 1 \dots n$ data points, and the form of the generated model is $x(t, \beta)$, where the β vector is varied. The LSF technique treats all data points equally, unlike the χ^2 method. Equation 3.23 calculates χ^2 minimization,

where E_k is the error or standard deviation that is previously calculated by methods in Section 3.6:

$$\chi^2 = \sum_{k=1}^n \left(\frac{F_k - x(t_k, \beta)}{E_k} \right)^2 \dots \dots \dots (3.23)$$

Both techniques can estimate the error of the amplitude variability, period and phase of a given lightcurve. Results showed that the final outcome from each method was very similar. Although other uses are also possible, the LCF was developed specifically to determine the amplitudes and periods of the 2M J0746+20B and 2M J1314+13A where the 2M J0746+20A and 2M J1314+13B amplitudes and periods are known. The function *LCF* is given by:

$$LCF = \underbrace{\left(A_1 \sin \left(\frac{2\pi t}{P_1} + \phi_1 \right) + O_1 \right)}_{\text{Primary Star}} + \underbrace{\left(A_2 \sin \left(\frac{2\pi t}{P_2} + \phi_2 \right) + O_2 \right)}_{\text{Secondary Star}} \dots \dots \dots (3.24)$$

where the dependent variables above are the phase of the first periodic signal, ϕ_1 , the amplitude of the first waveform, A_1 , the offset of the first waveform, O_1 , the phase of the second waveform, ϕ_2 , and P_2 period of the second waveform, the amplitude of the second waveform, A_2 , and the offset of the second waveform, O_2 ; and the independent variables were the period detected in our work, P_1 and time, t .

To explain the approach of LCF, consider the scenario of a binary star as a single source (for example 2M J0746+20AB), where we run LS and PDM on the combined flux of each observation epoch and then on all epochs combined, and the detected period represents the dominant source. Subsequently, to seek for the elusive secondary period a sinusoidal signal is set to the dominant rotation period in each of the original lightcurves (Figure 3.18). This fit is then subtracted

out, and the LS, PDM and MCMC are re-applied to the residual data points. This method can therefore identify the possible presence of an underlying period from the weaker member. If true, then this is repeated on the original time series, or on

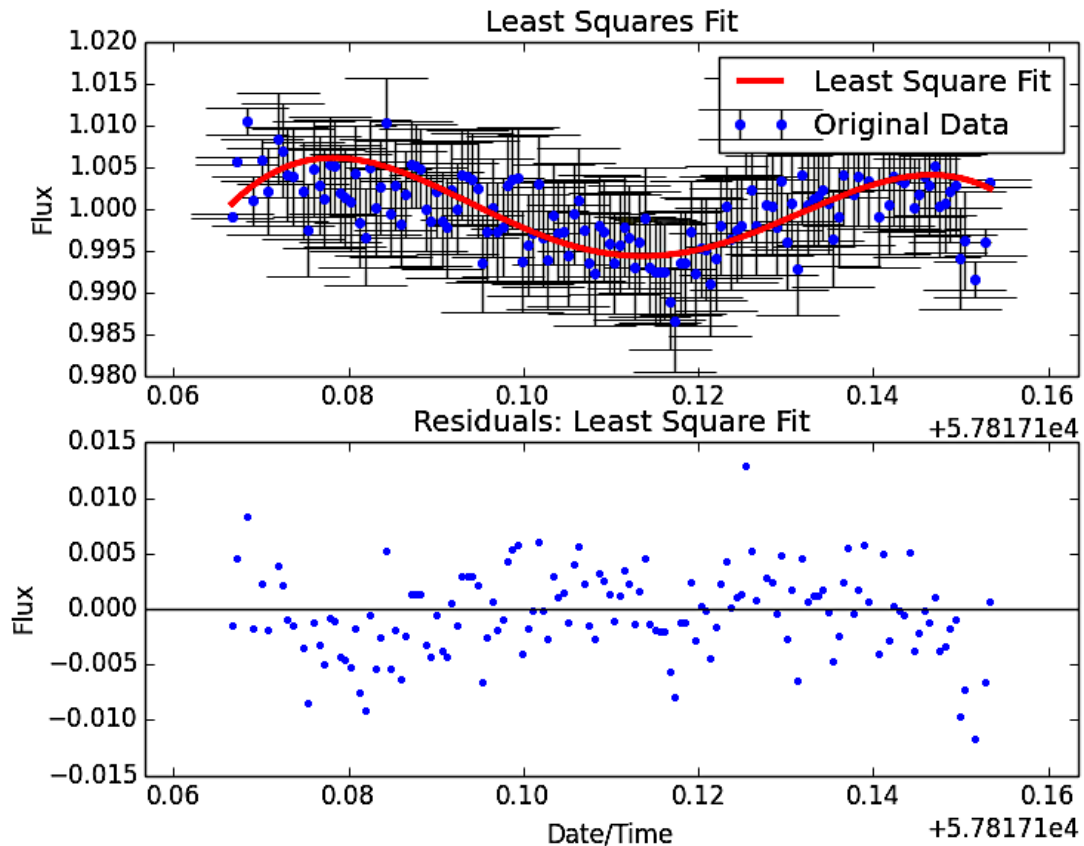


Figure 3.18 The March 04 2017 lightcurve of 2MASS J0746+2000AB. The red model sinusoid over-plotted is the best fit using the Least Squares Fit LSF in LCF routine.

the time series with one or both signals removed - for example, refining the strongest variability parameters, by using a sinusoidal model fit set to the period of the detected weaker signal. The LCF algorithm can determine the mean amplitude variability of the target lightcurve via sinusoid fitting, which permits variation in the amplitude and phase of the sinusoidal function. In addition, it is also possible to use this technique as an additional evaluation of the period

solutions obtained from the LS and PDM analyses of single and binary stars, based on the correlation of the model sinusoidal fit with the real lightcurve data.

The operational flow diagram for the LCF software is described below and illustrated in Figure 3.19 & Figure 3.20. The LCF was developed using the Agile software development lifecycle as outlined in Fitzgerald et al. (2019). We coded and tested this application on OSX using the PyCharm IDE (integrated development environment) 2018 Community Edition, in Python 2.7 with later iterations using Python 3.7. There were eight iterations of this application before the code was then Frozen, allowing for the creation of a single executable file that can be distributed to users. This executable contains all the code and any additional resources required to run the application, and includes the Python interpreter that it was developed on. The major advantage for distributing applications in this manner is that it will work immediately, without the need for the user to have the required version of Python (or any additional necessary libraries) installed on their system. For further information on this approach, see Fitzgerald et al. (2019).

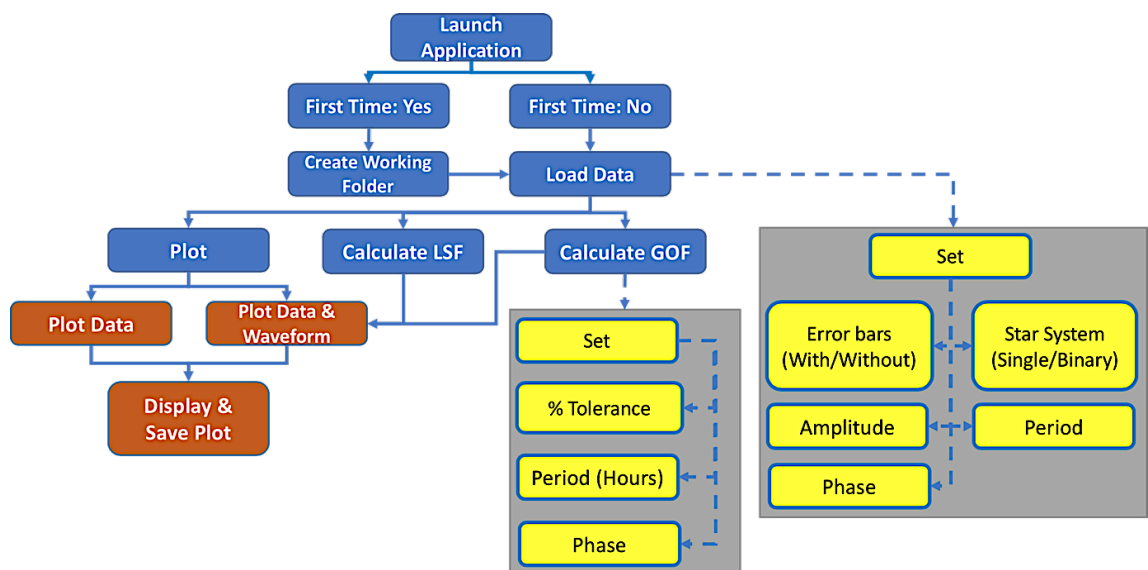


Figure 3.19 The operational flowchart for the Light Curve Fitter (LCF) application illustrated in Figure 3.20.

The following python packages were used:

- Numpy
- scipy.optimize
- scipy.stats
- matplotlib
- Tkinter
- csv
- pylab

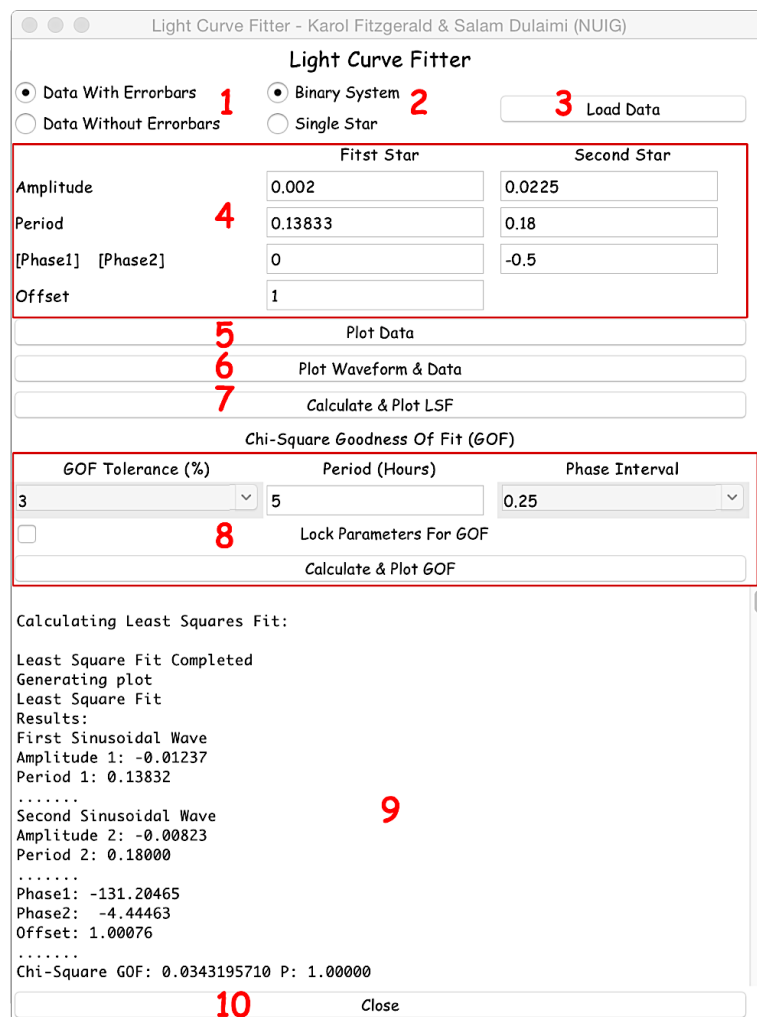


Figure 3.20 GUI outlining the sequence of steps to calculate and plot the LSF for data. The output of this sequence is illustrated in Figure 3.21.

The Graphical User Interface (GUI) is designed to be as intuitive as possible for users and does not require any previous training. The following sequence follows a path within the operational flowchart diagram (Figure. 3.19). The numbering sequence below corresponds to the functionality in Figure 3.20.

- 1- **Select data type** - The user must select one of the radio buttons informing the application whether they want to use data with/without error bars.
- 2- **Select star system type** - Single Star or binary. If Single Star is selected then the fields that set the parameters for the second star's amplitude, period and phase will be unavailable to the user, allowing them to only set the parameters for the first star. If a binary system is selected, then they have access to set parameters for both stars.
- 3- **Load data button** - Select a text file containing data. At this point users will have the option to plot and view the data contained within the selected file. This can be done by selecting the Plot Data button (number 5).
- 4- **Input parameters** – These parameters are set by the user and can be used to ascertain a good fit to the data when plotted (step 6).
- 5- **Plot Data button** - This button will plot the data in the selected text file and will include error bars if that option was selected.
- 6- **Plot Waveform & Data button** - This button will plot the data within the selected text file in addition to the sine wave based on the system type and parameters set by the user in step 4. This can then be used to determine a better LSF and Chi-Squared for goodness of fit GOF.

- 7- **Calculate & Plot LSF button** – This button will take the parameters from step 4 to calculate the LSF for the data selected in step 3. It is then plotted (see Figure 3.21) and a Chi-Squared GOF is calculated. The console (9) is updated to display all results.

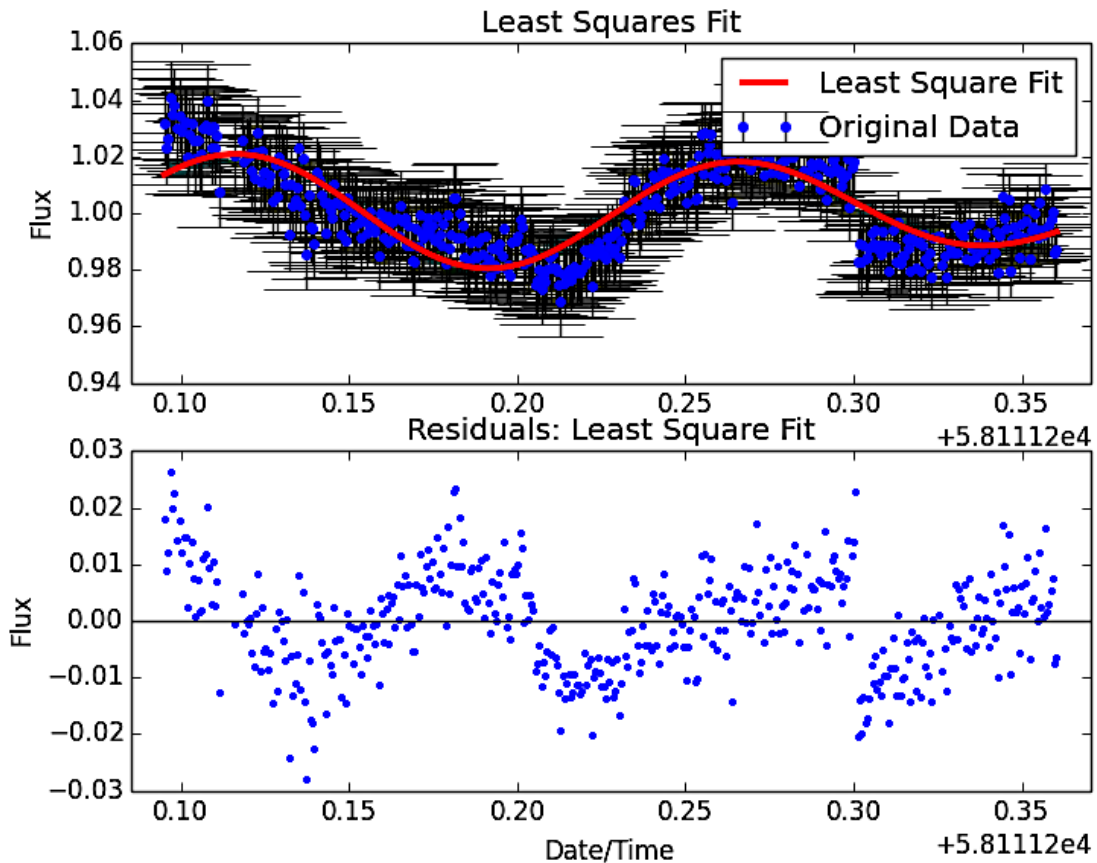


Figure 3.21 Output based on the sequence of events in Figure 3.20.

- 8- **Calculate and plot GOF button** - If the user knows (or even if they do not know) the amplitude or period for the primary star, they can then determine the Chi-Squared GOF by setting percentage tolerances for the amplitude, period and phase of the stars. The tolerance ranges from 3% to 20% for the amplitudes, and is calculated by selecting the parameters (which are determined based on the combinations generated) with the lowest Chi-

Squared GOF. This can take a considerable amount of time depending on how high the GOF tolerance (%) is set by the user.

9- **Console** - The GUI is also equipped with a console that provides feedback to the user on files selected, values updated, optimum values for the LSF and corresponding Chi-Squared GOF.

10- **Close button** – This button terminates the application.

3.8 Summary

This chapter has described the signal analysis methods used in this work to evaluate the periodic optical variability of our radio detected dwarfs. Once our GUF1 datasets were calibrated and reduced using the L3-CCD GUF1 Pipeline to create a time series, we used two photometric tools to perform differential photometry on our targets, and also to evaluate which tool used would produce lightcurves with a lower spread. In the case of the GUF1/aperture photometry tool, we computed a single optimum aperture and fixed it per night. The LuckyPhot method helped us to determine the optimum aperture for each image, and it also chooses frames that are most photometrically identical but cannot differentiate between atmospheric and instrumental effects. Once we had extracted differential lightcurves, we utilised the LS periodogram, PDM, MCMC and phase folding to detect and verify the periodic variability of our targets.

In the case of binary systems where there is suspected variability in both components, we have developed a new tool called Light Curve Fitter (LCF) to untangle the photometric signal of the weaker source from that the dominant source.

" I am just learning to notice the different colors of the stars, and already begin to have a new enjoyment."

Maria Mitchell

Chapter 4

Periodic Optical Variability in Single Ultracool Dwarfs

4.1 Introduction

Numerous observations to date have unmistakably shown that very low mass stars and brown dwarfs with spectral types of \sim M7 and later - collectively known as ultra-cool dwarfs (UCDs) - can generate and dissipate strong magnetic fields. Optical observations give a one of a kind insight into UCD magnetism, as magnetic activity is known to play a role in the characteristics of the optically variable nature of such stars. Therefore, we optically observed two radio-detected objects (late-M/early-L dwarfs) to determine whether optical periodicity was present over a scale of years and to examine the correlation, if any, between the optical and radio regimes. This correlation would imply that the periodic optical and radio emissions in UCD may be related by some kind of magnetic phenomenon (i.e. star spots or aurorae, see Hallinan et al., 2015). However, for the two selected objects in this work, it is not clear at this point whether such a possible connection is causal in nature.

There have been several studies conducted in recent years of the M9.5 dwarf BRI 0021+021 (hereafter BRI 0021) and the L3.5 dwarf 2MASS J00361617+18211 (hereafter 2M J0036) that led to the detection of periodic radio, optical emissions and an H α flare (e.g., Tinney and Reid, 1998; Reid et al., 1999; Martín et al., 2001; Berger, 2002; Ménard et al., 2002; Gelino et al., 2002; Berger et al., 2005; Lane et al., 2007; Maiti, 2007; Hallinan et al., 2008; Berger et al., 2009a; Goldman et al., 2009; Harding et al., 2013a; Metchev et al., 2015; Croll et al., 2016; Pineda et al., 2016).

In this chapter, we present photometric results, from multiple epoch I-band observations of these two ultracool dwarfs, obtained with the Galway Ultra Fast Imager (GUFI) on the 1.8m Vatican Advanced Technology Telescope (VATT) on Mt. Graham, Arizona. Each object exhibited periodic variability, and there were multiple epochs where the photometric variability is markedly present in the data. Two photometric analysis tools we used for comparison, as Lucky Photometry

analysis (Collins (2014), as discussed in Chapter 3) allowed to improve lightcurve solutions and to investigate the secular stability of these periods, amplitudes and phases. We also demonstrate how this approach reduces the uncertainty around periodicities detected using conventional photometric methods. 2M J0036 with its periodicity previously known, was chosen as the test case for results comparison to determine which of the two photometric techniques used in this work could improve differential photometric precision, the results are discussed in Section 4.4.3. We discovered a new periodic modulation in the photometry of BRI 0021. Our observations confirm the periodicity of 2M J0036 (Lane et al., 2007; Harding et al., 2013a; Croll et al., 2016).

This chapter is structured as follows; Section 4.2 discusses the stellar properties of each target. Section 4.3 discusses our optical observations. Sections 4.4 presents the photometric results of optical periodic and aperiodic variability for each source. We discuss the inclination angle relative to our line of sight of the two single dwarfs that we obtained from this work. We also present the results of the Lucky Photometry analysis with optimum aperture (O.A.) and compare it with fixed aperture (F.A.) with no Lucky Photometry (GUF1 photometry). This section concludes with a discussion of the proposed source of the periodicity.

4.2 Target Selection

4.2.1 BRI 0021+0214

BRI 0021, an M9.5 dwarf is a rapid rotator ($v \sin i = 34.2 \pm 1.6 \text{ km s}^{-1}$) (Basri and Marcy, 1995), and is located at a distance of $\sim 11.55 \text{ pc}$ (Basri et al., 1996; Reid et al., 1999). According to the evolutionary models of Chabrier et al. (2000), the absence of lithium in the object's spectrum implies that the object is no younger than 300 Myr nor less massive than $0.06 M_{\odot}$. Recently, Gonzales et al. (2018)

estimated age of BRI 0021 to be in the range of 500 – 10000 Myr. Filippazzo et al. (2015) used evolutionary model isochrones to derive mass and radius estimates of $0.075 \pm 0.010 M_{\odot}$ and $0.109 \pm 0.005 R_{\odot}$, respectively. Based on spectroscopic observation by Leggett et al. (2001), the effective temperature and bolometric magnitude ($\log L_{\text{bol}}/L_{\odot}$) obtained for this dwarf were, respectively, about 2100 K and ≈ -3.43 . Cesetti et al. (2013) developed spectroscopic diagnostics for cool stars and identified the effective temperature of ~ 2600 K. Based on the colour-temperature relation, Meneses-Goytia et al. (2015) found T_{eff} of ~ 2466 K. Following that, Gonzalez et al. (2018) derived the temperature T_{eff} and bolometric magnitude ($\log L_{\text{bol}}/L_{\odot}$) of 2385 ± 77 K and -3.44 ± 0.04 , respectively.

Early observations to discern magnetic activity were not promising. H_{α} emission was not detected (Basri and Marcy, 1995), nor were observations using ROSAT successful (Neuhäuser et al., 1998). Subsequent more sensitive observations by Reid et al. (1999) confirmed the presence of a magnetic field in this object by detecting extremely low levels of the H_{α} flare emission with a luminosity $\log L_{\alpha}/L_{\text{bol}} \approx 10^{-4.2}$, a factor of 3 lower than the average level of quiescent emission of early- to mid-type M dwarfs, and this was followed by the detection of low-level radio emission (average value of $40 \pm 13 \mu\text{Jy}$ at 8.46 GHz) with peak flux densities of $360 \pm 70 \mu\text{Jy}$ from the dwarf (Berger, 2002). Subsequent simultaneous X-ray, radio and H_{α} observations demonstrated clear evidence for a steady variability of H_{α} emission from BRI 0021 on a timescale of 0.5 - 2 hours, although there were no detected X-ray or radio emissions (Berger et al., 2009a).

A photometric campaign was carried out by Martín et al. (2001) to search for the presence of optical variability. They found I-band variability with periods of ~ 20 hrs and ~ 4.8 hrs. They inferred that the variability was likely not due to spots on the stellar surface, since preliminary studies showed the dwarf appeared to have low levels of magnetic activity. Rather, they argued that the cause would be

due to dust clouds in the dwarf's atmosphere, as there are silicate and iron clouds in the spectrum of BRI 0021 (Chabrier et al., 2000; Ackerman and Marley, 2001). However when Miles-Páez et al. (2013) studied near-infrared linear polarization of rapidly rotating ultracool dwarfs from late-M to early-T dwarfs, they detected no linear polarization of BRI 0021 at optical or near-infrared wavelengths during different observation epochs, which might have been expected for a dust-dominated modulated signal (Osorio et al., 2005).

Previously, Harding et al. (2013a) observed BRI 0021 in unfavourable conditions for a total of ~ 28 hrs using the same instrumentation configuration (GUFIVATT). They presented evidence for aperiodic variations with possible periodic variability with a period between 4 – 7 hrs, with the strongest evidence for a periodic solution of ~ 5 hours albeit at low significance. Although in agreement with the faster ~ 4.8 hours period found by Martín et al. (2001), this measured period is inconsistent with a maximum period of about 3.59 hrs inferred from $v \sin i$ observations (Mohanty and Basri, 2003). The target properties are shown in Table 4.1.

Given both the poor quality of the previous observations of BRI 0021, we decided to implement a follow-up observation campaign for this object using GUFIVATT over a longer baseline to definitively estimate an unambiguous rotational period for this dwarf.

4.2.2 2MASS J00361617+18211:

2MASS J00361617+18211 (hereafter 2M J0036) is a dwarf located at a distance of ~ 8.8 pc with a spectral type L3.5 (Reid et al., 2000; Dahn et al., 2002). It has a bolometric luminosity of $\log(L_{\text{bol}}/L_{\odot}) = -3.950 \pm 0.011$ (Dieterich et al., 2014). The temperature has been determined based on the spectra and models of Leggett et al. (2001) to be 1800 K (Berger, 2002), while Dahn et al. (2002) and Vrba et al. (2004) found $T_{\text{eff}} \sim 2000$ K and 1900 K, respectively. Recently, Vos et

al. (2017) calculated T_{eff} of 1909 ± 6 K. Based on a gravity measurement of surface $\log g \approx 5.5$, Schweitzer et al. (2001) concluded that the mass range is between $0.060 - 0.076 M_{\odot}$; the latter proves the star is located right at the substellar boundary. Based on evolutionary models, Filippazzo et al. (2015) derived surface gravity $\log g$ of 5.21 ± 0.17 and mass of $0.063 \pm 0.012 M_{\odot}$ ($66.07 \pm 12.98 M_{\text{J}}$). With the failure to detect lithium in the dwarf's spectrum thus far, Hallinan et al. (2008) suggesting the age is not younger than 0.8 Gyr, a range of possible radii of 0.092 to 0.098 R_{\odot} . Later, Filippazzo et al. (2015) assumed an age of 0.5 – 10 Gyr for 2M J0036. From observation by Japanese infrared astronomical satellite AKARI for 16 ultra-cool dwarfs, Sorahana et al. (2013) obtained a radius of $0.088 \pm 0.005 R_{\odot}$ for 2M J0036 based on the distance and the flux scaling factor. Their findings agreed with theoretical predictions for early-L and T dwarfs (Burrows et al., 2001). However, Filippazzo et al. (2015) predicted the range of radii between 0.94 - 1.08 R_{J} ($1.01 \pm 0.07 R_{\text{J}}$ or $0.101 \pm 0.007 R_{\odot}$) based on evolutionary models isochrones of Saumon & Marley (2008). Schweitzer et al. (2001) reported an initial estimate of a $v \sin i$ of $\sim 15 \text{ km s}^{-1}$. Two later studies Reiners and Basri (2008) and Blake et al. (2010) provided two separate values of $v \sin i$ of 45 ± 5 and $35.12 \pm 0.57 \text{ km s}^{-1}$, respectively. The most recent measured $v \sin i$ of $36 \pm 0.2 \text{ km s}^{-1}$ by Vos et al. (2017).

Observations with FORS1 instrument at the Very Large Telescope (VLT) showed that this dwarf is linearly polarized in the Bessel I filter (Ménard et al., 2002), while 4 years later another observation by Goldman et al. (2009) was carried out with the same instrument, which revealed no polarization above the 3σ level. Osorio et al. (2005) reported that no significant linear polarization in the Johnson I-band data. Very Large Array (VLA) observations were carried out on 2M J0036 at 8.5 GHz, which exhibited a flare and persistent emission, indicating this star appears to be variable (Berger, 2002). Following this, data were collected using multi-frequency 4.9 GHz and 8.5 GHz observations simultaneously, which yielded periodic radio variability, highly circularly polarized in both bands, with ~ 3 hr rotation period (Berger et al., 2005). This detection reveals a breakdown of

the Güdel and Benz relation (Benz, 1993; Benz and Güdel, 1994) by at least four orders of magnitude. The relation assumes an empirical correlation between radio and X-ray emissions which holds over many orders of magnitude and based on that, radio emissions from cool dwarfs and brown dwarfs in particular were generally assumed to be either absent or very weak (for further details, refer to Chapter 1). Gyrosynchrotron radiation was classified as a mechanism for the radio emission with a magnetic field strength of 175 G (Berger et al., 2005). An alternative mechanism responsible for the radio emissions from ultracool dwarfs was proposed by Hallinan et al. (2008) when they confirmed 2M J0036 has persistent radio emissions and 100% circularly polarized periodic pulses with a period of 3.08 ± 0.05 hrs. Periodic non-polarized radio emissions were also detected. It is somewhat surprising that the non-polarized emission showed brightness temperature constraints that ruled out gyrosynchrotron radiation as a potential mechanism for the observed radio emissions (Hallinan et al., 2008). This confirmed the electron cyclotron maser ECM process to be the cause of the pulsed radio emission, which requires a magnetic field strength of at least 1.7 kG.

Previous observations indicated that no H_{α} emission was detected in the L3.5 dwarf 2M J0036 (Berger et al. 2005), however later observations by Pineda et al. (2016) with the Keck telescope demonstrated the presence of H_{α} in the dwarf's magnetosphere/atmosphere.

Photometric campaigns were performed on 2M J0036 to search for optical variability in both the I-band and R-band. Gelino et al. (2002) detected no periodicity and considered 2M J0036 to be non-variable. Conversely, Maiti (2007) reported distinct optical variability in both the I and R-bands. There are a number of reasons why non-variability may have been reported in the Gelino et al. (2002) campaign, such as (1) undersampling, where they observed 2M J0036 for 1 to 2 hrs per night and used approximately half of the frames in their analysis, (2) noise and (3) there might have been non-variability in the object at that particular epoch. While Maiti (2007) observed 2M J0036 for a long period of time, only a very small

number of frames were taken each night. Therefore, the lightcurves from these data sets were undersampled with respect to the period of rotation. Following this observation, Lane et al. (2007) studied the photometric variability of 2M J0036 by conducting photometric monitoring over ~ 7.5 hrs. They found sinusoidal photometric variability in the I-band filter with a period of ~ 3 hrs subsequently determined, in agreement with its 3.08 hrs radio periodicity. This consistency between radio and optical periods confirms that the periodicity was associated with the stellar rotation of this dwarf. They attributed the ~ 3 hr period to a magnetic spot on the star's surface, coupled with the rotation of the star as the source of this variability, although Berger et al. (2005) found that the dwarf was not chromospherically active but radio active. Interestingly, they observed some aperiodic variations, which they imputed to atmospheric dust on the L dwarf. Following this, under very poor seeing conditions, Harding et al. (2013a) used

Parameter	BRI 0021	2M J0036
Spectral type	M9.5	L3.5
Distance d (pc)	~ 11.55	~ 8.8
$\log(L_{\text{bol}} / L_{\odot})$ (dex)	-3.44 ± 0.04	-3.950 ± 0.011
Rotational velocity (km s^{-1})	34.2 ± 1.6	36 ± 0.2
Rotation Period (hours)	3.052 ± 0.006 *	3.11 ± 0.03 (F.A.+ No LuckyPhot) * 3.081 ± 0.0005 (O.A.+ LuckyPhot) *
Radius (R/R_{\odot})	0.109 ± 0.005	0.101 ± 0.007
Estimated Mass (M_{\odot})	0.075 ± 0.010	0.063 ± 0.012
Inclination angle ($^{\circ}$)	$51.6^{+0.3}_{-0.2}$ *	62.6 ± 0.3 *

Table 4.1 A summary of the physical properties of the two targets in our campaign.

References: (1) * This work; (2) Reid et al. (1999); (3) Reid et al. (2000); (4) Leggett et al. (2001); (5) Martín et al. (2001); (6) Dahn et al. (2002); (7) Mohanty and Basri (2003); (8) Vrba et al. (2004); (9) Hallinan et al. (2008); (10) Crossfield (2014); (11) Dieterich et al. (2014); (12) Filippazzo et al. (2015); (13) Vos et al. (2017). and (14) Gonzalez et al. (2018).

GUPI on VATT at I-band wavelengths to monitor the object for a total of ~ 10 hr. The range of periods they obtained were in agreement with the I-band observations of Lane et al. (2007), as well as with Berger et al. (2005) and Hallinan et al. (2008) who detected a periodicity of ~ 3.08 hrs in radio. After that, Metchev et al. 2015 used 3.6 and 4.5 μm infrared Spitzer/IRAC to monitor 2M J0036 for a total of ~ 14 hrs and reported a period of 2.7 ± 0.3 hrs. Lastly, multi-wavelength observation for 22 nights was conducted by Croll et al. 2016 and the rotation period was determined to be 3.080 ± 0.001 hrs. This period was recovered from the *R*, *I*, *Z* and *J* bands and was highly consistent with the above-mentioned optical, radio and mid-infrared studies. The target properties are shown in Table 4.1.

Consequently, we concluded that further research on 2M J0036 would be appropriate to determine whether the optical periodicity is stable over a longer temporal baseline.

4.3 Photometric Observations and Analysis

Multi-epoch photometric observations were conducted of the two well-studied

Date of Obs. (UT)	Length of Obs. (hr)	Exp. Time (s x no. frames)	Readout Rate (MHz)	Amplifier	Reference Stars (No.)
2017 Oct 10	3.4	5 x 12	1	Conventional	1
2017 Oct 12	3.9	10 x 6	1	Conventional	1
2017 Oct 14	4	5 x 12	1	Conventional	1
2017 Oct 15	2.1	5 x 12	1	Conventional	1
2017 Dec 19	2.5	5 x 12	1	Conventional	1
2017 Dec 22	3.1	5 x 12	1	Conventional	1

Table 4.2 Observation details for BRI 0021.

UCDs, BRI 0021 and 2M J0036, using the VATT I-Arizona ($\sim 7200 - 9100 \text{ \AA}$) broadband filter with GUF1 photometer (Chapter 2) on 1.83 m VATT, Mt. Graham, Arizona.

BRI 0021 was observed on four occasions in October 2017 (10th, 12th, 14th and 15th) and on two occasions in December 2017 (19th and 22nd) for a total of ~ 19 hrs, shown in Table 4.2. In all cases, conditions were transparent, with seeing between 0.9" to 1.7".

In the case of 2M J0036, we used the same optical filter range that was used in previous observations by Lane et al. (2007), Harding et al. (2013a) and Croll et al. (2016). We observed this object for a total of ~ 14.5 hrs on the nights of 25 & 26 November 2017 and 15 December 2017 encompassing two separate epochs, see Table 4.3. The seeing was between 1.02" and 1.12" during the observation campaign. Unfortunately, due to tracking problems with the VATT telescope, other data acquired on 23 December 2017 were of poor quality and were not utilized in the analysis.

Date of Obs. (UT)	Length of Obs. (hr)	Exp. Time (s x no. frames)	Readout Rate (MHz)	Amplifier	Reference Stars (No.)
2017 Nov 25	5.4	10 x 6	1	Conventional	4
2017 Nov 26	5.1	10 x 6	1	Conventional	4
2017 Dec 15	4	5 x 12	1	Conventional	4

Table 4.3 Observation details for 2M J0036

We had another 11-night observing run in October 2018 on VATT to monitor 2M J0036; however even on the one relatively cloudless night, we could not open the dome due to high humidity and variable fog density throughout the night.

Science frames of BRI 0021 and 2M J0036 were processed using the in-house GUF1 L3 pipeline, as described in Chapter 2. Standard data reduction techniques were implemented on all frames. The science images were de-biased using nightly masterbias frames, and then flat-fielded using twilight flat-fields, which for any given observation, were made up of more than 90 median-combined dithered frames taken from a blank part of the sky. Once the science data were fully reduced, a de-fringing routine was then applied, using a fringing template produced from the median of a large number of dithered, reduced science frames. The frames were then registered to correct any potential guiding drift, and co-added in 1-minute batches to increase the signal-to-noise ratio (SNR). A registration process is essential if there has been de-rotation/tracking errors on-sky, and the VATT telescope has ~ 1 arcmin hr^{-1} of tracking errors. Differential photometry was carried out on all science data for BRI 0021 and 2M J0036.

The $3' \times 3'$ field of view of GUF1 provided between one and six reference stars for a given field. These reference stars must not be variable in nature over the timescales of the observation. This provides a basis for separating inherent variability in the target from external sources of noise. If the reference stars and the target are spectrally different, the atmosphere will affect both incoherently. In addition, there are other criteria according to the reference stars that have been selected (outlined in Chapter 3). Four reference stars were used in the differential photometry of 2M J0036, whereas only one reference star was used with BRI 0021.

The analysis was repeated only with 2M J0036 calibrated data, using a combination of optimum aperture (O.A.) and LuckyPhot (Chapter 3). A major problem was with the calculation of the appropriate photometric aperture and how to extract an estimate of the flux from a star as accurately as possible for every frame. The (O.A.) technique that is carried out using OVAR (Optical VARIability technique) utilises the SNR of a range of aperture sizes to determine the correct

aperture for each star within each frame, for all frames (Collins, 2014). Traditionally, the photometric aperture was calculated to provide the highest SNR for the target star and fixed it for each night, which is called fixed aperture (F.A.), and in our setup this was carried out using the L3-GUFI pipeline (Sheehan, 2008) (see Chapter 3). We tested these two methods on 2M J0036 for comparison to determine which gave the best results, characterized by lightcurves with a lower spread (lower scatter).

4.4 Results

4.4.1 BRI 0021+0214

We carried out F.A. differential photometry using the L3-GUFI pipeline and found I-band periodic variability with mean amplitude variability of 0.0031 to 0.0056 mag, which is shown in Figure 4.1 and Table 4.4. The 3' x 3' field of view (FOV) of GUFI is relatively small and in this case, it only contained one appropriate comparison star, since we discarded a number of reference stars from the analysis process due to their poor stability compared to the target star. The selected reference star ($00^{\text{h}} 24^{\text{m}} 24^{\text{s}}.636 -01^{\circ} 58' 20''.14$) is the same as the comparison star selected by Martín et al. (2001) and later by Harding et al. (2013a) based on its observed stability relative to the target star. Martín et al. (2001) identified two periods for this target which were ~ 4.8 hrs and ~ 20 hrs, respectively. However, Harding et al. (2013a) showed possible solutions of ~ 4 to 7 hrs. Because we observed BRI 0021 for a limited time of ~ 19 hrs, we do not have enough time coverage to evaluate the hypothesised 20 hrs period. Thus, technically, the longer rotation period for BRI 0021 cannot be excluded. Our analysis of the differential magnitudes, timestamped with Heliocentric Julian Date, revealed sinusoidal periodic variability of 3.052 ± 0.006 hrs (as shown in Figures 4.2A & 4.3). We used bootstrapping distribution for uncertainty determination,

which indicates an uncertainty of 0.001 hours (as shown in Figures 4.2B). We also used a sinusoidal fitting model using Markov Chain Monte Carlo (MCMC) algorithm to determine and evaluate the period of this object which will naturally include uncertainties on the parameters via the posterior probability distribution, as we selected randomly on the night of 22 December 2017 (Figure 4.4). The resulting periods and uncertainties of all statistical analysis are in agreement with each other. The MCMC method gives a rotational period of 3.048 ± 0.004 hrs.

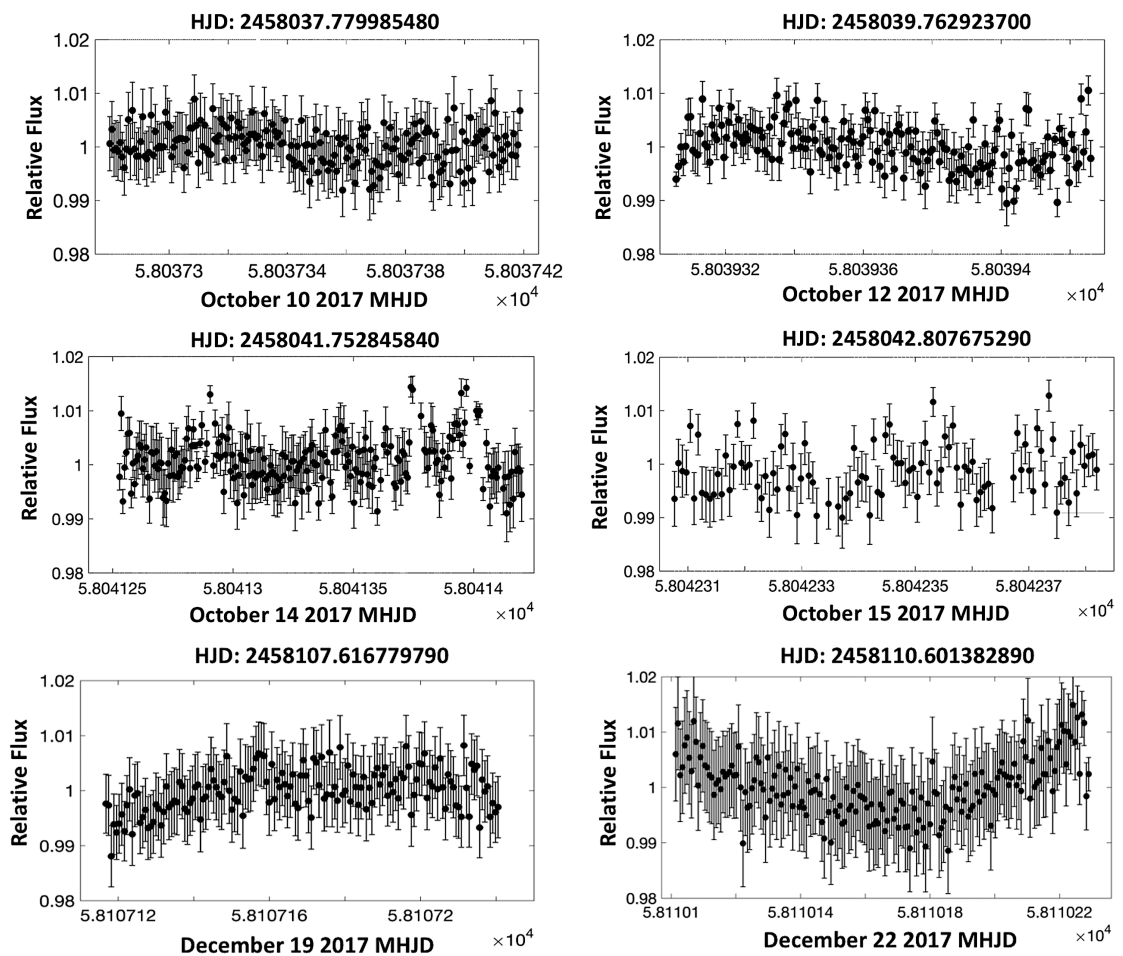
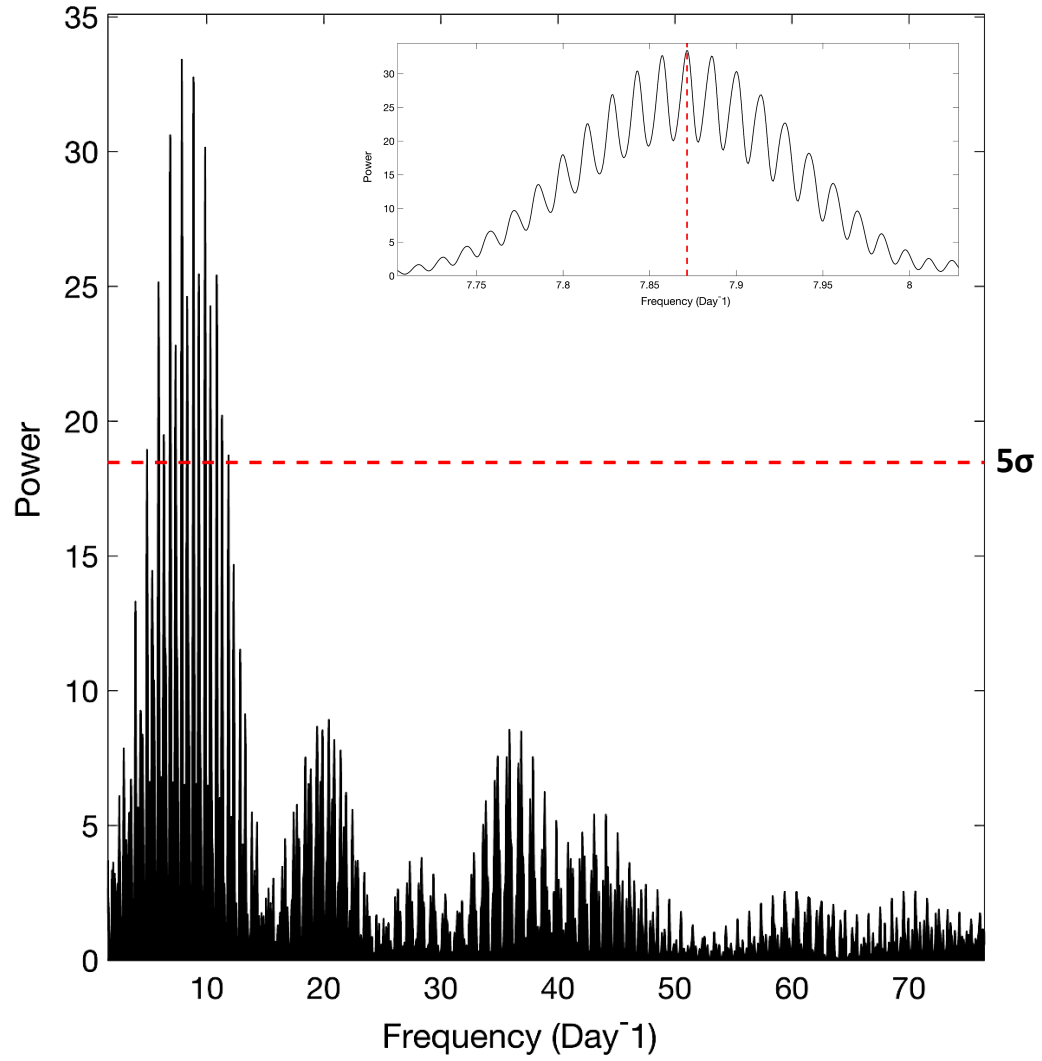
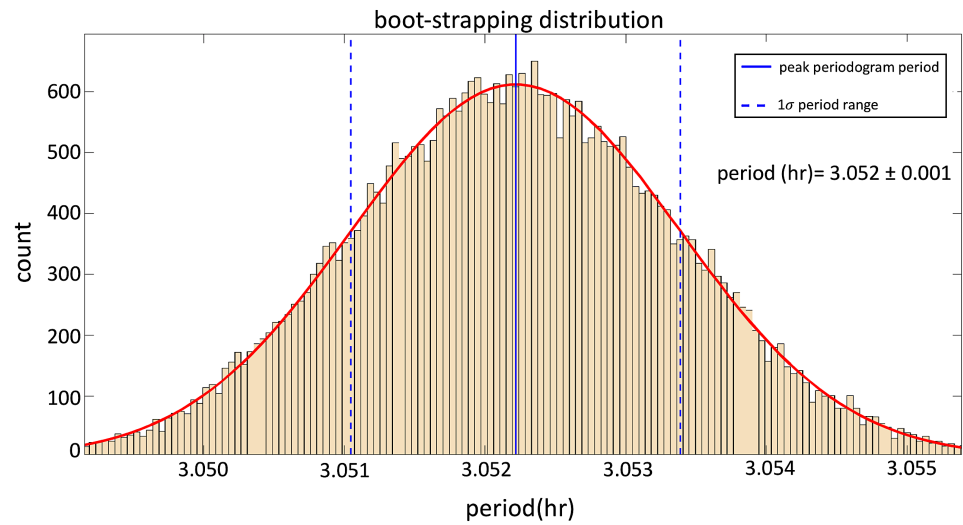


Figure 4.1 BRI 0021 was monitored for a total of six nights, over two separate epochs. The peak-to-peak amplitude variations throughout the observations varied from 0.0031 - 0.0056 mag, and photometric error bars were applied to each data point as calculated in Table 4.4. MHJD is Modified Heliocentric Julian Date (HJD - 2,400,000.5 days).

A.



B.



Caption of Figure 4.2 continued from previous page

Figure 4.2 **A.** Lomb-Scargle periodogram of all BRI 0021 epochs, calculated from the combined data set in Figure 4.1. The red dashed and dotted horizontal lines represent a 5σ false-alarm probability of the peaks, as determined by the LS periodogram algorithm. The x-axis is plotted in day^{-1} because each epoch was time-stamped in units of Heliocentric Julian Date (HJD). The vertical red dashed line at the most significant peak (shown in close-up in the inset plot) corresponds to a period of 3.052 ± 0.006 hrs at a significance of $> 5\sigma$. **B.** Distribution of retrieved highest power periods from bootstrapping indicates an uncertainty of 0.001 hr.

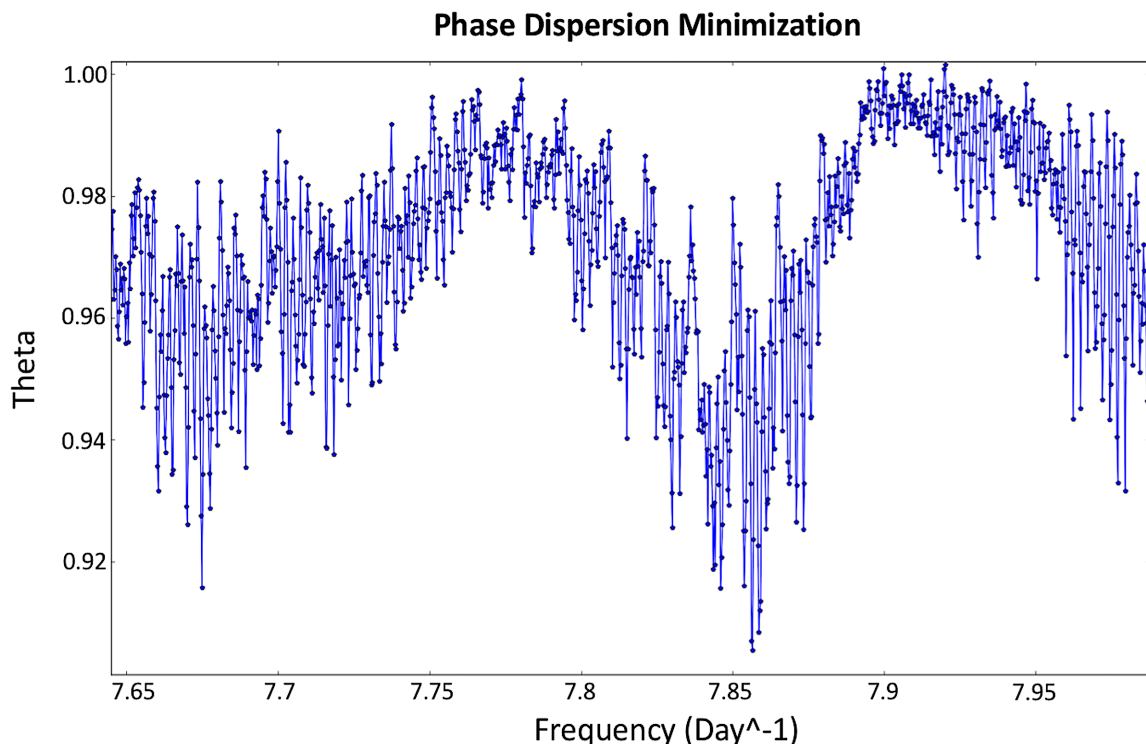


Figure 4.3 Phase dispersion minimization plot of all of the BRI 0021 data – Theta statistic against frequency (Day^{-1}) for 10^5 Monte-Carlo simulations. The minimum theta corresponds to ~ 3.05 hrs, which is largely consistent with the rotation period resulting from the LS periodogram.

Our period is in good agreement with the rotational velocity of $34 \pm 2 \text{ km s}^{-1}$ found by Mohanty and Basri (2003) - which implies to a maximum rotation period for this system of ~ 3.59 hrs. Two later studies Reiners and Basri (2010) and Crossfield (2014) reported two separate values of $v \sin i$ of 33 ± 3 and $34.2 \pm 1.6 \text{ km s}^{-1}$, respectively. In Figure 4.5 we show the combined lightcurve from all nights, phase folded on 3.052 hrs.

Assuming our measured periodic signal of 3.052 ± 0.001 hrs corresponds to the rotational period of BRI 0021, this data allows us to break the $v \sin i$ degeneracy and so calculate the inclination angle for the rotation axis of BRI 0021 relative to our line of sight. Using the dwarf's derived radius of $0.109 \pm 0.005 R_{\odot}$ or $1.09 \pm 0.05 R_J$, where $R_J \sim 69911 \text{ km}$ (Filippazzo et al., 2015), the most recent $v \sin i$ $34.2 \pm 1.6 \text{ km s}^{-1}$ (Crossfield, 2014), and our estimated rotation period.

The inclination angle, $\sin i$, is derived as follows:

$$\sin i = \frac{(v \sin i)}{2\pi \cdot R/P} \dots \dots \dots (4.1)$$

and the scaling relationship between v and object radius R follows from:

$$R = v P / 2\pi \dots \dots \dots (4.2)$$

We derive an inclination angle of $51.6^{+0.3}_{-0.2}$ degrees for the rotation axis relative to our line of sight and an equatorial rotational velocity of $43.6 \pm 2 \text{ km s}^{-1}$, as shown in Figure 4.6. The derived radius of $0.109 R_{\odot}$ from Filippazzo et al. (2015) is in good agreement with the predicted radius of $\sim 0.11 R_{\odot}$ from evolutionary models Chabrier et al. (2000), and consistent with Martín et al. (2001) who found

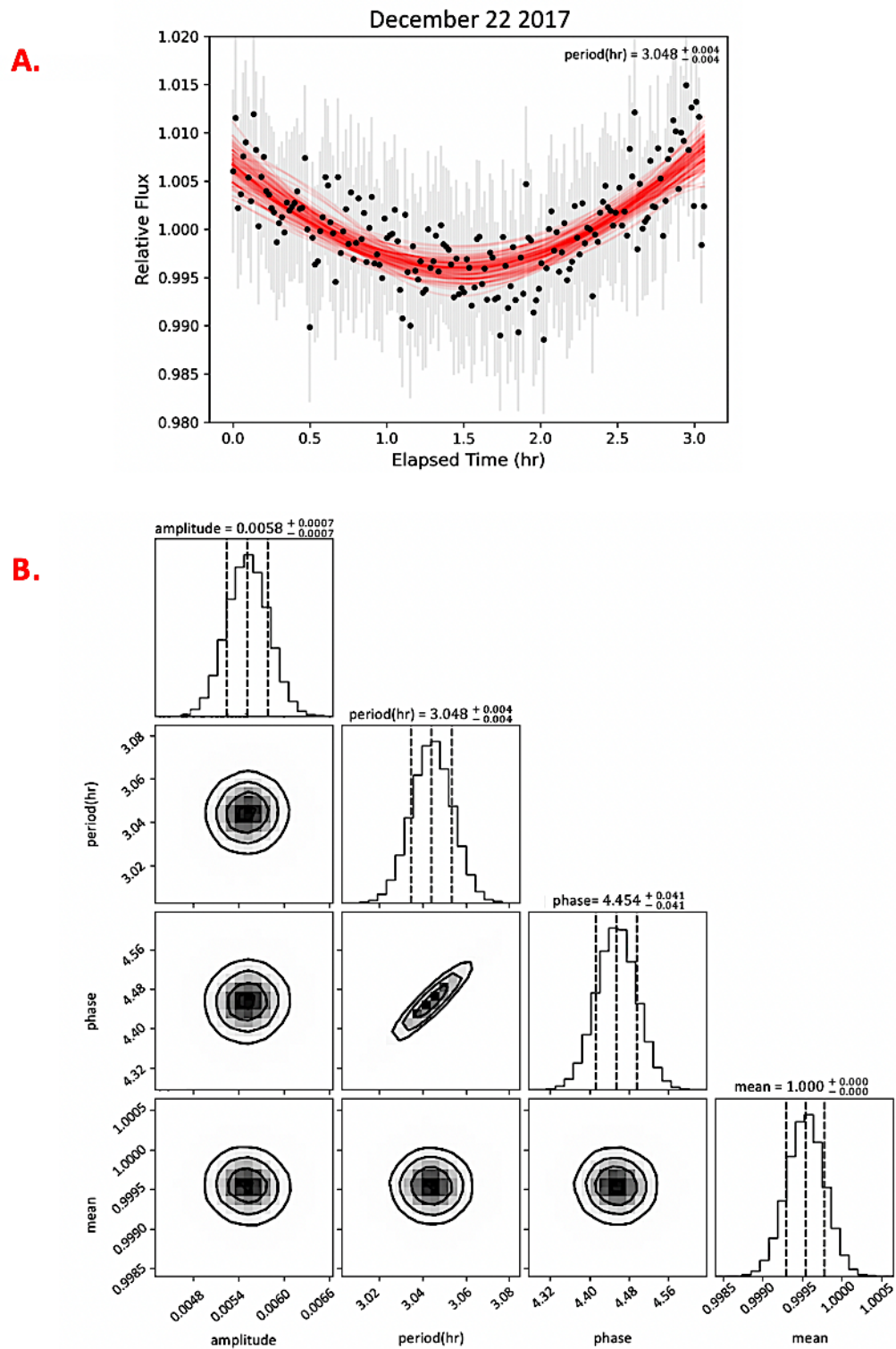


Figure 4.4 **A.** The fitted sinusoidal model (red curve) of BRI 0021 on December 22 2017.

B. Posterior probability distributions for the model parameters.

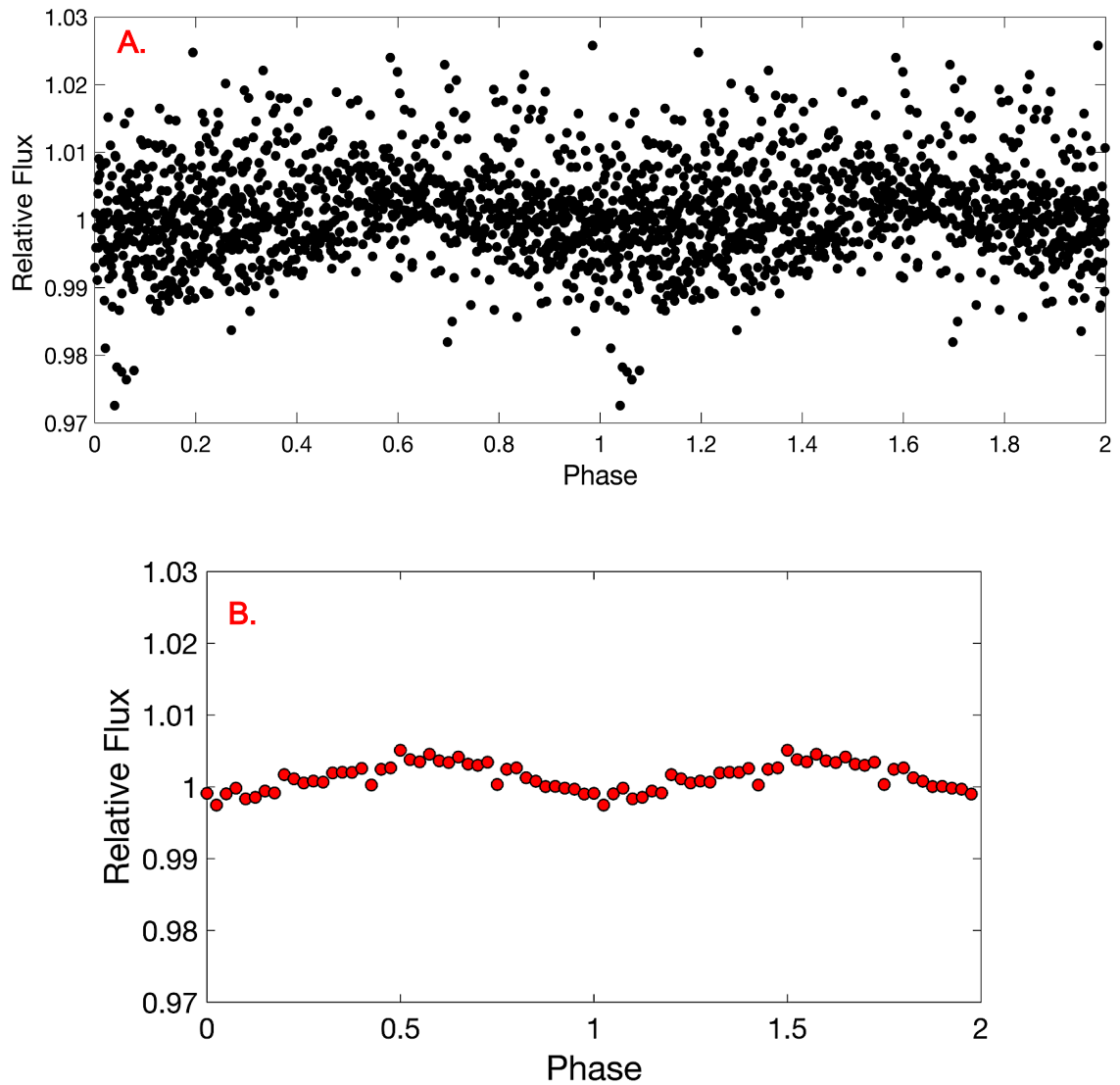


Figure 4.5 **A.** Phase-folded lightcurves of all epochs in the BRI 0021 observation campaign. **B.** The same binned by a factor of 10. Each lightcurve was phase-folded to the detected period of 3.052 ± 0.001 hrs. It is plausible that the periodicity of 3.05 hrs, as the most significant rotation period observed, is the true rotation periodicity.

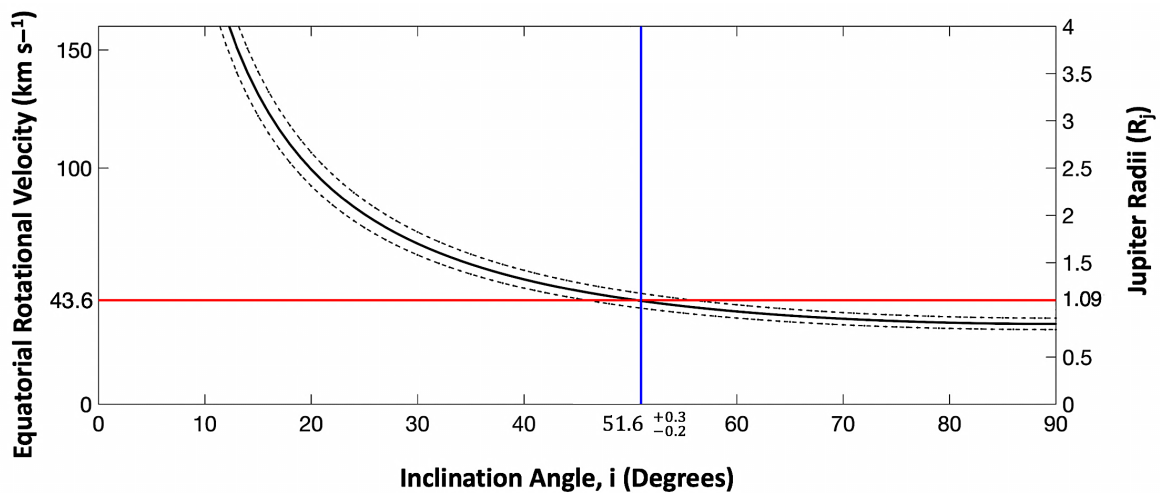


Figure 4.6 Here, we plot the $v \sin i$ of BRI 0021, $34.2 \pm 1.6 \text{ km s}^{-1}$ (Crossfield, 2014), shown by the solid black curve, with dashed lines representing the associated errors. Equatorial rotational velocity vs. the inclination angle for the rotation axis of BRI 0021 relative to our line of sight. The solid blue vertical line highlights the inclination angle, calculated using Equation (4.1). The second Y-axis, right, is the radius of the dwarf, tracking the equatorial rotational velocity as per equation (4.2), where we have marked the predicted radius of $1.09 \pm 0.05 R_J$ from Filippazzo et al. (2015) as a solid red line that indicates an equatorial velocity $43.6 \pm 2 \text{ km s}^{-1}$.

a radius of $\sim 0.14R_{\odot}$, which was considered to be 30% larger than the models had predicted, and explained that the radius may have been inflated due to stellar insolation. However, the radius of BRI 0021 cannot be increased in the same way because there is no nearby main sequence star. Due to a lack of detected X-ray emissions during previous observations (Neuhäuser et al., 1998), the probability of having a compact relativistic primary, like a neutron star or black hole, was ruled out.

Date of Observation (UT)	Band	Amplitude Variability _{Target} (mag)	Photometric Error (mag)
(1)	(2)	(3)	(4)
2017 Oct 10	/	0.0048±0.0003	0.0046
2017 Oct 12	/	0.0052±0.0003	0.0028
2017 Oct 14	/	0.0040±0.0004	0.0031
2017 Oct 15	/	0.0038±0.0003	0.0047
2017 Dec 19	/	0.0031±0.0004	0.0058
2017 Dec 22	/	0.0056±0.0004	0.0073

Table 4.4 Amplitude variability and photometric error analysis of BRI 0021. **Column 1:** Date of observation in UT. **Column 2:** Waveband used. **Column 3:** Peak-to-peak amplitude variability with associated errors as measured by the Chi-squared test. **Column 4:** Mean photometric error for lightcurve data points per night, as measured by the `iraf.phot` routines.

The derived radii of $\sim 1.09 \pm 0.05 R_J$ (Filippazzo et al., 2015), in addition to the well-established $v \sin i$ measurements (Crossfield, 2014), allow us to infer maximum rotation period for BRI 0021 of ~ 3.88 hrs. This means our established rotation period of 3.052 ± 0.001 hrs is more realistic and is in good agreement with the $v \sin i$ of 34 ± 2 km s⁻¹ (Mohanty and Basri, 2003), which indicates a maximum rotation period of ~ 3.59 hrs, and is also in agreement with Martín et al. (2001) who expected the rotation period to be ~ 3.36 hrs.

As stated in Section 4.2.1, BRI 0021 has been associated with intermittent H α flaring activity, and coherent radio emission, certainly suggestive of magnetic activity on this M9.5 dwarf. Under the auroral model, best demonstrated to be operating within the magnetosphere of the nearby M8.5 dwarf LSR J1835+3259, beamed radio emission is coincident with an auroral oval emitting in H α and the underlying atmosphere heated by associated particle beams yielding

differing radiated response as a function of frequency depending on the resulting plasma's optical thickness (Hallinan et al., 2015). Critical to the radio beams' visibility is the inclination angle of the dwarf's rotation axes to our line of sight, as when coherent radio emission originates from the electron cyclotron maser instability, the maximum intensity is beamed perpendicular to the dwarf's rotation axis. For the case of BRI 0021, with an inclination angle of $51.6^{+0.3}_{-0.2}$ degrees, significantly less beamed emission is anticipated, although any particle beams impacting the dwarf's atmosphere would be likely to yield a discernible modulated optical signature. Given the intermittent nature of BRI 0021's H_{α} and radio emission, combined with the weak optical signal presented in this work, the evidence is consistent with an intermittent auroral mechanism associated with its magnetosphere.

That being said, this intriguing dwarf's variability is likely due to more than one astrophysical cause. Time-evolving atmospheric dust clouds could periodically conceal the cool/hot spots on the stellar surface (Lane et al. 2007; Heinze et al. 2013; Metchev et al. 2015), with the auroral activity previously described playing an occasional role in this process (Hallinan et al. 2015).

Further multiwavelength observations are required to determine if BRI 0021 hosts a functioning auroral mechanism, along with the necessary stable and structured kG fields to sustain such magnetospheric processes, or whether this dwarf is the exception to the rule as regards the subset of known radio-active dwarfs spanning the substellar boundary. In addition, further research with a wide field of view that allows more comparison stars to be used for differential photometry. In fact, more coverage is needed on a given night to confirm the presence of the ~ 3.05 hrs period.

4.4.2 2MASS J00361617+18211

We selected 2M J0036 as a test specimen to carry out photometry with a fixed an aperture and optimum aperture and compare them to determine which would have a lower scatter. We find sinusoidal periodic variability of 3.11 ± 0.03 hrs and 3.081 ± 0.001 hrs, with mean peak-to-peak amplitude variability of $0.0013 - 0.0051$ mag and $0.0012 - 0.0046$ mag, respectively for a fixed aperture without LuckyPhot and an optimum aperture with LuckyPhot technique (Table 4.5, Figure 4.7, Figure 4.8A and Figure 4.8B). We also used bootstrapping distribution method for O.A.+LuckyPhot, indicates an uncertainty of ~ 0.0005 hr (as shown in

Date of Observation n (UT)	Band	Amplitude Variability _{Target}	Amplitude Variability _{Target}	Photometric Error	Photometric Error
		F.A.+No LuckyPhot (mag) (3)	O.A.+LuckyPhot (mag) (4)	F.A.+No LuckyPhot (mag) (5)	O.A.+LuckyPhot (mag) (6)
2017 Nov 25	/	0.0051±0.0005	0.0046±0.0003	0.0039	0.0028
2017 Nov 26	/	0.0034±0.0004	0.0032±0.0003	0.0031	0.0025
2017 Dec 15	/	0.0013±0.0003	0.0012±0.0002	0.0021	0.0018

Table 4.5 Amplitude variability and photometric error analysis of 2M J0036.

Column 1: Date of observation in UT. **Column 2:** Waveband used. **Column 3 & Column 4:** Show the peak-to-peak amplitude variability using the two different methods with associated errors as measured by the Chi-squared test. **Column 5 & Column 6:** Show the mean random photometric error for lightcurve data points per night using the two different methods as predicted by the iraf.phot routine.

Figure 4.8C). We randomly selected the night of 22 December 2017 for O.A.+LuckyPhot, and used MCMC approach which gives a period of 3.082 ± 0.004 hrs (Figure 4.10).

From the LS periodogram, PDM and MCMC (see Figures 4.8, 4.9 & 4.10), we find the optical periodic modulation detected by both photometric technique is largely consistent. In addition, they are in good agreement with earlier observations that reported a period of 3.08 ± 0.05 hrs in radio (Hallinan et al., 2008) and a period of ~ 3 hrs in optical I-band (Lane et al., 2007; Harding et al., 2013a) and a period of 2.7 ± 0.3 hrs in mid-infrared (Metchev et al., 2015).

The amplitude variability calculated with all techniques was lower than the amplitude variability reported by Harding et al. (2013a) (as shown in Figure 4.7 & Table 4.5). This may be due to a decrease in magnetic activity during our photometric observations or a change in atmospheric conditions, akin to the evolution in the size or extent of Jupiter's Red Spot.

We determined the periods in LS by establishing the FWHM of the highest peak which is the real period that is clearly located within the allowable range (Figure 4.8). It is clear that 2M J0036 exhibits a periodicity of ~ 3 hrs in the optical I-band which confirms the reported periods from previous studies in radio (Berger et al., 2005; Hallinan et al., 2008) and optical (Lane et al., 2007; Harding et al., 2013a; Croll et al., 2016) and infrared (Metchev et al., 2015). In Figure 4.11 we show the combined lightcurve from all nights, phase folded on the periods found by our analyses (3.1 hrs and 3.08 hrs). We overplotted a sinusoidal model of 3.11 ± 0.03 hrs, on a randomly selected night (15th Dec 2017), to demonstrate the accuracy of the 3.1 hrs period derived from the lightcurve measured through F.A. with no LuckyPhot (Figure 4.12).

The estimated radius from evolutionary models of $1.01 \pm 0.007 R_J$ (Filippazzo et al., 2015), in addition to the well-established $v \sin i$ measurements (Vos et al.,

2017), allow us to infer maximum rotation period for 2M J0036 of ~ 3.42 hrs. As mentioned in Section 4.2.2, the source of the variability of this target has been attributed to a magnetic spot (Lane et al., 2007), while the level of variability in this object would assume a significant contrast between the spot and the photosphere. However, Berdyugina (2005) found that the contrast in temperature between the spots and photosphere decreases in cool stars. Recently, Croll et al. (2016) suggested that the plausible cause of variability is a magnetic spot, with some complex interaction between hot (aurora)/cool magnetic spots and clouds of dust. In line with previous studies, we attributed the variability in I-band lightcurves of the L3.5 dwarf to auroral activity, similar to that result in periodic H_{α} emission and periodic radio emission (Hallinan et al. 2015). In the case of ECM process, Hallinan et al., (2008) found that the mechanism driving of periodic radio emission is consistent with the ECM process which requires a magnetic field strength of at least 1.7 kG. This process provides evidence for the presence of stable auroral current systems in a large-scale magnetosphere, and could be associated with periodic optical and Balmer variability (Hallinan et al. 2015). The auroral effect could be responsible for the stability of the photometric variability of 2M J0036 over ~ 13 years, as the previous study attributed long-lived stable surface features to this effect (Pineda et al., 2017).

A possible explanation for the greater level of variability observed by Harding et al. (2013a) is that the size of the magnetic spot may be larger. Or perhaps another mechanism incites the level of variability. On the other hand, during our observation, magnetic effects may be responsible for the low-amplitude I-band variability. We cannot give any insight into these possibilities from our optical data.

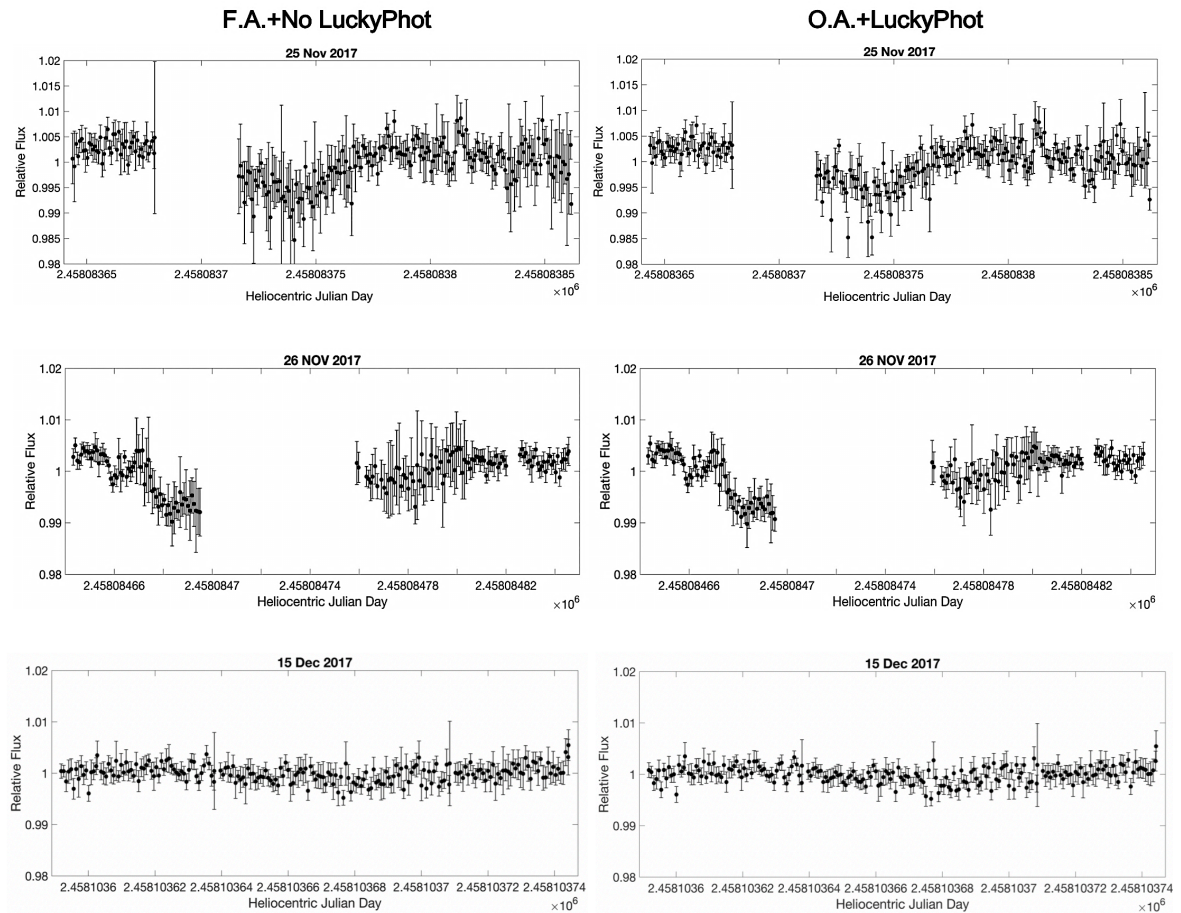
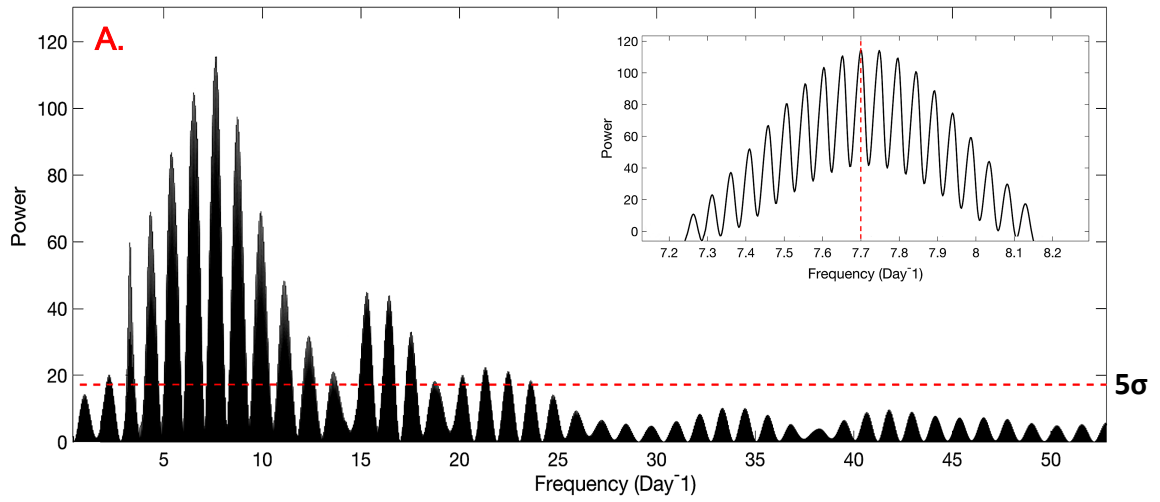
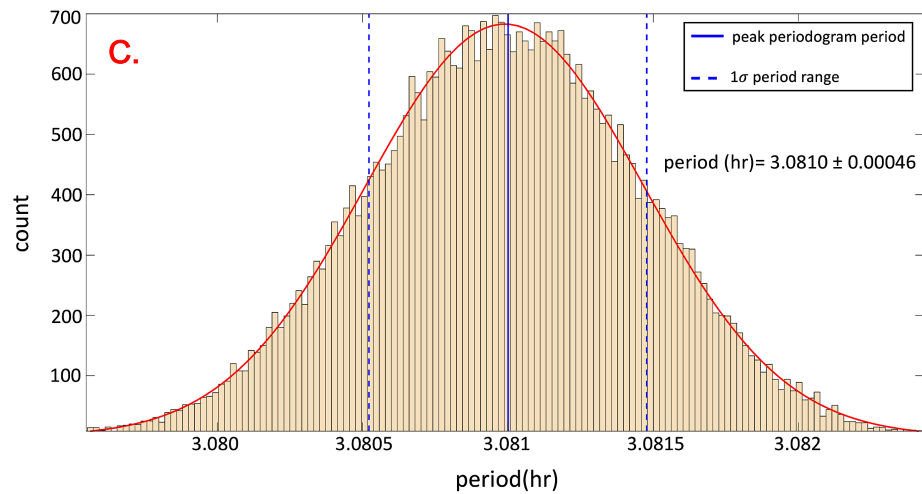
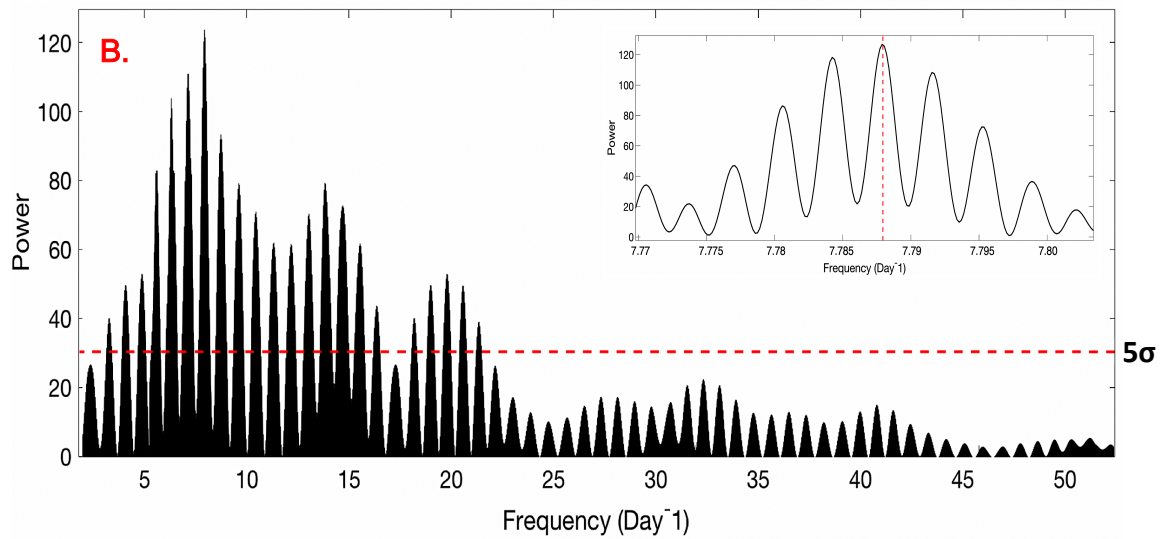


Figure 4.7 Lightcurves of 2M J0036 taken in VATT I-band over three nights (25th and 26th November 2017 and 15th December 2017) for a total of ~ 14 hrs. Unfortunately, the data acquired on 23th December 2017 was not usable due to tracking problems with the VATT telescope. This figure compares the results obtained with the two different techniques to compute a differential lightcurve for 2M J0036. The left column shows the lightcurves using an F.A. size without LuckyPhot. While the right column shows the lightcurves after applying O.A. with LuckyPhot. Photometric error bars from Table 4.5 were applied to each data point. These data exhibit changes in amplitude between the three nights (as shown in Table 4.6). Gaps in the lightcurves for 25th and 26th November 2017 correspond to periods of cloudy sky, and therefore, these data have been removed.

F.A.+No LuckyPhot



O.A.+LuckyPhot



Caption of Figure 4.8 continued from previous page

Figure 4.8 **A** and **B** – Lomb-Scargle Periodogram analysis of F.A. with No LuckyPhot (GUF1 photometry) and O.A. with LuckyPhot on 2M J0036 for the entire 2017 epoch. The dashed and dotted line on each plot represents a 5σ false-alarm probability. The x-axis is plotted in day^{-1} , since each epoch was time-stamped in units of Heliocentric Julian Date (HJD). The vertical dashed red line (shown in close-up in the inset plots) corresponds to 3.11 ± 0.03 hrs and 3.081 ± 0.001 hrs for Figures A and B, respectively. **C**. Using bootstrapping distribution method of retrieved highest power periods (O.A. with LuckyPhot), shows the uncertainty of ~ 0.0005 hr.

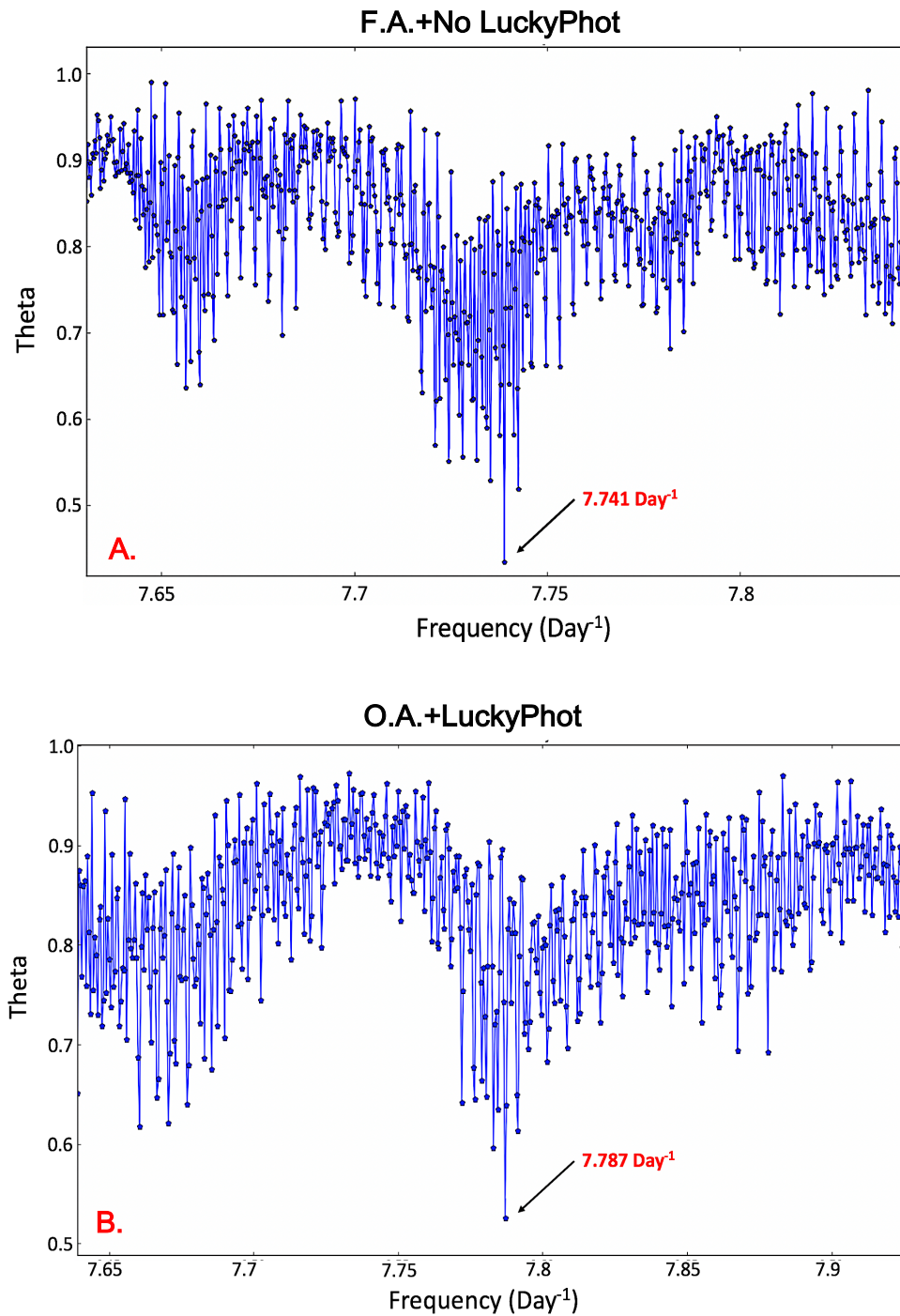


Figure 4.9 Plots **A** and **B** compare the results obtained from PDM using F.A. with No LuckyPhot (GUF1 photometry) and O.A. with LuckyPhot on 2M J0036 for the entire 2017 epoch: the theta statistic (10^5 Monte Carlo simulations) against frequency (Day⁻¹). The minimum theta corresponds to the determined rotation period ~ 3.1 and ~ 3.08 hrs for F.A.+No LuckyPhot and O.A.+LuckyPhot, respectively. These solutions are highly consistent with the rotation period resulting from the LS periodogram.

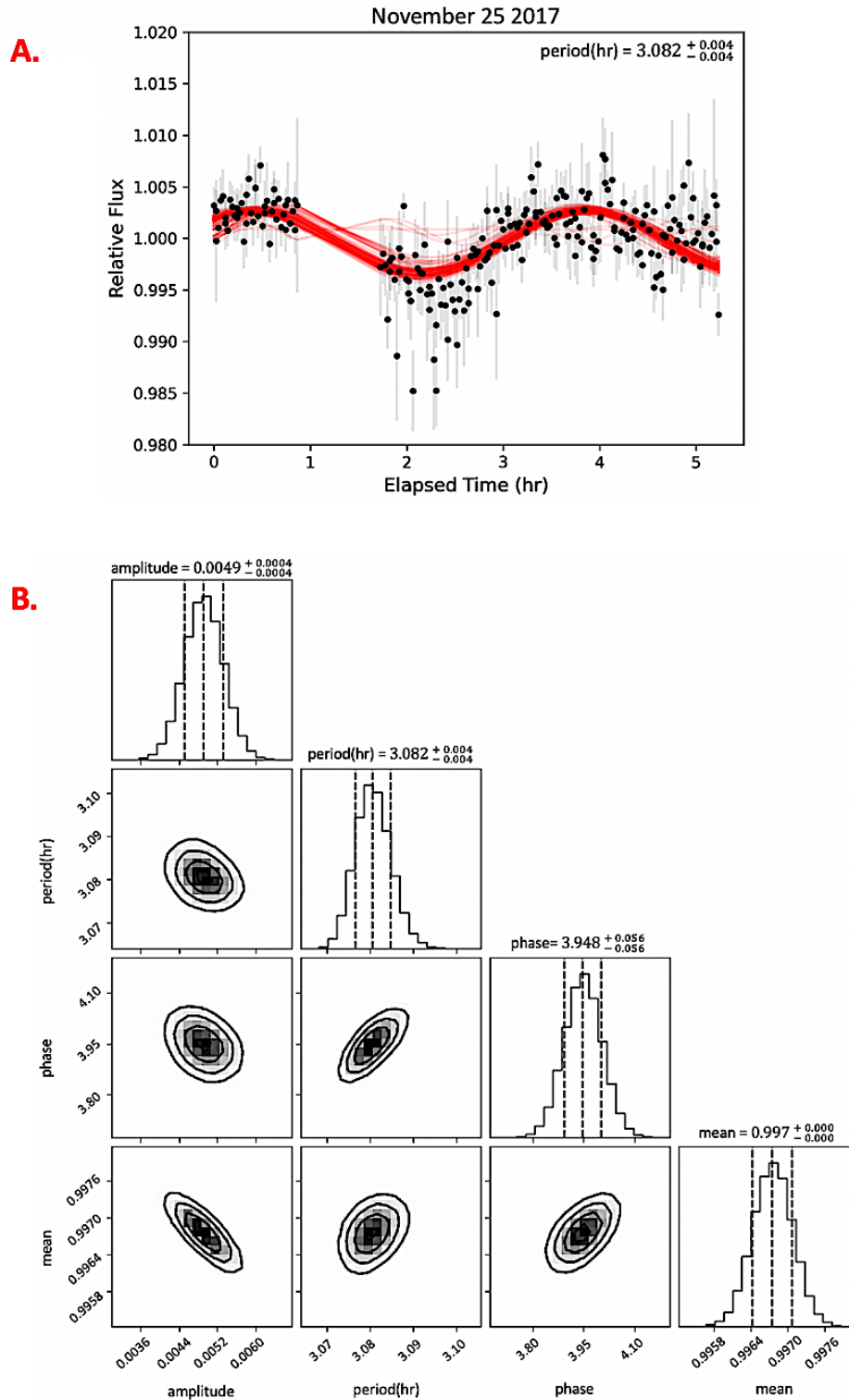


Figure 4.10 **A.** The fitted sinusoidal model (red curve) of 2M J0036 on November 25 2017. **B.** Posterior probability distributions for the model parameters.

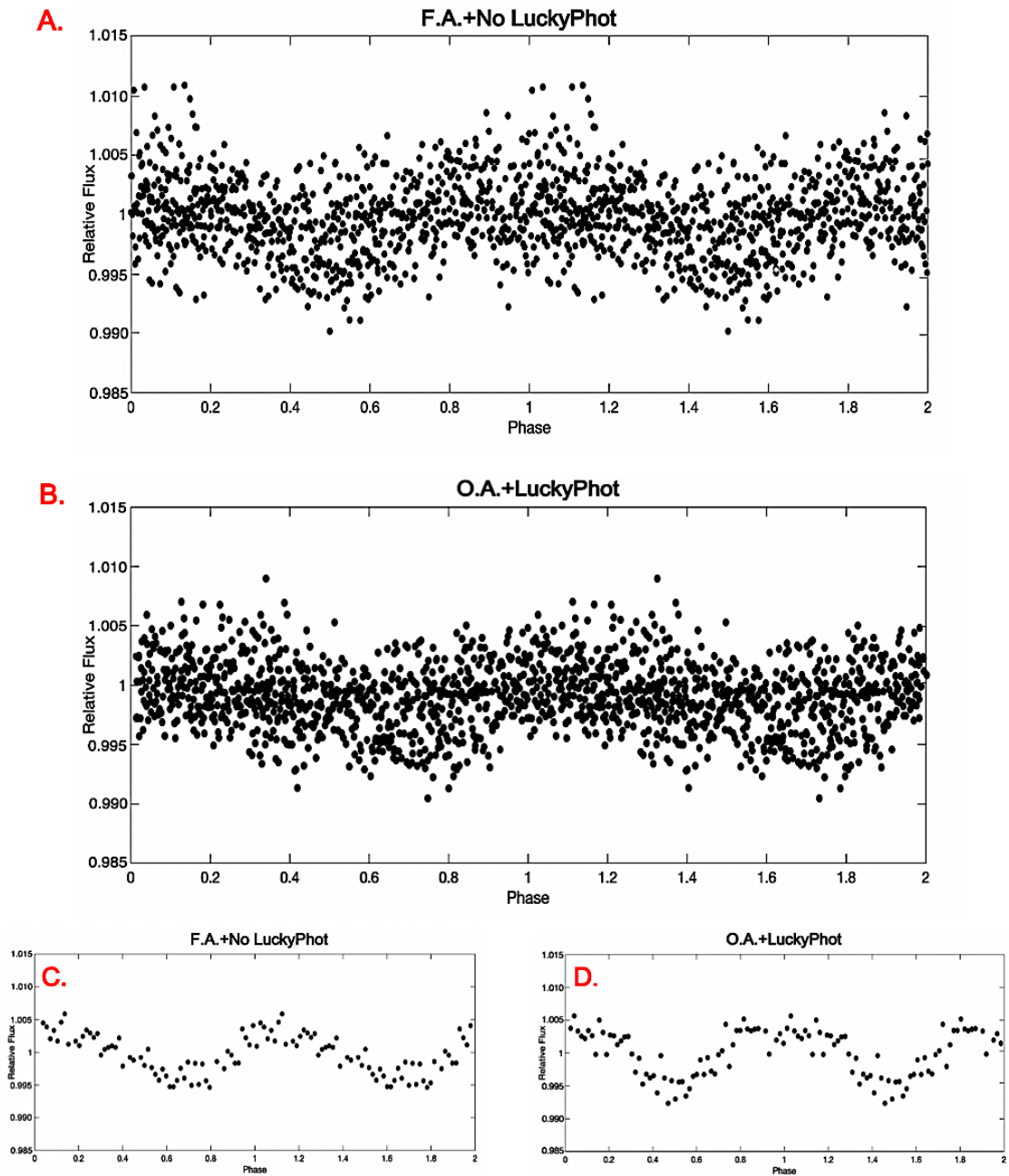


Figure 4.11: **A** and **B** are unbinned phase-folded lightcurves of all data for 2M J0036. They are folded to the periods found by the LS analysis (3.1 hrs and 3.08 hrs) using F.A. with No LuckyPhot (GUF1 photometry) and O.A. with LuckyPhot, respectively. **C** and **D** show the results of binning A and B by a factor of 20.

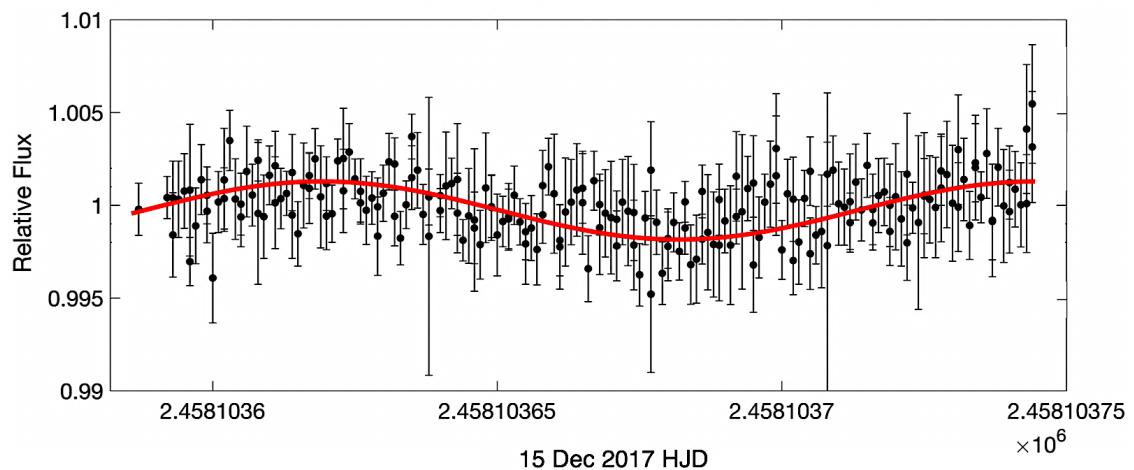


Figure 4.12 We overplotted a sinusoidal model of 3.11 ± 0.03 hrs, on a randomly selected night (15th Dec 2017), to demonstrate the accuracy of the period derived from the light-curve measured through F.A. with no LuckyPhot. The lightcurve shows relative flux versus Heliocentric Julian Date (HJD).

One of the objectives of this research was to determine the inclination angle relative to the observer's line of sight. Previous studies have pointed out that the angle of inclination affects the measured variability amplitudes, and that the highest variability amplitudes were observed in different bands when i was close to 90° (Crossfield et al. 2014; Metchev et al. 2015; Vos et al. 2017). This makes sense when the dwarf is almost equator-on, it will allow us to measure the maximum amplitude variability through optical monitoring. In contrast, the low inclination angle results in lower amplitudes of variability (Kostov & Apai 2013). To calculate the inclination angle of the L3.5 dwarf, we adopted the $1.01 \pm 0.007 R_J$ the mean of predicted range of radii of $0.94 - 1.08 R_J$ (Filippazzo et al., 2015). In addition, we used the 3.081 ± 0.0005 hrs rotation period from using O.A.+LuckyPhot technique, found in Figure 4.8. This indicates an inclination angle of 62.6 ± 0.3 degrees (as shown in Figure 4.13). This gives a value outside range of inclination angle between 70 and 90 degrees determined by Hallinan et

al. (2008), but in agreement with Vos et al. (2017) who calculated an angle of 51 ± 9 degrees.

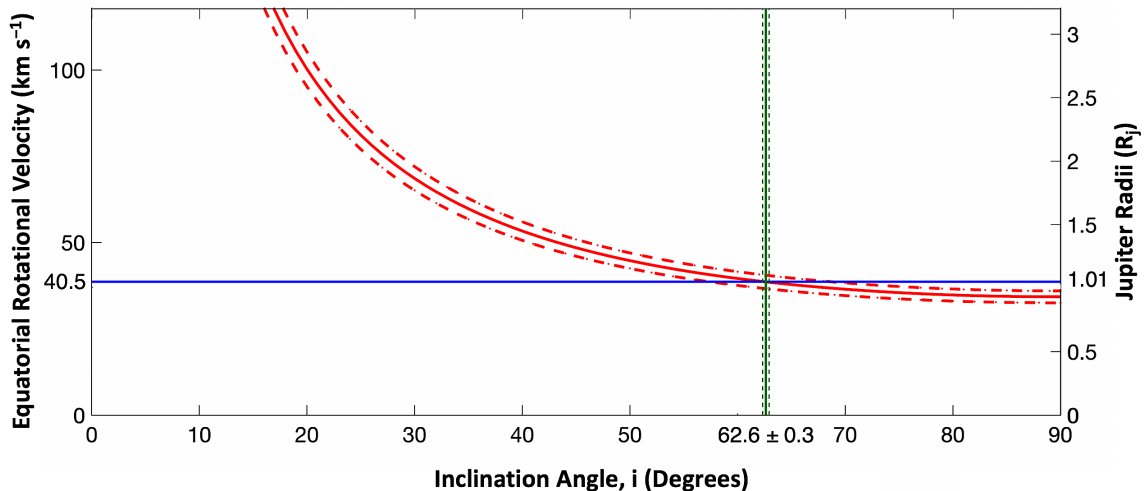


Figure 4.13 The latest value of $v \sin i$ for 2M J0036, $36 \pm 0.2 \text{ km s}^{-1}$, is shown by the solid red curve; the dashed lines represent the associated errors. Equatorial rotational velocity (y-axis, left) is shown versus the inclination angle for the rotation axis to the observer's line of sight. The solid green vertical line highlights the inclination angle relative to our line of sight. The y-axis, right, corresponds to the radius of the dwarf (in units of Jupiter radii, $R_J \sim 69911 \text{ km}$), where we have marked the predicted radius of $\sim 1.01 R_J$ ($\sim 0.101 R_\odot$), the mean of predicted range of radii $0.94 - 1.08 R_J$ (Filippazzo et al., 2015). The solid blue horizontal lines show the corresponding equatorial velocity of $\sim 40.5 \pm 0.1 \text{ km s}^{-1}$.

4.4.3 Optimum Aperture vs. Fixed Aperture

An important part of this project was to produce better lightcurves i.e. higher SNR with lower photometric scatter. According to (Collins, 2014), the LuckyPhot technique has been utilised to reduce photometric scatter introduced by the atmosphere, by rejecting frames that cause the photometric variations in the reference stars. Once data calibration and reduction had been completed using

the in-house L3-GUFI Pipeline, we applied F.A. without LuckyPhot and O.A. with LuckyPhot. We selected the 2M J0036 dataset as a test case for comparing techniques to determine which would improve differential photometric precision. The data was binned at 60 seconds in both systems. The final differential lightcurves of 2M J0036 are presented in Figure 4.14, measured through both techniques. This allows a direct comparison to be made. The lightcurves do show important evidence of variation, with mean peak-to-peak amplitude variability of 0.0013 to 0.0051 mag and of 0.0012 to 0.0046 mag for F.A.+ without LuckyPhot and O.A.+ LuckyPhot, respectively. The LuckyPhot technique does not add new structure to the lightcurve, and the original structure remains, but the errors have been reduced as shown in Table 4.5 and Figure 4.15. We find that the LuckyPhot technique along with O.A. has obvious benefits to improve the photometric precision achievable for a given data set by reducing photometric errors, where the mean RMS error was reduced by $\sim 22\%$ with respect to the errors produced by the more standard GUFI pipeline method.

The difference between the rotation periods resulting from both techniques can be attributed to the frame selection process in LuckyPhot, which selects only the frames which are most photometrically similar (Figure 4.16).

A simple Python script was written called results comparison tool, to compare and quantify which system had a lower scatter. For each differential lightcurve, we grouped the relative fluxes at set time intervals or bins, and then found the standard deviation of the data in each bin. A smoothly varying lightcurve, with small random fluctuations, would yield small standard deviation values in each bin, so this process allows for greater clarity to evaluate which photometric analysis technique has a lower scatter (lower spread) (Figure 4.17). It is obvious that with a combination of O.A. and an optimum frame selection routine (LuckyPhot), the error on a photometric data set is significantly reduced.

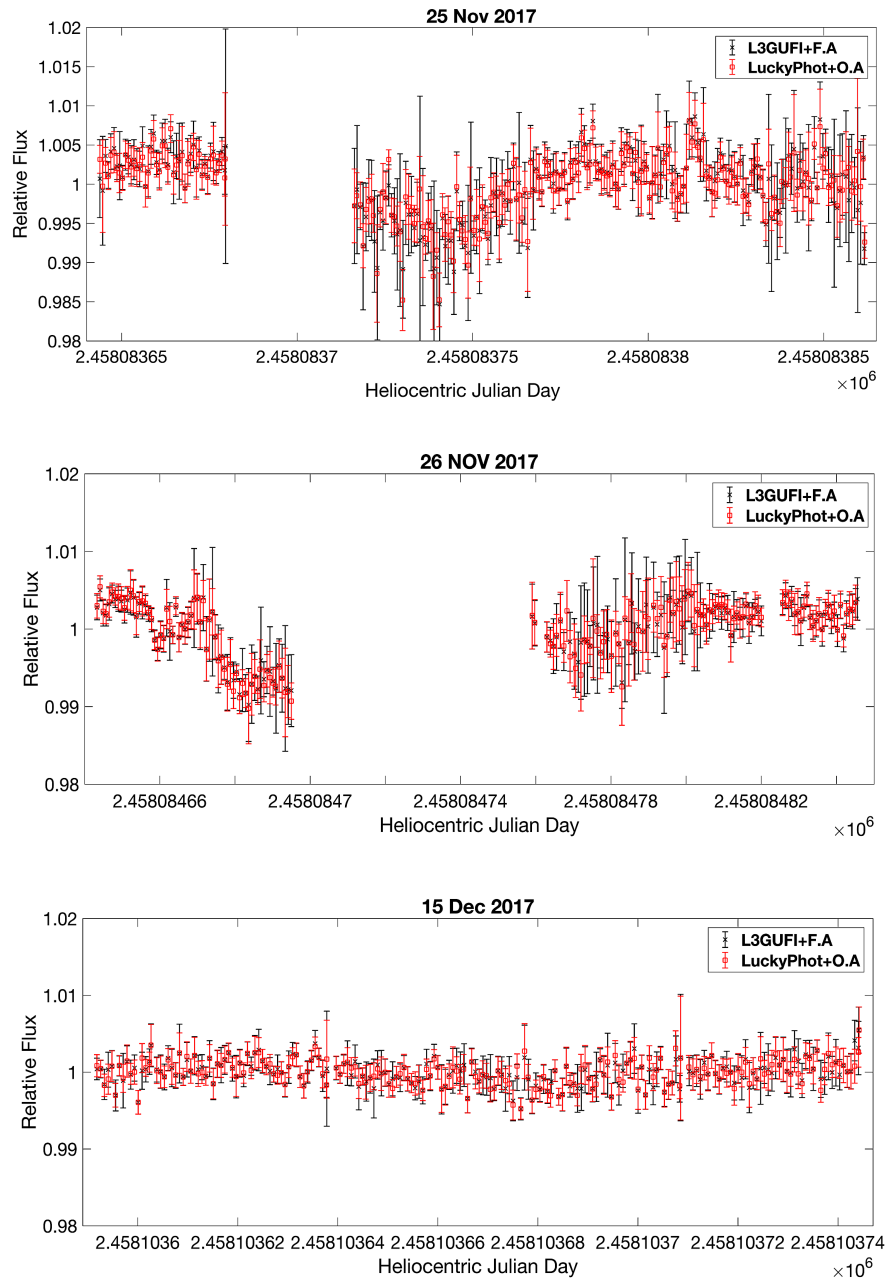


Figure 4.14 We present the 2M J0036 differential lightcurves using the entire data set of 25 and 26 November 2017 and 15 December 2017, when an F.A. with no LuckyPhot (GUF1 photometry) (black star marker) is used and when O.A. with LuckyPhot (red square marker) is used. Relative differential flux is plotted against Heliocentric Julian Date. This plot shows the effectiveness of the O.A. with LuckyPhot technique. The nights of 25 and 26 November 2017 were taken under thin cloud and high wind conditions, and therefore, these data have been removed.

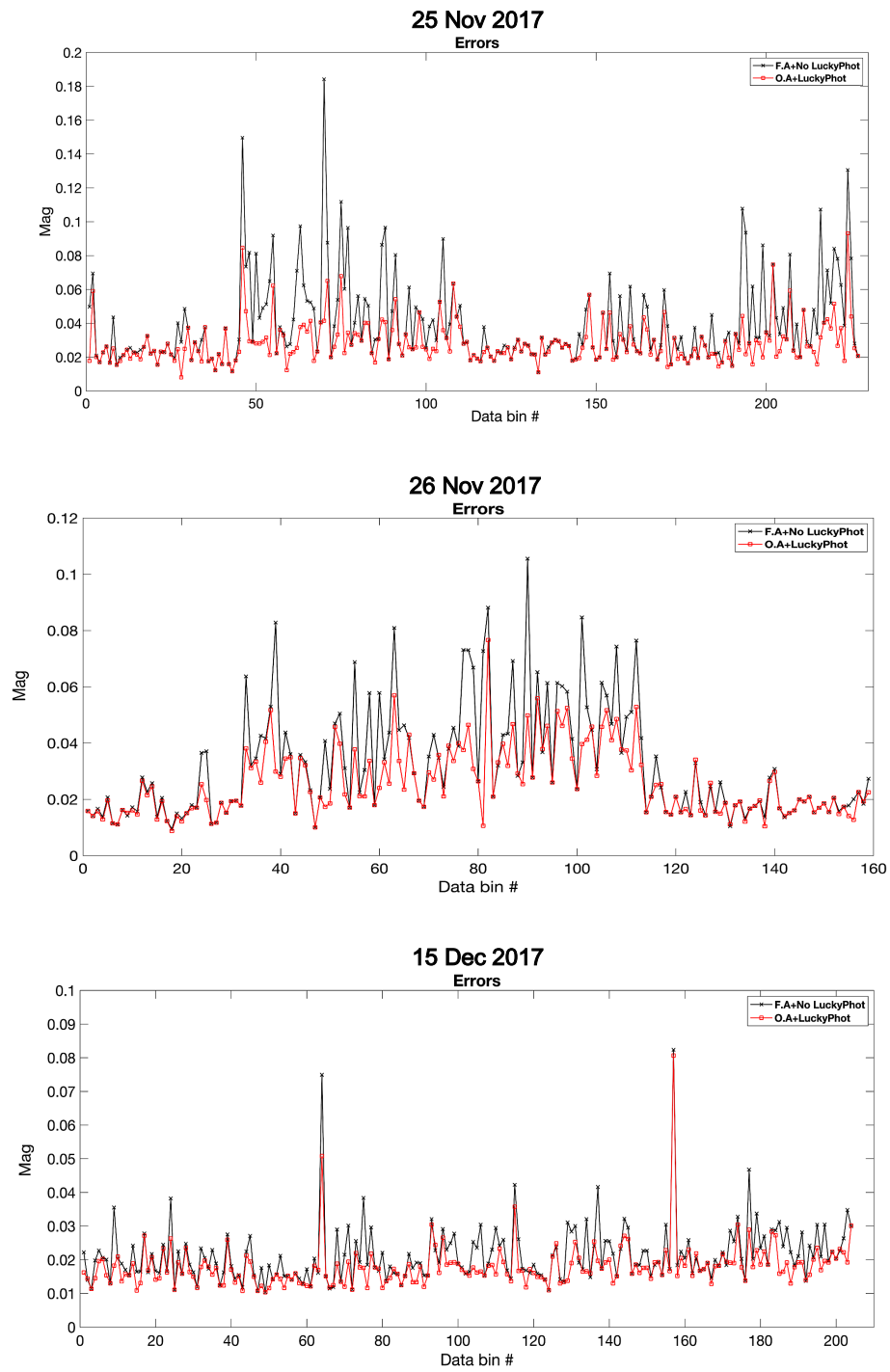


Figure 4.15 The errors from the lightcurves (shown in Figure 4.14). Table 4.5 shows the mean of these errors.

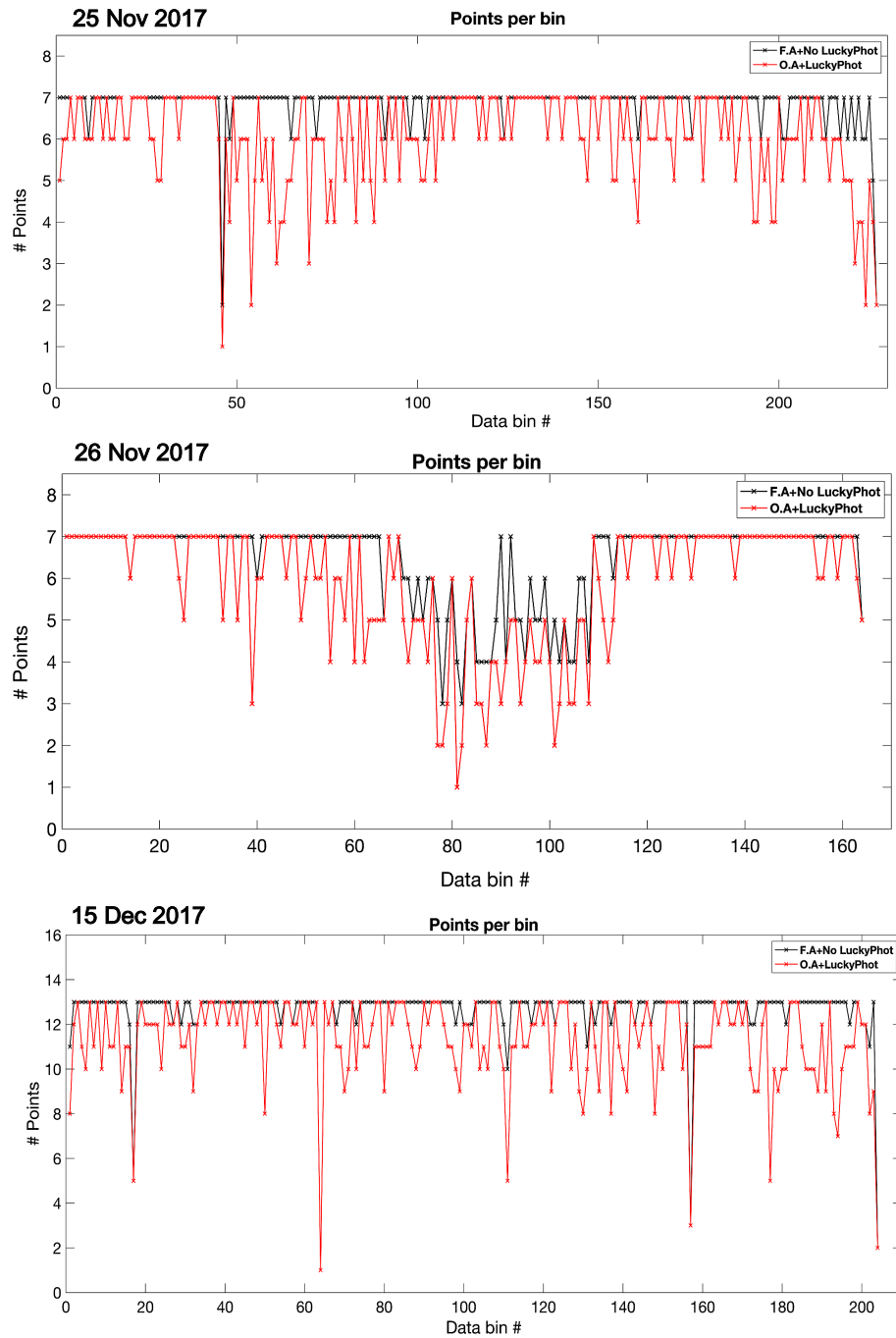


Figure 4.16 The number of points within each data bin before and after the LuckyPhot process for the 2M J0036 data set. Clearly, the level of selection varies from bin to bin, highlighting the impact of the technique. The data gaps seen in Figure 4.14 also affected the selection of points per bin.

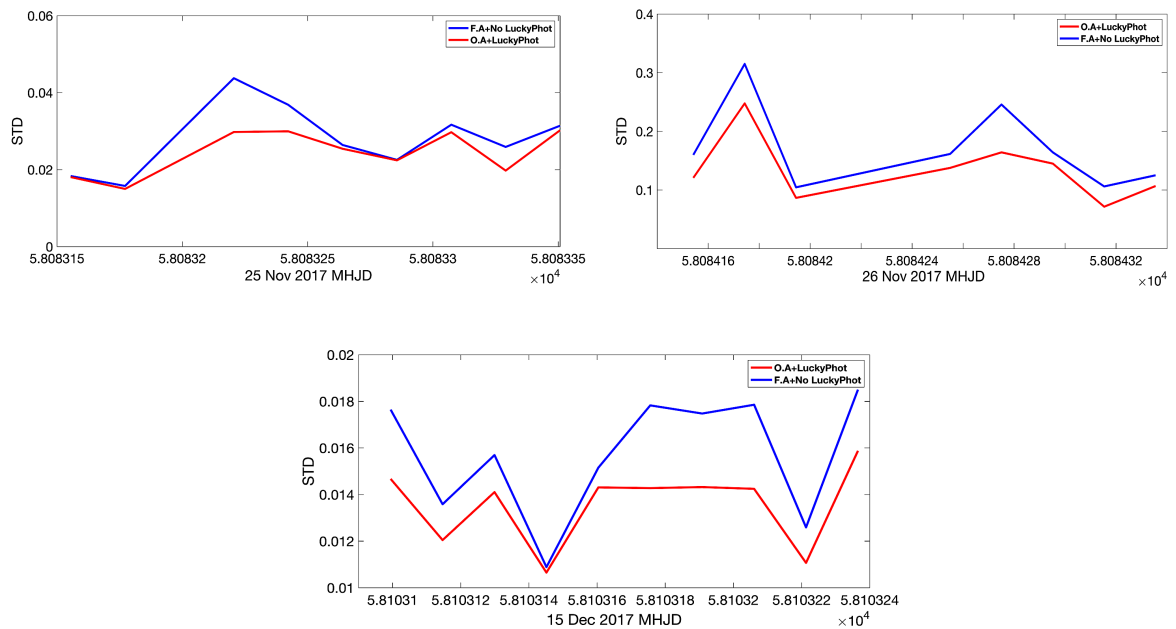


Figure 4.17 Comparison of techniques to determine which one has a lower spread. Each figure shows the standard deviation (STD) of the lightcurve in temporal bins, each containing a number of data points varying between ~ 16 and ~ 25 , versus Modified Heliocentric Julian Date (MHJD).

4.5 Summary

We report the results of a recent I-band photometric study of two ultracool dwarfs that of spectral types M9.5 and L3.5 using the GUF1 high speed photometer. We discovered a new periodic variability for one of these dwarfs for the first time. In the case of 2M J0036, preliminary work undertaken by Berger et al. (2005), Lane et al. (2007), Hallinan et al. (2008), Harding et al. (2013a), Metchev et al. (2015) and Croll et al. (2016) revealed a periodicity of ~ 3 hrs in infrared, optical and radio. Our result ties well with previous studies and improves on their accuracy wherein since we reported a very consistent optical rotation period of 3.11 ± 0.03

hrs and 3.081 ± 0.0005 hrs for F.A. with No LuckyPhot (GUF1 photometry) and O.A. with LuckyPhot, respectively.

Even though we did not replicate the previously reported rotation period (~ 4.8 hrs), our results suggest that we discovered a new periodic variability for BRI 0021 that is more consistent with previous studies. Our results for this object go beyond previous reports, showing that the M9.5 dwarf exhibited a consistent periodic signal of 3.052 ± 0.001 hrs over two separate epochs (October and December 2017). From the latest $v \sin i$ measurements and estimated radius, we inferred a maximum rotation period of ~ 3.88 hrs. This shows our new rotation period is well within the maximum bound of 3.59 hrs inferred from previous $v \sin i$ observations (Mohanty and Basri, 2003) and in agreement with Martín et al. (2001) who expected the rotation period to be ~ 3.36 hrs.

When combined with rotational velocity data obtained from previous work, our newly discovered rotation periods for BRI 0021 and 2M J0036, give interesting results: inclination angles of $51.6^{+0.3}_{-0.2}$ and 62.6 ± 0.3 degrees for the rotation axis relative to our line of sight for BRI 0021 and 2M J0036, respectively.

The viewing angle of BRI 0021 is likely to significantly diminish the anticipated duty cycle associated with the presence of any suspended dust clouds and/or auroral ovals co-rotating with the dwarf, and in particular, to significantly diminish the likelihood of auroral associated beams of coherent radio emission crossing our line of sight; and it is certainly consistent with observations made to date of this rapidly rotating substellar object.

Our results for 2M J0036 indicate a possible correlation between the sources of the optical and radio periodic variability. This correlation implies that the optical and radio periodic behaviour may be related to some kind of magnetic

phenomena (i.e. star spots or aurorae (Hallinan et al., 2015)). The reasons for this, and whether such a possible connection is causal in nature, are not clear.

In the last part of this chapter, we discussed the main reasons for using the LuckyPhot technique. It has the clear benefit to high-precision photometry of reducing the effect of atmospheric variations, through frame selection. It does not alter structures in the lightcurve, when compared to the results of standard photometric techniques.

" Do not look at stars as bright spots only. Try to take in the vastness of the universe."

Maria Mitchell

Chapter 5

Periodic Optical Variability in Very Low Mass Binary Systems

5.1 Introduction

In this chapter, we present multi-epoch optical observations of the L0+L1.5 binary system 2MASS J0746425+200032AB (hereafter known as 2M J0746+20AB) and the M7 binary system 2MASS J1314203+132001AB (hereafter known as 2M J1314+13AB). We again used the VATT I-Arizona ($\sim 7200 - 9100 \text{ \AA}$) broadband filter with our GUF1 photometer on the 1.83 m Vatican Advanced Technology Telescope (VATT), Mt. Graham, Arizona. Due to the close separation between the two components in each of 2M J0746+20AB and 2M J1314+13AB ($\sim 2.7 \text{ AU}$ and $\sim 1.6 \text{ AU}$, respectively), we were unable to monitor each component of these binary systems as separate point sources in our campaign. Therefore, we wrote a Python code, called Light Curve Fitter, capable of detecting the superposition of two sinusoidal waves, and applied it to decouple the weaker component's variability signature from that of the dominant signal. By running Light Curve Fitter on the time-series data, and subtracting the period of each component out in turn, we successfully deconvolved the optical behaviour of each component of the two binary systems. The rotation period is one of the 3 significant parameters of a system, along with a radius estimate and a $v \sin i$ measurement, to infer spin-orbit alignment of the binary members (Harding et al., 2013b), which can be an important diagnostic of formation and evolution theories. Our results indicate that we identified the secondary and primary rotation periods of 2M J0746+20AB and 2M J1314+13AB. Allowing us to investigate their orbital properties, and can probe the formation of very low mass VLM binary stars. Our results suggest that a scaled-down version of the formation mechanism for solar-type binary systems still holds in this regime.

As in Chapter 4, we also used two photometric analysis tools with 2M J1314+13AB to test which system produces the best lightcurves: Optimum Aperture (O.A.) with Lucky Photometry analysis and Fixed Aperture (F.A.) with no Lucky Photometry (as discussed in Sections 4.4.2 and 4.4.3.).

This chapter is structured as follows; Section 5.2 discusses the stellar properties of each binary system and explains further details about findings from previous observation campaigns of the targets. Section 5.3 discusses the optical observations. Section 5.4 presents the photometric results for each source, including the comparison of the results from the two photometric techniques. Section 5.5 discusses some background theory of previous coplanarity studies of binary systems, and the results obtained for the two binary systems in this work. Finally, Section 5.6 is a discussion of all these results.

5.2 Targets

5.2.1 2MASSW J0746425+200032AB

2M J0746+20AB is a binary system of two L-dwarfs in the Gemini constellation. It was discovered by Kirkpatrick et al. (2000) and was later unequivocally determined to be a binary system by Reid et al. (2001) with a separation of 2.7 AU. Bouy et al. (2004) measured the spectral types of the two components ($L0 \pm 0.5$ for A and $L1.5 \pm 0.5$ for B). The system is located at a distance of only 12.2 pc (Dahn et al., 2002). The A and B components have effective temperatures of 1900 K and 2225 K and bolometric magnitudes of $\log(L_{\text{bol}}/L_{\odot}) \approx -3.64$ and -3.77 (Vrba et al., 2004; Konopacky et al., 2010). The initial total mass measurements by Bouy et al. (2004) yielded, $m \sim 0.146_{-0.006}^{+0.016} M_{\odot}$, which placed the dwarfs in the VLM binary regime. This was revised by Konopacky et al. (2010) who measured the total dynamical mass to be $0.151 \pm 0.003 M_{\odot}$ based on observations over a longer time baseline. Later, Harding et al. (2013b) estimated individual masses of $\sim 0.078 M_{\odot}$ and $\sim 0.073 M_{\odot}$ for 2M J0746+20A and 2M J0746+20B, respectively, more consistent with (Konopacky et al., 2010). After that, Dupuy & Liu (2017) measured individual masses of $0.0787_{-0.0014}^{+0.0013} M_{\odot}$ and $0.0749 \pm 0.0013 M_{\odot}$ for A and B, respectively. More recently, Zhang et al. (2020) found the masses of A ($0.07954 \pm 0.00034 M_{\odot}$) and B ($0.0756 \pm 0.00025 M_{\odot}$). Blake et al (2010) and Konopacky et al (2012) both measured an unresolved $v \sin i$ for 2M J0746+20AB, and obtained almost identical values: $33 \pm 3 \text{ km s}^{-1}$. A summary of object properties is shown in Table 5.1.

Several studies revealed H_{α} variability which indicates chromospheric and/or magnetic activity (Bouy et al., 2004). A radio detection at 4.86 GHz was published and indicated a magnetic field strength of $\sim 1.7 \text{ kG}$ which is based on the detection of a single highly circularly polarized burst of emission (Antonova et al., 2008). Following this observation, Berger et al. (2009b) conducted joint VLA/ H_{α} /X-ray observations to (at the time) confirm correlated coronal incoherent

gyrosynchrotron processes from both dwarfs. These authors detected variable coherent radio emission at 4.86 GHz with a period of 2.07 ± 0.002 hrs, in addition to a quasi-sinusoidal H_α emission with the same period. They suggested that the source of both periodic emissions originated from the same binary member, 2M J0746+20A, because the magnetic field strength was consistent with Antonova et al. (2008). Lynch et al. (2015) used the VLA to obtain multi-epoch radio observations of 2M J0746+20AB, and reported a period of 2.071481 ± 0.000002 hrs, which lies within the uncertainty range of the 2.072 ± 0.001 hour period measured by Berger et al. (2009b). Recently, Zhang et al. (2020) used VLBI observations and found that both binary members are radio emitters.

In terms of optical variability, weak evidence of periodicity (of a few hours) was reported by Clarke et al. (2002) and Bailer-Jones (2004). After that, Harding et al. (2013b) ruled out the idea that the 2.07 hours period emanated from the primary component, since they revealed a period of 3.32 ± 0.15 hrs for 2M J0746+20A and calculated maximum rotation periods for 2M 0746+20A and 2M J0746+20B of ~ 4.22 hrs and ~ 2.38 hrs, respectively. Thus, they deduced that Berger et al. (2009b) had, in fact, detected the less-massive secondary component in the radio. These findings were confirmed by Zhang et al. (2020), who detected radio periods of 3.2 ± 0.2 hrs and 2.1 ± 0.1 hrs for the primary and secondary sources. Previous observation of this system, by a collaboration using the Giant Metre Radio Telescope array at 600 MHz and 1.3 GHz (Zic et al., 2018), demonstrated the presence of stable radio emission in both bands, with suggestions of a dominant coherent component at 1.3 GHz. The tentative detection of highly polarized emission at 1.3 GHz is consistent with auroral emission.

Thus far, no periodic optical variability has been detected for 2M 0746+20B. Therefore, we chose to monitor the binary to investigate the presence of optical variability in the secondary component, and to determine whether the optical variability of the primary, 2M J0746+20A, was stable over a timescale of years. We report on our campaign of observations in Section 5.3.

Property	2M J0746+20A	2M J0746+20B	Reference
Spectral type	$L0 \pm 0.5$	$L1.5 \pm 0.5$	Bouy et al. (2004)
Total mass (M_{\odot})	0.151 ± 0.003	0.151 ± 0.003	Konopacky et al. (2010)
Mass(M_{\odot})	0.07954 ± 0.00034	0.0756 ± 0.00025	Zhang et al. (2020)
Distance d (pc)	12.20 ± 0.05	12.20 ± 0.05	Dahn et al. (2002)
Orbital Inclination (°)	41.8 ± 0.5	41.8 ± 0.5	Konopacky et al. (2012)
$v \sin i$ (km s⁻¹)	19 ± 2	33 ± 3	Konopacky et al. (2012)
Age (log yrs)	9.1 ± 0.1	9.1 ± 0.1	Harding et al. (2013b)
Radius (R_{Jup})	0.99 ± 0.03	0.96 ± 0.02	Harding et al. (2013b)
$\log(L_{bol}/L_{\odot})$ (dex)	-3.64 ± 0.02	-3.77 ± 0.02	Vrba et al. (2004) & Konopacky et al. (2010)

Gravity (log g) (cm s⁻²)	5.34 ± 0.02	5.34 ± 0.02	Harding et al. (2013b)
Semimajor axis (mas)	237.3 ^{+1.5} _{-0.4}	237.3 ^{+1.5} _{-0.4}	Konopacky et al. (2010)

Table 5.1 A summary of properties of 2M J0746+20AB with relevant references.

5.2.2 2MASS J1314203+132001AB

This M7 binary dwarf was discovered as a radio-emitting source in 2007 during a Very Large Array (VLA) survey of nearby mid-and late-M dwarfs (McLean et al., 2011). Lucky imaging at z' and i' bands of 2M J1314+13AB resolved it into a binary with a separation of ~ 1.6 AU and a companion fainter by ~ 1 mag than the primary in the i' band (Law et al., 2006). Lepine et al. (2009) measured its parallactic distance of 16.39 ± 0.75 pc, in addition to determining its $M7.0 \pm 0.5$ spectral type. More recently, the joint analysis of Keck adaptive optics and Very Long Baseline Array (VLBA) radio interferometry determined that the binary is located at a distance of 17.249 ± 0.013 pc (Forbrich et al., 2016). A combination of spectral analysis and resolved JHKL'-band photometry has estimated an effective temperature of 3200 ± 500 K and 3100 ± 500 K for the A and B components, respectively (Schlieder et al., 2014). Dupuy et al. (2016) used the evolutionary models of Baraffe et al. (2015) to determine that the average T_{eff} is 2950 ± 5 K, which is 180 K hotter than the 2770 ± 100 K expected from a spectral type - T_{eff} relation (Herczeg and Hillenbrand, 2014) based on BT-Settl models (Allard et al., 2012). Dupuy et al. (2016) proposed that this T_{eff} contradiction may be due to systematic errors in either or both of the evolutionary and atmosphere models. Dupuy et al. (2016) and Forbrich et al. (2016) determined that the A and B members have nearly identical (to within $\pm 2\%$) masses of $92.8 \pm 0.6 M_{\text{J}}$ (0.0885

$\pm 0.0006 M_{\odot}$) and $\sim 91.7 M_J$ ($0.0875 \pm 0.0010 M_{\odot}$) ($M_{total} = 0.1761 \pm 0.0015 M_{\odot}$). These mass estimates are in good agreement with Schlieder et al. (2014), who also used the evolutionary models of Baraffe et al. (2003) and derived masses of $\sim 0.0925 M_{\odot}$ and $\sim 0.0868 M_{\odot}$ for the A and B components, respectively, indicating that both components are near the substellar boundary. A study by McLean et al. (2011), inferred the radii of both components to be $\sim 0.13 R_{\odot}$ ($\sim 1.29 R_J$) which is 30% larger than the $\sim 0.1 R_{\odot}$ ($\sim 0.99 R_J$) model predictions for a field age M7 dwarf by Demory et al. (2009). But the high levels of magnetic activity present in 2M J1314+13AB may alter their radii, making them oversized by $\sim 20\%$ (Williams et al., 2015). More recent studies - (Dupuy et al., 2016; Forbrich et al., 2016) which represent the more precise data so far – found model radii that are too small by $\sim 13\%$, which yielded component radii of $\sim 1.831 R_J$ and $\sim 1.808 R_J$, respectively. Schlieder et al. (2014) derived bolometric luminosities for the A and B components: $\log_{10} (L/L_{\odot}) = -2.64 \pm 0.06$ and $\log_{10} (L/L_{\odot}) = -2.68 \pm 0.06$, respectively. This was based on resolved photometry, distances, and the bolometric corrections of Liu et al. (2010) for spectral types of M7. Dupuy et al. (2016) measured bolometric luminosities of $\log (L_{bol}/L_{\odot}) = -2.616 \pm 0.010$ and -2.631 ± 0.010 for 2M J1314+13A and B, respectively. Target properties are shown in Table 5.2.

The system has strong chromospheric H_{α} emission, confirming the presence of magnetic activity (Lepine et al., 2009). Activity is not only present in optical radiation, since radio emission has been reported in several studies.

Property	2M J1314+13A	2M J1314+13B	Reference
Spectral type	M7.0 ± 0.2 (Integrated)		Dupuy et al. (2016)
Age (Myr)	79.9 ^{+2.5} _{-2.7}	81.7 ^{+2.9} _{-3.3}	Dupuy et al. (2016)
Total mass (M _{Jup})	184.5 ± 1.6	184.5 ± 1.6	Dupuy et al. (2016)
Mass (M _{Jup})	92.8 ± 0.6	91.7 ± 1.0	Dupuy et al. (2016)
Distance d (pc)	17.249 ± 0.0136	17.249 ± 0.0136	Forbrich et al. (2016)
Orbital Inclination (°)	49.34 ^{+0.28} _{-0.23}	49.34 ^{+0.28} _{-0.23}	Dupuy et al. (2016)
$v \sin i$ (km s ⁻¹)		45 ± 5	McLean et al. (2011)
Radius (R _{Jup})	1.831 ± 0.018	1.808 ± 0.018	Dupuy et al. (2016)
log(L _{bol} /L _☉) (dex)	-2.616 ± 0.010	-2.631 ± 0.010	Dupuy et al. (2016)

Gravity (log g) (cm s⁻²)	4.836 ± 0.010	4.842 ± 0.011	Dupuy et al. (2016)
Semimajor axis (mas)	146.6 ± 0.5	146.6 ± 0.5	Dupuy et al. (2016)

Table 5.2 A summary of properties of 2M J1314+13AB with relevant references.

This binary system revealed highly circularly polarised periodic radio pulses due to the electron cyclotron maser instability (ECMI) process. McLean et al. (2011) detected persistent radio emission from 2M J1314+13AB with a flat spectrum over a range of frequencies at 1.43, 4.86, 8.46 and 22.5 GHz, and reported radio emission varying sinusoidally with a period of 3.89 ± 0.05 hrs at two of these frequencies (4.86 and 8.46 GHz) in multi-epoch VLA observations. They also found periodic modulation in g and i band filters with a period of ~ 3.79 hrs and measured $v \sin i$ of 45 ± 5 km s⁻¹. They suggested the optical-radio period difference could be due to differential rotation, with $\Delta\Omega \approx 1$ rad day⁻¹ between the equatorial and polar regions of this target. The same phenomenon had been observed previously in the magnetic chemically peculiar star CU Virginis as well, but the period difference was much smaller (around 1 sec). It was suggested that an unseen companion or instability in the emission could be the origin of this behaviour (Ravi et al., 2010; Pyper et al., 2013). They attributed this measured rotation period in both radio and optical to the primary component (McLean et al., 2012; Schlieder et al., 2014). VLBI observations revealed that the origin of the radio emission is only from the secondary component (Forbrich et al., 2016). Williams et al. (2015) detected two optical periodicities, 3.7859 ± 0.0001 hrs and 3.7130 ± 0.0002 hrs - both of which are compatible with the relatively large uncertainties of the F.A. and O.A./LuckyPhot periods we report in Table 5.10. Williams et al. (2015) ruled out that the two similar rotation periods were a result of differential rotation, as it not expected to occur in the UCDs mass range.

Instead, they attributed this extraordinary differential rotation to the unusually magnetically active system. Indeed, this system outputs the highest X-ray and radio luminosities detected from an ultracool dwarf to date, due to its extreme levels of magnetic activity (Williams et al., 2015). McLean et al. (2011) found that g- and i- band variations are correlated, indicating that magnetic spots are the likely explanation. Using the Giant Metre Radio Telescope array at 6 GHz and 1.3 GHz, Zic et al. (2018) reported the lowest-frequency detections of 2M J1314+13AB and 2M J0746+20AB to date at ~ 610 and 1300 MHz.

Based on all of this reported radio and optical activity, we chose to monitor the binary to investigate the existence of such variations in optical wavelengths in both components, but in particular 2M J1314+13A, where no one had discovered optical variability so far. We report on our campaign of observations in the next Section (5.3).

5.3 Optical Observation and Outline of Data Analysis

Observations for 2M J0746+20AB and 2M J1314+13AB were carried out on the 1.83 m VATT, Mt. Graham, Arizona, to investigate the presence of periodic optical variability from both or either components of the binary systems. We used the VATT I-Arizona ($\sim 7200 - 9100 \text{ \AA}$) broadband filter with the GUF1 photometer for both targets (Section 2.3). A total of 72.3 hrs of optical observation were made of 2M J0746+20AB over the course of three separate epochs (March, November and December 2017), shown in Table 5.3, where typical values of seeing range from $0.8''$ to $1.6''$.

Unfortunately, due to very poor weather on some nights in the December 2017 epoch, we did not include this data in the determination of the period of rotation of 2M J0746+20AB.

We monitored 2M J1314+13AB for a total of 47.2 hrs in I band, encompassing three separate epochs (February 2017, March 2017 and May 2018) , as listed in Table 5.4. The seeing was between 1.1" to 1.7" during the campaign.

Date of Obs. (UT)	Length of Obs. (hr)	Exp. Time (s x no. frames)	Readout Rate (MHz)	Amplifier	Reference Stars (No.)
2017 March 04	2.5	5 x 12	1	Conventional	6
2017 March 17	2.3	5 x 12	1	Conventional	6
2017 March 19	2.6	5 x 12	1	Conventional	5
2017 March 20	3.5	5 x 12	1	Conventional	6
2017 March 21	3.5	5 x 12	1	Conventional	6
2017 November 22	4.3	5 x 12	1	Conventional	5
2017 November 23	4.7	3 x 20	1	Conventional	5
2017 November 24	4.9	5 x 12	1	Conventional	6
2017 November 26	3.9	5 x 12	1	Conventional	6
2017 December 19	6	5 x 12	1	Conventional	5
2017 December 23	6.5	5 x 12	1	Conventional	5
2017 December 24	5.7	5 x 12	1	Conventional	6
2017 December 25	5.8	5 x 12	1	Conventional	5
2017 December 27	4.7	5 x 12	1	Conventional	6
2017 December 28	4.9	5 x 12	1	Conventional	5
2017 December 29	6.5	5 x 12	1	Conventional	5

Table 5.3 Observation Details of 2M J0746+20AB. Here, "no. frames" means the number of successive CCD frames stored together in each datacube file.

Differential photometry was performed on the calibrated frames, comparing 2M J0746+20AB and 2M J1314+13AB to a small number of field stars. We applied

Date of Obs. (UT)	Length of Obs. (hr)	Exp. Time (s x no. frames)	Readout Rate (MHz)	Amplifier	Reference Stars (No.)
2017 February 24	4.5	5 x 12	1	Conventional	4
2017 February 28	2.8	5 x 12	1	Conventional	4
2017 March 01	3.7	5 x 12	1	Conventional	4
2017 March 03	4.1	10 x 6	1	Conventional	4
2018 May 04	3	5 x 12	1	Conventional	4
2018 May 05	7.2	5 x 12	1	Conventional	4
2018 May 07	6.6	5 x 12	1	Conventional	4
2018 May 08	6	5 x 12	1	Conventional	4
2018 May 09	6.2	5 x 12	1	Conventional	4
2018 May 11	3.1	5 x 12	1	Conventional	4

Table 5.4 Observation Details of 2M J1314+13AB. Here, "no. frames" means the number of successive CCD frames stored together in each datacube file.

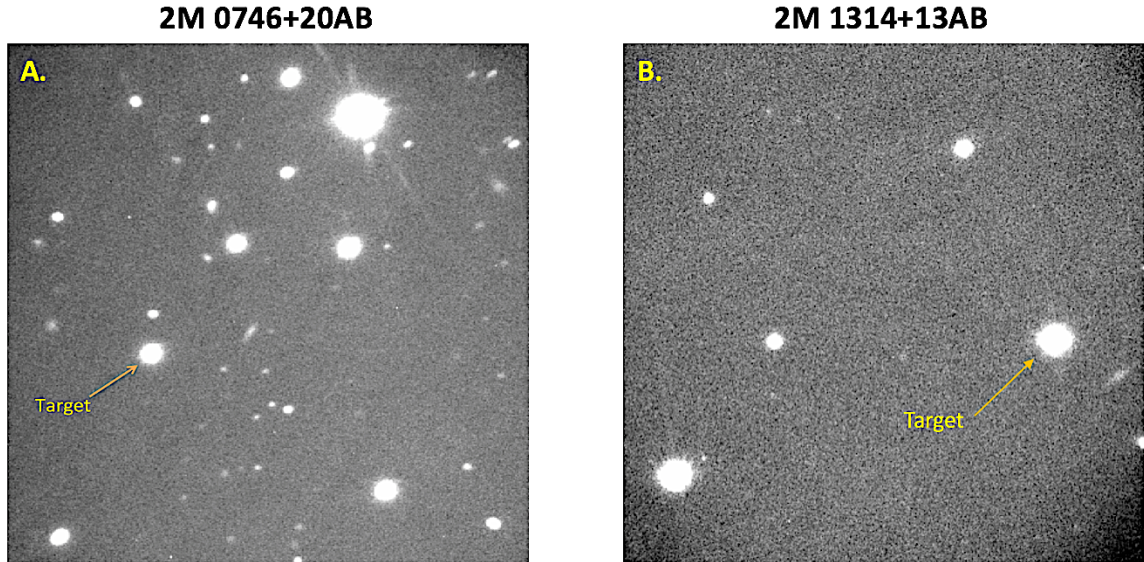


Figure 5.1 I-band images of the 2M J0746+20AB and 2M J1314+13AB fields, obtained at the 1.8m VATT using our GUF1 photometer.

O.A. with LuckyPhot to data sets of 2M J1314+13AB to test the performance of the system and compared it with F.A. without using LuckyPhot (We used the same photometric analysis process that we used with 2M J0036 in Chapter 4).

The photometric aperture used encloses the combined flux of both components in each binary system, due to the close separation of the binary members of the two targets (Figure 5.1). The presence of two periodically varying sources in this data (as the results in Section 5.4 will illustrate) produces superimposed variability and a complex lightcurve shape. Our Light Curve Fitter Python code (Section 3.7.4) was used to dismantle the weaker variability signature from that of the dominant variability.

5.4 Results

5.4.1 2M J0746+20AB

We performed aperture photometry with a fixed aperture (F.A.) on the target and a selection of reference stars, using the L3-GUFI pipeline. As mentioned in Section 5.3, we could not image each component of 2M J0746+20AB as a point source due to ~ 2.7 AU ($\sim 0''.23$) the separation between the A and B components (Figure 5.1). As a result, Light Curve Fitter was used to separate the superposition of two periodically varying sources, by producing a χ^2 /LSF fitting model to the I-band lightcurves of 2M J0746+20AB (Figure 5.2). Light Curve Fitter would help to refine the primary's variability parameters and search for the elusive secondary period.

We ran Light Curve Fitter with a period of 3.32 hrs (the rotation period of the dominant source) on each of the nightly lightcurves independently. We then subtracted the 3.32 hr waveform out and re-ran LS periodograms, PDM and MCMC on the residual data points to see if any other variability signature under

the primary variability could be present. Our statistical analysis of these residuals (LS periodogram and PDM) show periodic optical variability with mean peak-to-peak amplitude variability of 0.0011 to 0.0053 mag in I-band (Table 5.5, Figure 5.4, Figure 5.8, Figure 5.9). This is attributed to the secondary 2M J0746+20B; with a periodicity of 2.14 ± 0.07 hrs, discovered optically for the first time (Table 5.6). This agrees with Berger et al. (2009b) and Lynch et al. (2015) who reported radio pulses with a period of ~ 2.07 hrs, and highly consistent with radio period of 2.1 ± 0.1 hrs revealed by Zhang et al. (2020). We randomly selected the night of 27 December 2017 for O.A.+LuckyPhot, and used MCMC approach which shows a period of 2.14 ± 0.08 hrs (Figure 5.10). We phase folded the residual data points to 2.14 hrs, and the resulting phase curve supports the possibility of an underlying period from the secondary component (Figure 5.12).

This process was repeated again on the original I-band lightcurves of 2M J0746+20AB (Figure 5.2) by running Light Curve Fitter and subtracting the 2.14 hrs period out (Figure 5.3). We then re-ran our statistical analysis tools on the residual data points (Figure 5.5, Figure 5.6), and phase folded on the detected primary period to confirm whether 2M J0746+20A is a periodic source (Figure 5.11). We randomly selected the night of 24 November 2017 for O.A.+LuckyPhot, and used MCMC approach which yields a period of 3.32 ± 0.018 hrs (Figure 5.10). We confirm periodic optical variability of 3.32 ± 0.003 hrs with mean peak-to-peak amplitude variability of 0.0014 to 0.0154 mag (Figure 5.3, Figure 5.5, Table 5.5 & Table 5.6), largely consistent with a previous study by Harding et al. (2013a and 2013b), who reported a period of ~ 3.32 hrs for the slower component. Our period is broadly consistent with 3.2 ± 0.2 hrs radio periodicity measured by Zhang et al. (2020). This demonstrates that the variability parameters of the primary 2M J0746+20A are stable on timescales of years. Such stability is unlikely in the case of dust clouds on the surface of the object.

Due to large gaps in the data between consecutive observations that cause spectral leakage, we noticed multiple LS power spectra peaks and PDM theta

minima around (left and right of) the discovered rotation periods (Figure 5.5 & Figure 5.6 for A component; Figure 5.8 & Figure 5.9 for B component). However, this does not compromise our analysis, since we detected the same period for each component when we ran our statistical methods in each epoch separately.

Date of Obs. (UT) (1)	Band (2)	Amplitude of the Variability 2M J0746+20A (mag) (3)	Amplitude of the Variability 2M J0746+20B (mag) (4)	Photometric Error (mag) (5)
2017 March 04	/	0.0040 ± 0.0003	0.0028 ± 0.0005	0.0056
2017 March 17	/	0.0026 ± 0.0004	0.0023 ± 0.0004	0.0052
2017 March 19	/	0.0093 ± 0.0002	0.0013 ± 0.0003	0.0038
2017 March 20	/	0.0086 ± 0.0005	0.0053 ± 0.0004	0.0057
2017 March 21	/	0.0014 ± 0.0002	0.0031 ± 0.0003	0.0039
2017 November 22	/	0.0027 ± 0.0004	0.0041 ± 0.0004	0.0048
2017 November 23	/	0.0036 ± 0.0003	0.0014 ± 0.0003	0.0110
2017 November 24	/	0.0154 ± 0.0002	0.0042 ± 0.0005	0.0092
2017 November 26	/	0.0033 ± 0.0004	0.0019 ± 0.0006	0.0043
2017 December 19	/	0.0034 ± 0.0003	0.0014 ± 0.0004	0.0106
2017 December 23	/	0.0018 ± 0.0005	0.0017 ± 0.0003	0.0046
2017 December 24	/	0.0067 ± 0.0006	0.0038 ± 0.0005	0.0121
2017 December 25	/	0.0027 ± 0.0002	0.0011 ± 0.0003	0.0059
2017 December 27	/	0.0061 ± 0.0003	0.0017 ± 0.0003	0.0018
2017 December 28	/	0.0024 ± 0.0004	0.0028 ± 0.0003	0.0108
2017 December 29	/	0.0032 ± 0.0002	0.0016 ± 0.0003	0.0052

Table 5.5 Amplitude variability and photometric error analysis of 2M J0746+20A & 2M J0746+20B. **Column 1:** Date of observation in UT. **Column 2:** Waveband used. **Columns 3 & 4:** Peak-to-peak amplitude variability with associated errors as measured by the Chi-squared test. **Column 5:** Mean photometric error for lightcurve data points per night, as measured by the `iraf.phot` routines.

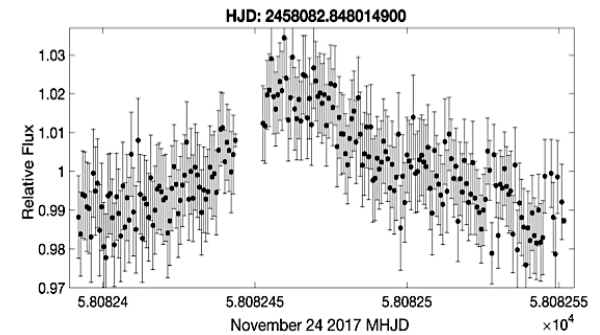
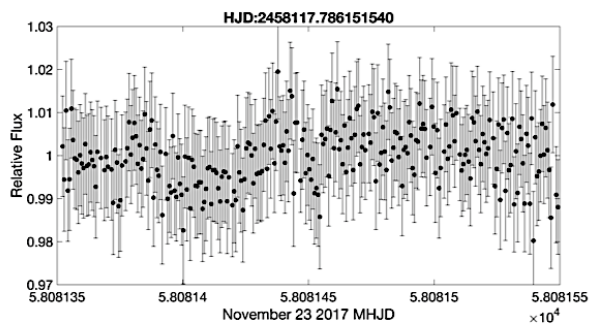
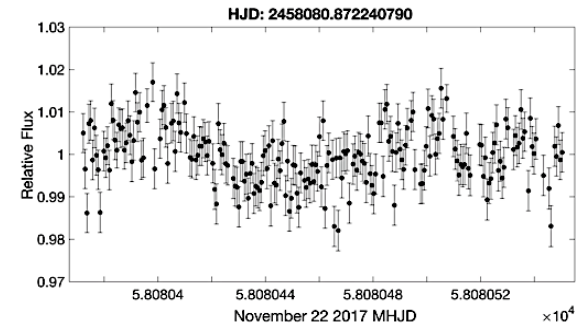
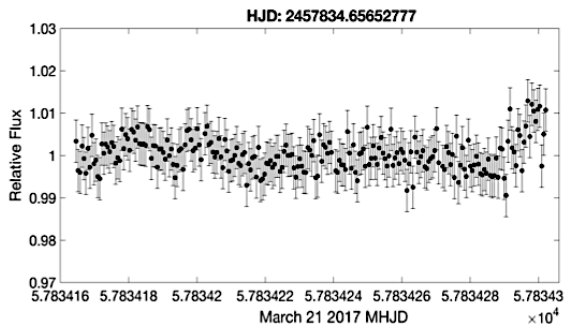
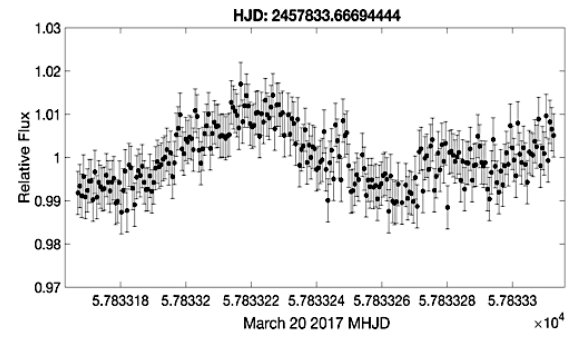
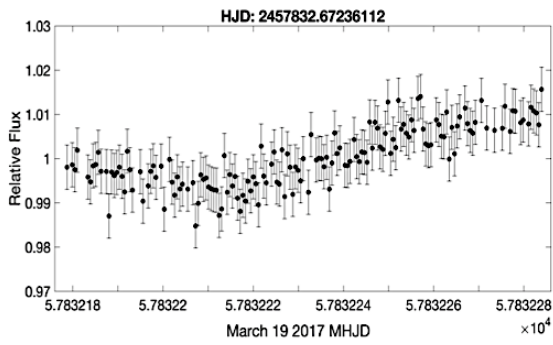
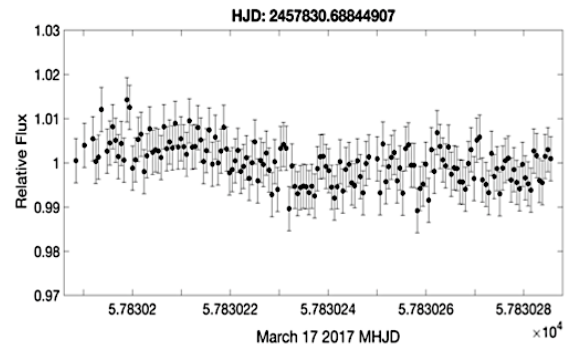
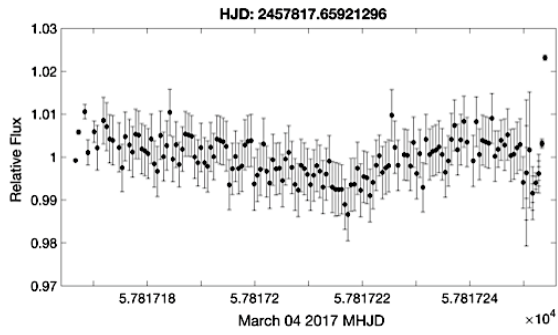
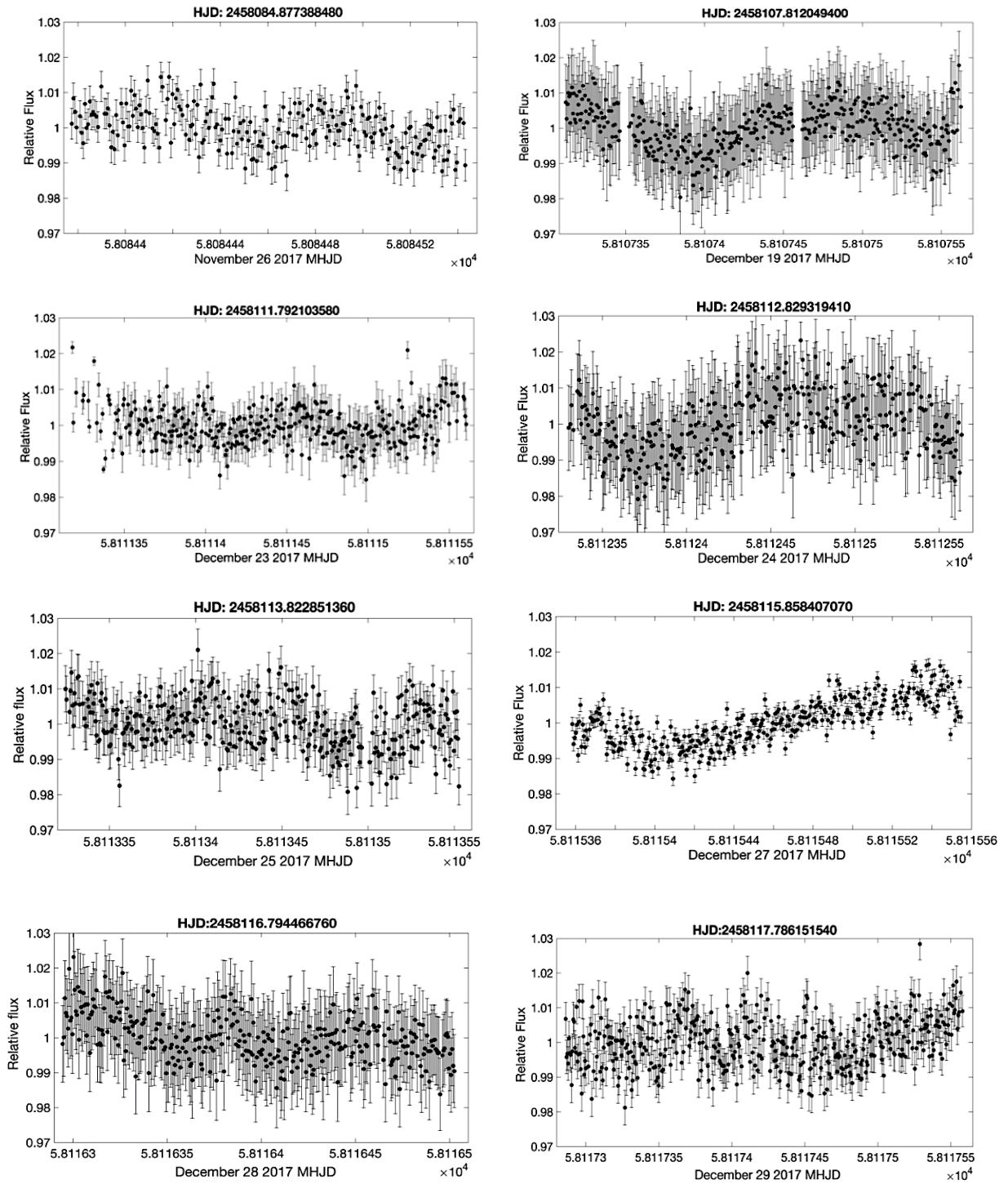


Figure 5.2 continued from previous page



Caption of Figure 5.2 continued from previous page

Figure 5.2 2M J0746+20AB: I-band lightcurves showing target flux relative to 5 to 6 reference stars vs. Modified Heliocentric Julian Date (MHJD). The HJD time above each figure denotes the start-point of each observation night. Both components of the binary contribute to the variability seen here. Some possibly aperiodic variations are observed during some observations (e.g. 29th December 2017). The arrow marked on the 24th November 2017 lightcurve indicates a period of full cloud coverage, and this data has been removed. We note that on 23rd November 2017 and December 19th, 24th and 28th 2017, the data were taken during bad weather conditions (thin cloud). The impact is shown clearly by an increase in the photometric error estimates and an increase in the scatter of the lightcurve itself.

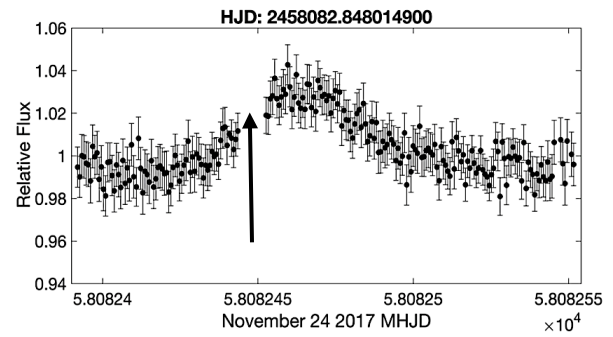
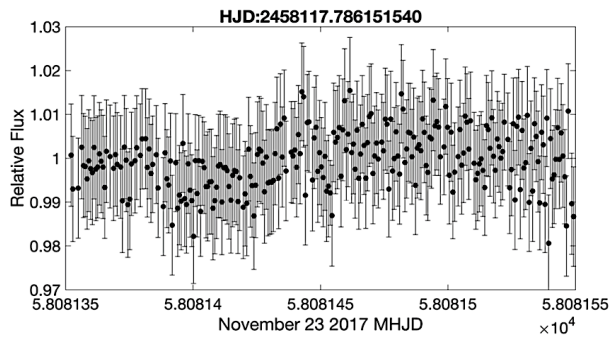
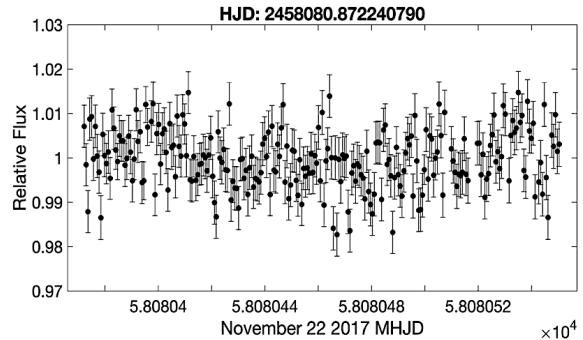
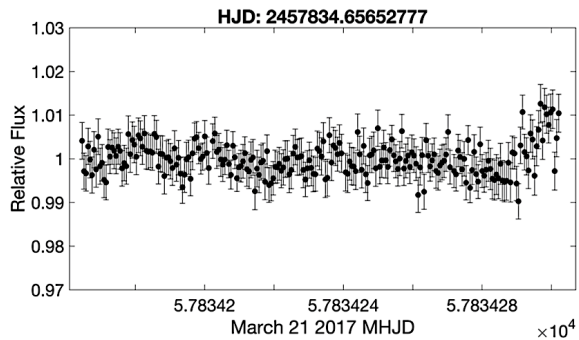
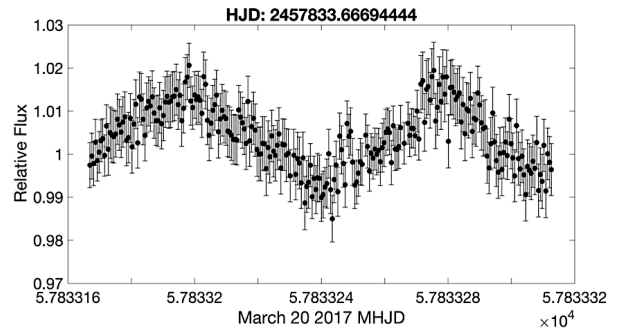
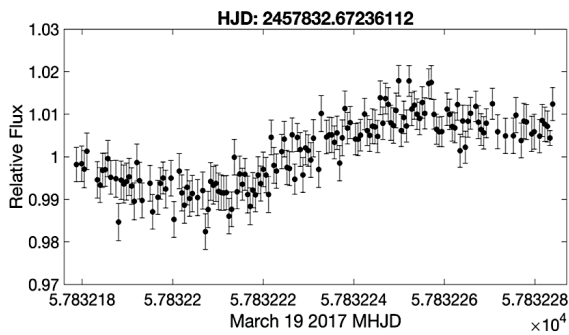
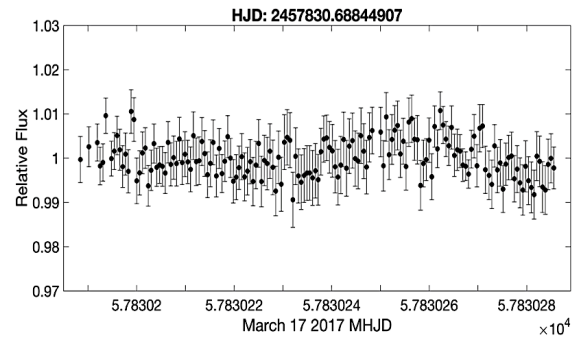
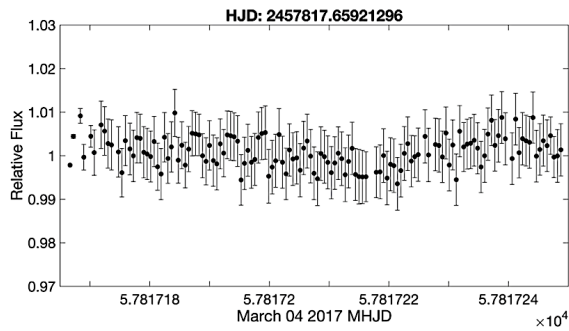
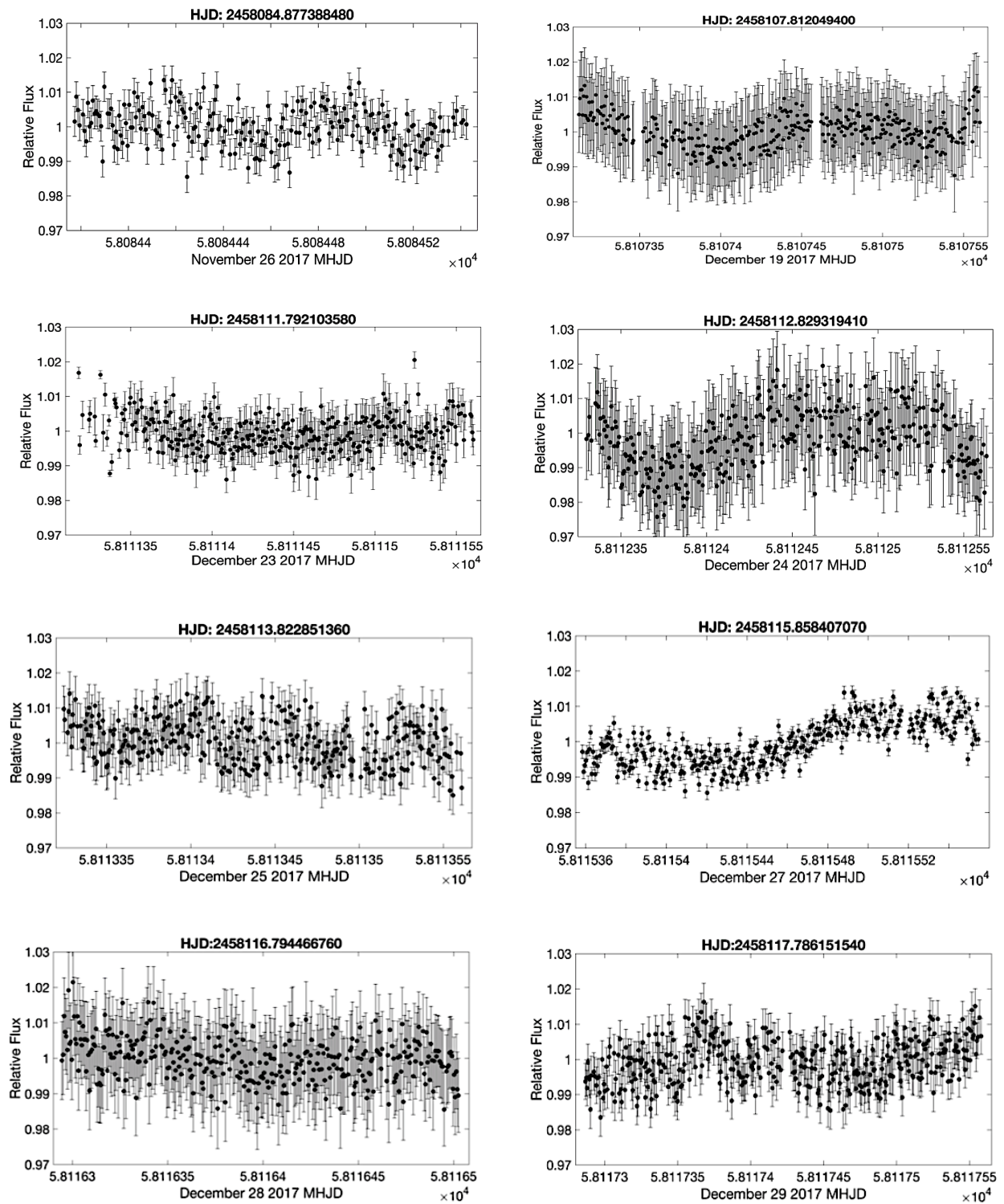


Figure 5.3 continued from previous page



Caption of Figure 5.3 continued from previous page

Figure 5.3 2M J0746+20A: The same lightcurves as Figure 5.2, after running Light Curve Fitter to subtract out the secondary component. Each figure shows relative flux vs. Modified Heliocentric Julian Date (MHJD) time. Note the difference in scale on the y-axis for the 24th November 2017 plot, due to the lightcurve exhibiting a larger amplitude variation of 1.54%. Photometric error bars for 2M J0746+20AB are applied here as listed in Table 5.5.

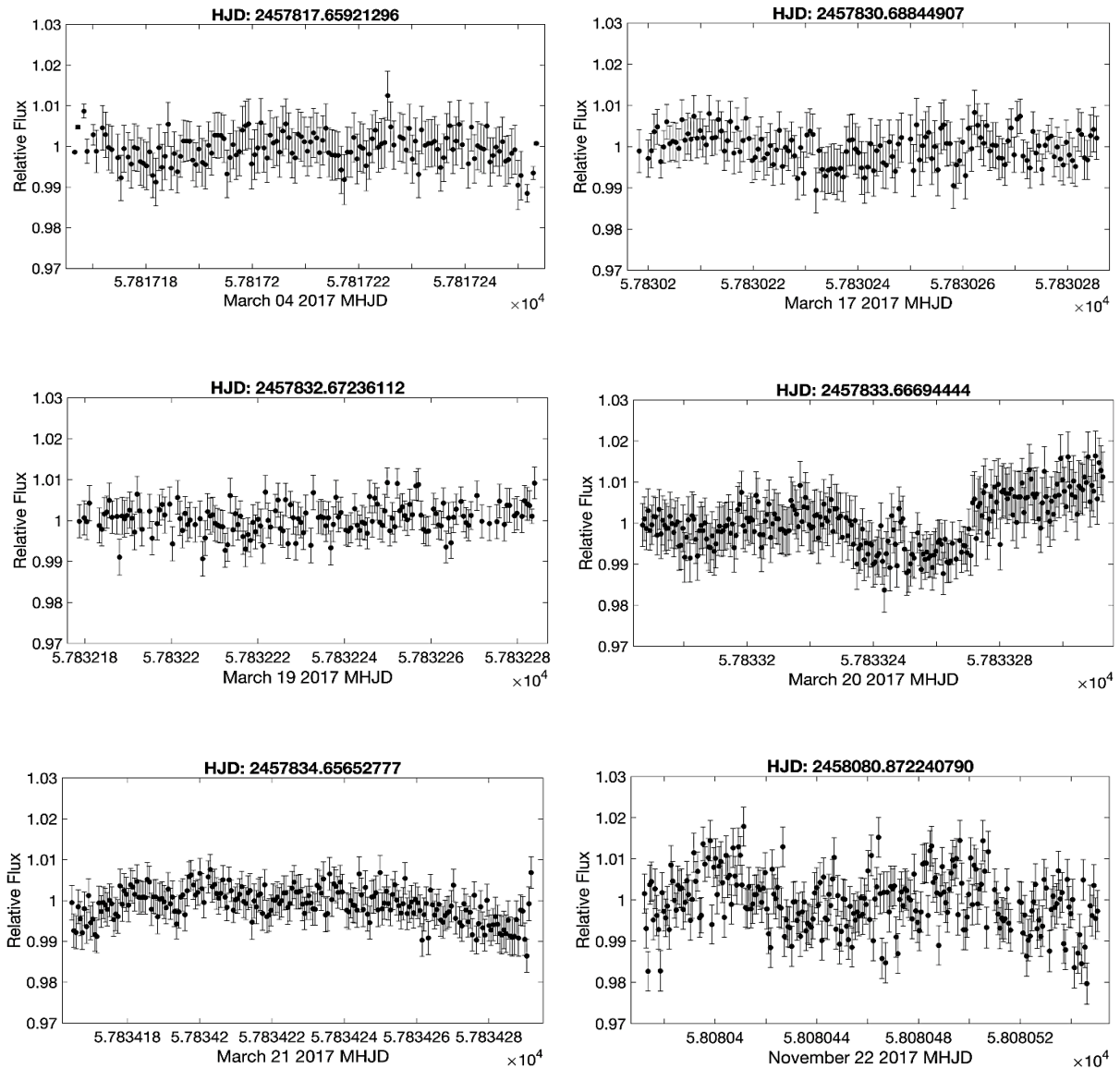


Figure 5.4 continued from previous page

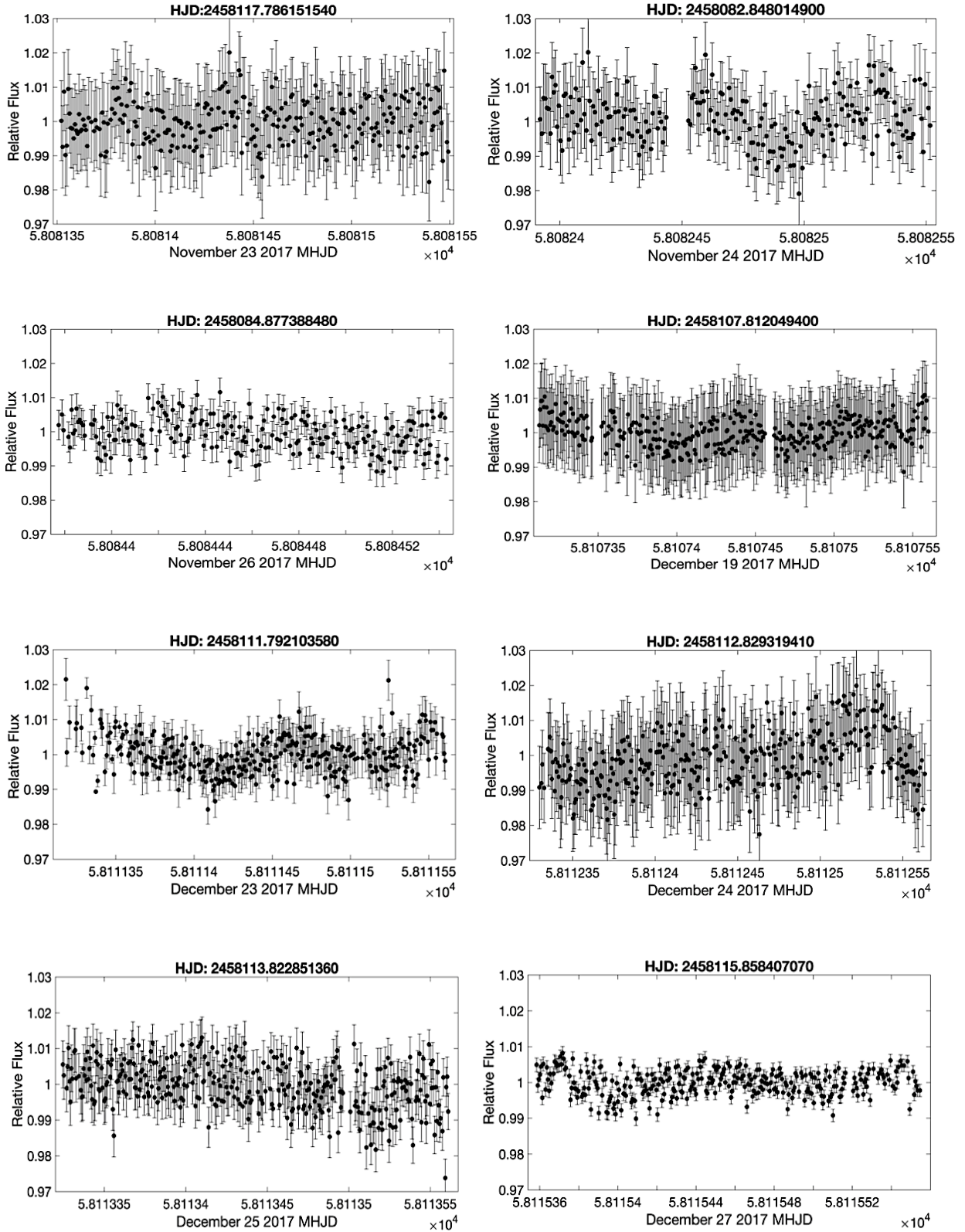


Figure 5.4 continued from previous page

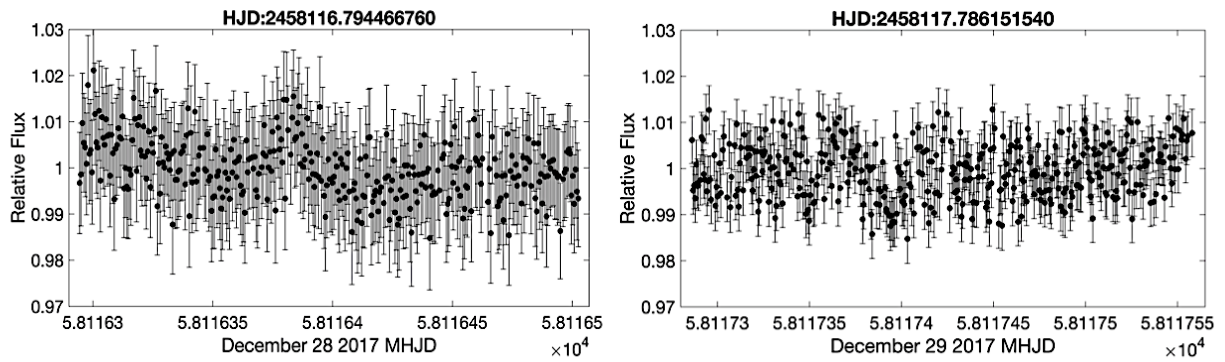


Figure 5.4 2M J0746+20B: The same lightcurves as Figure 5.2, after running Light Curve Fitter to subtract out the 3.32 hrs rotational period of the primary component. Each figure shows relative flux vs. Modified Heliocentric Julian Date (MHJD) time. Photometric error bars for 2M J0746+20AB are applied here as listed in Table 5.5.

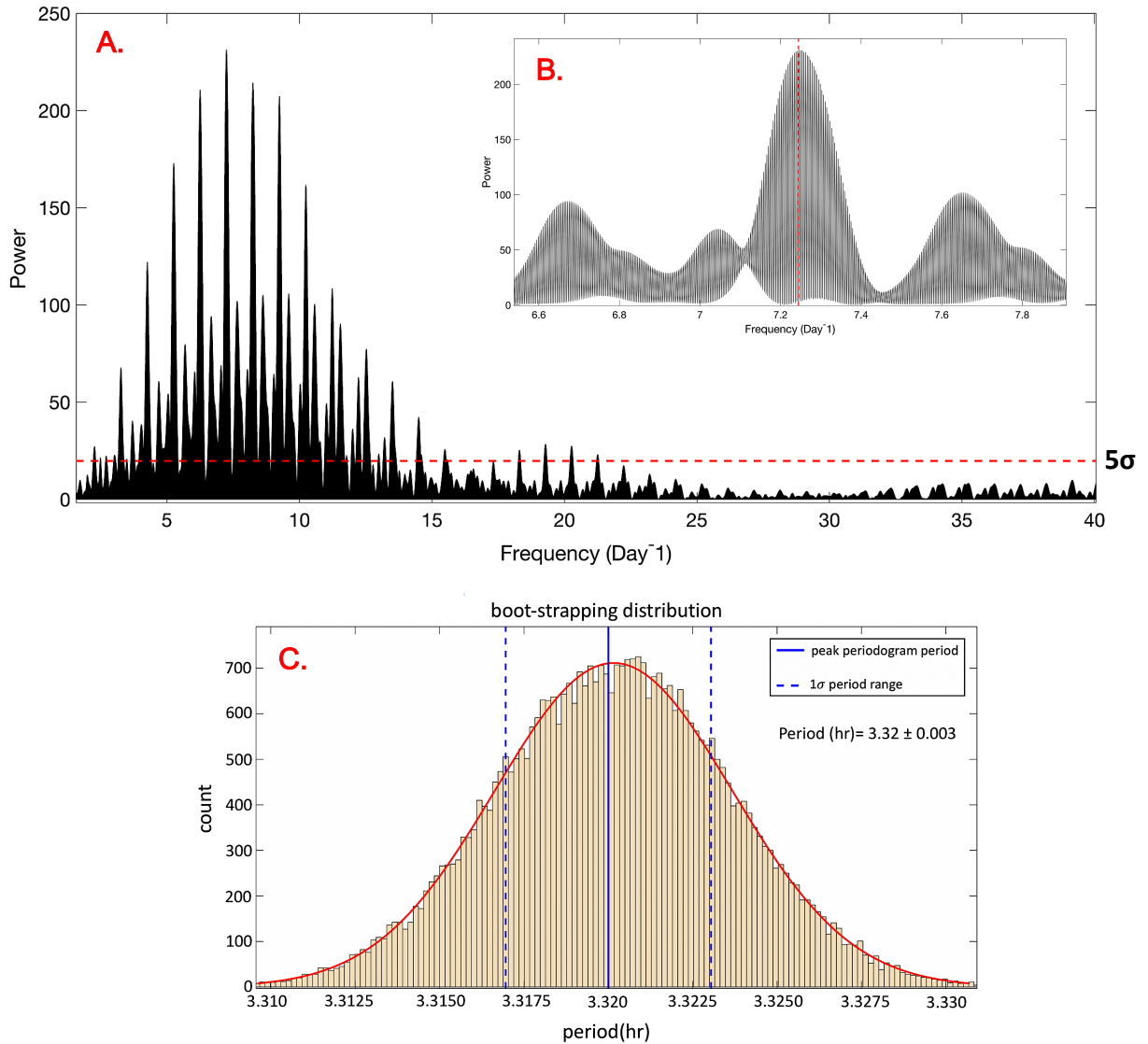


Figure 5.5 **A.** Lomb-Scargle (LS) periodogram of all three epochs of the I-band GUF1 photometric data of 2M J0746+20A, after subtraction of the putative ~ 2.14 hrs rotational period of the secondary component. The x-axis is plotted in Days^{-1} , since each epoch was time-stamped in units of Modified Heliocentric Julian Date (MHJD). The red dashed and dotted horizontal lines represent a 5σ false-alarm probability of the peaks, as defined by the LS periodogram algorithm. The mean peak-to-peak amplitude variability of 2M J0746+20A varied between 0.0014 to 0.0154 mag on different nights. **B.** The same LS periodogram, zoomed into the area around the highest peak. The vertical red dashed line corresponds to 3.32 ± 0.08 hrs, the detected optical period from our work. **C.** Distribution of retrieved highest power periods from boot-strapping, gives an uncertainty of 0.003 hr.

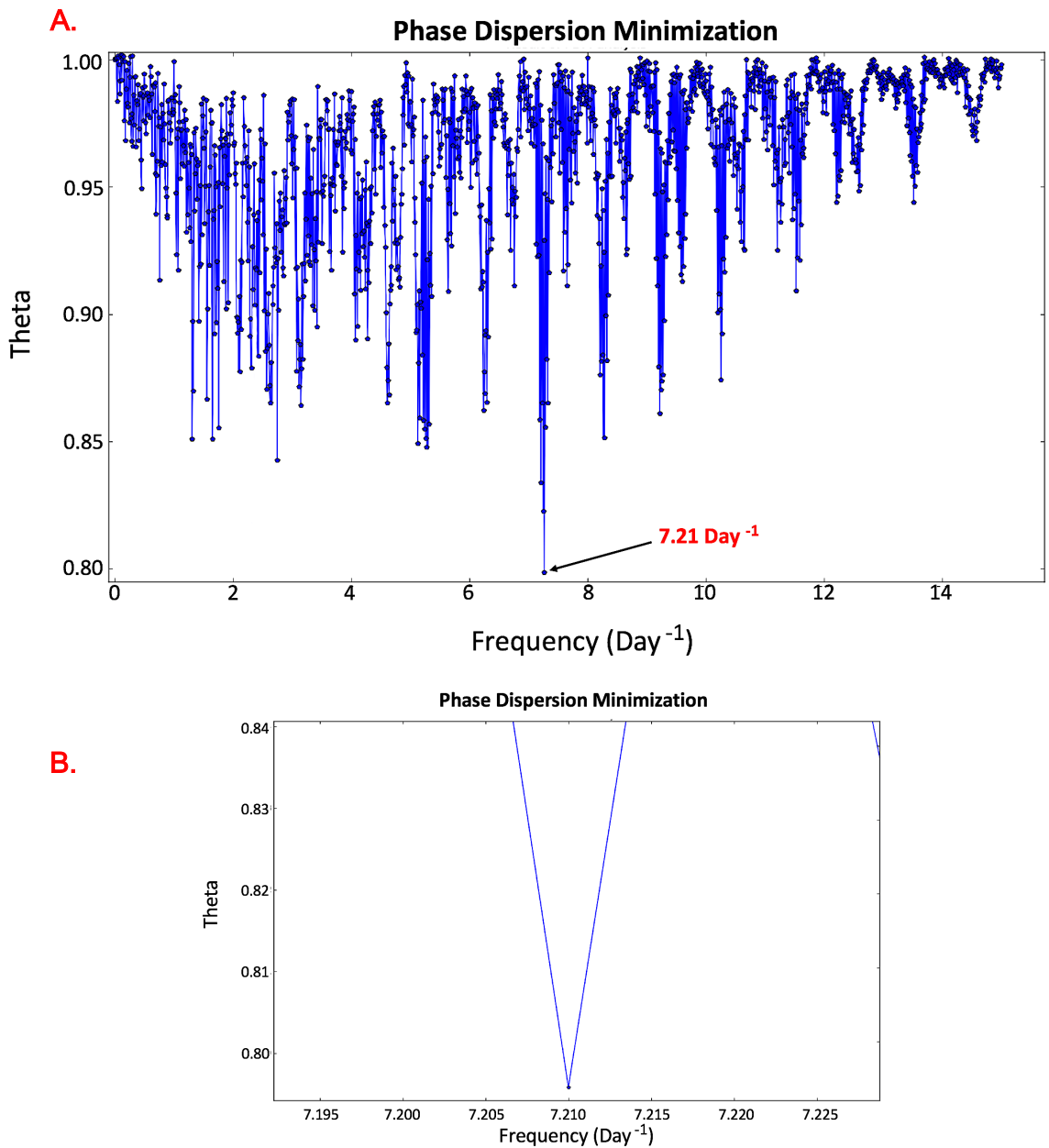


Figure 5.6 **A.** Phase dispersion minimization (PDM) plot of all epochs of 2M J0746+20A, showing a plot of theta statistic against frequency (Day^{-1}). This statistic was determined based on 10^5 Monte Carlo simulations which relies on repeated random sampling to obtain numerical results and test whether the result at any given theta level is caused by noise. The deepest minimum of the quantity theta marks the most likely rotational period of ~ 3.32 hrs. **B.** The same PDM theta plot, zoomed into the area around the deepest minimum theta statistic that corresponds to the primary's period of rotation established in this work, which is largely consistent with the rotation period resulting from LS periodogram.

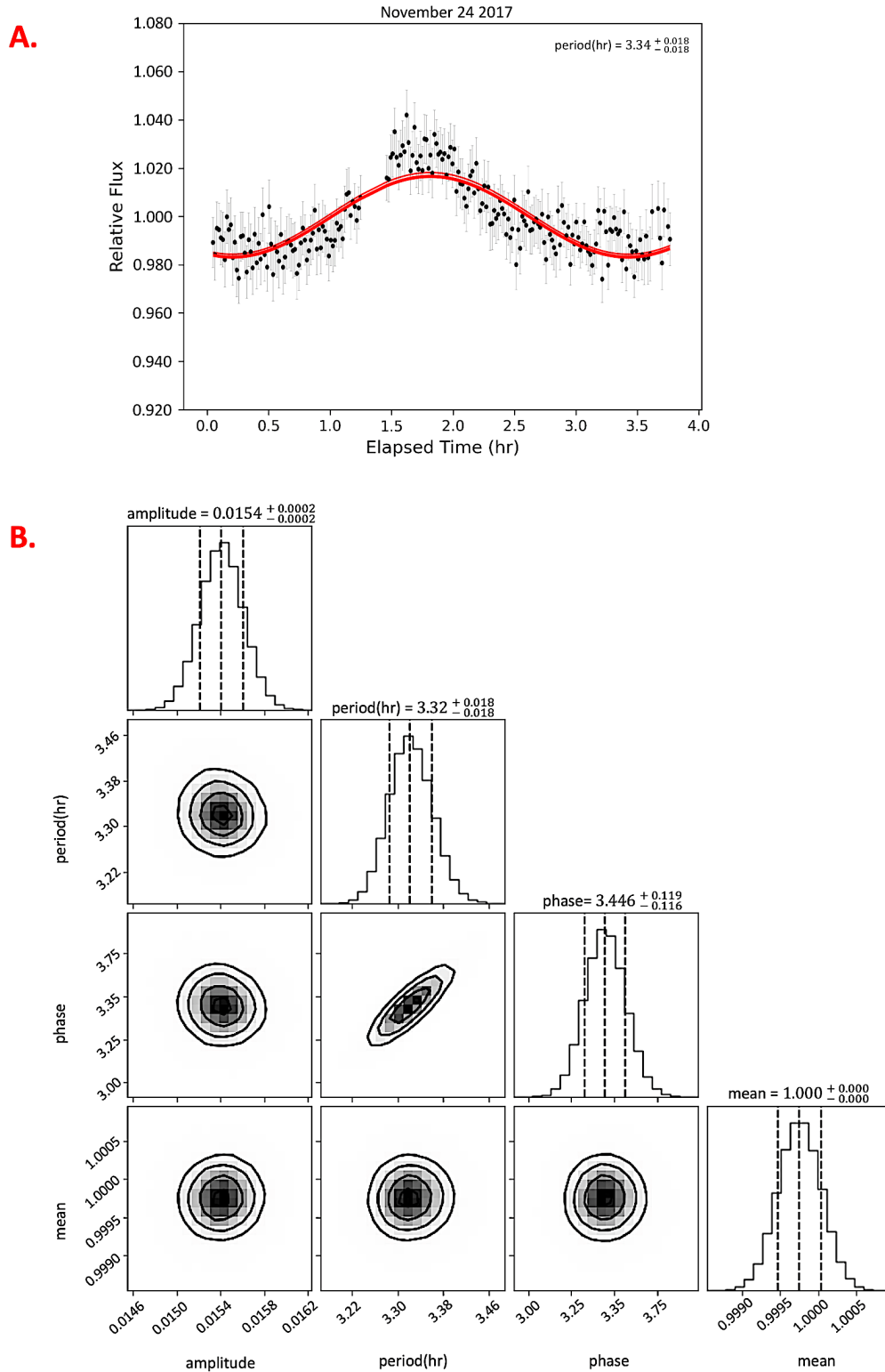


Figure 5.7 **A.** The fitted sinusoidal model (red curve) of 2M J0746+20A on November 24 2017 (O.A.+LuckyPhot). **B.** Posterior probability distributions for the model parameters. The MCMC method yields a rotational period of 3.32 ± 0.018 hrs.

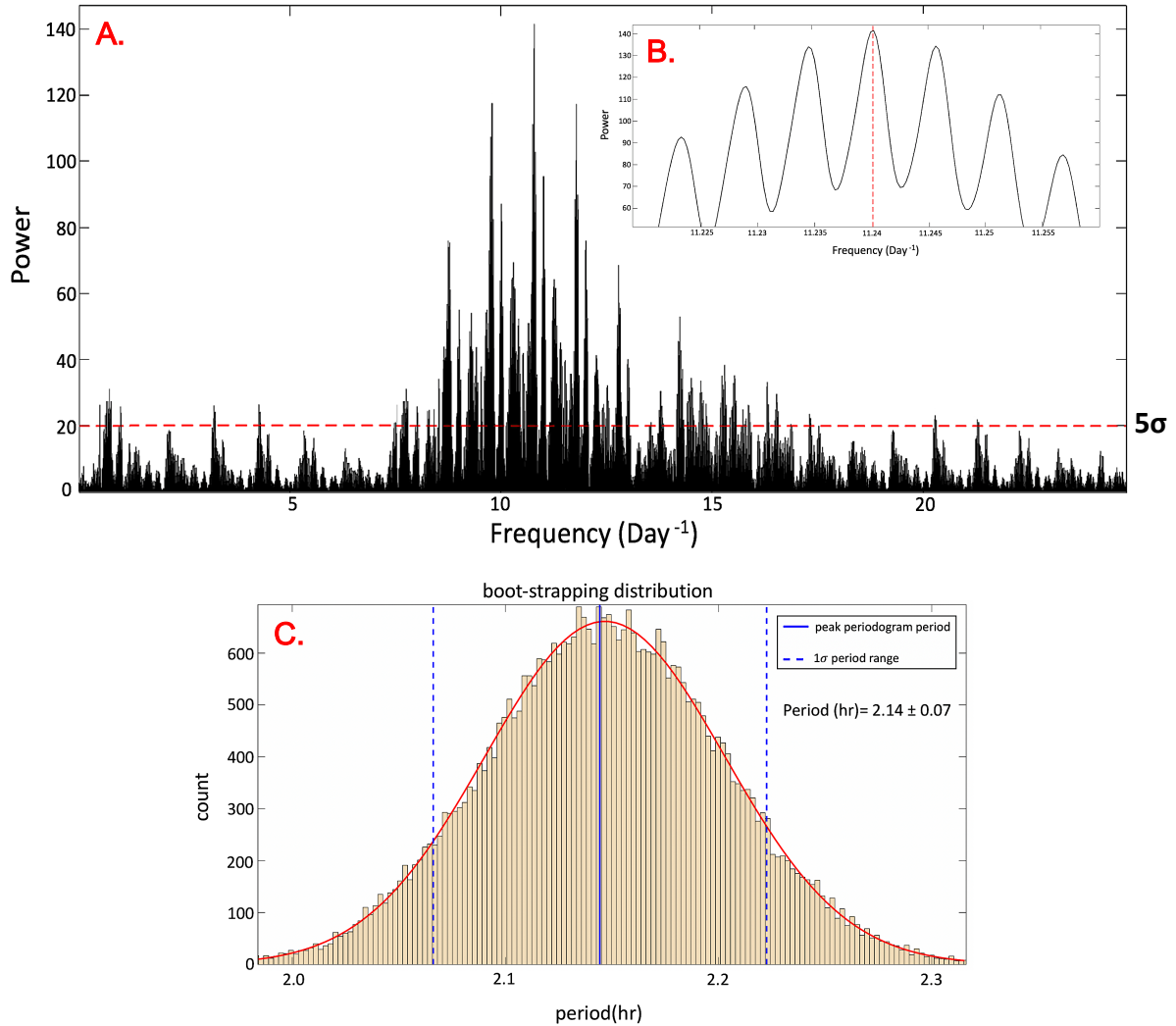
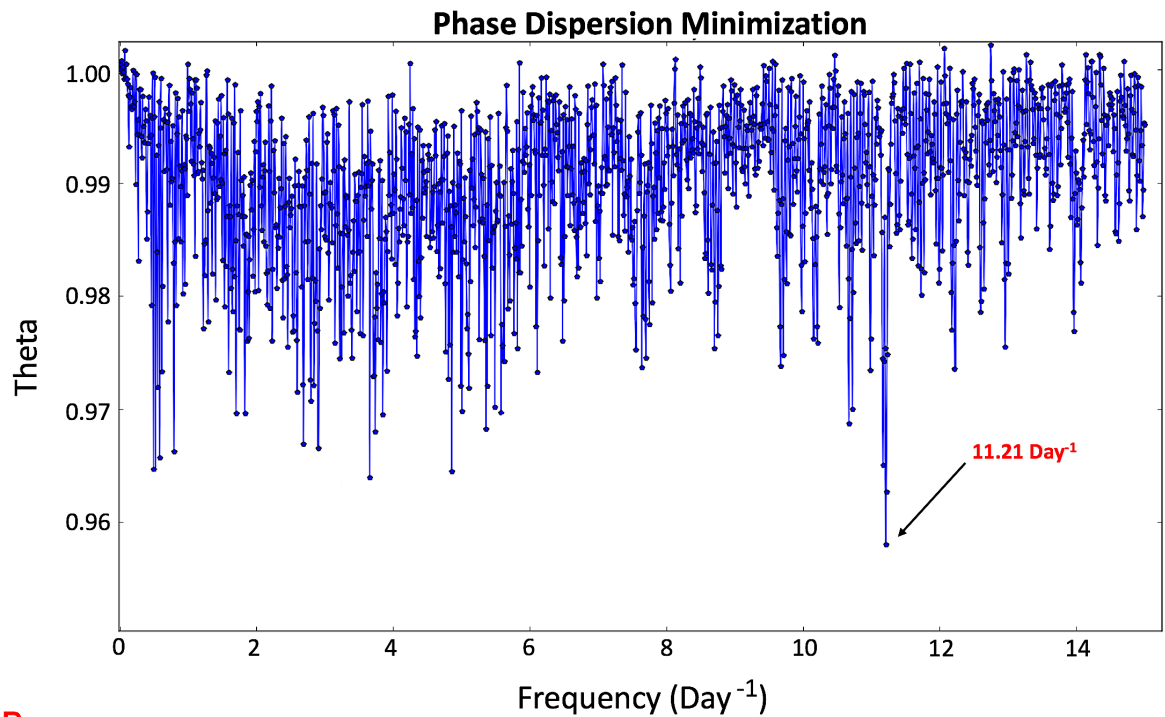


Figure 5.8 **A.** Lomb Scargle (LS) Periodogram of all epochs of 2M J0746+20B (Figure 5.4), after subtraction of the primary 3.32 hrs period: power spectra vs. frequency (Day⁻¹). Dashed, horizontal red lines denote the 5 σ , false alarm probability of the peaks. The period obtained for the combined dataset is ~ 2.14 hrs, a newly discovered optical period. This periodicity lies within the period uncertainty range of Berger et al. (2009b), Lynch et al. (2015) and Zhang et al. (2020) who measured the radio period at 2.072 ± 0.001 hrs, 2.071481 ± 0.000002 hrs and 2.1 ± 0.1 hrs, respectively, as well as being consistent with the 2.07 hrs period of quasi-sinusoidal H α emission (Berger et al., 2009b). **B.** The same LS periodogram, zoomed into the area around the highest peak. The dashed red line corresponds to our detected optical secondary period of 2.14 ± 0.11 hrs. **C.** Distribution of retrieved highest power periods from boot-strapping, shows an uncertainty of 0.07 hrs.

A.



B.

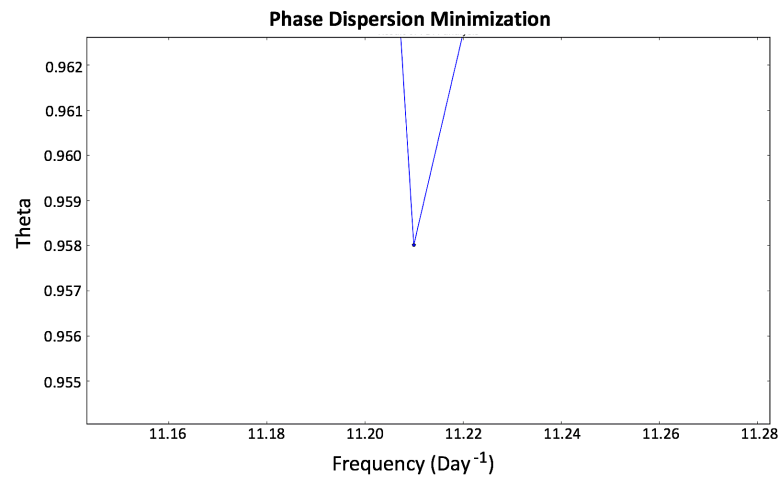


Figure 5.9 **A.** Phase dispersion minimization plot for all three epochs of 2M J0746+20B. The theta statistic was determined from 10^5 Monte-Carlo simulations. The minima theta indicates the most likely rotational period of ~ 2.14 hrs, in agreement with the rotation period resulting from the LS periodogram. **B.** The same PDM theta plot, zoomed into the area around the minimum theta statistic.

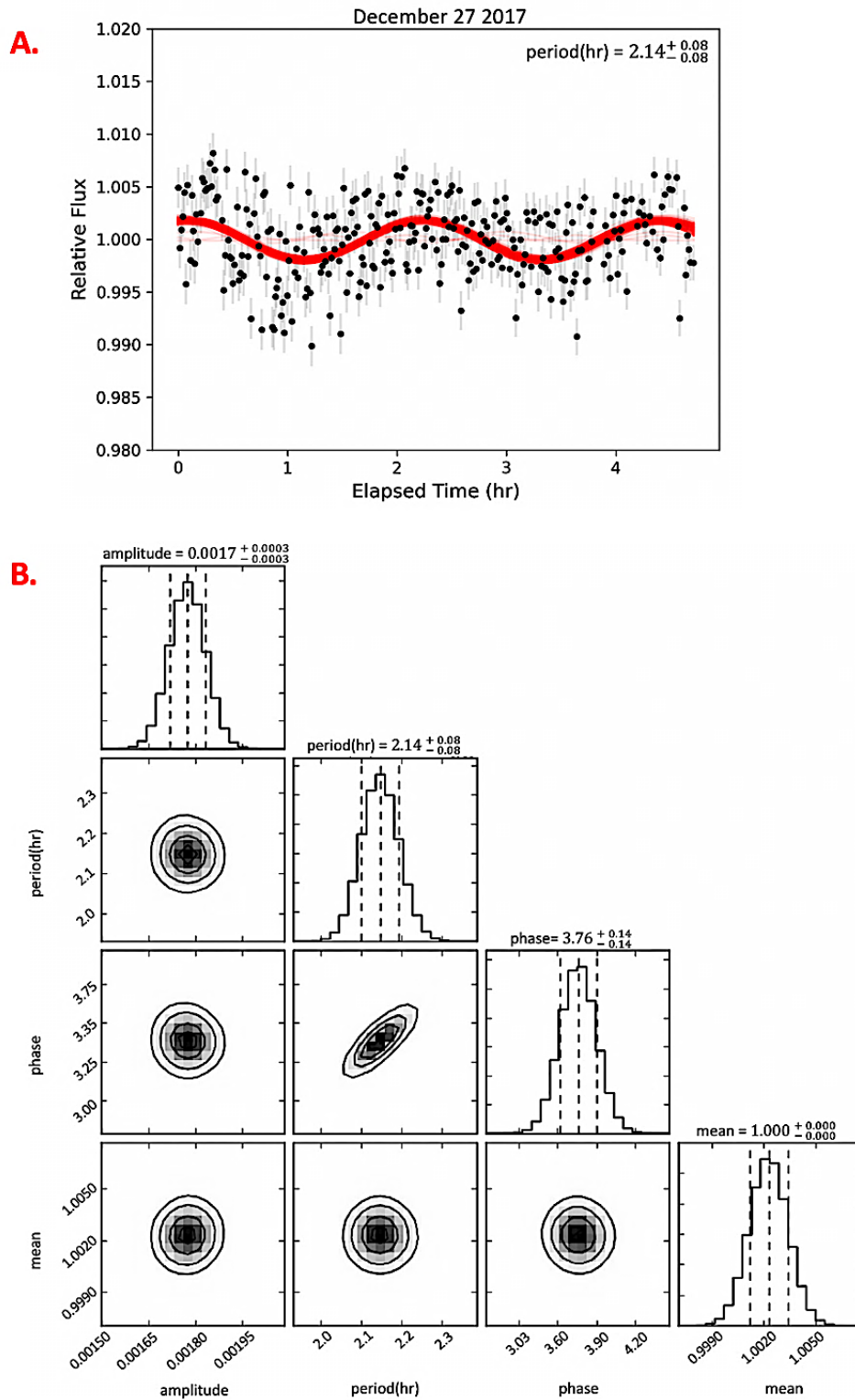


Figure 5.10 **A.** The fitted sinusoidal model (red curve) of 2M J0746+20B on December 27 2017 (O.A.+LuckyPhot). **B.** Posterior probability distributions for the model parameters. The MCMC method gives a period of 2.14 ± 0.08 hrs.

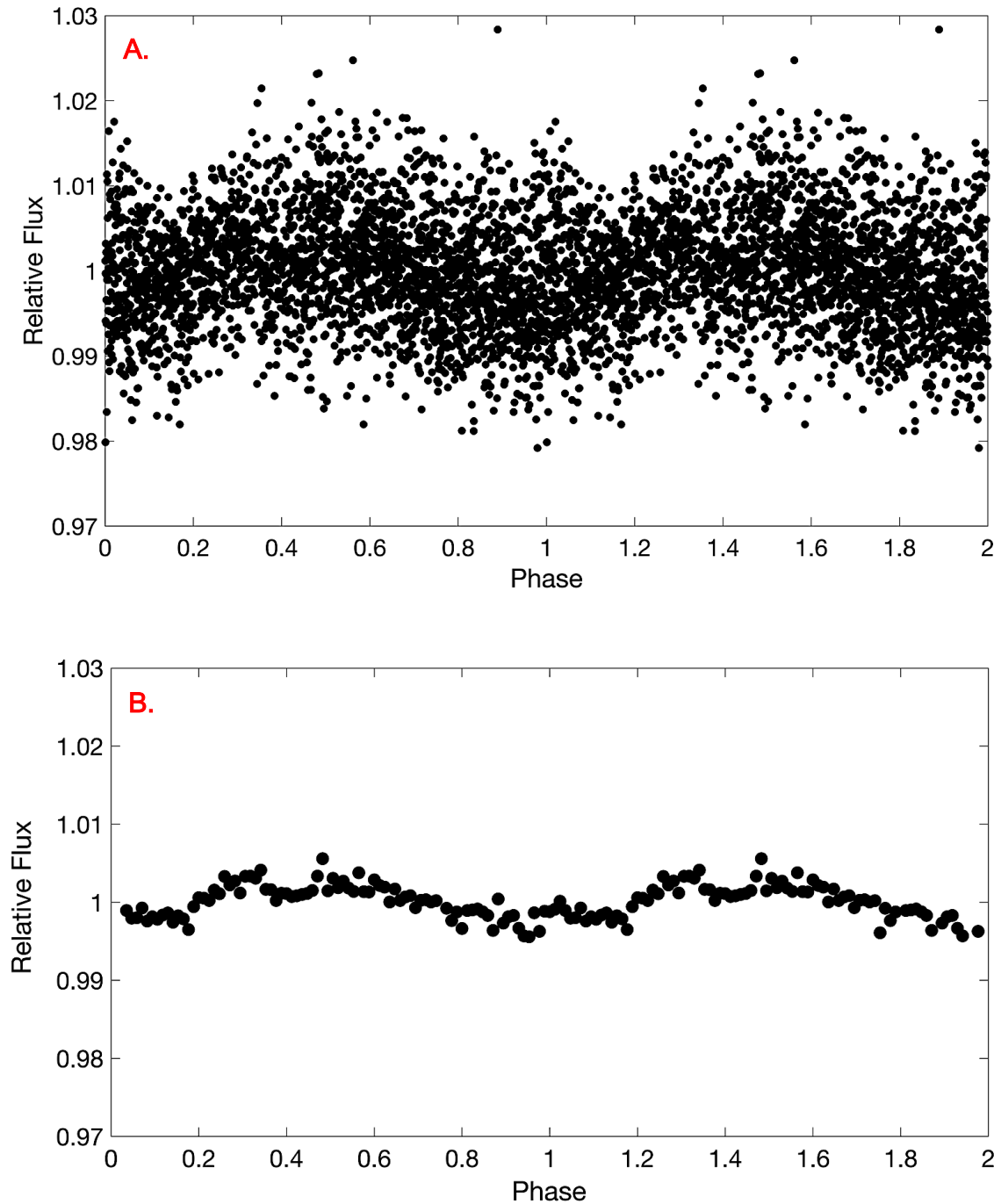


Figure 5.11 **A.** Phase-folded lightcurve of 2M J0746+20A from all three epochs, after subtracting out the secondary period of 2.14 hrs. These unbinned data points are folded to a period of ~ 3.32 hrs. The observed sinusoidal variability to the same reported period from Harding et al. (2013a), shows that this dwarf is stable on timescales of years. **B.** The same data in plot A except binned in phase by factors of 20.

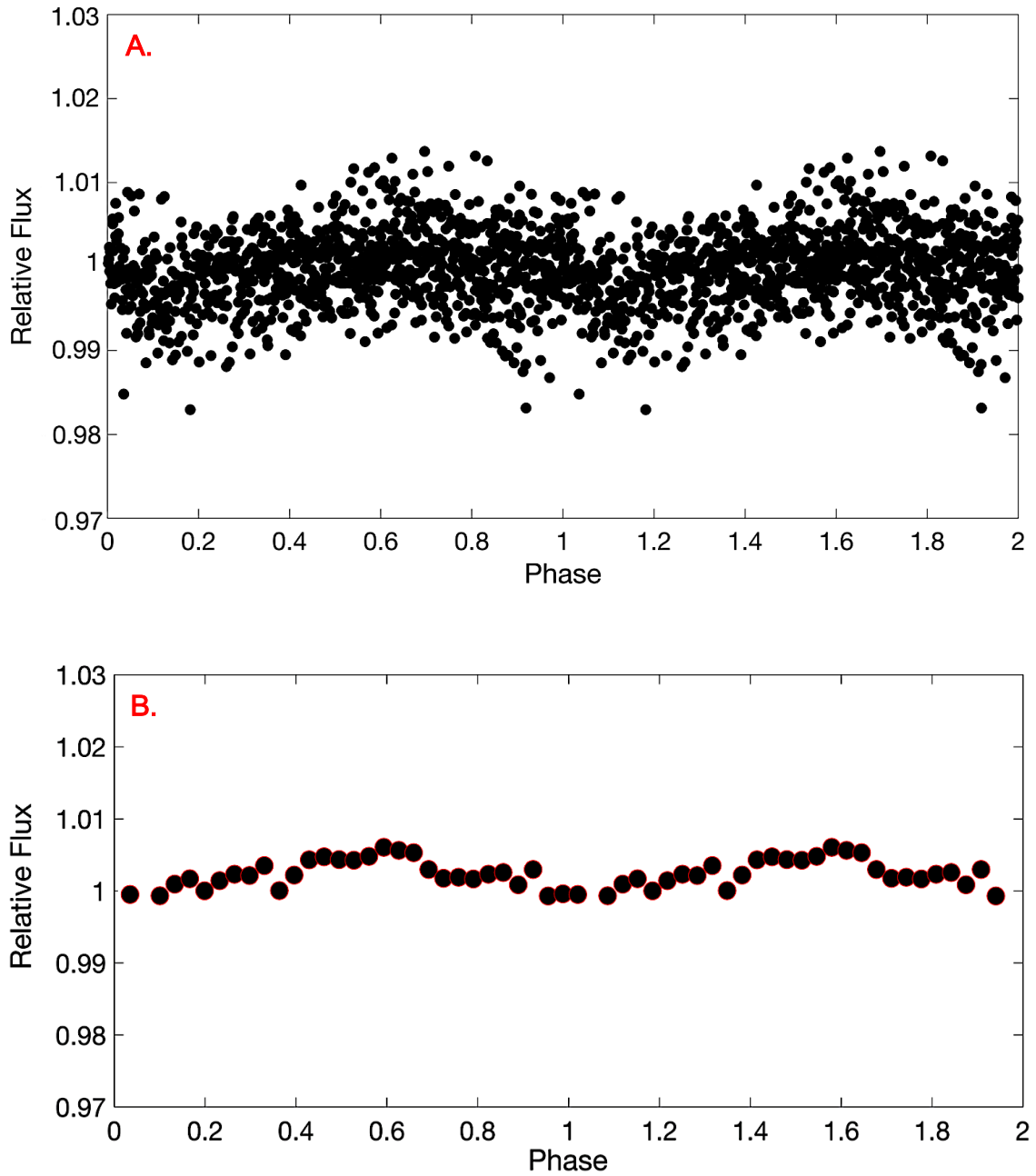


Figure 5.12 **A.** Phase-folded lightcurve of 2M J0746+20B from all epochs combined, after subtracting out the ~ 3.32 hrs periodicity attributed to the rotational period of the primary component. These unbinned data are folded to our newly discovered rotation period in the optical of ~ 2.14 hrs. **B.** The same data in plot A except binned in phase by factors of 10.

As previously discussed, 2M J0746+20AB has 4.86 GHz radio emission with a period of 2.07 hrs (Berger et al., 2009b; Lynch et al., 2015; Zhang et al., 2020). Harding et al. (2013b) previously used our high speed optical photometer GUF1 to observe this system regularly over a 2 year baseline. They analyzed optical periodic lightcurve variations and detected a 3.32 hrs period, which when combined with rotational velocity analysis helped to calculate maximum rotation periods of ~ 4.22 hrs and ~ 2.38 hrs for binary components A and B, respectively (Table 5.6). These data allowed them to assign the rotation period of 3.32 hrs to the primary, implying that the 2.07 hrs periodic radio and H_{α} emissions are from the secondary component (Harding et al., 2013b). This conclusion was confirmed by Zhang et al. (2020), who revealed radio periodicity of ~ 3.2 hrs and ~ 2.1 hrs for A and B components, respectively. In this work, we have demonstrated evidence of the presence of periodic optical emission in both components, by using Light Curve Fitter to decouple the optical behaviour of each component of the binary. However, we noticed that on some nights we only observed periodic I-band modulation of 2M J0746+20A, and some nights only 2M J0746+20B showed modulation, and on some nights both were variable (Figure 5.2, Figure 5.3 & Figure 5.4). These results need to be interpreted with caution. One of the scenarios considered for this behaviour is that the magnetic activity of each binary component may be lower during some nights. This finding corroborates the ideas of Lynch et al. (2015), who suggested that radio over-luminous UCD's like 2M J0746+20AB have a weak field and non-axisymmetric magnetic topologies that lead to a quiescent component and small regions with strong fields giving rise to the pulsed emission.

To assess this further, we combined the raw differential flux of 2M J0746+20AB from all three epochs and re-ran LS (Figure 5.13), and then phase-folded the lightcurve on the dominant period of 3.32 hrs (Figure 5.14). In Figure 5.13, the two sets of peaks that were detected above the noise-floor (exceeding 5σ) confirm the presence of optical variability signatures of both components in our datasets.

Comparing the complex double-peaked shape and relatively high scatter of Figure 5.14 to the cleaner sinusoids of the separated component signals in Figures 5.11 and 5.12 also affirms the double period detection. We also overplotted the best fit model combining two sinusoidal waves on randomly selected nights (17th and 20th March 2017), to visualize the superposition of the two varying sources (Figure 5.15).

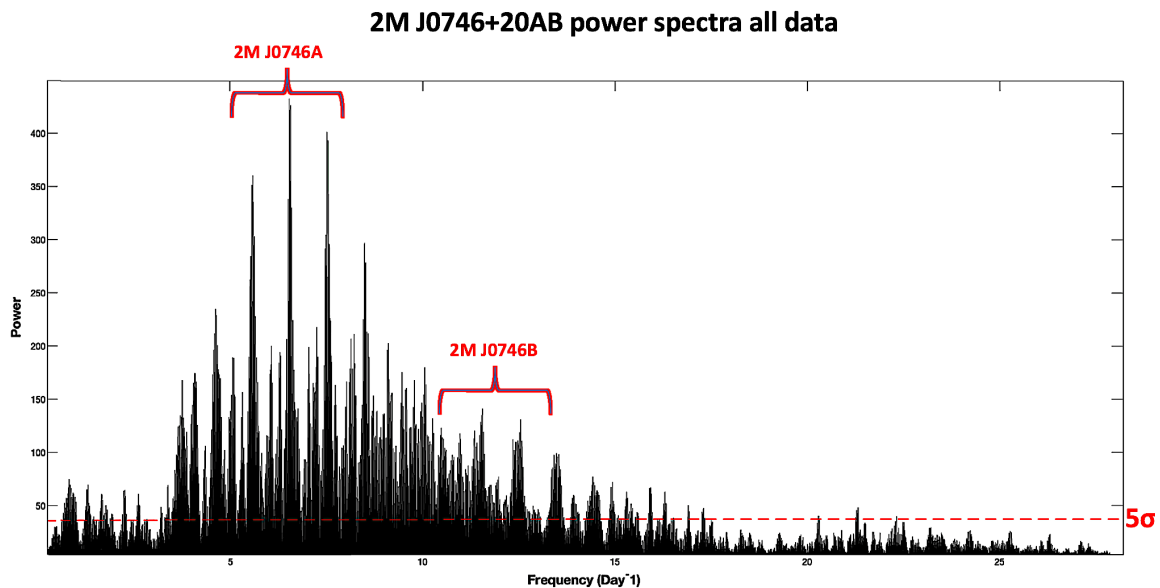


Figure 5.13 Lomb-Scargle (LS) periodogram of all epochs combined of I-band GUF1 photometric data of 2M J0746+20AB. We adopted the LS periodogram analysis which is designed to detect a periodic photometric signal of the target whether it is present in datasets. From the plot we can see that evidence of optical variability of each component of this binary system in our data.

The question posed now is what are the probable causes of optical variability of each component? As we described earlier, we found that the variability parameters of the primary 2M J0746+20A are stable on timescales of years. Dust clouds are less stable over long timescales and there are also magnetic surface features, which offer an alternative mechanism to dust. Berger et al. (2009b) reported variable chromospheric emission and an active magnetosphere. Zhang et al. (2020) found that both binary members are radio emitters. Thus, the

presence of magnetic surface features such as hot or cool spots should be considered for both components.

Property	2M J0746+20A	2M J0746+20B	Reference
Rotation period (hrs) (Optical)	3.32 ± 0.003	2.14 ± 0.07	This work
Maximum rotation period (hrs)	~ 4.23	~ 2.37	This work
Equatorial Inclination ($^{\circ}$)	32 ± 4	37 ± 4	This work
Equatorial Velocity (km s^{-1})	36 ± 4	$55^{+4.5}_{-6}$	This work

Table 5.6 Preview of 2M J0746+20AB results from this work.

We identify a newly discovered optical variability in the secondary component of pulsating ultracool dwarf binary 2M J0746+20AB with a period of 2.14 ± 0.07 hrs. This value lies within the period uncertainty range of Berger et al. (2009b), Lynch et al. (2015) and Zhang et al. (2020) who reported radio periodicity of 2.072 ± 0.001 hrs, 2.071481 ± 0.000002 hrs and 2.1 ± 0.1 hrs, respectively. Berger et al. (2009b) also detected quasi-sinusoidal H_{α} emission modulated with the same period, although not in phase, and confirmed the presence of a ~ 1.7 kG magnetic field, which is consistent with Antonova et al. (2008). The recent observation of this system by a collaboration using the Giant Metre Radio Telescope array at 600 MHz and 1.3 GHz (Zic et al. 2018) - demonstrated the presence of stable radio emission at both bands, with suggestions of a dominant coherent component at 1.3 GHz, although sensitivity and instrumentation constraints limited their ability to definitively assert this as being the case, nor indeed to

discern any pulsed or periodic modulations in the radio data. It is important to state that, whilst low frequency (i.e. 600 MHz) emission is expected to be dominated by incoherent gyrosynchrotron processes, the tentative detection of highly polarized emission at 1.3 GHz is consistent with auroral emission, albeit from a lower magnetic field environment (as the fundamental emission modes from the electron cyclotron maser instability scales as $\nu_c \equiv 2.8 \times 10^6 B$ Hz, where B is in Gauss). All these findings support the idea of a correlation between radio, spectroscopic and photometric wavelengths in both components, and therefore the observed optical variability in 2M J0746+20A and 2M J0746+20B may be attributed to stellar rotation coupled with magnetic spots on the surface, or auroral emission.

Harding et al. (2013b) showed that auroral activity could be the cause of periodic optical variability produced by most radio-detected ultracool dwarfs, similar to Hallinan et al. (2015), who spectroscopically observed LSR J183513259 in radio and optical bands simultaneously, to establish the relationship (or lack thereof) between periodic emissions in a range of wavelength domains. They detected periodic radio, broadband optical and Balmer line emission from LSR J183513259, and argued that this variability was due to an auroral hot spot.

Further radio/ H_α observations of 2M J0746+20AB are required for a multiple of the A component's 3.32 hrs rotation period; **1)** to confirm the presence of quiescent and periodic modulations in H_α emission from the system, coincident with the radio data, **2)** to test the hypothesis that the auroral emission from this binary system is not unique to the 2.07 hrs B component, by assessing whether auroral activity is present on the slower component; and furthermore **3)** to test whether such auroral emission from these L dwarfs is less stable than that observed from spectral class M brown dwarfs.

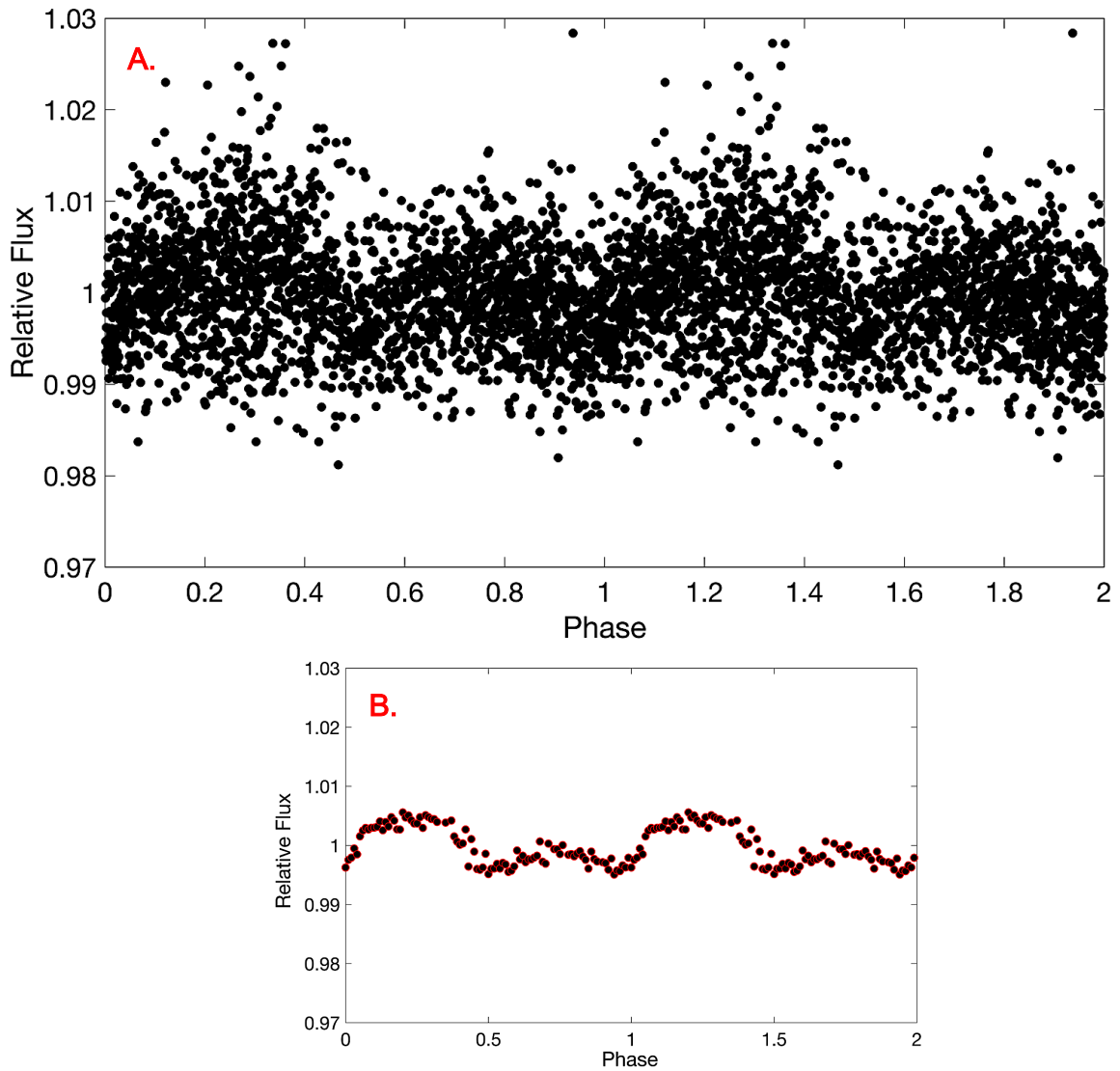


Figure 5. 14 **A.** Phase-folded lightcurves of 2M J0746+20AB from all epochs combined. Both component's variability signals are present here. In Figure 5.11 & 5.12 we can see the effect of isolating each signal and phase-folding the data to their respective periods after using Light Curve Fitter. **B.** The same data in plot A, except binned in phase by factors of 20.

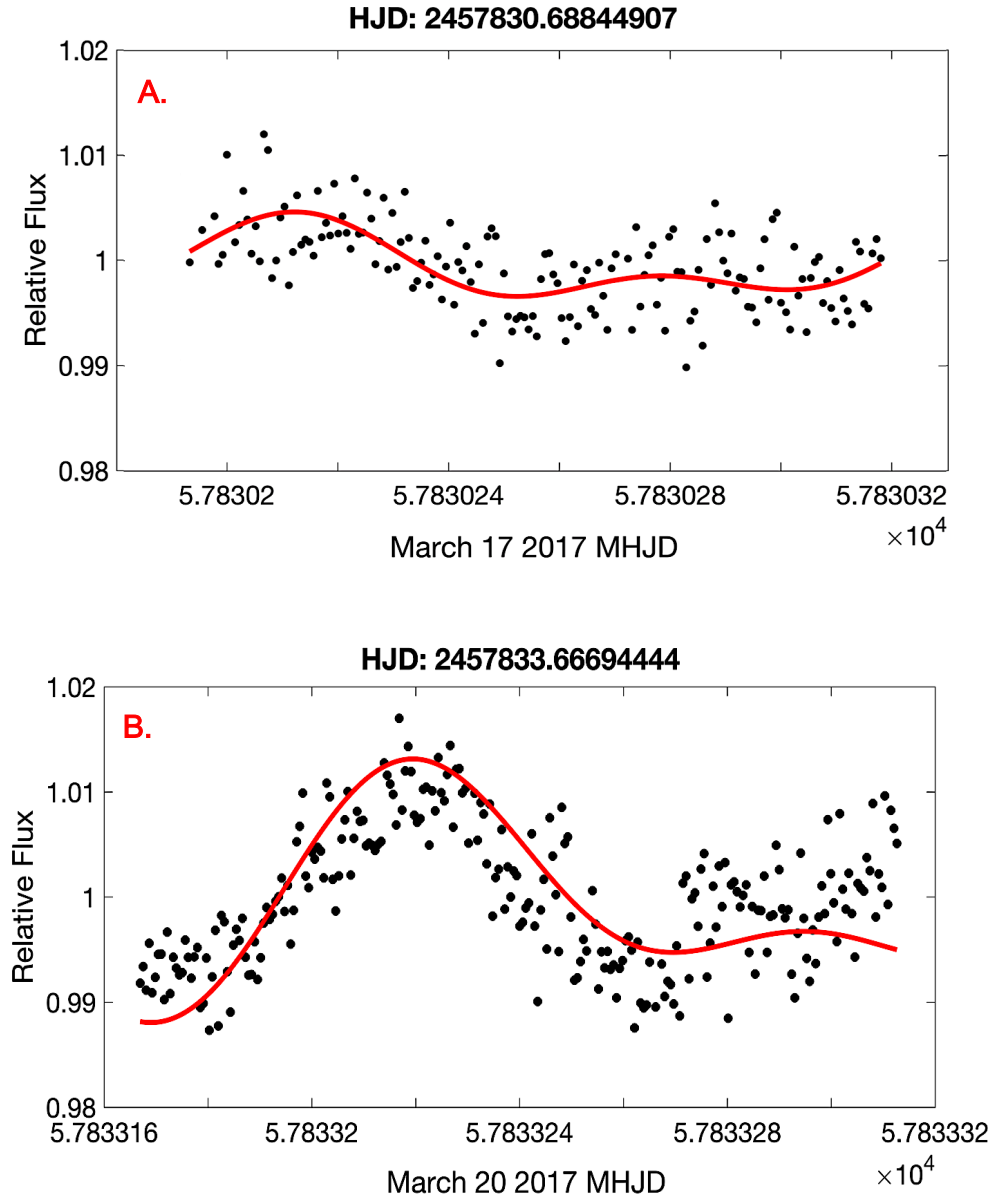


Figure 5.15 **A** and **B** - Lightcurves of 2M J0746+20AB from two nights (17th and 20th March), selected randomly from the 2017 March epoch. We overplotted the fitted model (red) consisting of superimposed sinusoids with periods of 3.32 hrs and 2.14 hrs detected from the primary and secondary component, respectively. What is evident in these plots is the presence of both binary components, varying with different rotation periods.

5.4.2 2M J1314+13AB

In this chapter, we performed GUF1 photometry with a fixed aperture on 2M J1314+13AB, and we also applied the “LuckyPhot” technique (Collins, 2014) to this data. Since after 2M J0036 (Section 4.4.2), another test case was needed to assess whether LuckyPhot delivered benefits to high precision photometry. Since we found that the use of LuckyPhot had obvious benefits to high precision photometry of the single dwarf 2M J0036. Due to a separation of ~ 1.6 AU between the two binary components, their angular separation of $\sim 0''.130$ is not resolvable with a conventional ground-based telescope (Figure 5.1), and no optical variability of the primary component had yet been detected. Therefore, we used Light Curve Fitter to search for optical variability in the primary component, and to determine whether the variability of the secondary component was stable over timescales of years.

Once the I-band lightcurves were obtained for 2M J1314+13AB using the two photometric systems (F.A. without using LuckyPhot and O.A. with LuckyPhot), the next step was to untangle the optical behavior of each binary component, by running Light Curve Fitter on these lightcurves (Figure 5.16 & Figure 5.17). First, we subtracted out the putative rotational period of 3.79 hrs for the secondary component. Our LS analysis detected a period of 2.06 ± 0.05 hrs and 2.05 ± 0.04 hrs for a fixed No LuckyPhot (GUF1 photometry) and Optimum Aperture LuckyPhot techniques, respectively (Figure 5.20A, Figure 5.20B & Table 5.10). We used bootstrapping distribution for O.A.+ LuckyPhot technique, indicates an uncertainty of 0.006 hours (as shown in Figures 5.20C). This is a newly discovered optical period (2.05 ± 0.006 hrs) of the primary component (as was also the case with 2M J0746+20B). On different nights, the peak-to-peak sinusoidal amplitude of 2M J1314+13A varied between 0.0011 - 0.0086 mag in the standard GUF1 photometry, and between 0.00122 - 0.0092 mag with Optimum Aperture with LuckyPhot (Table 5.7, Figure 5.18). The above process was repeated again after subtracting out the discovered primary period. We detected

periods of 3.79 ± 0.05 hrs and 3.78 ± 0.04 hrs from 2M J1314+13B (Figure 5.20D, Figure 5.20E & Table 5.10), with peak-to-peak sinusoidal variability on different nights varying between 0.0022 - 0.0154 mag and 0.0019 - 0.0152 mag, for standard GUF1 photometry and Optimum Aperture + LuckyPhot techniques, respectively (Table 5.8, Figure 5.19). With the bootstrapping distribution, we find an uncertainty of 0.008 hrs for O.A.+ LuckyPhot technique (as shown in Figures 5.20F).

Date of Obs. (UT) (1)	Amplitude Variability _{Target} F.A.+No LuckyPhot (mag) (2)	Amplitude Variability _{Target} O.A.+LuckyPhot (mag) (3)
24 Feb 2017	0.0029 ± 0.0004	0.0034 ± 0.0004
28 Feb 2017	0.0086 ± 0.0005	0.0092 ± 0.0003
01 March 2017	0.00152 ± 0.0003	0.00122 ± 0.0003
03 March 2017	0.0034 ± 0.0003	0.0037 ± 0.0002
04 May 2018	0.00124 ± 0.0003	0.00127 ± 0.0003
05 May 2018	0.0030 ± 0.0003	0.0028 ± 0.0003
07 May 2018	0.0033 ± 0.0003	0.0031 ± 0.0002
08 May 2018	0.0031 ± 0.0003	0.0029 ± 0.0003
09 May 2018	0.0011 ± 0.0003	0.00124 ± 0.0002
11 May 2018	0.0034 ± 0.0008	0.0045 ± 0.0005

Table 5.7 Amplitude variability of 2M J1314+13A using F.A. + No LuckyPhot & O.A. + LuckyPhot. **Column 1:** Date of observation in UT. **Column 2 & Column 3:** Peak-to-peak amplitude variability using F.A. + No LuckyPhot (GUF1 photometry) & O.A. + LuckyPhot with associated errors as measured by the Chi-squared test.

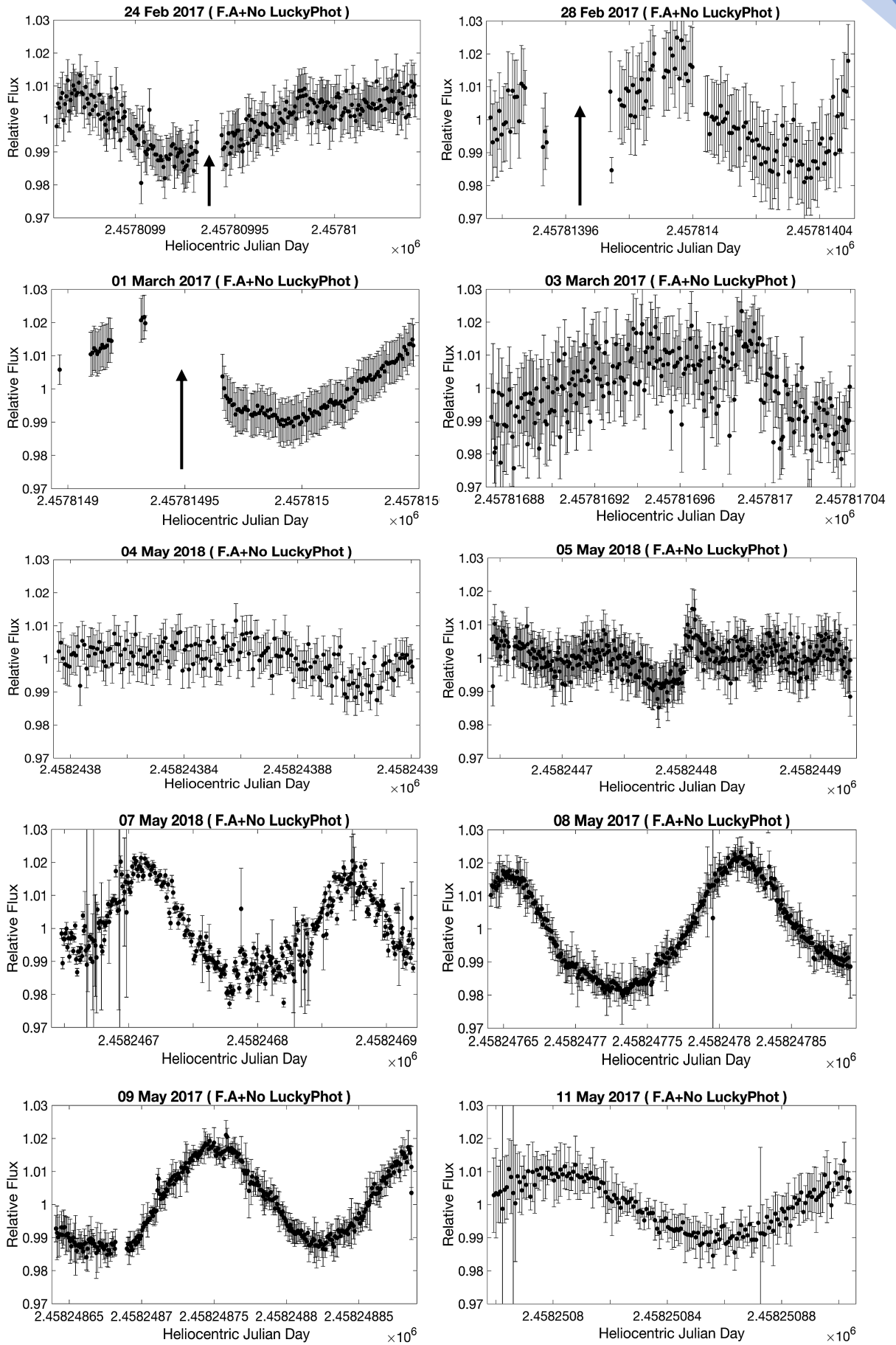
Our F.A. and O.A./LuckyPhot periods (Figure 5.20 & Figure 5.21) are marginally compatible with the 3.89 ± 0.05 hrs radio pulses period reported by McLean et al. (2011). However, both our periods are compatible with the 3.785 ± 0.002 hrs optical period also reported by McLean et al. (2011), and with the 3.7859 ± 0.0001 hrs and 3.7130 ± 0.0002 hrs periods reported by Williams et al. (2015), which are by some distance the most accurate periods to date reported for this component of the binary.

The rotation period of 2M J1314+13B reported in this study is a clear indication that the photometric I-band periodic variability appears to be stable over timescales of up to 8 years in this case.

Date of Obs.	Amplitude Variability _{Target}	Amplitude Variability _{Target}
(UT)	F.A.+No LuckyPhot	O.A.+LuckyPhot
(1)	(2)	(3)
24 Feb 2017	0.0083 ± 0.0005	0.0079 ± 0.0004
28 Feb 2017	0.0042 ± 0.0003	0.0041 ± 0.0002
01 March 2017	0.0113 ± 0.0004	0.0117 ± 0.0003
03 March 2017	0.0107 ± 0.0003	0.0105 ± 0.0003
04 May 2018	0.0027 ± 0.0006	0.0019 ± 0.0004
05 May 2018	0.0022 ± 0.0003	0.0020 ± 0.0002
07 May 2018	0.0127 ± 0.0003	0.0129 ± 0.0003
08 May 2018	0.0154 ± 0.0004	0.0149 ± 0.0002
09 May 2018	0.0150 ± 0.0003	0.0152 ± 0.0003
11 May 2018	0.0031 ± 0.0003	0.0034 ± 0.0002

Table 5.8 Amplitude variability of 2M J1314+13B. **Column 1:** Date of observation in UT. **Column 2 & Column 3:** Peak-to-peak amplitude variability using F.A. + No LuckyPhot (GUFI photometry) & O.A. + LuckyPhot, with associated errors as measured by the Chi-squared test.

For another evaluation of A and B component periods, we chose randomly February 24th 2017 and run the MCMC method, which yielded periods of 2.05 ± 0.009 hrs and 3.78 ± 0.009 hrs for A and B members (O.A.+ LuckyPhot), respectively (Figure 5.22).



Caption of Figure 5.16 continued from previous page

Figure 5.16 The I-band lightcurves of 2M J1314+13AB using a Fixed Aperture (F.A.) without LuckyPhot. Photometric error bars were applied to each data point as listed in Table 5.8. Both A and B components contribute to the variability seen here. The arrows marked on the 24th and 28th Feb 2017 and 01 March 2017 lightcurves indicate an interval of complete cloud cover; therefore these data were removed.

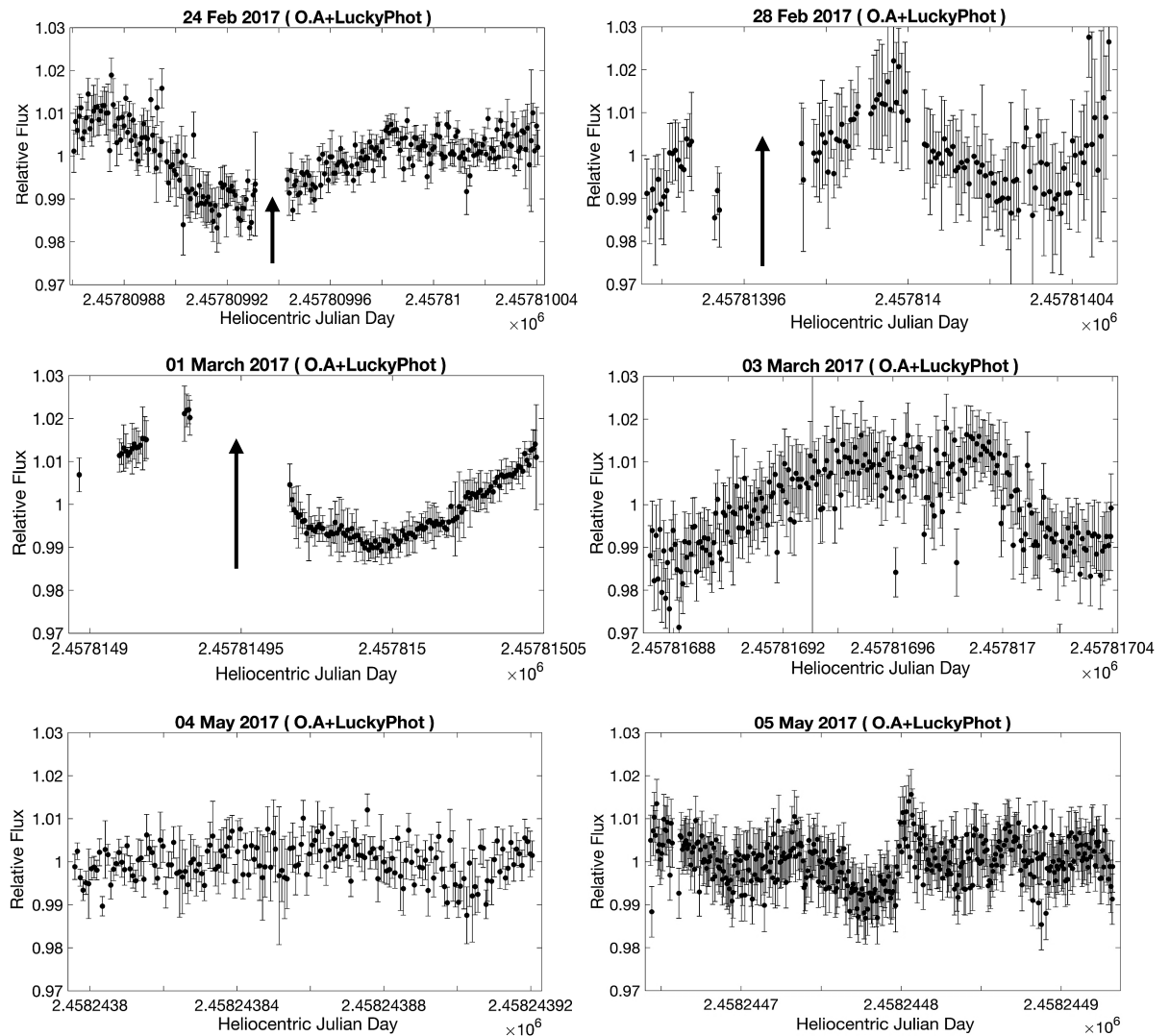


Figure 5.17 continued from previous page

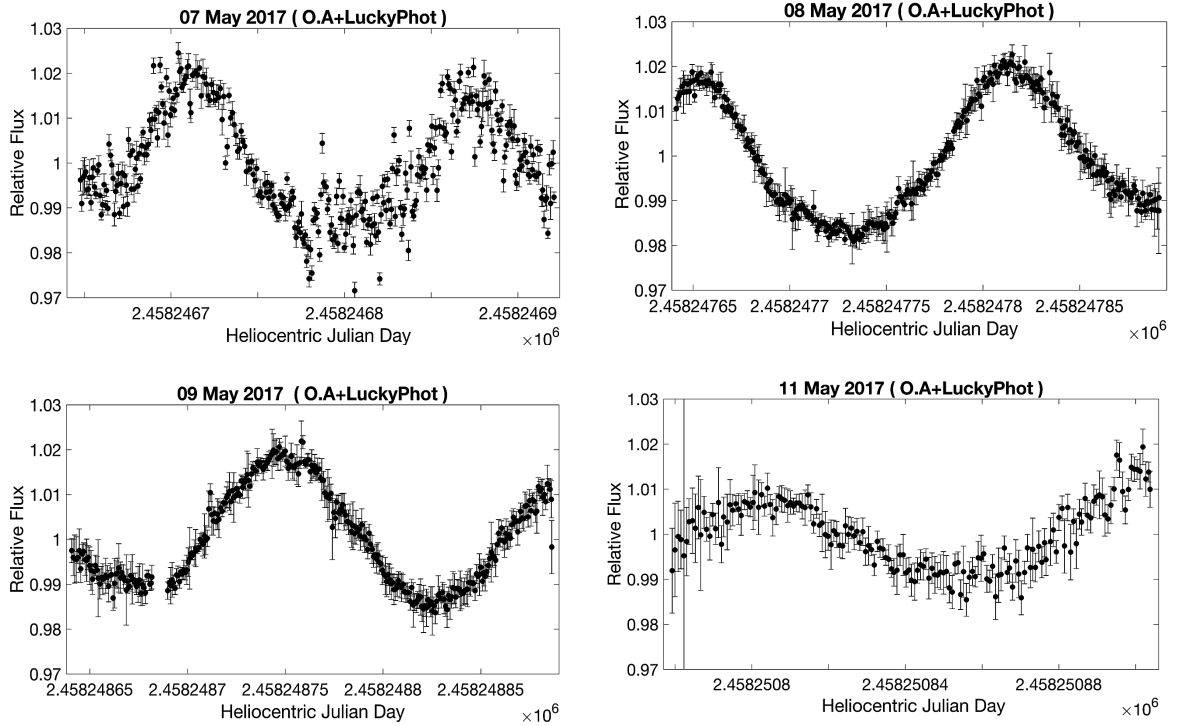
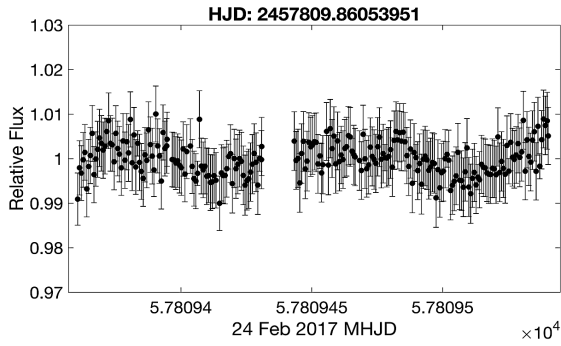


Figure 5.17 The same data of 2M J1314+13AB as Figure 5.16, after applying O.A. with LuckyPhot. Each figure shows relative flux vs. Heliocentric Julian Date. Photometric error bars were applied to each data point as listed in Table 5.8. The arrows marked on the 24th and 28th Feb 2017 and 01 March 2017 lightcurves indicate that this data has been removed due to an interval of complete cloud cover.

Date of Obs. (UT) (1)	Band (2)	Photometric Error F.A.+No LuckyPhot (mag) (3)	Photometric Error O.A.+LuckyPhot (mag) (4)
24 Feb 2017	/	0.0062	0.0037
28 Feb 2017	/	0.011	0.0094
01 March 2017	/	0.0063	0.0034
03 March 2017	/	0.0209	0.0104
04 May 2018	/	0.0054	0.0045
05 May 2018	/	0.0068	0.0056
07 May 2018	/	0.0029	0.0019
08 May 2018	/	0.0038	0.0024
09 May 2018	/	0.0034	0.0027
11 May 2018	/	0.0064	0.0039

Table 5.9 Photometric error analysis of 2M J1314+13AB. **Column 1:** Date of observation in UT. **Column 2:** Waveband used. **Column 3 & Column 4:** Mean photometric error for lightcurve data points per night using F.A. + No LuckyPhot (GUFI photometry) & O.A. + LuckyPhot, as estimated by

F.A. + No LuckyPhot



O.A. + LuckyPhot

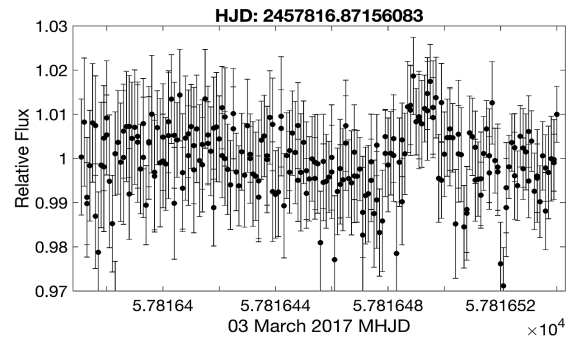
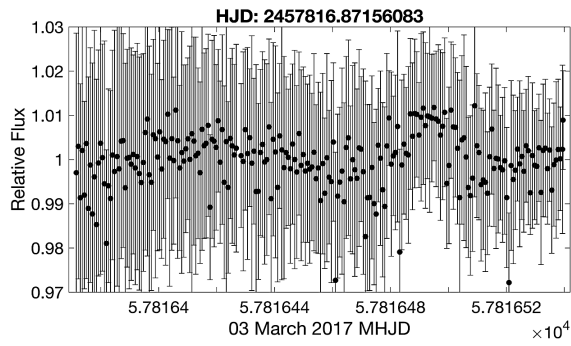
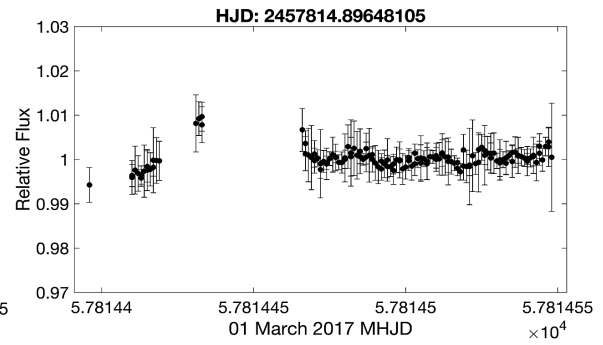
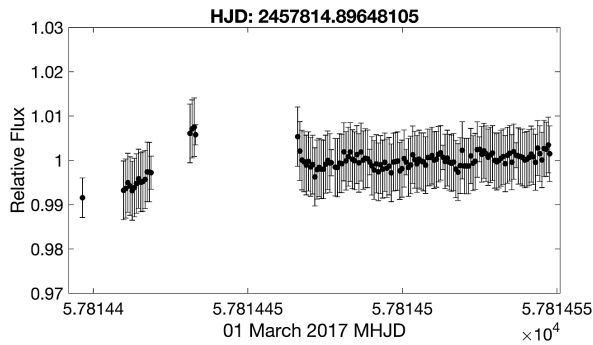
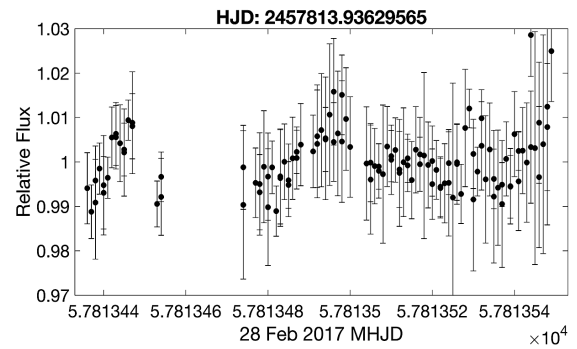
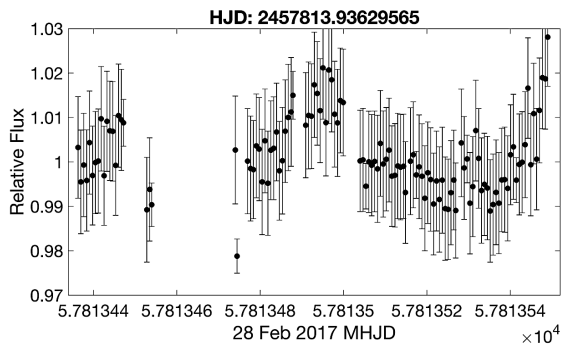
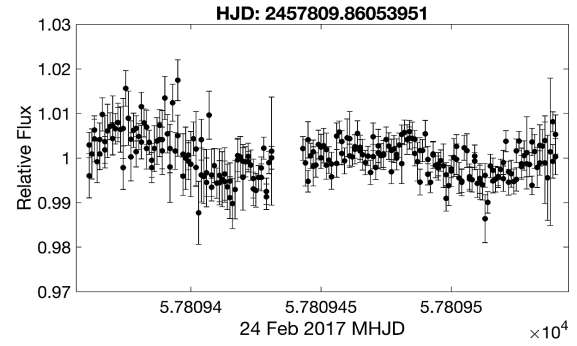


Figure 5.18 continued from previous page

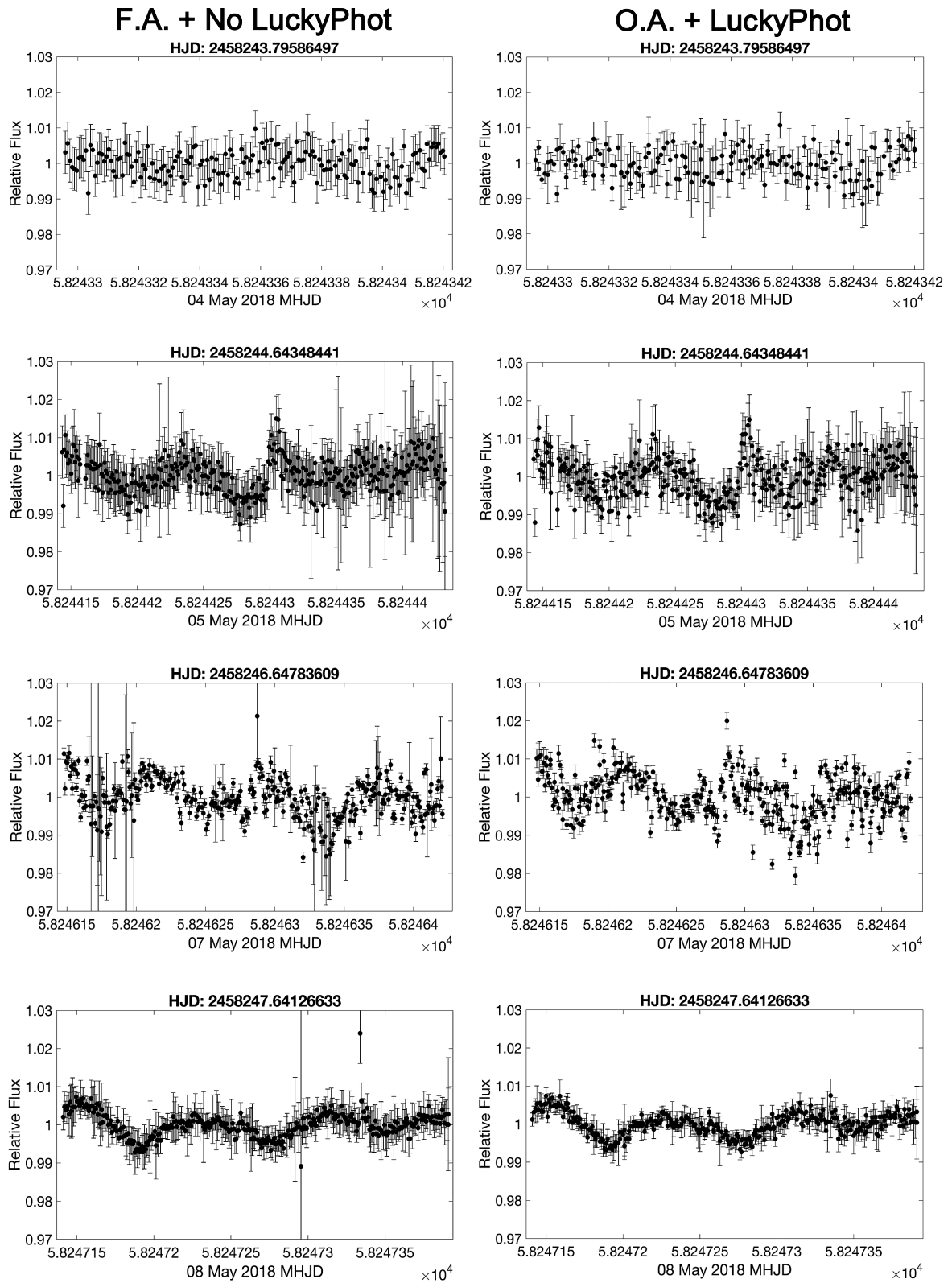


Figure 5.18 continued from previous page

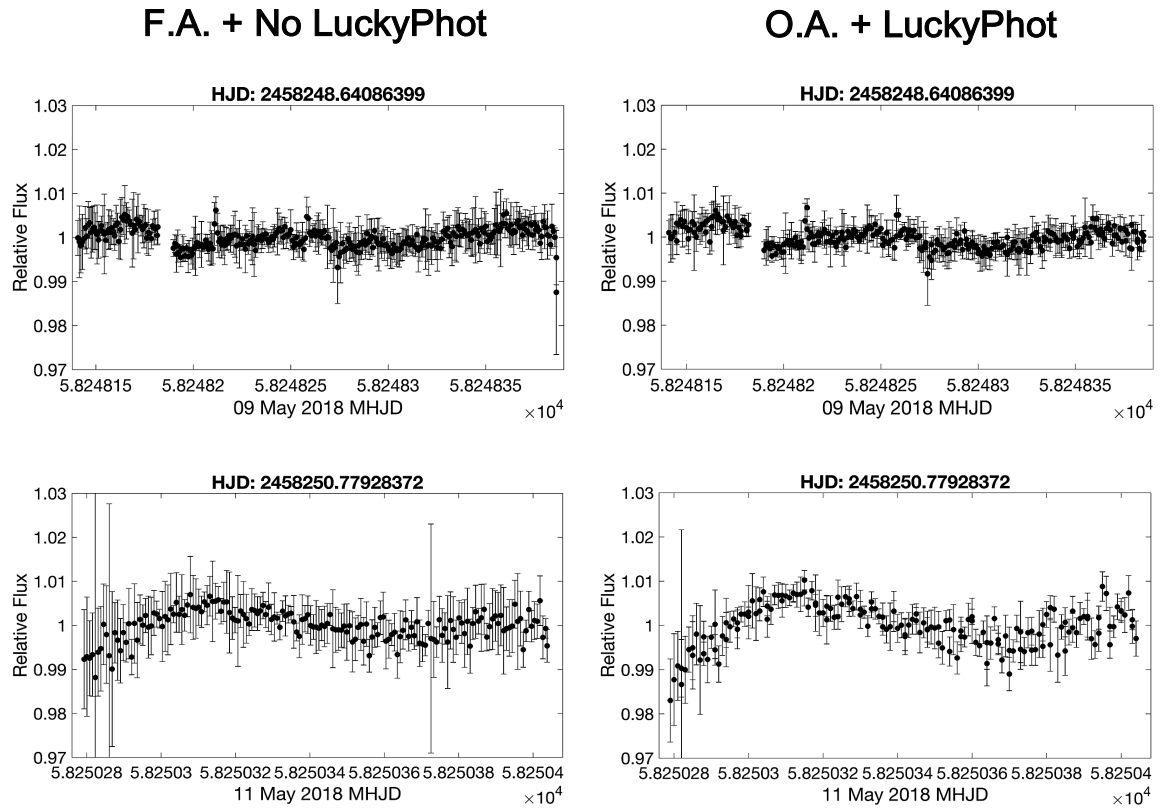
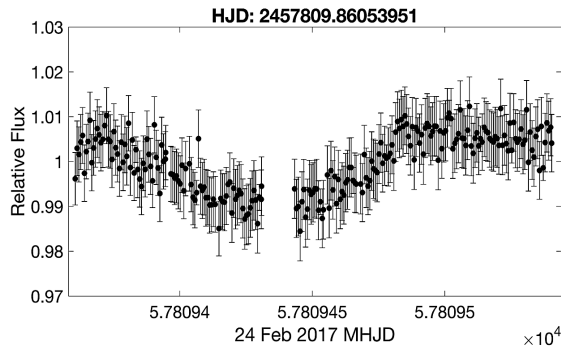


Figure 5.18 2M J1314+13A: Comparison of the results from utilizing F.A.+ No LuckyPhot (GUF1 photometry: left column) and O.A.+ LuckyPhot (right column) on 2M J1314+13A after subtracting out the signal of 2M J1314+13B. These lightcurves plot relative flux vs. Modified Heliocentric Julian Date (MHJD). The HJD time above each figure denotes the start-point of each observation night. Photometric error bars of each 2M J1314+13AB measurement are applied here (Table 5.8). This figure shows clearly the difference between the two photometric methods in terms of the photometric error estimates. LuckyPhot selects frames which are affected by the most similar atmosphere (the most stable conditions).

F.A + No LuckyPhot



O.A + LuckyPhot

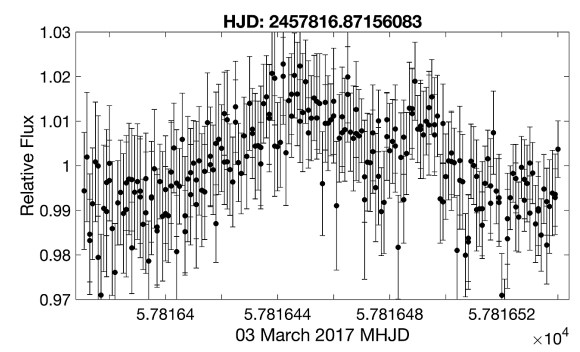
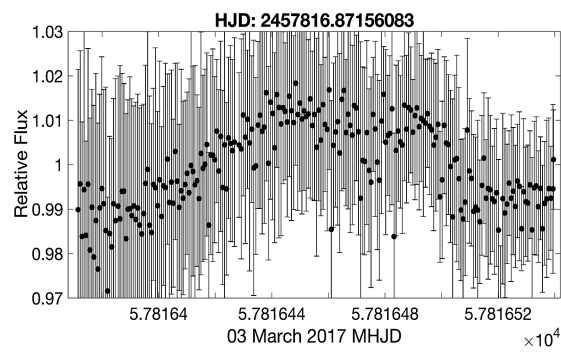
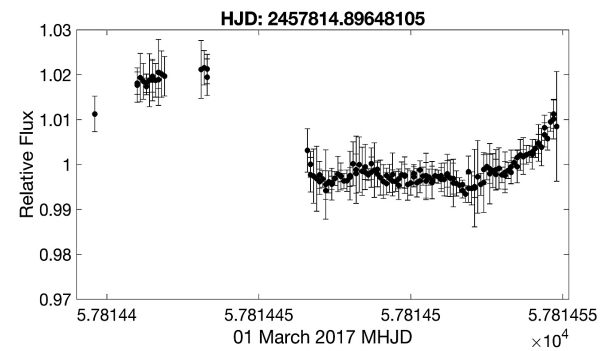
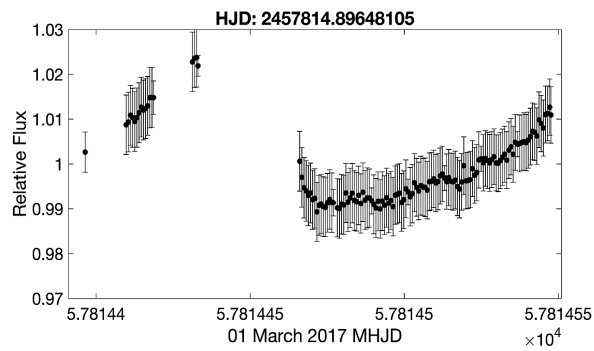
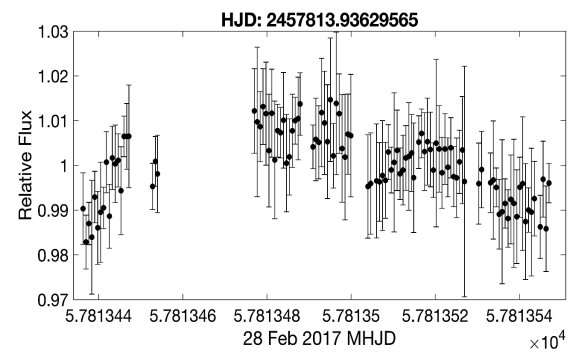
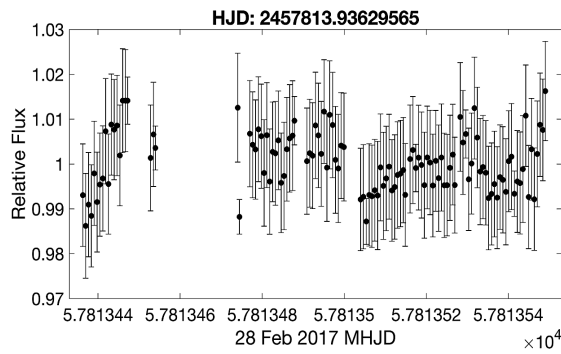
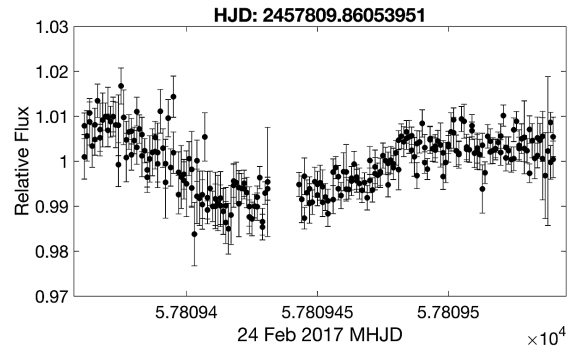


Figure 5.19 continued from previous page

F.A. + No LuckyPhot

O.A. + LuckyPhot

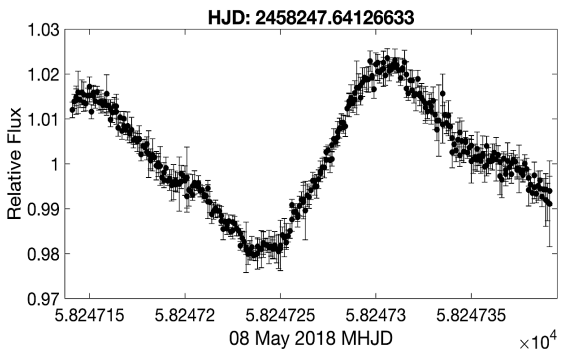
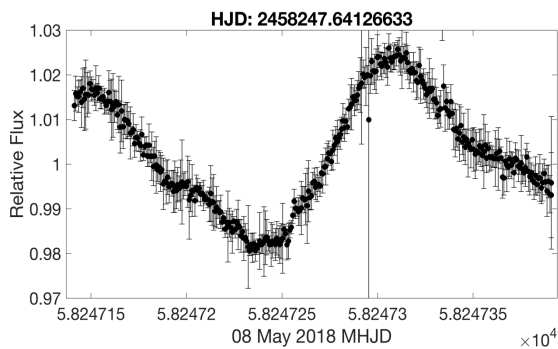
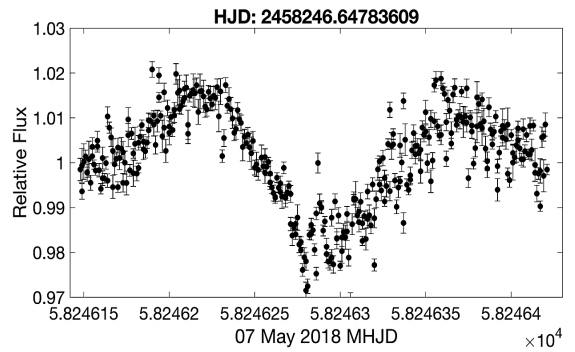
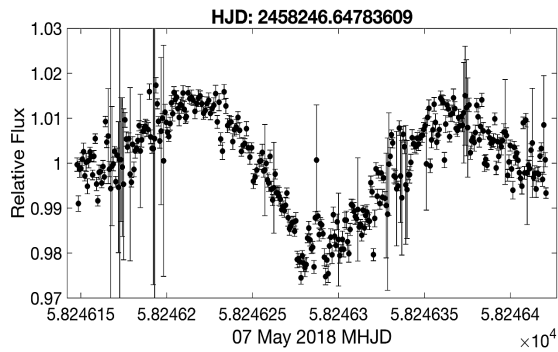
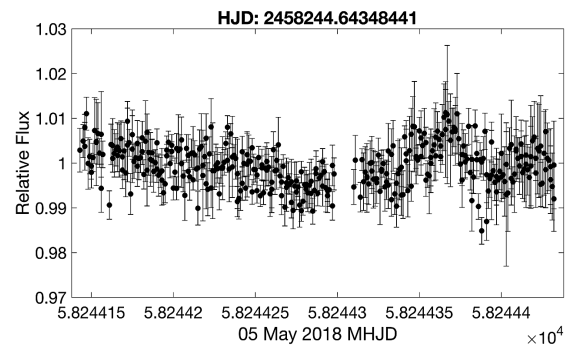
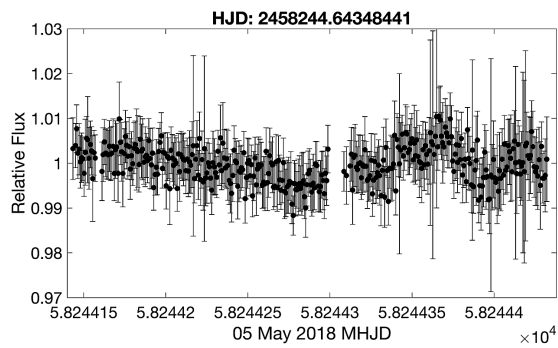
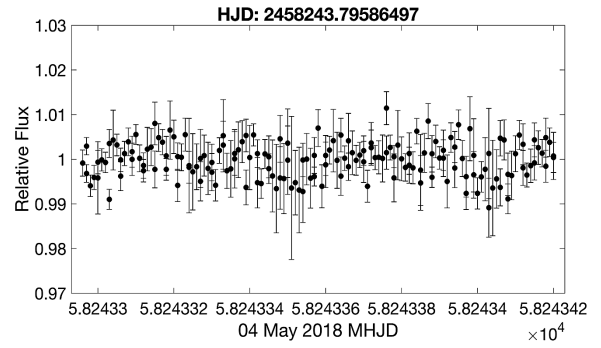
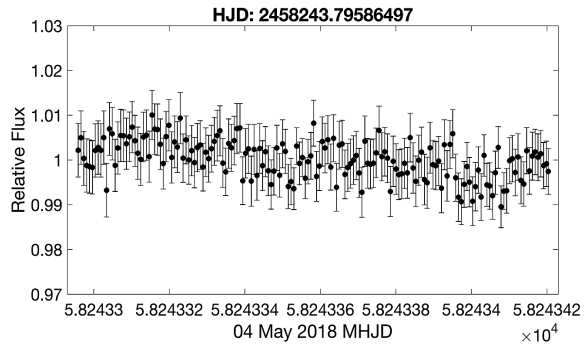


Figure 5.19 continued from previous page

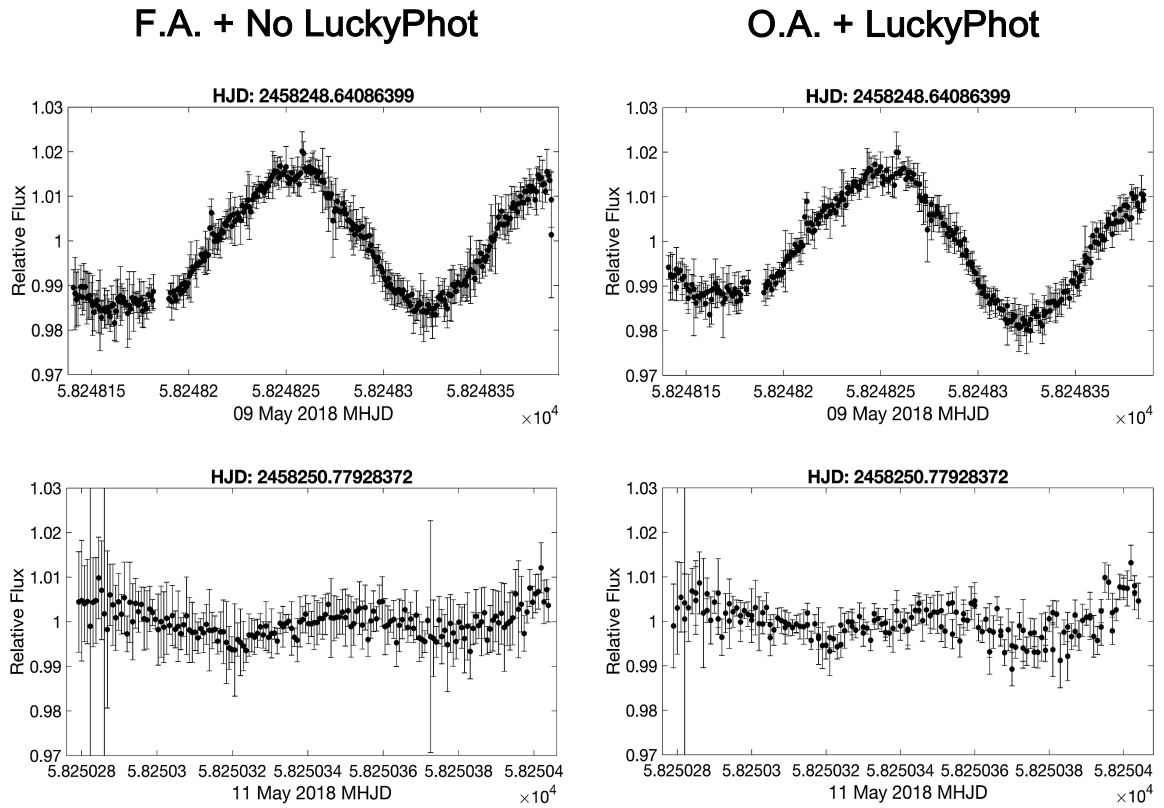
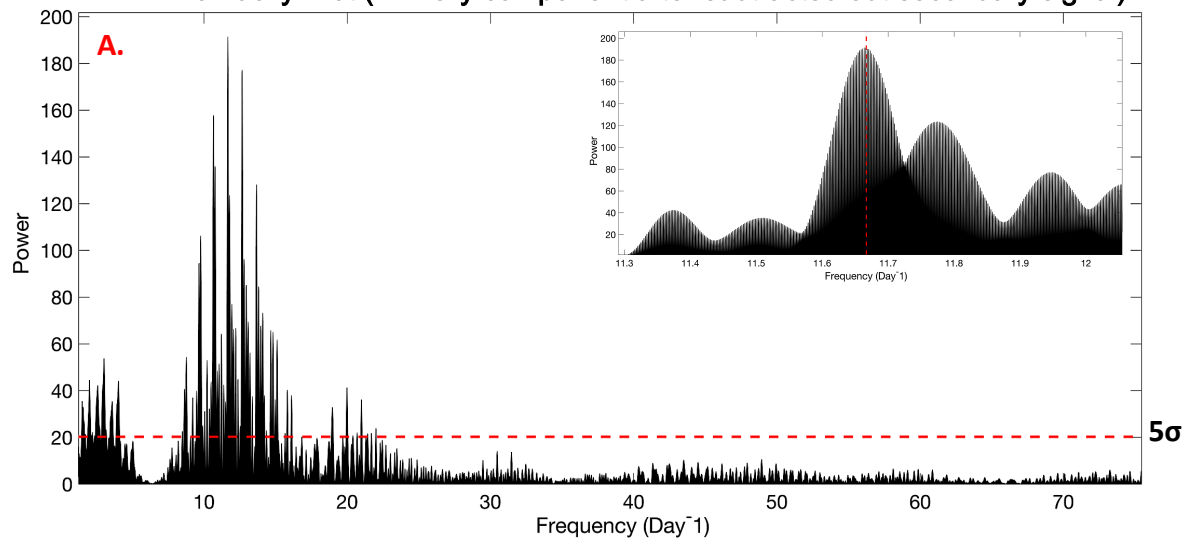


Figure 5.19 2M J1314+13B: The results obtained from using F.A. with no LuckyPhot (GUFI photometry) and O.A. with LuckyPhot after subtracting out the primary component. Photometric error bars for 2M J1314+13AB are applied here.

F.A. + No LuckyPhot (Primary component after subtracted out secondary signal)



O.A. + LuckyPhot (Primary component after subtracted out secondary signal)

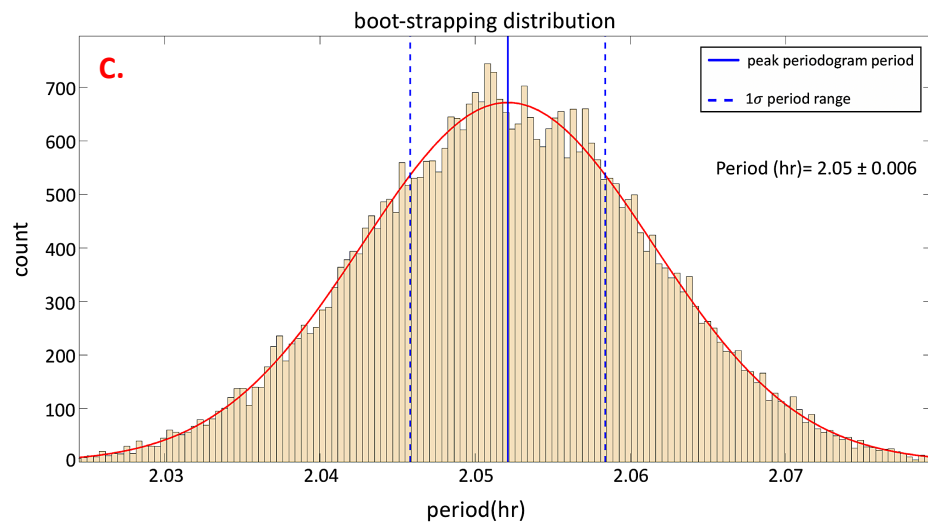
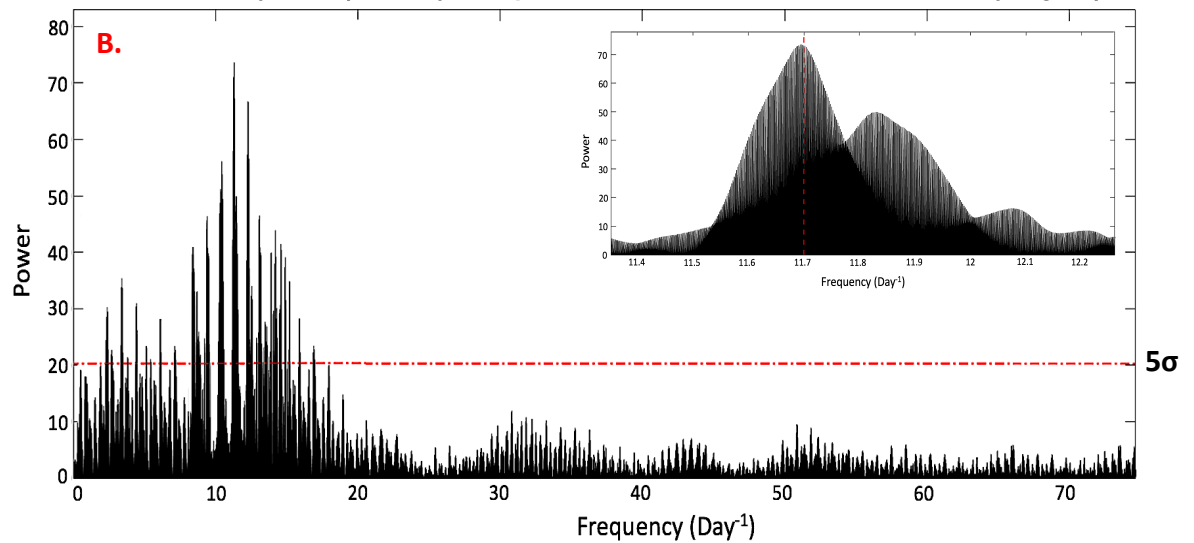
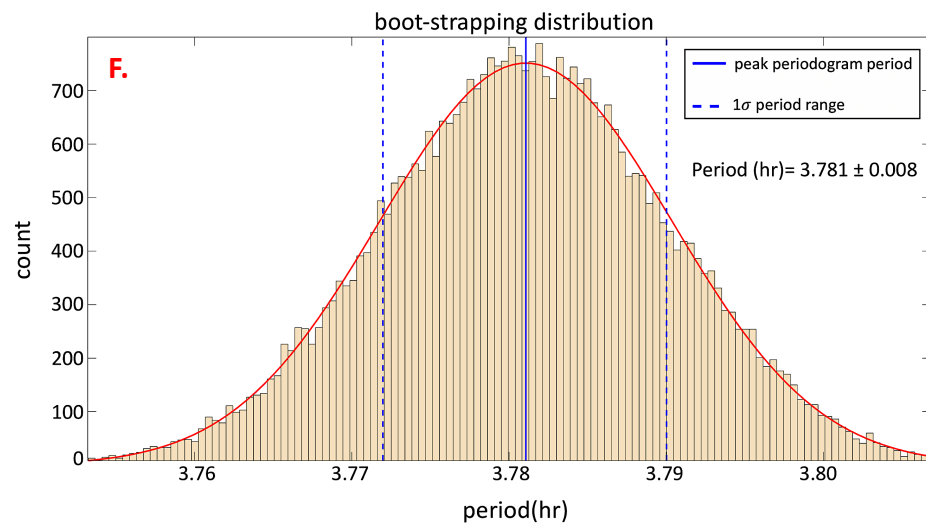
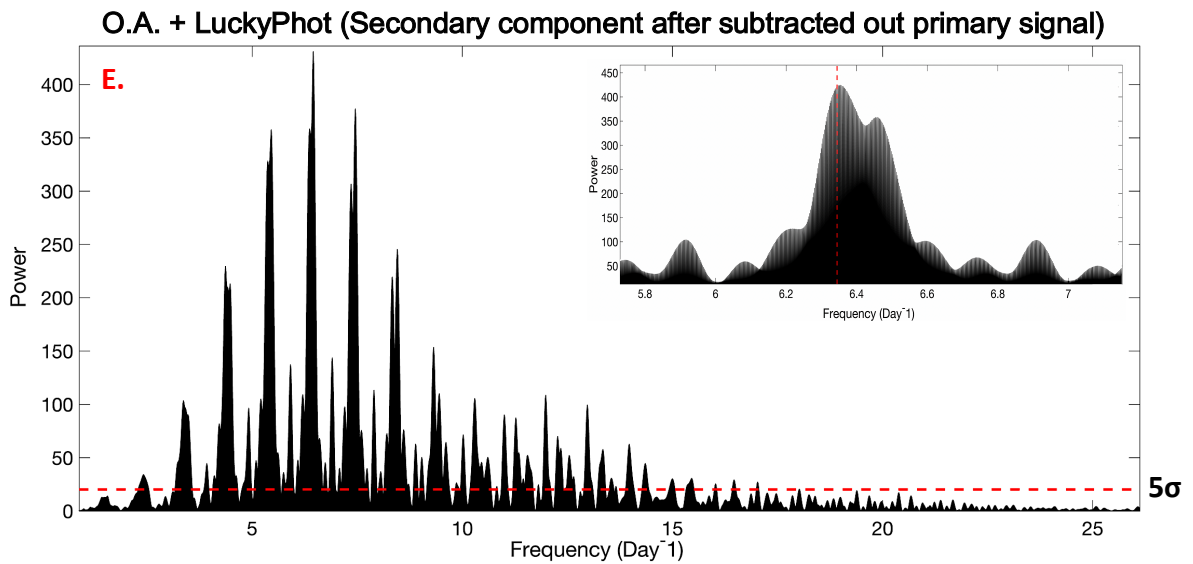
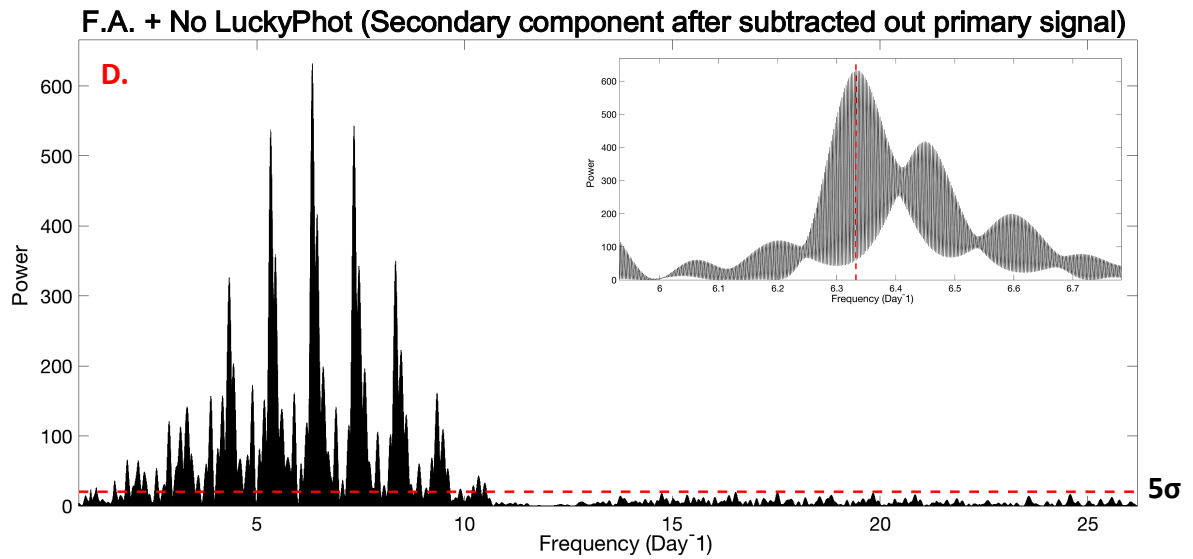


Figure 5.20 continued from previous page



Caption of Figure 5.20 continued from previous page

Figure 5.20 Periodograms (power spectra) for each permutation of binary component and photometric technique, after isolating signal for each binary component by running Light Curve Fitter. Panels **A & B**: Lomb-Scargle (LS) periodogram of all epochs of the I-band GUF1 photometric data of 2M J1314+13A, after subtraction of the putative rotational period of the secondary component. We discovered optical variability of 2.06 ± 0.05 hrs and 2.05 ± 0.04 hrs, detected as the highest peak in the periodogram for F.A. + No LuckyPhot (GUF1 photometry) and O.A. + LuckyPhot, respectively. Panels **D & E**: Lomb-Scargle (LS) periodograms of all epochs of the I-band GUF1 photometric data of 2M J1314+13B, after subtracting out the primary period. We indicated a periodicity of 3.79 ± 0.05 hrs and 3.78 ± 0.04 hrs, detected as the highest peak in the periodogram for F.A. + No LuckyPhot (GUF1 photometry) and O.A. + LuckyPhot, respectively. The vertical red dashed line (shown in close-up in the inset plot) corresponds to the detected optical periods using each technique for each component. The dashed-dotted line on each plot which represents a 5σ false-alarm probability. Panels **C & F**: The bootstrapping distribution method of retrieved highest power periods (Panels **B & E**), yields uncertainties of 0.006 and 0.008 hrs for the A and B members, respectively.

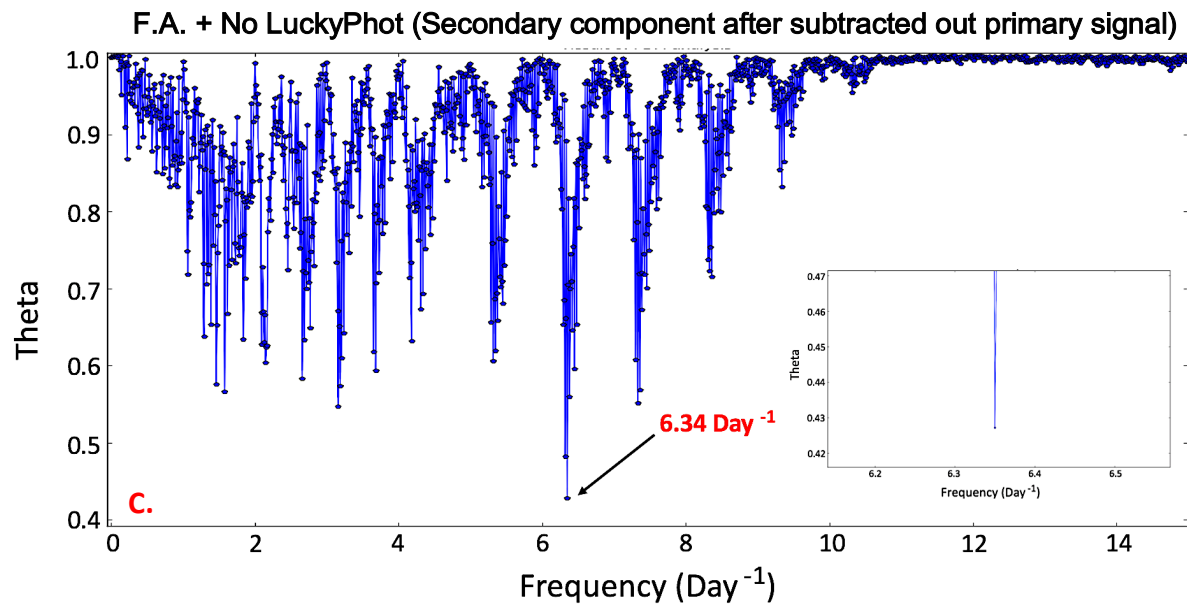
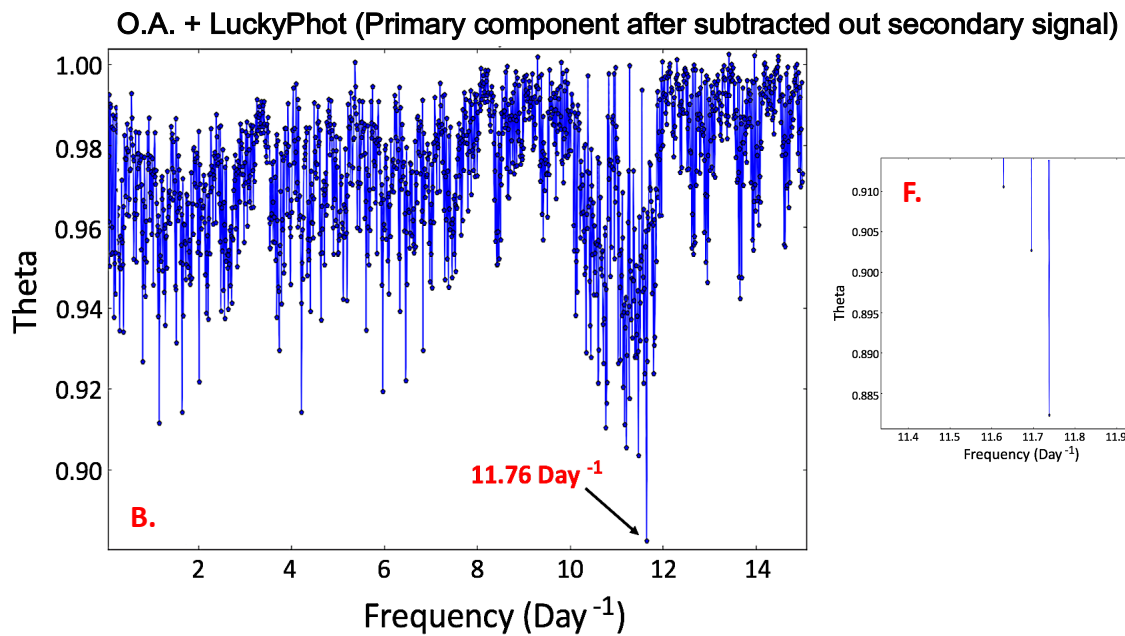
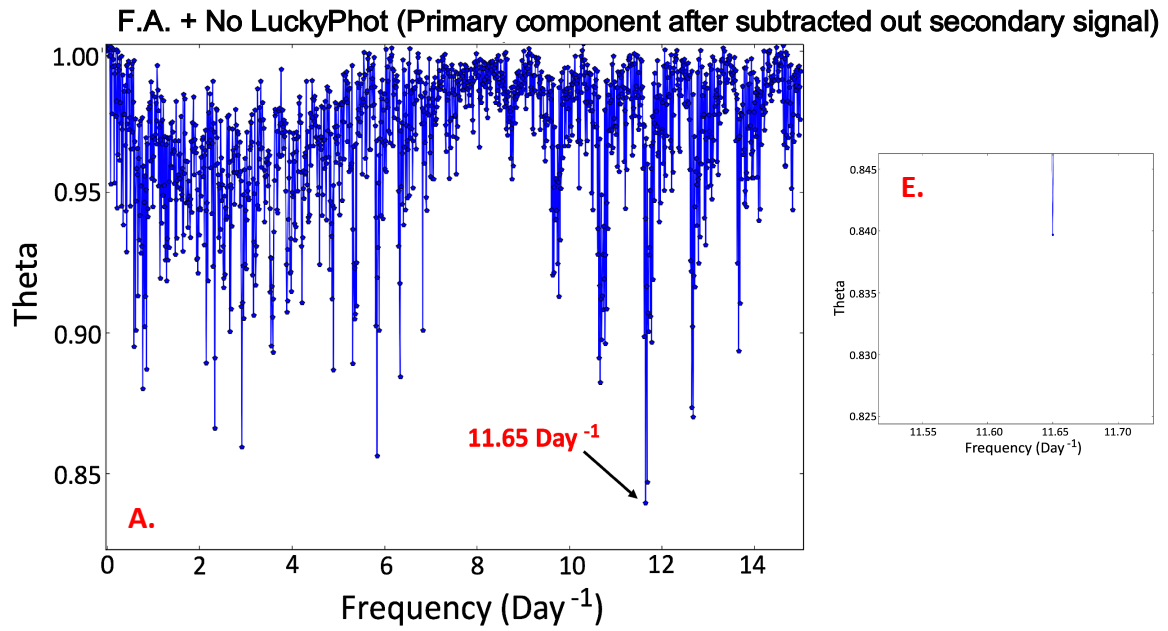


Figure 5.21 continued from previous page

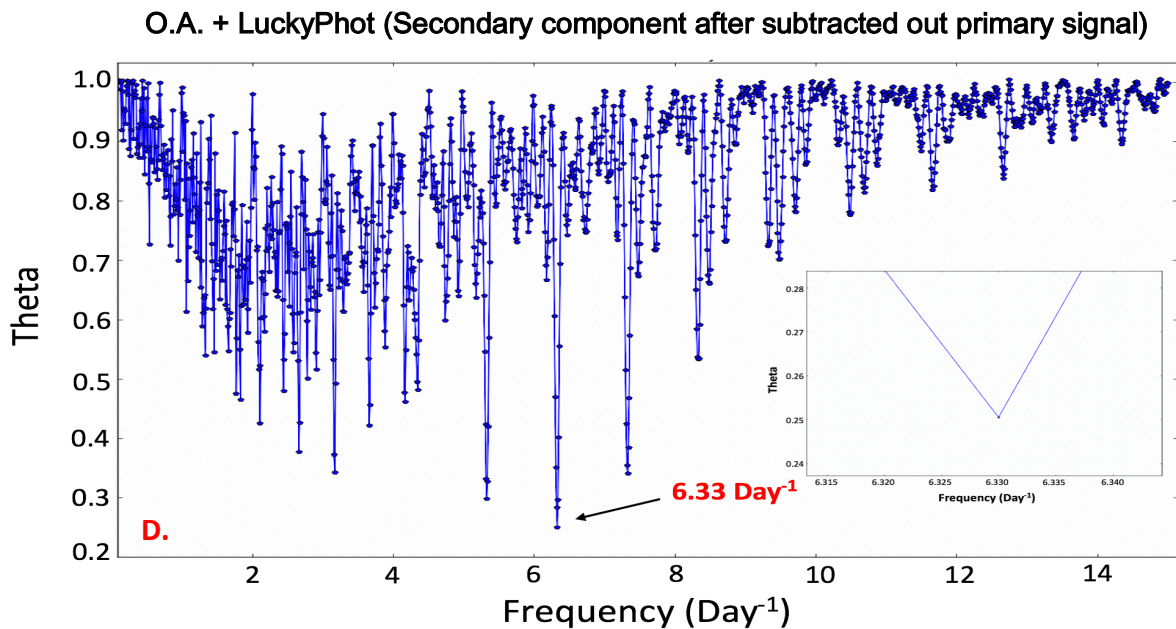


Figure 5.21 Phase Dispersion Minimization (PDM) plots of the entire ~ 1.3 year baseline for each permutation of binary component and photometric technique after running Light Curve Fitter. The arrow marked on each figure indicate the most significant periods after trying 10^5 Monte-Carlo simulations. Panels **A & B**: PDM of all epochs of the I-band data sets of 2M J1314+13A. We discovered sinusoidal photometric variability with a period of ~ 2.06 hrs and ~ 2.04 hrs, for F.A. + No LuckyPhot (GUFI photometry) and O.A. + LuckyPhot, respectively. Panels **C & D**: PDM of all epochs of the GUFI I-band data of 2M J1314+13B. We detected a period of ~ 3.785 hrs and ~ 3.791 hrs, for F.A. + No LuckyPhot (GUFI photometry) and O.A. + LuckyPhot, respectively. Panels **E & F** and inset plots of **A & B**: close-ups of the region where theta reaches its minimum, yielding our reported periods. The findings of PDM for each component using both photometric techniques are highly consistent with those of LS (Figure 5.20).

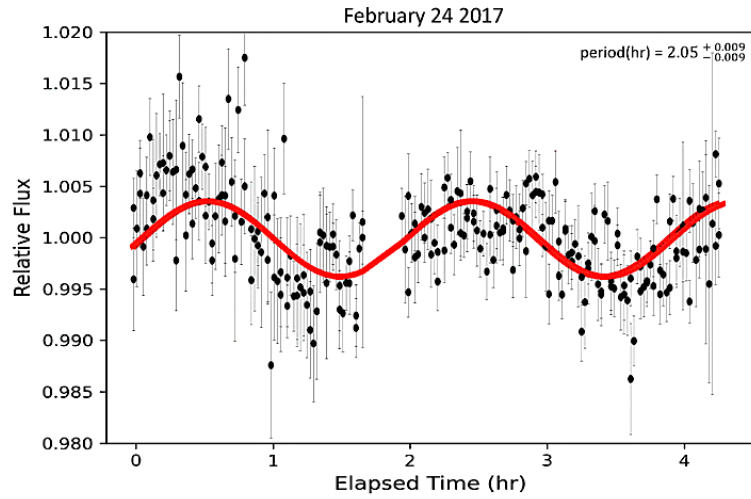
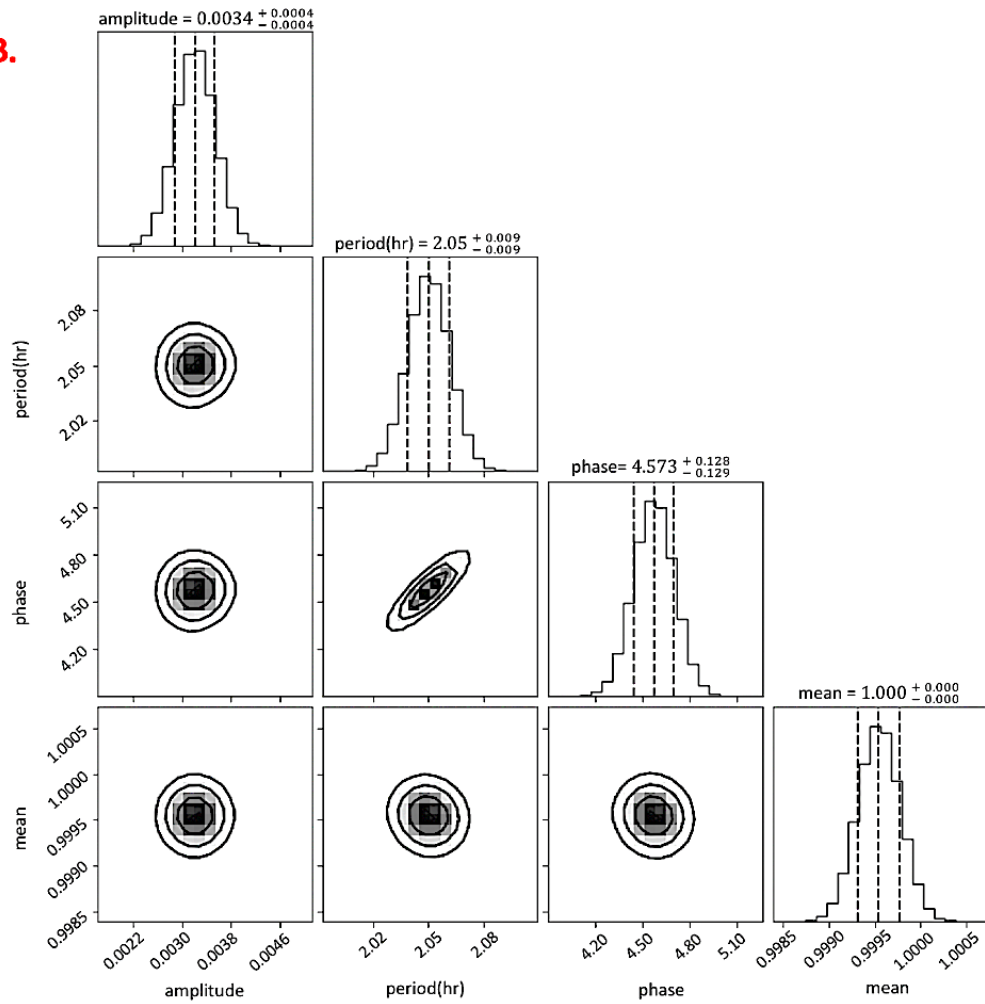
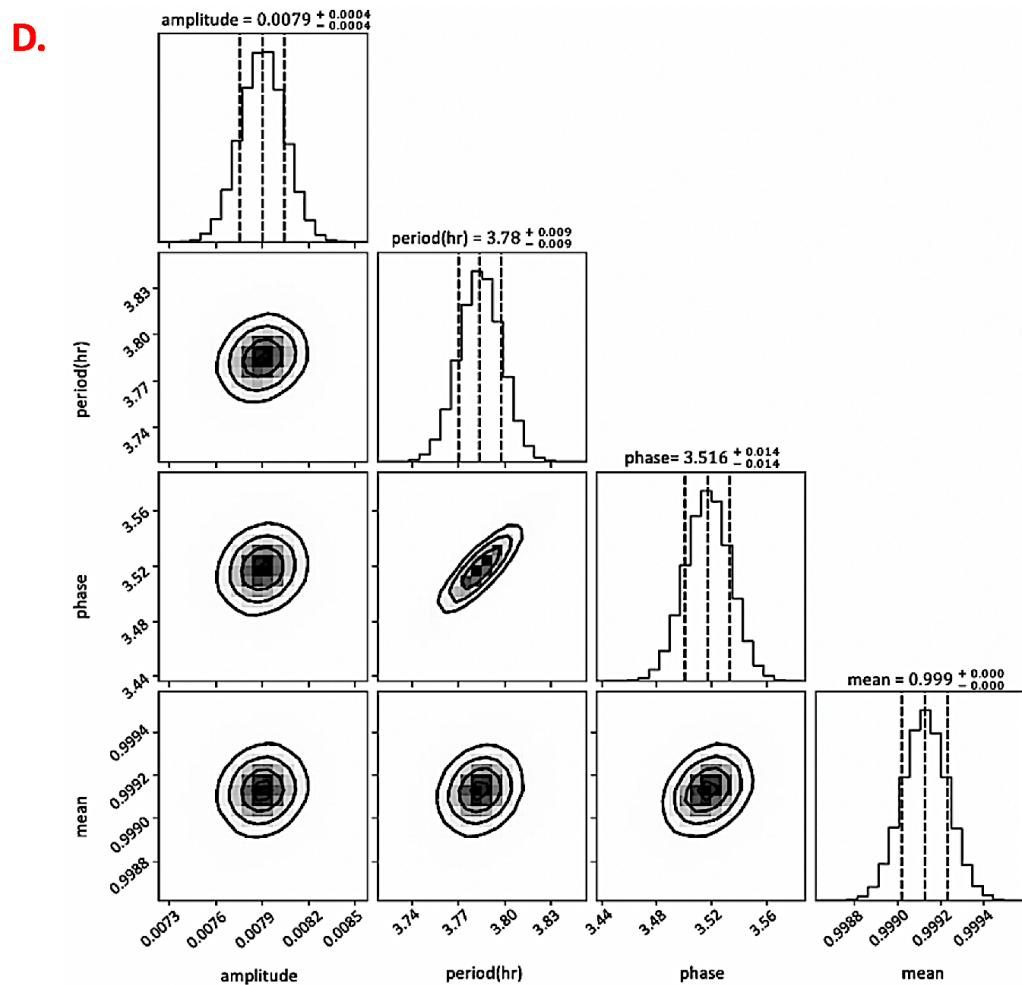
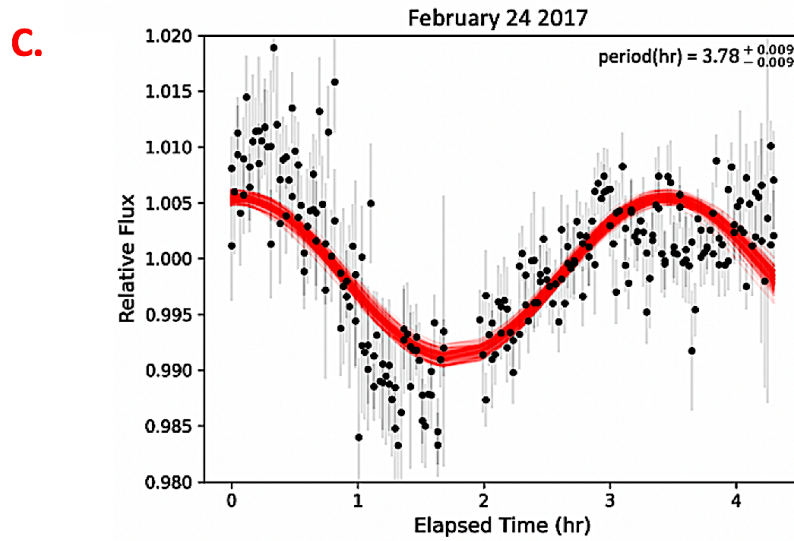
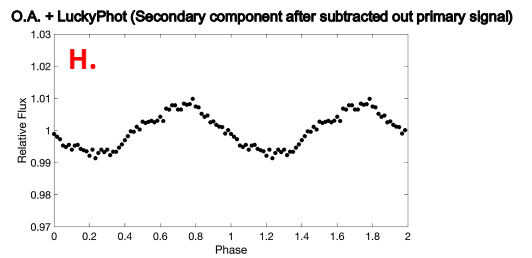
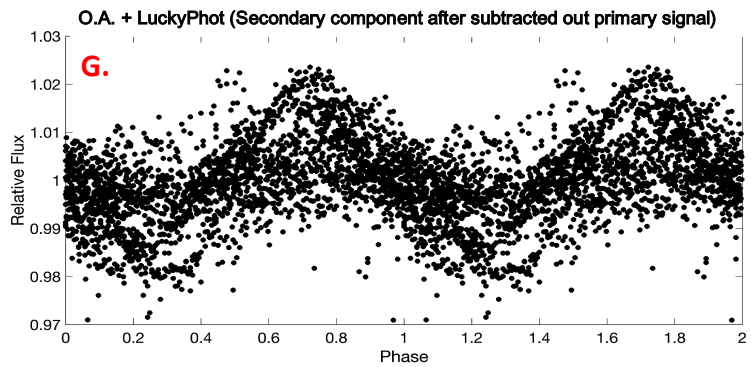
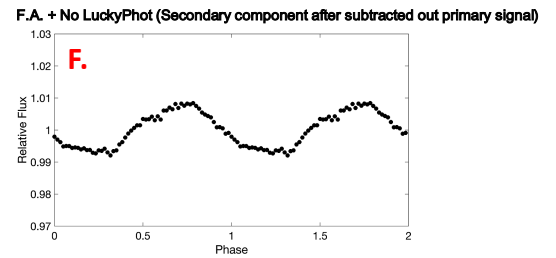
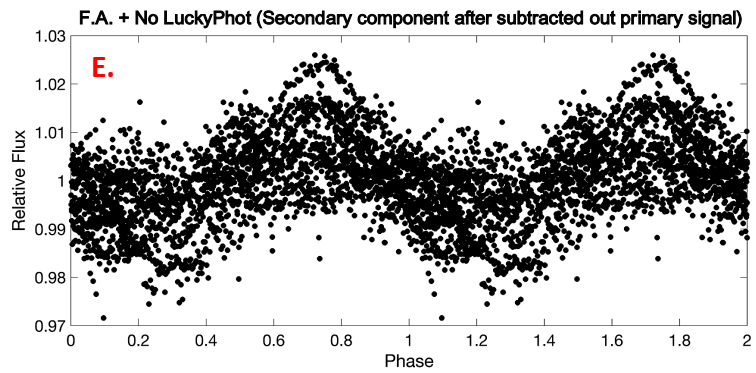
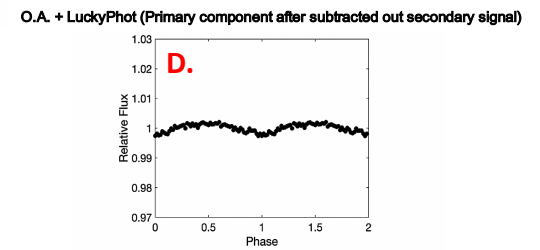
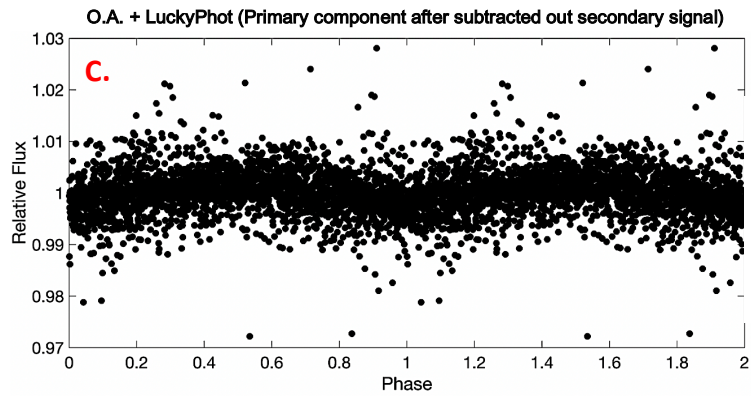
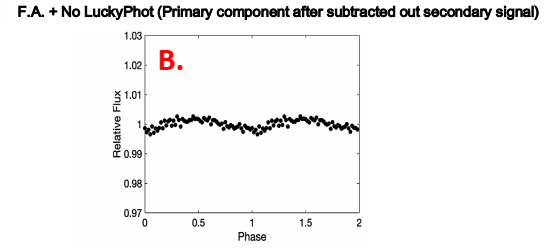
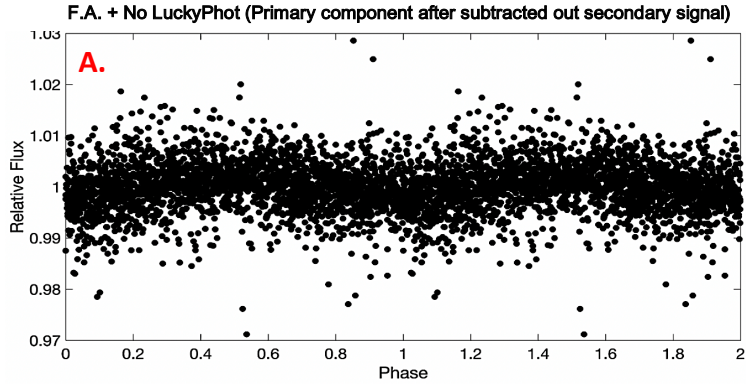
A**B.**

Figure 5.22 continued from previous page



Caption of Figure 5.22 continued from previous page

Figure 5.22 **A** and **C**: The fitted sinusoidal model (red curve) of 2M J1314+13A and 2M J1314+13B on February 24 2017 (O.A.+LuckyPhot). Figures **B** and **D**: Posterior probability distributions of the model parameters for the A and B components. The MCMC method produces a period of 2.05 ± 0.009 hrs and 3.78 ± 0.009 hrs, respectively, for A and B members.



Caption of Figure 5.23 continued from previous page

Figure 5.23 **A, C, E** and **G**: Phase-folded photometric lightcurves of 2M J1314+13A and 2M J1314+13B respectively, from all three epochs. We phase-folded the lightcurves produced by both photometry techniques to their detected periods from LS. The observed sinusoidal amplitude variability shows that this dwarf is extremely stable in period and phase, though not in amplitude, over a one-year timeline. Figures **B, D, F** and **H**: The same data as Figures **A, C, E** and **G**, except binned in phase by factors of 20.

We showed the effect of isolating each signal, in Figures 5.16 to 5.19. Then, the differential lightcurves of each component from both photometric techniques were phase folded to their respective optical periods from LS (Figure 5.23). In the same way as with the binary dwarf 2M J0746+20AB, we combined all 3 epochs, using

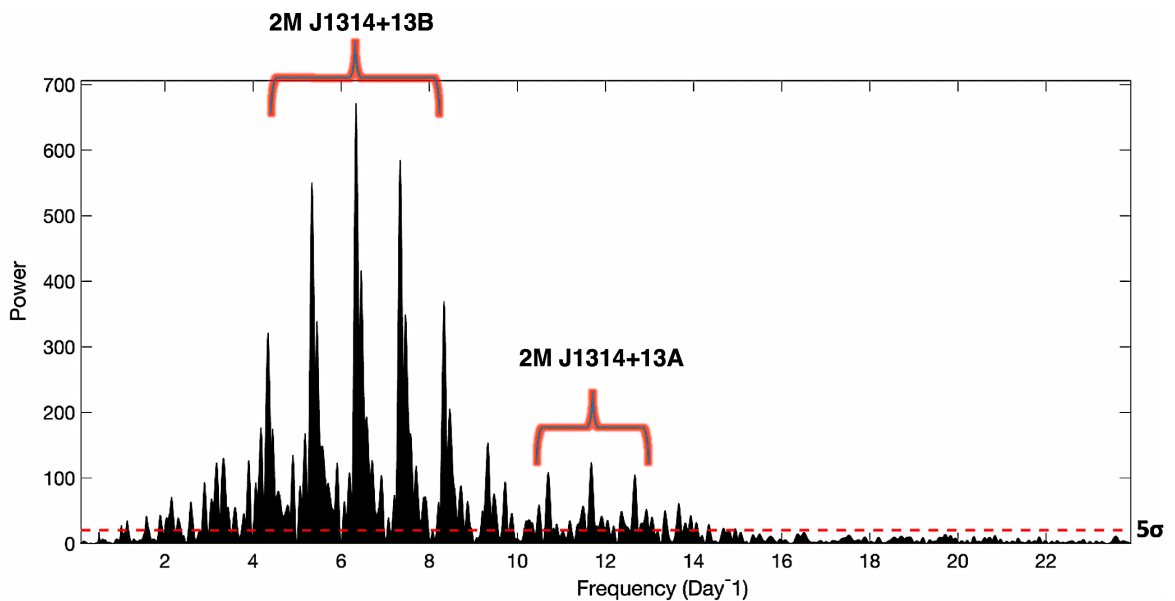


Figure 5.24 Lomb-Scargle (LS) periodogram of all epochs combined of I-band GUF1 data of 2M J1314 13AB. This finding of the presence of two optical variability sources in our data is in accordance with findings obtained from Light Curve Fitter code.

F.A.+ No LuckyPhot (GUFI photometry) as a random selection in terms of the photometric method, and ran again LS. This analysis found evidence for the presence of two variable sources in our datasets (Figure 5.24).

Property	2M J1314+13A	2M J1314+13B	Reference
Rotation period (hrs) (Optical)	2.06 ± 0.05 (F.A.)	3.79 ± 0.05 (F.A.)	This work
	2.05 ± 0.006 (O.A.)	3.78 ± 0.008 (O.A.)	
Maximum rotation period (hrs)		~ 3.93	This work
Equatorial Inclination (°)		50.6 ⁺⁹ _{-7.5}	This work
Equatorial Velocity (km s⁻¹)		58.2 ± 2	This work

Table 5.10 Preview of 2M J1314+13AB results from this work. F.A. and O.A. refer to the two different photometry methods employed: Fixed Aperture, and Optimum Aperture/Lucky Photometry.

The performance of the proposed method (O.A.+LuckyPhot) was compared against traditional methods (F.A.+GUFI photometry) for 2M J1314+13AB. We selected the night of 24 Feb 2017 randomly as the comparison sample. The data was binned at 60 sec, which provided a good compromise between temporal sampling of the source and good statistical sampling for each data bin. The results can be seen in Figure 5.25. The number of frames for each data bin varied in part

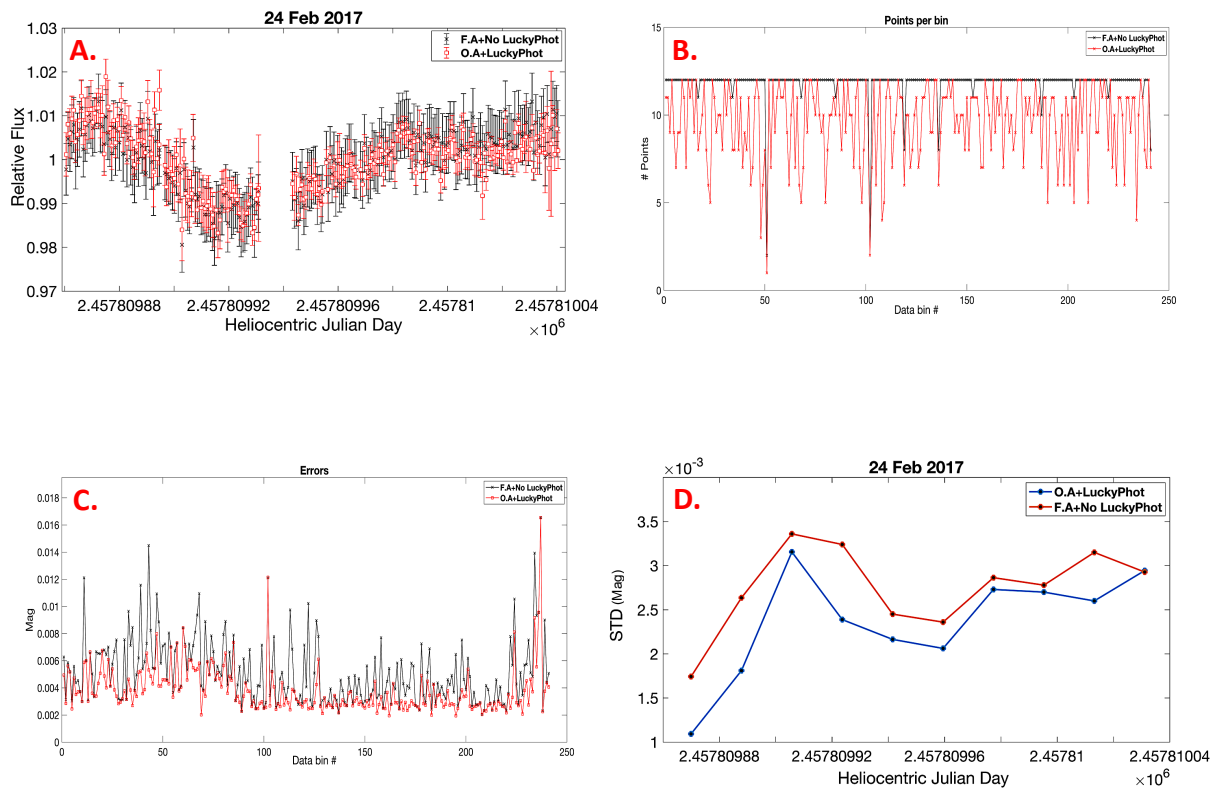


Figure 5.25 **A.** Comparison of the differential lightcurves for the night of 24 Feb 2017, obtained from using O.A. with LuckyPhot (red square marker) and a F.A. with no LuckyPhot (GUFI photometry) (black star marker). The use of O.A. and LuckyPhot on 2M J1314+13AB shows a remarkable reduction in estimated error (see Table 5.8). **B.** The number of points within each data bin before and after the LuckyPhot process. The higher point values correspond to a higher number of selected frames (a period of greater atmospheric consistency). **C.** The photometric errors corresponding to the lightcurves in Figure A. This plot illustrates, with greater clarity, the effect of the LuckyPhot technique. **D.** Comparison of techniques to determine which one has a lower spread after applying results comparison tool. The Y-axis represents the standard deviation (STD) within bins that each contained 25 consecutive relative flux values. This appears to be a straightforward confirmation that O.A. and an optimum frame selection routine (LuckyPhot), can indeed reduce scattering.

due to stoppages in acquisition and also due to rejections from the LuckyPhot technique; therefore, we notice a slight difference between the rotation periods resulting from the two techniques. To quantify the performance comparison, we used results comparison tool, a simple python script that we wrote to show any significant differences between the two methods used in terms of scattering. Panels A, C and especially D of Figure 5.25 provide confirmation that for this dataset, the LuckyPhot technique along with O.A. does indeed have the effect of reducing the scatter and producing a better lightcurve. We find that the O.A. with LuckyPhot technique has clear benefits to improve the photometric precision achievable for a given data set by reducing photometric errors, where the mean RMS error was reduced by $\sim 48\%$ with respect to the errors produced by our standard GUF1 pipeline method.

Overall, we obtained good results with the two photometric methods used, which yielded a secondary component rotation period from all three epochs of 3.79 ± 0.05 hrs and 3.78 ± 0.008 hrs of using F.A. with GUF1 photometry (no LuckyPhot) and O.A. with LuckyPhot, respectively. This result ties well with previous optical studies (McLean et al., 2011; Williams et al., 2015) and is also in good agreement with its 3.89 ± 0.05 hrs radio periodicity (McLean et al., 2011). These data infer a maximum period value of ~ 3.93 hrs for the secondary component by applying the following formula:

$$P_{max} = \frac{2\pi \cdot R(B) \cdot \sin(i)}{v \sin i (B)} \dots \dots \dots (5.1)$$

where B is the secondary member, R is the latest estimated radius of $1.808 \pm 0.018 R_J$ (Dupuy et al., 2016), $v \sin i = 45 \pm 5 \text{ Km s}^{-1}$ (McLean et al., 2011) and orbital inclination $i = 49.34_{-0.23}^{+0.28}$ degrees (Dupuy et al., 2016).

As noted earlier, McLean et al. (2012) attributed the measured rotation periods of the 2M J1314 + 13AB to the A member. However, this is contrary to the findings

of Dupuy et al. (2016) and Forbrich et al. (2016), the radio emission detected is entirely attributable to its secondary component, which is detected at an average flux density of $666 \mu\text{Jy}$. They derived a limit of $22 \mu\text{Jy bm}^{-1}$ for radio emission of the primary component. Given that, Dupuy et al. (2016) and Forbrich et al. (2016) determined that the A and B members have nearly identical masses (to within $\pm 2\%$), this difference in radio emission by a factor more than 30 is noticeable between the two members. Forbrich et al. (2016) argued many scenarios that could explain this difference, as they pointed to differences in stellar rotation that are considered to be the key factor governing stellar activity, or differences in the evolution of stellar rotation over time, both of which lead to different magnetic field configurations. Alternatively, misaligned rotation axes of the two components could mean that the radio emission from the secondary component could be beamed toward the observer but not for the primary component. Further speculation about the complexities of the dwarf's radio emission and the geometry of beaming is outside the scope of this thesis.

As indicated in Table 5.2, the two binary members appear to have almost similar physical properties, such as mass, radius, age, temperature, luminosity (Dupuy et al., 2016; Forbrich et al., 2016). Previous studies also assumed that the rotation periods and rotational velocities of the A and B components were similar (McLean et al., 2011; Forbrich et al., 2016; Pineda et al., 2017). We disagree with these assumptions, as our I-band results demonstrated that for the first time, we discovered the primary rotation period of ~ 2 hrs. In addition to that, the 2M J1314+13AB case looks nearly similar to 2M J0746+20AB, as both of its components have similar physical properties but showed very different magnetic emissions. Based on the observations of the VLBI by Forbrich et al. (2016), we refer the periodic radio and optical emission (McLean et al., 2011; Williams et al., 2015) to the secondary member. Resolved $v \sin i$ measurements of the two objects could potentially elucidate the optical emission source for each component.

In this section, we will explore the cause of this optical variability in the A and B components of 2M J1314+13. Optical rotational modulation in M dwarfs is commonly attributed to magnetic spots on the surface of the object as the most likely cause of periodic variability. Alternatively, since ultracool dwarfs have very cool neutral atmospheres, photospheric clouds are expected to also form and cause optical modulation as the object rotates (Bailer-Jones, 2002). 2M J1314+13AB is an M7 binary dwarf, so its atmosphere is still somewhat warm (2950 ± 5 K, as noted in Section 5.2.2) and clouds of dust are less likely. More generally, our basic findings may be consistent with research suggesting that magnetically-induced spots are the cause of the rotational modulation in both binary components. Since McLean et al. (2011) found that g- and i- band variations are in phase, this correlation is compatible with models of star spots induced variability.

Broadly translated the data presented here indicate a likely association between the source of optical and radio periodic variability in late-M dwarfs, where we speculate that the same magnetic features may be responsible for the periodic behavior at radio and optical wavelengths. Indeed, this correlation variability observed in the photometric and radio measurements in the 2M J1314+13B can be induced by an auroral electrodynamic engine. Forbrich et al. (2016) further used their astrometric observations to explain how auroral currents can be generated. They excluded the scenario of Jupiter mass companions in orbit around 2M J1314+13B. Alternatively, a smaller rocky planet could be sufficient to generate auroral emissions.

Further research is needed in the future to monitor the radio and optical emission of 2M J1314+13AB simultaneously and long-term. This may point to an origin of magnetic field structure if the optical/radio variability maintains a similar period and phase, and will be key in untangling the nature of the auroral phenomena.

5.5 Spin-Orbit Alignment Of the two binary systems: 2M J0746+20AB and 2M J1314+13AB

5.5.1 Introduction

A close look at VLM dwarfs reveals that binaries are the best calibrators to test stellar models because their components share a common age and composition. These binaries provide a rare opportunity to directly identify masses and to provide necessary reference points for the direct calibration of models. The dynamical masses of VLM binary can be attained from their orbital motion by the use of high angular resolution imaging such as adaptive optics imaging (hereafter AO). Knowing the dynamical masses can be a valuable resource for understanding the limitations of theoretical models (Bouy et al., 2004; Bouy et al., 2008; Dupuy et al., 2010; Konopacky et al., 2010; Blake et al., 2010).

Spin axis (the true obliquity or spin-orbit angle) is a fundamental geometric property of such systems. It has been recognised as an important diagnostic of the theories of binary star formation and evolution. There have been a number of longitudinal studies in recent years involving the alignment of the equatorial and orbital axes in the substellar regime and the possible formation mechanisms that are responsible for such alignment (Harding et al., 2013a; Harding et al., 2013b; Dupuy et al., 2016). This followed preliminary work that was carried out several years ago, which examined the topic of the rotational evolution of interstellar clouds and the spin and orbital properties of solar-type binaries (Weis, 1974; Abt and Levy, 1976; Bodenheimer, 1978; Fekel Jr, 1981; Hale, 1994). Hale (1994) found that a separation of (30 - 40) AU or less between solar-type binary components would have reasonable coplanarity with respect to orbit and equators. Weis (1974) showed that there is an orthogonal alignment between

rotation axes and orbital planes over a wider range of spectral classes [B-F]. While several observational studies of forming binaries have indicated that discs (protostellar disc) appear to be aligned for wide binaries, others conclude that such binaries with separations larger than 100 AU have strongly misaligned discs (Monin et al., 1998; Donar et al., 1999; Bate et al., 2000; Jensen, 2000; Wolf et al., 2001; Jensen et al., 2004; Monin et al., 2006). In the same context, in the case of very close binaries of semi-major axis ~ 0.3 AU, there have been some examples of systems showing both aligned and misaligned axes (Albrecht et al., 2009; Albrecht et al., 2011). Most published theoretical nebula fragmentation calculations have produced aligned discs due to the fact that all of the components are from the same region of a molecular cloud, but misaligned systems are also a possible outcome, depending on initial conditions (Bate et al., 2000; Albrecht et al., 2011; Harding et al., 2013b).

Rotational velocity is an important diagnostic parameter for examining stellar objects as it opens a window into the angular momentum evolution of a given source. A star's rotation can provide an important guide to its formation and can furnish diagnostics of its interior structure and evolution. Once all necessary parameters are provided such as rotation periods of the binary components, rotational velocity and estimated radii, the orbital coplanarity of the system can be assessed. Blake et al. (2010) reported their results of a Doppler survey using the NIRSPEC instrument on the Keck II telescope, by which they obtained radial velocity and rotational velocity measurements of 59 ultracool dwarfs, spanning spectral types M8/L0 to L6, over a period of six years. Following that, Konopacky et al. (2012) used AO on Keck II to measure $v \sin i$ for individual components of 11 very low mass binaries with spectral types between M7.5 to L7.5. However, masses and $v \sin i$ are not sufficient in themselves to probe spin-orbit alignment.

The rotational periods that we measured for all 4 components of the binaries 2M J0746+20AB and 2M J1314+13AB, combined with well-constrained orbital parameters and rotational velocity measurements, allow us to deduce the

alignment of the equatorial planes of both members of the selected binary systems with the orbital plane of the systems, an exemplar for evolutionary models of coplanarity in binary substellar systems. This investigation can probe the formation of VLM binary stars, and could signal that a scaled-down version of the formation mechanism for solar-type binary systems holds in this regime.

5.5.2 2M J0746+20AB

In this section, we will illustrate the spin-orbit alignment of the L binary system 2M J0746+20AB. We adopted the radii of $0.99 \pm 0.03 R_J$ and $0.96 \pm 0.02 R_J$ for the A and B members, respectively (Harding et al., 2013b). In addition, we used the $v \sin i$ measurements of $19 \pm 2 \text{ km s}^{-1}$ and $33 \pm 3 \text{ km s}^{-1}$ from spectroscopic observations (Konopacky et al., 2012). Together with our discovered optical rotation periods for both components, we assess the orbital coplanarity of the system by applying the following formulas:

$$\sin i(A) = \frac{(v \sin i(A))}{2\pi \cdot R(A)/P(A)} \dots\dots\dots (5.2)$$

$$\sin i(B) = \frac{(v \sin i(B))}{2\pi \cdot R(B)/P(B)} \dots\dots\dots (5.3)$$

where v is the rotational velocity, R is the radius, P is the rotation period, and A & B identify each binary component. Our results indicate that the axes are oriented with respect to the observer at 32 ± 4 degrees and 37 ± 4 degrees, respectively (Figure 5.26, Figure 5.27 & Table 5.6). These findings are entirely consistent with an equatorial inclination angle of 32 ± 4 degrees for component A (Harding et al., 2013b), and 36 ± 4 degrees for component B (Harding et al.,

2013b; Lynch et al., 2015). When comparing our findings for 2M J0746+20AB to those of Harding et al. (2013b), which was the first direct evidence of spin-orbit alignment in the VLM binary regime, it must be pointed out that we confirm that the rotational and orbital planes of 2M J0746+20AB are consistent with a coplanar alignment to within 10 degrees, and that this is in line with the assumption that

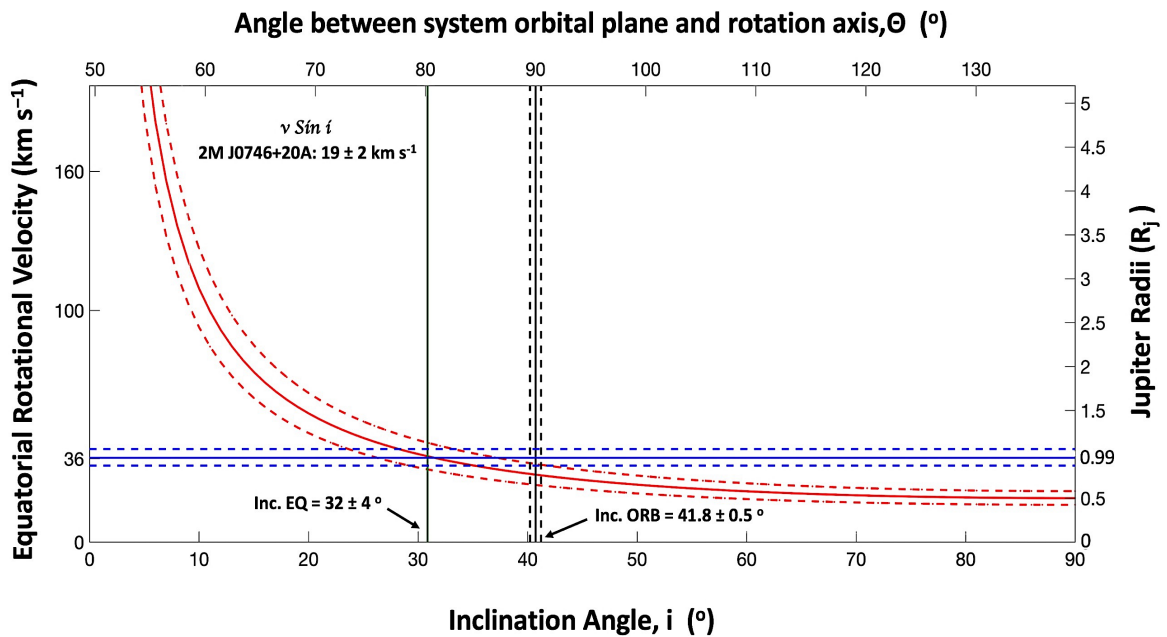


Figure 5.26 Equatorial rotational velocity (y-axis, left) vs. inclination angle of the orbital plane (x-axis, bottom). The solid red curve plots the $v \sin i$ of 2M J0746+20A (Konopacky et al., 2012). The black vertical solid line and top x-axis scale refer to the alignment of the spin and orbit axes. The right-hand Y axis, corresponds to the radius of the dwarf, $\sim 0.99 R_J$ ($\sim 0.0995 R_\odot$) where $R_J \sim 69911 \text{ km}$, as calculated by Harding et al. (2013b), from evolutionary models (Chabrier et al., 2000). This radius corresponds to an equatorial velocity of $\sim 36 \text{ km s}^{-1}$ from this work, highlighted as the solid blue line. The 41.8 degree orbital inclination angle is adopted from Konopacky et al. (2012). The dashed lines in all cases represent the associated errors. We measured equatorial inclination of 32 ± 4 degrees marked with the solid green line, which is exactly consistent with what has been found in previous study (Harding et al., 2013b) and also confirmed that the 2M J0746+20A equatorial inclination is within 10 degrees of the orbital inclination angle.

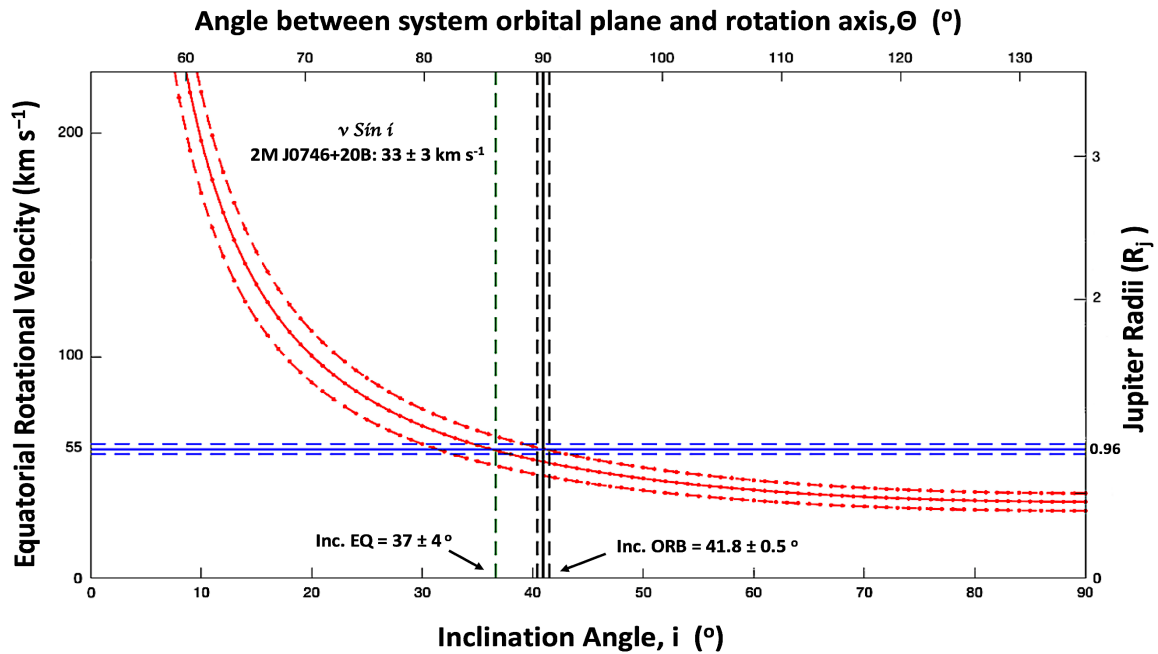


Figure 5.27 Same axis layout and illustration as Figure 5.26, except for the case of 2M J0746+20B. Its $v \sin i$ of $33 \pm 3 \text{ km s}^{-1}$ (Konopacky et al., 2012) is shown by the red solid line, where the dashed lines represent the errors in this measurement. We highlight the adopted radius of $\sim 0.96 R_J$ ($\sim 0.0964 R_\odot$) (Harding et al., 2013b) with the dotted green vertical track, which appears to have an equatorial inclination angle of 37 ± 4 degrees, aligned with the orbital plane of the system to within ~ 5 degrees. We calculated an equatorial velocity of $\sim 55 \text{ km s}^{-1}$ which is marked by the solid blue line, in exact agreement with Harding et al. (2013b) who used the ~ 2.07 hrs radio period for the secondary member in his work.

solar-type binaries, with separations of (30 - 40) AU or less, would have a reasonable coplanarity between the spin axis and orbital plane (Hale, 1994).

We used Monte Carlo simulations to estimate the uncertainty in these equatorial inclinations. The aim of using this method is to calculate the results based on repeated random sampling and statistical analysis. Each of the variables in Equations 5.2 and 5.3 had known uncertainties for $v \sin i$ (Konopacky et al., 2012),

P_A & P_B (this work) and R_A & R_B (Harding et al., 2013b). We generated 10^5 copies for each of these input values in Equations 5.2 and 5.3, where each repetition had added random noise distributed normally, based on the reported errors. We measured the resulting standard deviation of the variables and then calculated a mean value or expected value for each of the 10^5 simulations. This mean standard deviation over all of the simulations is taken as the uncertainty in each quantity and associated with the final calculation of the equatorial inclinations (as shown in Table 5.1 and Figure 5.26 & Figure 5.27).

Harding et al. (2013b) discussed the formation scenarios that are consistent with the observed alignment; they concluded that solar-type binary formation may extend to the brown dwarfs domain, supporting the disk fragmentation model as the formation mechanism of low mass binary regimes. This work with the new rotational data for this binary system supports this.

5.5.3 2M J1314+13AB

In the case of the M7 dwarf 2M J1314+13AB, to determine whether the binary member's equatorial axes are coplanar with the system's orbital plane, we have used the latest radii estimates (Dupuy et al., 2016) of $1.831 \pm 0.018 R_J$ and $1.808 \pm 0.018 R_J$ for 2M J1314+13A and 2M J1314+13B, respectively. We assigned the periods of rotation of 2.06 ± 0.05 hrs and 3.79 ± 0.05 hrs discovered here for components A and B, respectively, by using the F.A. with No LuckyPhot technique. Based on VLBI observations by Forbrich et al. (2016), we refer $v \sin i$ value to the B component. Due to the lack of $v \sin i$ (the missing piece of the puzzle) for the primary component, we decided to investigate the alignment of the spin-orbital axes of 2M J1314+13B. By applying Equations 5.2 and 5.3, we find evidence for the alignment of the spin and orbital axes of 2M J1314+13B, because we calculated the spin axis for B at an inclination of $50.6^{+9}_{-7.5}$ degrees (Table 5.10),

which would be aligned with the orbital plane (orbital inclination $i = 49.34^{+0.28}_{-0.23}$ degrees (Dupuy et al., 2016)) as shown in Figure 5.28. Our results appear consistent with Dupuy et al. (2016), who measured the inclination of the stellar rotation axis with respect to the plane of sky to be $i = 49 \pm 8$ degrees. As with 2M J0746+20AB, we used Monte Carlo simulations to estimate the uncertainty in the equatorial inclination of the B member.

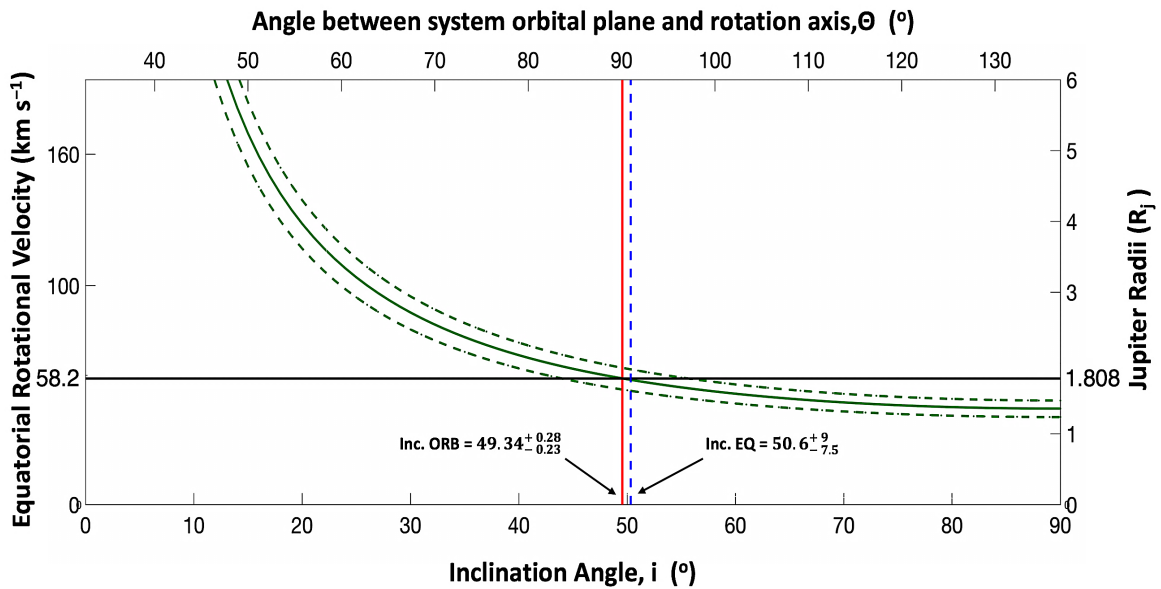


Figure 5.28 The equatorial rotational velocity (y-axis, left) vs. inclination angle of the orbital plane (x-axis, bottom). The green solid curve plots the $v \sin i$ of 2M J1314+13B ($45 \pm 5 \text{ km s}^{-1}$) (McLean et al., 2011). We find that our photometric period of rotation, combined with the latest estimated radius of $\sim 1.808 \pm 0.018 R_J$ (Dupuy et al., 2016), results in a very close coplanar alignment: an equatorial inclination angle of $50.6^{+9}_{-7.5}$ degrees, which is orthogonal to the orbital plane of $49.34^{+0.28}_{-0.23}$ degrees (Dupuy et al., 2016). The black horizontal lines show the corresponding equatorial velocity of $58.2 \pm 0.2 \text{ km s}^{-1}$. The dashed green and black lines correspond to the error in this measurement.

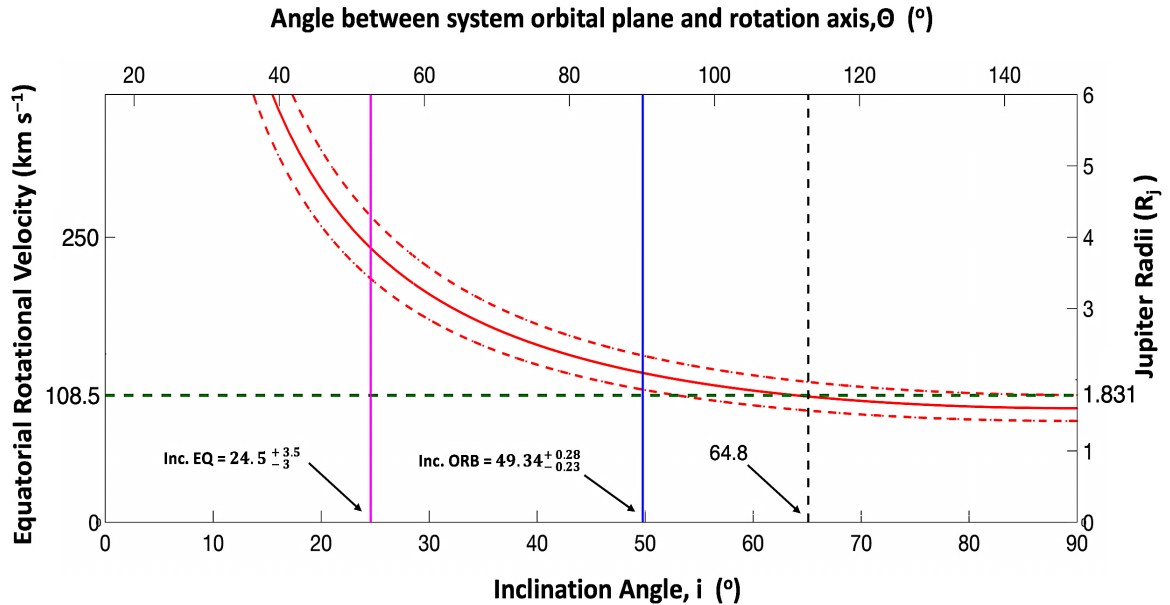


Figure 5.29 Same axis layout and illustration as Figure 5.28, but here we plot the results obtained from the scenario that the $v \sin i$ of $45 \pm 5 \text{ km s}^{-1}$ (red solid curve), measured by McLean et al. (2011), was originally a combination of the two rotations within 2M J1314+13AB. The dashed red line corresponds to the measured error in the $v \sin i$. We placed explicit constraints around this assumption: the detected rotation period in this work for the A component and the A component's radius estimated by Dupuy et al. (2016). These three values were used to calculate the second equatorial inclination angle and investigate whether it is coplanar with the system's orbital plane, as with 2M J1314+13B (Figure 5.28). The horizontal green dashed line in the plot represents the $1.831 \pm 0.018 R_J$ radius estimate for the secondary component (Dupuy et al., 2016). The magenta vertical solid line shows the corresponding tentative equatorial inclination angle of 24.5 ± 3.5 degrees for 2M J1314+13B. The orbital inclination angle of this system of 49.34 ± 0.28 degrees (Dupuy et al., 2016) is highlighted by the blue vertical solid line. If the assumed scenario is true, we found that the equatorial inclination angle for the companion is not aligned with orbital plane system. The vertical black dashed line represents the likely inclination of the B component at ~ 64.8 degrees and in alignment with the orbital plane.

If we assume the same spin-orbit alignment for the A and B members (same equatorial inclination angle $50.6_{-7.5}^{+9}$), then the ratios of v should track the ratios derived from P . If we also assume that the $v \sin i$ of $45 \pm 5 \text{ km s}^{-1}$ (McLean et al., 2011) is absolutely from the secondary, then by adopting the latest estimate of the radius of 2M J1314+13A ($1.831 \pm 0.018 R_J$) (Dupuy et al., 2016) and our measured rotation period ($2.06 \pm 0.05 \text{ hrs}$), we derived $v \sin i$ for the primary component of $83.8_{-8.6}^{+8.4} \text{ km sec}^{-1}$. However, another scenario could be that if we assume that the $v \sin i$ measured by McLean et al. (2011) is actually a mixture of the two rotations, and that the weaker source would have a weaker signal (about 1 mag fainter in the Sloan z' filter; therefore its flux is $\sim 40\%$ of the flux of the dominant and $< 30\%$ of the combined flux (Law et al., 2006)) contributing to the observed $v \sin i$, that places it within the $45 \pm 5 \text{ km s}^{-1}$ range. With this caveat, we determined the lower limit of the primary's equatorial inclination angle to be in the range of $24.5_{-3}^{+3.5}$ degrees, and so it is not orthogonally aligned to the system orbital plane (the vertical magenta line in Figure 5.29). However, for spin axes be aligned with the orbital plane, we inferred that an inclination of ~ 64.8 degrees is expected for 2M J1314+13A (the vertical black dashed line in Figure 5.29).

It will be important that future research investigates an absolutely independent $v \sin i$ measurement for the primary, which would constrain its orbital properties and provide further insight into the possible formation mechanisms responsible for such alignments in this regime.

5.6 Summary

Within this chapter, we have reported on optical observations of two UCD binary systems of spectral types $\sim M7$ and $L1.5$. As we mentioned earlier (section 5.2.1), previous work on 2M J0746+20AB, a brown dwarf binary pair (spectral types $L0 + L1.5$), showed periodic optical variability with periods of approximately 3.3 hrs.

This signal is presumed to originate from one component of the binary. A report of periodic 4.86 GHz radio emission with a 2.07 ± 0.002 hrs period due to the secondary component had, so far, not been matched by a corresponding optical detection of the secondary period. Therefore, one of the more significant findings to emerge from this study is the detection of optical variability in the secondary component of 2M J0746+20AB. We reported on ~ 72 hrs monitoring in I-band of 2M J0746+20AB during three epochs in 2017, using the GUF1 photometer. Utilizing our in-house GUF1 Pipeline and Light Curve Fitter code, all three epochs yielded a rotation period of ~ 3.3 hrs from the slower component, consistent with previous studies (Harding et al., 2013a; Harding et al., 2013b). The results indicate that we discovered the secondary rotation period of 2.14 ± 0.07 hrs, which agrees with the reported secondary period in radio (Berger et al., 2009b). We find the presence of magnetic surface features such as hot or cool spots should be taken into account as the cause of periodic variability in both components.

Several studies of 2M J1314+13AB revealed clear, sinusoidal photometric variability in several optical filters with a period of 3.79 hrs, in good agreement with its 3.89 ± 0.05 hrs radio periodicity (McLean et al., 2011; Williams et al., 2015) and Both the radio and the optical periods measured were attributed to the rotation of the primary component of the binary (McLean et al., 2011; McLean et al., 2012; Williams et al., 2015). Subsequently, Forbrich et al. (2016) detected radio emissions from only one component, the secondary, as identified in the VLBI observations. We therefore attribute that the radio and optical periods detected above are the rotation period of the B component. We present optical photometry of 2M J1314+13AB over a period of ~ 1.3 yrs, encompassing three separate epochs, obtained with the GUF1 photometer. We obtained ~ 50 hrs of monitoring in I-band, used two different photometric tools, and in addition, used our Light Curve Fitter code. All three epochs, and both photometric techniques, showed clearly that we discovered the primary rotation period of 2.06 ± 0.05 hrs and 2.05 ± 0.006 hrs for Fixed Aperture + No LuckyPhot (GUF1 photometry) and

Optimum Aperture + LuckyPhot techniques, respectively. Also, our results revealed a rotation period for the secondary component of 3.79 ± 0.05 hrs for F.A. + No LuckyPhot (GUF1 photometry) and 3.78 ± 0.008 hrs for O.A. + LuckyPhot, in agreement with McLean et al. (2011) and Williams et al. (2015). Our results demonstrate two things. First, our findings are consistent with research showing the existence of such optical variation in 2M J1314+13B and 2M J0746+20A. Second, our findings support the presence of optical variability in the primary and secondary components of both binaries. In addition, our results add further weight to a likely association between the source of optical and radio periodic variability in late-M dwarfs. However, at this point, the underlying physical cause of such a possible connection remains unclear.

Our newly discovered or confirmed rotation periods, in addition to other variables available in the literature, have allowed us to investigate the orientation of the binary equatorial axes with respect to the system orbital plane, thus investigating the orbital coplanarity of these very low mass binary systems. Our results on the axial properties of 2M J0746+20A, 2M J0746+20B and 2M J1314+13B, are broadly consistent with previous work (Harding et al., 2013b; Dupuy et al., 2016).

We have demonstrated the effectiveness of using the LuckyPhot technique on every night of data of 2M J1314+13AB. Since the LuckyPhot technique can reduce the short timescale atmospheric scatter in the reference stars, which also leads to a reduction in photometric error in the selected target star, this improved the confidence of short term variability observed in this target.

"The grand aim of all science is to cover the greatest number of empirical facts by logical deduction from the smallest number of hypotheses or axioms."

Einstein

Chapter 6

Conclusions and Future Work

6.1 Discussion and Conclusions

In this work, we have presented a comprehensive analysis of dozens of nights of I-band observations of cool stars and brown dwarfs, searching for subtle variabilities in their light output, and relating this behaviour to their magnetic fields and aurorae. Using the Galway Ultra Fast Imager (GUFi) installed on the Vatican Advanced Technology Telescope at Mount Graham Observatory, in Arizona, we obtained over ~ 160 hrs monitoring in I-band to study periodic variability in the optical emission from four radio detected ultracool dwarfs: the M7 dwarf tight binary 2M J1314+13AB and the L0+L1.5 dwarf tight binary 2M J0746+20AB, the M9.5 dwarf BRI 0021, and the L3.5 dwarf 2M J0036. All selected objects are known rapid rotators ($v \sin i > 19 \text{ km s}^{-1}$).

This thesis in addition assessed the use of two photometric analysis tools, (1) GUFi pipeline with Fixed Aperture photometry (F.A.) and (2) Optimum Aperture (O.A.) with LuckyPhot, to determine which analysis tool could maximize the quality of ground-based photometric measurements so as to allow better lightcurves to be produced (with lower photometric scatter) from a given data set. The test cases were one of our single dwarfs (2M J0036) and one of our binary dwarfs (2M J1314+13AB). LuckyPhot proved to be the better technique in this regard. The effectiveness of the LuckyPhot technique along with O.A. is shown in all examples, as the photometric scatter caused by the turbulent atmosphere effects was considerably decreased through its frame selection routine. On the evidence of the 4 nights analysed in Figures 4.14 - 4.17 and Figure 5.25, the photometric scatter caused by atmospheric turbulence effects was decreased by between 14% and 59%, and it never increased.

In this work, we report optical photometric periodic modulations from all selected dwarfs and confirm the periodicity revealed in previous optical/radio studies. In

each case, the optical periodicity was revealed in the form of quasi-sinusoidal periodic modulations.

For the magnetically active L3.5 dwarf 2M J0036, preliminary work undertaken by Lane et al. (2007); Harding et al. (2013a); Metchev et al. (2015); Croll et al. (2016); Berger et al. (2005); and Hallinan et al. (2008) revealed a periodicity of ~ 3 hrs in the optical, radio and infrared. Our measured result ties well with these previous studies since we report a very consistent optical rotation period of 3.11 ± 0.03 hrs using F.A. (GUFI photometry) and 3.081 ± 0.0005 using O.A. with LuckyPhot. The variation had a peak-to-peak amplitude of 0.0013 - 0.0051 mag for F.A. and 0.0012 - 0.0046 mag for O.A. with the LuckyPhot.

Another dwarf, BRI 0021, was identified as a newly discovered optical variable in our data. Our findings for BRI 0021-0214 go beyond previous studies, showing that the M9.5 dwarf exhibited periodic modulation of 3.052 ± 0.001 hrs, with an amplitude variability of 0.0031- 0.0056 mag. This new rotation period is consistent with a maximum rotation period of ~ 3.59 hrs inferred from the $v \sin i$ observations (Mohanty and Basri, 2003), and in good agreement with Martín et al. (2001) who expected the rotation period to be ~ 3.36 hrs (error bars not given). When combined with rotational velocity data obtained from previous work, our newly discovered rotation periods for BRI 0021 and 2M J0036 give an interesting result: an inclination angle of $51.6^{+0.3}_{-0.2}$ and 62.6 ± 0.3 degrees for the rotation axis relative to our line of sight for BRI 0021 and 2M J0036, respectively.

Part of our original motivation for carrying out these observations was to seek and characterize any optical modulations in each component of the tight binaries in our sample, 2M J1314+13AB and 2M J0746+20AB. To do so, we applied a novel tool, Light Curve Fitter (LCF), designed to deconvolve two component signals within a combined binary optical time series. Applied to both binaries, this was used to refine the dominant's variability parameters and search for the

elusive weaker period. The data for 2M J0746+20AB confirmed the periodic nature of the 2M J0746+20A, yielding a rotation period of 3.32 ± 0.003 hrs with peak-to-peak amplitude variability of $0.0014 - 0.0154$ mag, consistent with previous optical and radio studies (Harding et al., 2013a; Harding et al., 2013b; Zhang et al. 2020). Our results also indicate that, for the first time, we have detected an optical periodicity of 2.14 ± 0.07 hrs with an amplitude of $0.0011 - 0.0053$ mag for the secondary. This agrees with the secondary radio period detected by Berger et al. (2009b), Lynch et al. (2015) and Zhang et al. (2020), who reported periodicity of 2.072 ± 0.001 hrs, 2.071481 ± 0.000002 hrs and 2.1 ± 0.1 hrs, respectively.

Using the same strategy, we detected periodic modulation in the photometry of the first binary sample 2M J1314+13AB. All three observation epochs revealed rotation periods of 3.79 ± 0.05 hrs and 3.78 ± 0.008 hrs using the F.A. and O.A. techniques, respectively. This is in exact agreement with McLean et al. (2011) and Williams et al. (2015) who detected radio and optical periods of 3.89 ± 0.05 hrs and 3.7859 ± 0.0001 hrs, respectively, in both cases attributed to the B component of the binary. In addition, we discovered a new optical period of 2.06 ± 0.05 hrs with an amplitude variation between $0.0011 - 0.0086$ mag for the standard GUF1 photometry and 2.05 ± 0.006 hrs with an amplitude variation between $0.0012 - 0.0092$ mag for O.A. + LuckyPhot. We attribute this shorter period to the primary component. The stability of periodicity in the secondary variable signal of these tight binaries had been seen in both radio and spectroscopic data, and the mechanism behind these processes could possibly be fundamentally linked. We speculate that the underlying physical cause of such a possible connection could be related to some kind of magnetic phenomenon (e.g. auroral activity).

The rotation periods we discovered or confirmed in the tight binaries in our sample, have allowed us to investigate the alignment of the spin-orbital axes of

2M J0746+20A, 2M J0746+20B and 2M J1314+13B, thus investigating the orbital coplanarity of these very low mass binary systems. Our results on the orbital properties of these objects are broadly consistent with previous work (Harding et al., 2013b; Dupuy et al., 2016; Dupuy & Liu, 2017), as the 2M J0746+20A and 2M J0746+20B equatorial inclinations are within ~ 10 and ~ 5 degrees, respectively, of the orbital inclination angle of ~ 41.8 degrees. Assuming that the known $v \sin i$ is entirely due to the secondary component, 2M J1314+13B appears to have an equatorial inclination angle of ~ 50.6 degrees, orthogonal to the orbital plane of ~ 49.34 degrees. The established geometric results of 2M J0746+20A, 2M J0746+20B and 2M J1314+13B may support the detectable beaming of each system (Figure 5.26, Figure 5.27 and Figure 5.28). However, this relies on the alignment of the magnetic field of each binary member being equal to its rotation axes.

In all cases, our observed periodic modulations are correlated with stellar rotation periods in the literature. To explain this rotational modulation, we consider a number of probable sources for producing optical variability. These include magnetic-induced spots, atmospheric dust, and auroral hot spots, or alternatively a mix of them. A number of studies have pointed out that M, L, and T dwarfs exhibit magnetic activity including auroral, even in a regime where dust is believed to be dominant. Therefore, any of the three mechanisms might be responsible for, or perhaps affect the shape of the photometric lightcurve of our samples. But the other characteristics known for 2M J0746+20AB, 2M J0036, BRI 0021 and 2M J1314+13AB (radio – active and H_{α} – active) can be combined with our results to narrow the possibilities. We found that the variability parameters of the 2M J0746+20A are stable on timescales of years. Such stability is unlikely in the case of dust clouds on the surface of the object, since Berger et al. (2009) reported a variable H_{α} chromospheric emission and an active magnetosphere. In addition Zhang et al. (2020) found that both binary members are radio emitters, and discovered radio periodicity in the slower member of 3.2 ± 0.2 hrs. Our newly

discovered optical variability for 2M J0746+20B is consistent with the reported 4.86 GHz radio emission with a period of ~ 2.07 hrs period, as well as quasi sinusoidal H_{α} emission with the same period (Berger et al., 2009b; Lynch et al., 2015; Zhang et al. 2020), confirming the presence of a ~ 1.7 kG magnetic field for the 4.86 GHz radio detected pulse (Berger et al., 2009b), which is consistent with (Antonova et al., 2008). These findings may support the idea of a correlation between radio, spectroscopic and photometric wavelengths in components A and B. Zic et al. (2018) used the Giant Metre Radio Telescope array at 600 MHz and 1.3 GHz, showed the presence of stable radio emission in both bands, with suggestions of a dominant coherent component at 1.3 GHz. The tentative detection of highly polarized emission at 1.3 GHz is consistent with auroral emission. Thus, the presence of magnetic surface features such as auroral hot spot or cool spots should be considered for both binary components. In the case of the intriguing L3.5 ultra-cool dwarf 2M J0036, the source of the variability of this dwarf has been attributed to a magnetic spot (Lane et al., 2007). Croll et al. (2016) suggested that the plausible cause of variability is a magnetic spot, with some complex interaction between hot (aurora)/cool magnetic spots and clouds of dust. We cannot give any insight into these possibilities from our optical data. Notwithstanding the foregoing, we report a degree of variability for 2M J0036.

As a result, the auroral mechanism appears to be the most likely process to generate such radio beams in these UCDs, as demonstrated for the first time in the nearby M8.5 dwarf LSR J1835+3259 by synchronizing periodic H_{α} modulations with beamed coherent emission (Hallinan et al., 2015). In the case of the M9.5 dwarf, BRI 0021 was associated with intermittent H_{α} flaring activity and coherent radio emission, which is certainly a hint of magnetic activity of this object. We suggest that this dwarf is likely to be variable due to more than one astrophysical cause. Time-evolving atmospheric dust clouds could periodically conceal the cool/hot spots on the stellar surface (Lane et al. 2007; Heinze et al. 2013; Metchev et al. 2015), with the auroral activity which could play an

occasional role in the ultracool dwarf regimes (Hallinan et al., 2015). Lastly, In the case of 2M J1314+13AB, authors e.g. McLean et al. (2011) suggested that magnetically induced spots are the cause of the rotational modulation in both components of 2M J1314+13AB. Since they found that g- and i- band variations are in phase, this correlation is compatible with models of star spots induced variability. We speculate that the same magnetic features may be responsible for the periodic behavior at radio and optical wavelengths. Indeed, the correlation optical/radio variability observed in the B component can be caused by an auroral electrodynamic engine.

6.2 Future Work

6.2.1 LuckyPhot Development

Some aspects in the LuckyPhot technique require further development that could fruitfully yield better results. For instance, we aggregated data points into groups by fixed time sections, which is convenient but this may not be optimal. The selection process of reference stars for the differential photometry may be another area of potential development of LuckyPhot technique. In its current state, LuckyPhot is based on a pre-selection process by the user. As we discussed in Section 3.4, the LuckyPhot technique requires that for a frame to be selected all reference (comparison) stars within that frame must be chosen through its σ limits. The least coherent reference star, therefore, dominates the process. An analysis of which ensemble stars would deliver better results would prove to be a reasonable approach. There may be a trade-off between the number of comparison stars used in this photometric analysis and the quality of each comparison star.

6.2.2 Upgrading the Galway Ultra Fast Imager (GUFImk. III)

As detailed in Section 2.3, GUFImk. III is an imaging photometer designed for, and dedicated to, studying variable astronomical objects at the highest temporal resolutions. GUFImk. III uses an Andor iXon CCD (Charge Coupled Device) camera with an 8.2mm sensor diagonal. Considered top of the range in 2005, this camera

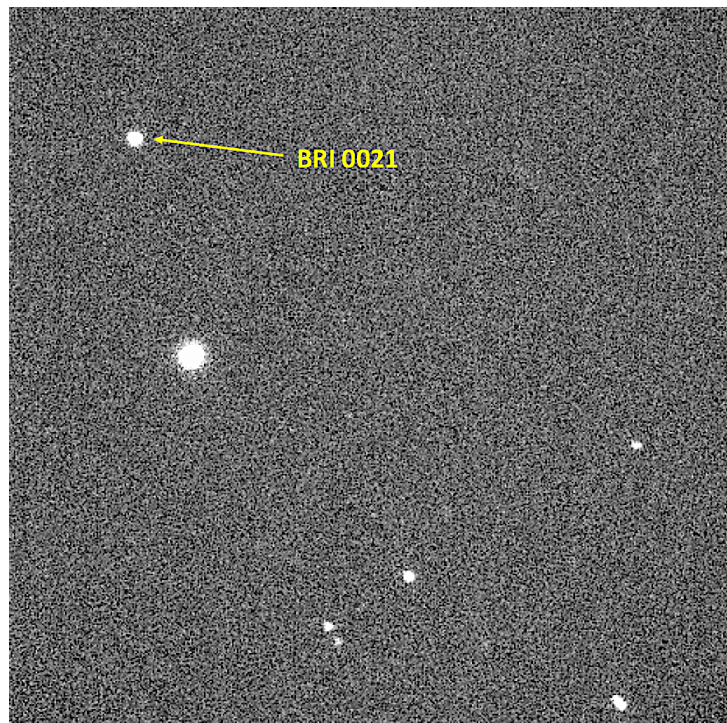


Figure 6.1 I-band image of the BRI 0021 field, obtained at the 1.8m VATT using our GUFImk. III photometer. The 3' x 3' FOV of GUFImk. III is relatively small and there was a lower chance of finding a suitable comparison star nearby.

is dated compared to current models, making GUFImk. III borderline obsolete. Therefore, we propose to upgrade GUFImk. III with a much larger sensor employing new, low-noise sCMOS (scientific Complementary Metal Oxide Semiconductor) technology: an Andor Marana camera with a 32mm sensor diagonal. Integrated

into GUF1, we could observe a 15 times larger area of sky at greater sensitivity, which will confer huge advantages. Its current small CCD sensor limits the field of view size to 3' x 3' with its focal reducer, so in some cases we cannot capture the minimum viable number of comparison stars for differential photometry, e.g. our target BRI 0021 where we were limited to one comparison star (Figure 6.1)

Upgrading GUF1 with the Marana sensor would not only make such targets observable, it would also yield better signal-to-noise results for all observations. This would extend the photometer's ability to study aurorae and space weather around fainter brown dwarfs and stellar systems containing known planets.

Bibliography

- Abt, H. A. and Levy, S. G. (1976) 'Multiplicity among solar-type stars', *The Astrophysical Journal Supplement Series*, 30, 273-306.
- Ackerman, A. S. and Marley, M. S. (2001) 'Precipitating condensation clouds in substellar atmospheres', *The Astrophysical Journal*, 556(2), 872.
- Albrecht, S., Reffert, S., Snellen, I. A. and Winn, J. N. (2009) 'Misaligned spin and orbital axes cause the anomalous precession of DI Herculis', *Nature*, 461(7262), 373.
- Albrecht, S., Winn, J., Fabrycky, D., Torres, G. and Setiawan, J. (2011) 'The BANANA Survey: Spin-Orbit Alignment in Binary Stars', *Proceedings of the International Astronomical Union*, 7(S282), 397-398.
- Alard, C. (2000). Image subtraction using a space-varying kernel. *Astron. & Astrophys. Suppl. Ser.*, 144, 363–370.
- Alard, C., & Lupton, R. H. (1998). A Method for Optimal Image Subtraction. *Astrophys. J.*, 503, 325.
- Allard, F., Hauschildt, P. H., Alexander, D. R., Tamanai, A. and Schweitzer, A. (2001) 'The limiting effects of dust in brown dwarf model atmospheres', *The Astrophysical Journal*, 556(1), 357.
- Allard, F., Hauschildt, P. H., Baraffe, I. and Chabrier, G. (1996) 'Synthetic spectra and mass determination of the brown dwarf Gliese 229B', *The Astrophysical Journal Letters*, 465(2), L123.
- Allard, F., Homeier, D. and Freytag, B. (2012) 'Models of very-low-mass stars, brown dwarfs and exoplanets', *Phil. Trans. R. Soc. A*, 370(1968), 2765-2777.
- Allers, K.N., Vos, J.M., Biller, B.A. and Williams, P.K., 2020. A measurement of the wind speed on a brown dwarf. *Science*, 368(6487), pp.169-172.
- Antonova, A., Doyle, J., Hallinan, G., Bourke, S. and Golden, A. (2008) 'A mini-survey of ultracool dwarfs at 4.9 GHz', *Astronomy & Astrophysics*, 487(1), 317-322.
- Antonova, A., Doyle, J., Hallinan, G., Golden, A. and Koen, C. (2007) 'Sporadic long-term variability in radio activity from a brown dwarf', *Astronomy & Astrophysics*, 472(1), 257-260.

- Artigau, É., Bouchard, S., Doyon, R. and Lafrenière, D. (2009) 'Photometric variability of the T2. 5 brown dwarf SIMP J013656. 5+ 093347: Evidence for evolving weather patterns', *The Astrophysical Journal*, 701(2), 1534.
- Bailer-Jones, C. (2002) 'Dust clouds or magnetic spots? Exploring the atmospheres of L dwarfs with time-resolved spectrophotometry', *Astronomy & Astrophysics*, 389(3), 963-976.
- Bailer-Jones, C. and Mundt, R. (2001) 'Variability in ultra cool dwarfs: Evidence for the evolution of surface features', *Astronomy & Astrophysics*, 367(1), 218-235.
- Bailer-Jones, C. A. (2004) 'Spectroscopic rotation velocities of L dwarfs from VLT/UVES and their comparison with periods from photometric monitoring', *Astronomy & Astrophysics*, 419(2), 703-712.
- Baluev, R. V. (2012) 'Distinguishing between a true period and its alias, and other tasks of model discrimination', *Monthly Notices of the Royal Astronomical Society*, 422(3), 2372-2385.
- Banse, K., Grosbol, P. and Baade, D. (1992) *MIDAS as a Development Environment*, translated by 120.
- Baraffe, I., Chabrier, G., Barman, T. S., Allard, F. and Hauschildt, P. (2003) 'Evolutionary models for cool brown dwarfs and extrasolar giant planets. The case of HD 209458', *Astronomy & Astrophysics*, 402(2), 701-712.
- Baraffe, I., Homeier, D., Allard, F. and Chabrier, G. (2015) 'New evolutionary models for pre-main sequence and main sequence low-mass stars down to the hydrogen-burning limit', *Astronomy & Astrophysics*, 577, A42.
- Barnes, J.R., Jeffers, S.V., Jones, H.R.A., Pavlenko, Y.V., Jenkins, J.S., Haswell, C.A. and Lohr, M.E., 2015. Starspot distributions on fully convective M dwarfs: implications for radial velocity planet searches. *The Astrophysical Journal*, 812(1), p.42.
- Basden, A., Tubbs, B. and Mackay, C. (2004) 'L3CCD's: Low readout noise CCDS in astronomy' in *Scientific Detectors for Astronomy*, Springer, 599-602.
- Basri, G. (2000) 'Observations of brown dwarfs', *Annual Review of Astronomy and Astrophysics*, 38(1), 485-519.
- Basri, G. and Marcy, G. W. (1995) 'A surprise at the bottom of the main sequence: Rapid rotation and NO H-alpha emission', *The Astronomical Journal*, 109, 762-773.

- Basri, G., Marcy, G., Oppenheimer, B., Kulkari, S. R., & Nakajima, T. (1996) 'Rotation and activity in the coolest stars', *Cool stars; stellar systems; and the sun : 9 : Astronomical Society of the Pacific Conference Series*, volume 109; Proceedings of the 9th Cambridge workshop; held 3-6 October 1995 in Florence; Italy; San Francisco: Astronomical Society of the Pacific (ASP); |c1996; edited by Roberto Pallavicini and Andrea K. Dupree, p.587.
- Batalha, N. M., Rowe, J. F., Bryson, S. T., Barclay, T., Burke, C. J., Caldwell, D. A., Christiansen, J. L., Mullally, F., Thompson, S. E. and Brown, T. M. (2013) 'Planetary candidates observed by Kepler. III. Analysis of the first 16 months of data', *The Astrophysical Journal Supplement Series*, 204(2), 24.
- Bate, M., Bonnell, I., Clarke, C., Lubow, S., Ogilvie, G., Pringle, J. and Tout, C. (2000) 'Observational implications of precessing protostellar discs and jets', *Monthly Notices of the Royal Astronomical Society*, 317(4), 773-781.
- Benz, A. (2002) 'Plasma astrophysics: kinetic processes in solar and stellar coronae, astrophysics and space science library', Kluwer, Dordrecht. doi, 10, 0-306.
- Benz, A. and Güdel, M. (1994) 'The soft X-ray/microwave ratio of solar and stellar flares and coronae'.
- Benz, A. O. (1993) 'X-ray/microwave relation of different types of active stars', *Astrophysical Letters & Communications*, 405(Astrophysical Letters & Communications).
- Berdyugina, S. V. (2005) 'Starspots: a key to the stellar dynamo', *Living Reviews in Solar Physics*, 2(1), 8.
- Berger, E. (2002) 'Flaring up All Over—Radio Activity in Rapidly Rotating Late M and L Dwarfs', *The Astrophysical Journal*, 572(1), 503.
- Berger, E. (2006) 'Radio observations of a large sample of late m, l, and t dwarfs: The distribution of magnetic field strengths', *The Astrophysical Journal*, 648(1), 629.
- Berger, E., Ball, S., Becker, K., Clarke, M., Frail, D., Fukuda, T., Hoffman, I., Mellon, R., Momjian, E. and Murphy, N. (2001) 'Discovery of radio emission from the brown dwarf LP944-20', *Nature*, 410(6826), 338.
- Berger, E., Basri, G., Fleming, T., Giampapa, M., Gizis, J., Liebert, J., Martín, E., Phan-Bao, N. and Rutledge, R. (2009a) 'Simultaneous multi-wavelength observations of magnetic activity in ultracool dwarfs. III. X-ray, radio, and H α activity trends in M and L dwarfs', *The Astrophysical Journal*, 709(1), 332.

- Berger, E., Gizis, J., Giampapa, M., Rutledge, R., Liebert, J., Martín, E., Basri, G., Fleming, T., Johns-Krull, C. and Phan-Bao, N. (2008) 'Simultaneous multiwavelength observations of magnetic activity in ultracool dwarfs. I. The complex behavior of the M8. 5 dwarf TVLM 513–46546', *The Astrophysical Journal*, 673(2), 1080.
- Berger, E., Rutledge, R., Phan-Bao, N., Basri, G., Giampapa, M., Gizis, J., Liebert, J., Martín, E. and Fleming, T. (2009b) 'Periodic Radio and H α emission from the L dwarf binary 2MASSW J0746425+ 200032: exploring the magnetic field topology and radius of an L dwarf', *The Astrophysical Journal*, 695(1), 310.
- Berger, E., Rutledge, R., Reid, I., Bildsten, L., Gizis, J., Liebert, J., Martín, E., Basri, G., Jayawardhana, R. and Brandeker, A. (2005) 'The magnetic properties of an L dwarf derived from simultaneous Radio, X-Ray, and H α Observations', *The Astrophysical Journal*, 627(2), 960.
- Bingham, R., Cairns, R. and Kellett, B. (2001) 'Coherent cyclotron maser radiation from UV Ceti', *Astronomy & Astrophysics*, 370(3), 1000-1003.
- Blake, C. H., Charbonneau, D. and White, R. J. (2010) 'The NIRSPEC ultracool dwarf radial velocity survey', *The Astrophysical Journal*, 723(1), 684.
- Bodenheimer, P. (1978) 'Evolution of rotating interstellar clouds. III-On the formation of multiple star systems', *The Astrophysical Journal*, 224, 488-496.
- Bouy, H., Duchêne, G., Köhler, R., Brandner, W., Bouvier, J., Martín, E., Ghez, A., Delfosse, X., Forveille, T. and Allard, F. (2004) 'First determination of the dynamical mass of a binary L dwarf', *Astronomy & Astrophysics*, 423(1), 341-352.
- Bouy, H., Martín, E., Brandner, W., Forveille, T., Delfosse, X., Huélamo, N., Basri, G., Girard, J., Osorio, M.-R. Z. and Stumpf, M. (2008) 'Follow-up observations of binary ultra-cool dwarfs', *Astronomy & Astrophysics*, 481(3), 757-767.
- Bowdalo, D. R., Evans, M. J. and Sofen, E. D. (2016) 'Spectral analysis of atmospheric composition: application to surface ozone model–measurement comparisons', *Atmospheric Chemistry and Physics*, 16(13), 8295-8308.
- Browning, M. K. (2008) 'Simulations of dynamo action in fully convective stars', *The Astrophysical Journal*, 676(2), 1262.
- Buenzli, E., Apai, D., Radigan, J., Reid, I. N. and Flabelau, D. (2014) 'Brown dwarf photospheres are patchy: a hubble space telescope near-infrared spectroscopic survey finds frequent low-level variability', *The Astrophysical Journal*, 782(2), 77.

- Burgasser, A. J. (2001) 'The spectra and classification of L and T dwarfs', arXiv preprint astro-ph/0109422.
- Burgasser, A. J., Kirkpatrick, J. D., Brown, M. E., Reid, I. N., Burrows, A., Liebert, J., Matthews, K., Gizis, J. E., Dahn, C. C. and Monet, D. G. (2002) 'The spectra of T dwarfs. I. Near-infrared data and spectral classification', *The Astrophysical Journal*, 564(1), 421.
- Burgasser, A. J. and Putman, M. E. (2005) 'Quiescent Radio Emission from Southern Late-Type M Dwarfs and a Spectacular Radio Flare from the M8 Dwarf DENIS 1048–3956', *The Astrophysical Journal*, 626(1), 486.
- Burrows, A., Hubbard, W. B., Lunine, J. and Liebert, J. (2001) 'The theory of brown dwarfs and extrasolar giant planets', *Reviews of Modern Physics*, 73(3), 719.
- Burrows, A., Hubbard, W. B., Saumon, D. and Lunine, J. (1993) 'An expanded set of brown dwarf and very low mass star models', *The Astrophysical Journal*, 406, 158-171.
- Burrows, A., Marley, M., Hubbard, W. B., Lunine, J., Guillot, T., Saumon, D., Freedman, R., Sudarsky, D. and Sharp, C. (1997) 'A nongray theory of extrasolar giant planets and brown dwarfs', *The Astrophysical Journal*, 491(2), 856.
- Bushby, P. and Mason, J. (2004) 'Understanding the solar dynamo', *Astronomy & Geophysics*, 45(4), 4.7-4.13.
- Catalano, S., Biazzo, K., Frasca, A. and Marilli, E. (2002) 'Measuring starspot temperature from line depth ratios-I. The method', *Astronomy & Astrophysics*, 394(3), 1009-1021.
- Cesetti, M., Pizzella, A., Ivanov, V.D., Morelli, L., Corsini, E.M. and Dalla Bontà, E., 2013. The Infrared Telescope Facility (IRTF) spectral library:-Spectral diagnostics for cool stars. *Astronomy & Astrophysics*, 549, p.A129.
- Chabrier, G. and Baraffe, I. (1997) 'Structure and evolution of low-mass stars', arXiv preprint astro-ph/9704118.
- Chabrier, G. and Baraffe, I. (2000) 'Theory of low-mass stars and substellar objects', *Annual Review of Astronomy and Astrophysics*, 38(1), 337-377.
- Chabrier, G., Baraffe, I., Allard, F. and Hauschildt, P. (2000) 'Evolutionary models for very low-mass stars and brown dwarfs with dusty atmospheres', *The Astrophysical Journal*, 542(1), 464.

- Chabrier, G. and Küker, M. (2006) 'Large-scale-dynamo in low-mass stars and brown dwarfs', *Astronomy & Astrophysics*, 446(3), 1027-1037.
- Christensen, U.R., Holzwarth, V. and Reiners, A., 2009. Energy flux determines magnetic field strength of planets and stars. *Nature*, 457(7226), pp.167-169.
- Clarke, F., Hodgkin, S., Oppenheimer, B., Robertson, J. and Haubois, X. (2008) 'A search for J-band variability from late-L and T brown dwarfs', *Monthly Notices of the Royal Astronomical Society*, 386(4), 2009-2014.
- Clarke, F., Oppenheimer, B. and Tinney, C. (2002) 'A mini-survey for variability in early L dwarfs', *Monthly Notices of the Royal Astronomical Society*, 335(4), 1158-1162.
- Clarke, J., Moos, H., Atreya, S. and Lane, A. (1980) 'Observations from Earth orbit and variability of the polar aurora on Jupiter', *The Astrophysical Journal*, 241, L179-L182.
- Coates, C. (2006) 'EMCCD cameras take imaging to a new level', *OPTO AND LASER EUROPE*, 135, 29.
- Collins, A. (2014) '<Development of an Automated Astronomical_Data Reduction Pipeline.pdf>', Ph.D thesis.
- Colón, K. D., Ford, E. B., Lee, B., Mahadevan, S. and Blake, C. H. (2010) 'Characterizing transiting extrasolar planets with narrow-band photometry and GTC/OSIRIS', *Monthly Notices of the Royal Astronomical Society*, 408(3), 1494-1501.
- Cowley, S.W.H. and Bunce, E.J., 2001. Origin of the main auroral oval in Jupiter's coupled magnetosphere-ionosphere system. *Planetary and Space Science*, 49(10-11), pp.1067-1088.
- Cowley, S.W.H., Bunce, E.J. and Prangé, R., 2004. Saturn's polar ionospheric flows and their relation to the main auroral oval.
- Croll, B., Muirhead, P. S., Han, E., Dalba, P. A., Radigan, J., Morley, C. V., Lazarevic, M. and Taylor, B. (2016) 'Long-term, Multiwavelength Light Curves of Ultra-cool Dwarfs: I. An Interplay of Starspots & Clouds Likely Drive the Variability of the L3.5 dwarf 2MASS 0036+ 18', arXiv preprint arXiv:1609.03586.
- Crossfield, I., Biller, B., Schlieder, J., Deacon, N., Bonnefoy, M., Homeier, D., Allard, F., Buenzli, E., Henning, T. and Brandner, W. (2014) 'A global cloud map of the nearest known brown dwarf', *Nature*, 505(7485), 654-656.

- Crossfield, I.J., 2014. Doppler imaging of exoplanets and brown dwarfs. *Astronomy & Astrophysics*, 566, p.A130.
- Dahn, C. C., Harris, H. C., Vrba, F. J., Guetter, H. H., Canzian, B., Henden, A. A., Levine, S. E., Luginbuhl, C. B., Monet, A. K. and Monet, D. G. (2002) 'Astrometry and photometry for cool dwarfs and brown dwarfs', *The Astronomical Journal*, 124(2), 1170.
- Davis, L. (1987) 'Specifications for the aperture photometry package', National Optical Astronomy Observatories.
- De Kleer, K. R. (2009) Photometry and transit-timing analysis for eleven transiting exoplanets, unpublished thesis Massachusetts Institute of Technology.
- Deeg, H. J. and Doyle, L. R. (2001) VAPHOT-A Package for Precision Differential Aperture Photometry, translated by.
- Demory, B.-O., Ségransan, D., Forveille, T., Queloz, D., Beuzit, J.-L., Delfosse, X., Di Folco, E., Kervella, P., Le Bouquin, J.-B. and Perrier, C. (2009) 'Mass-radius relation of low and very low-mass stars revisited with the VLT', *Astronomy & Astrophysics*, 505(1), 205-215.
- Donar, A., Jensen, E. and Mathieu, R. (1999) Protoplanetary Disks in Young Binaries: Testing Coplanarity, translated by 1490.
- Donati, J.-F., Forveille, T., Cameron, A. C., Barnes, J. R., Delfosse, X., Jardine, M. M. and Valenti, J. A. (2006) 'The large-scale axisymmetric magnetic topology of a very-low-mass fully convective star', *Science*, 311(5761), 633-635.
- Donati, J.-F., Morin, J., Petit, P., Delfosse, X., Forveille, T., Aurière, M., Cabanac, R., Dintrans, B., Fares, R. and Gastine, T. (2008) 'Large-scale magnetic topologies of early M dwarfs', *Monthly Notices of the Royal Astronomical Society*, 390(2), 545-560.
- Doyle, P. (2015) 'Building a scalable global data processing pipeline for large astronomical photometric datasets', arXiv preprint arXiv:1502.02821.
- Dravins, D., Lindegren, L., Mezey, E. and Young, A. T. (1997) 'Atmospheric intensity scintillation of stars, I. statistical distributions and temporal properties', *Publications of the Astronomical Society of the Pacific*, 109(732), 173.
- Dulk, G. and Marsh, K. (1982) 'Simplified expressions for the gyrosynchrotron radiation from mildly relativistic, nonthermal and thermal electrons', *The Astrophysical Journal*, 259, 350-358.

- Dulk, G. A. (1985) 'Radio emission from the sun and stars', *Annual review of astronomy and astrophysics*, 23(1), 169-224.
- Dupuy, T. J., Forbrich, J., Rizzuto, A., Mann, A. W., Aller, K., Liu, M. C., Kraus, A. L. and Berger, E. (2016) 'High-Precision Radio and Infrared Astrometry of Lspm J1314+1320ab. II. Testing Pre-Main-Sequence Models at the Lithium Depletion Boundary With Dynamical Masses', *The Astrophysical Journal*, 827(1), 23.
- Dupuy, T. J., Liu, M. C., Bowler, B. P., Cushing, M. C., Helling, C., Witte, S. and Hauschildt, P. (2010) 'Studying the physical diversity of late-M dwarfs with dynamical masses', *The Astrophysical Journal*, 721(2), 1725.
- Dupuy, T.J. and Liu, M.C., 2017. Individual Dynamical Masses of Ultracool Dwarfs. *The Astrophysical Journal Supplement Series*, 231(2), p.15.
- Durney, B. R., De Young, D. S. and Roxburgh, I. W. (1993) 'On the generation of the large-scale and turbulent magnetic fields in solar-type stars', *Solar Physics*, 145(2), 207-225.
- Dieterich, S.B., Henry, T.J., Jao, W.C., Winters, J.G., Hosey, A.D., Riedel, A.R. and Subasavage, J.P., 2014. The solar neighborhood. XXXII. The hydrogen burning limit. *The Astronomical Journal*, 147(5), p.94.
- Enoch, M. L., Brown, M. E. and Burgasser, A. J. (2003) 'Photometric variability at the L/T dwarf boundary', *The Astronomical Journal*, 126(2), 1006.
- Everett, M. E. and Howell, S. B. (2001) 'A Technique for Ultrahigh-Precision CCD Photometry', *Publications of the Astronomical Society of the Pacific*, 113(789), 1428.
- Fegley Jr, B. and Lodders, K. (1996) 'Atmospheric chemistry of the brown dwarf Gliese 229B: Thermochemical equilibrium predictions', *The Astrophysical Journal Letters*, 472(1), L37.
- Fekel Jr, F. (1981) 'The properties of close multiple stars', *The Astrophysical Journal*, 246, 879-898.
- Filippazzo, J.C., Rice, E.L., Faherty, J., Cruz, K.L., Van Gordon, M.M. andLooper, D.L., 2015. Fundamental parameters and spectral energy distributions of young and field age objects with masses spanning the stellar to planetary regime. *The Astrophysical Journal*, 810(2), p.158.

- Fitzgerald, K., Browne, L.-M. and Butler, R. F. (2019) 'Using the Agile software development lifecycle to develop a standalone application for generating colour magnitude diagrams', *Astronomy and Computing*, 28, 100283.
- Forbrich, J., Dupuy, T. J., Reid, M. J., Berger, E., Rizzuto, A., Mann, A. W., Liu, M. C., Aller, K. and Kraus, A. L. (2016) 'High-Precision Radio and Infrared Astrometry of Lspm J1314+ 1320ab. I. Parallax, Proper Motions, and Limits on Planets', *The Astrophysical Journal*, 827(1), 22.
- Foreman-Mackey, D., Hogg, D.W., Lang, D. and Goodman, J., 2013. emcee: the MCMC hammer. *Publications of the Astronomical Society of the Pacific*, 125(925), p.306.
- Fuhrmeister, B. and Schmitt, J. (2004) 'Detection and high-resolution spectroscopy of a huge flare on the old M 9 dwarf DENIS 104814.7-395606.1', *Astronomy & Astrophysics*, 420(3), 1079-1085.
- Fukugita, M., Shimasaku, K., Ichikawa, T. and Gunn, J. (1996) The Sloan digital sky survey photometric system, SCAN-9601313.
- Gaponov, A. (1959a) 'Interaction between electron fluxes and electromagnetic waves in waveguides', *Izv. Vyssh. Uchebn. Zaved. Radiofiz*, 2, 450.
- Gaponov, A. (1959b) 'Interaction of irrectilinear electron beams with electromagnetic waves in transmission lines', *Izu. VUZov Radiofizika*, 2, 836-837.
- Gelino, C. R., Marley, M. S., Holtzman, J. A., Ackerman, A. S. and Lodders, K. (2002) 'L dwarf variability: I-band observations', *The Astrophysical Journal*, 577(1), 433.
- Gillon, M., Triaud, A., Jehin, E., Delrez, L., Opitom, C., Magain, P., Lendl, M. and Queloz, D. (2013) 'Fast-evolving weather for the coolest of our two new substellar neighbours', *Astronomy & Astrophysics*, 555, L5.
- Gizis, J. E., Monet, D. G., Reid, I. N., Kirkpatrick, J. D., Liebert, J. and Williams, R. J. (2000) 'New neighbors from 2MASS: activity and kinematics at the bottom of the main sequence', *The Astronomical Journal*, 120(2), 1085.
- Gizis, J. E., Paudel, R. R., Mullan, D., Schmidt, S. J., Burgasser, A. J. and Williams, P. K. (2017) 'K2 Ultracool Dwarfs Survey. II. The White Light Flare Rate of Young Brown Dwarfs', *The Astrophysical Journal*, 845(1), 33.
- Goodman, J. and Weare, J., 2010. Ensemble samplers with affine invariance. *Communications in applied mathematics and computational science*, 5(1), pp.65-80.

- Goldman, B., Cushing, M., Marley, M., Artigau, É., Baliyan, K., Béjar, V., Caballero, J., Chanover, N., Connelley, M. and Doyon, R. (2008) 'CLOUDS search for variability in brown dwarf atmospheres-Infrared spectroscopic time series of L/T transition brown dwarfs', *Astronomy & Astrophysics*, 487(1), 277-292.
- Goldman, B., Pitann, J., Osorio, M.Z., Bailer-Jones, C.A.L., Béjar, V.J.S., Caballero, J.A. and Henning, T., 2009. Polarisation of very-low-mass stars and brown dwarfs-i. vlt/fors1 optical observations of field ultra-cool dwarfs. *Astronomy & Astrophysics*, 502(3), pp.929-936.
- Gonzales, E.C., Faherty, J.K., Gagné, J., Artigau, É. and Gagliuffi, D.B., 2018. Understanding Fundamental Properties and Atmospheric Features of Subdwarfs via a Case Study of SDSS J125637. 13–022452.4. *The Astrophysical Journal*, 864(1), p.100.
- Guedel, M. and Benz, A. O. (1993) 'X-ray/microwave relation of different types of active stars', *The Astrophysical Journal*, 405, L63-L66.
- Güdel, M. (2002) 'Stellar radio astronomy: probing stellar atmospheres from protostars to giants', *Annual Review of Astronomy and Astrophysics*, 40(1), 217-261.
- Hale, A. (1994) 'Orbital coplanarity in solar-type binary systems: Implications for planetary system formation and detection', *The Astronomical Journal*, 107, 306-332.
- Hallinan, G., Antonova, A., Doyle, J., Bourke, S., Briskin, W. and Golden, A. (2006) 'Rotational Modulation of the Radio Emission from the M9 Dwarf TVLM 513–46546: Broadband Coherent Emission at the Substellar Boundary?', *The Astrophysical Journal*, 653(1), 690.
- Hallinan, G., Antonova, A., Doyle, J., Bourke, S., Lane, C. and Golden, A. (2008) 'Confirmation of the electron cyclotron maser instability as the dominant source of radio emission from very low mass stars and brown dwarfs', *The Astrophysical Journal*, 684(1), 644.
- Hallinan, G., Bourke, S., Lane, C., Antonova, A., Zavala, R., Briskin, W. F., Boyle, R., Vrba, F., Doyle, J. and Golden, A. (2007) 'Periodic bursts of coherent radio emission from an ultracool dwarf', *The Astrophysical Journal Letters*, 663(1), L25.
- Hallinan, G., Littlefair, S., Cotter, G., Bourke, S., Harding, L., Pineda, J., Butler, R., Golden, A., Basri, G. and Doyle, J. (2015) 'Magnetospherically driven optical and radio aurorae at the end of the stellar main sequence', *Nature*, 523(7562), 568.

- Harding, L. K. (2012) '<The Optical Signatures of Magnetospheric Phenomena at the_End of the Main Sequence and Beyond.pdf>', Ph.D thesis.
- Harding, L. K., Hallinan, G., Boyle, R. P., Golden, A., Singh, N., Sheehan, B., Zavala, R. T. and Butler, R. F. (2013a) 'Periodic optical variability of radio-detected ultracool dwarfs', *The Astrophysical Journal*, 779(2), 101.
- Harding, L. K., Hallinan, G., Konopacky, Q. M., Kratter, K. M., Boyle, R. P., Butler, R. F. and Golden, A. (2013b) 'Spin-orbit alignment in the very low mass binary regime-The L dwarf tight binary 2MASSW J0746425+ 200032AB', *Astronomy & Astrophysics*, 554, A113.
- Hauschildt, P. H., Allard, F. and Baron, E. (1999) 'The NEXTGEN model atmosphere grid for $3000 \leq T_{\text{eff}} \leq 10,000$ K', *The Astrophysical Journal*, 512(1), 377.
- Hayashi, C. and Nakano, T. (1963) 'Evolution of Stars of Small Masses in the Pre-Main-Sequence Stages', *Progress of Theoretical Physics*, 30(4), 460-474.
- Heinze, A.N., Metchev, S., Apai, D., Flateau, D., Kurtev, R., Marley, M., Radigan, J., Burgasser, A.J., Artigau, É. and Plavchan, P., 2013. Weather on Other Worlds. I. Detection of Periodic Variability in the L3 Dwarf DENIS-P J1058. 7-1548 with Precise Multi-wavelength Photometry. *The Astrophysical Journal*, 767(2), p.173.
- Herczeg, G. J. and Hillenbrand, L. A. (2014) 'An optical spectroscopic study of T Tauri stars. I. Photospheric properties', *The Astrophysical Journal*, 786(2), 97.
- Hewitt, R., Melrose, D. and Rönmark, K. (1981) 'A cyclotron theory for the beaming pattern of Jupiter's decametric radio emission', *Publications of the Astronomical Society of Australia*, 4(2), 221-226.
- Hirsch, M., Wareham, R. J., Martin-Fernandez, M. L., Hobson, M. P. and Rolfe, D. J. (2013) 'A stochastic model for electron multiplication charge-coupled devices—from theory to practice', *PLoS one*, 8(1), e53671.
- Howe, R. (2009) 'Solar interior rotation and its variation', *Living Reviews in Solar Physics*, 6(1), 1.
- Howell, S. B. (2006) *Handbook of CCD astronomy*, Cambridge University Press.
- Hoxie, D. T. (1970) 'The structure and evolution of stars of very low mass', *The Astrophysical Journal*, 161, 1083.
- Janesick, J. R. (2001) *Scientific charge-coupled devices*, SPIE press Bellingham.

- Jensen, E. L., Mathieu, R. D., Donar, A. X. and Dullighan, A. (2004) 'Testing protoplanetary disk alignment in young binaries', *The Astrophysical Journal*, 600(2), 789.
- Jensen, E. L. N. D., Arianne X.; Mathieu, Robert D. (2000) '<Aligned Disks in Pre--Main Sequence Binaries.pdf>'.
<https://arxiv.org/abs/astro-ph/0005111>
- Johns-Krull, C. M. and Valenti, J. A. (1996) 'Detection of strong magnetic fields on M dwarfs', *The Astrophysical Journal Letters*, 459(2), L95.
- Johnson, H. and Morgan, W. (1953) 'Fundamental stellar photometry for standards of spectral type on the revised system of the Yerkes spectral atlas', *The Astrophysical Journal*, 117, 313.
- Jones, H. R., Pavlenko, Y., Viti, S., Barber, R., Yakovina, L. A., Pinfield, D. and Tennyson, J. (2005) 'Carbon monoxide in low-mass dwarf stars', *Monthly Notices of the Royal Astronomical Society*, 358(1), 105-112.
- Kao, M. M., Hallinan, G., Pineda, J. S., Escala, I., Burgasser, A., Bourke, S. and Stevenson, D. (2016) 'Auroral radio emission from late L and T dwarfs: A new constraint on dynamo theory in the substellar regime', *The Astrophysical Journal*, 818(1), 24.
- Kellett, B., Bingham, R., Cairns, R. and Tsikoudi, V. (2002) 'Can late-type active stars be explained by a dipole magnetic trap?', *Monthly Notices of the Royal Astronomical Society*, 329(1), 102-108.
- Kirkpatrick, J. D. (2005) 'New spectral types L and T', *Annu. Rev. Astron. Astrophys.*, 43, 195-245.
- Kirkpatrick, J. D., Henry, T. J. and McCarthy Jr, D. W. (1991) 'A standard stellar spectral sequence in the red/near-infrared--Classes K5 to M9', *The Astrophysical Journal Supplement Series*, 77, 417-440.
- Kirkpatrick, J. D., Reid, I. N., Liebert, J., Cutri, R. M., Nelson, B., Beichman, C. A., Dahn, C. C., Monet, D. G., Gizis, J. E. and Skrutskie, M. F. (1999) 'Dwarfs cooler than "M": The definition of spectral type "L" using discoveries from the 2-Micron All-Sky Survey (2MASS)', *The Astrophysical Journal*, 519(2), 802.
- Kirkpatrick, J. D., Reid, I. N., Liebert, J., Gizis, J. E., Burgasser, A. J., Monet, D. G., Dahn, C. C., Nelson, B. and Williams, R. J. (2000) '67 additional L dwarfs discovered by the Two Micron All Sky Survey', *The Astronomical Journal*, 120(1), 447.
- Koen, C. (2006) 'Evidence for rapid evolution of periodic variations in an ultracool dwarf', *Monthly Notices of the Royal Astronomical Society*, 367(4), 1735-1738.

- Konopacky, Q., Ghez, A., Barman, T., Rice, E., Bailey III, J., White, R., McLean, I. and Duchêne, G. (2010) 'High-precision dynamical masses of very low mass binaries', *The Astrophysical Journal*, 711(2), 1087.
- Konopacky, Q., Ghez, A., Fabrycky, D., Macintosh, B., White, R., Barman, T., Rice, E., Hallinan, G. and Duchêne, G. (2012) 'Rotational velocities of individual components in very low mass binaries', *The Astrophysical Journal*, 750(1), 79.
- Kostov, V. and Apai, D., 2013. Mapping directly imaged giant exoplanets. *The Astrophysical Journal*, 762(1), p.47.
- Kumar, S. S. (1963) 'The structure of stars of very low mass', *The Astrophysical Journal*, 137, 1121.
- Lane, C. (2008) 'A Photometric Search for Magnetic Spots on Radio Transient Ultracool Dwarfs', Ph.D thesis.
- Lane, C., Hallinan, G., Zavala, R., Butler, R., Boyle, R., Bourke, S., Antonova, A., Doyle, J., Vrba, F. and Golden, A. (2007) 'Rotational modulation of M/L dwarfs due to magnetic spots', *The Astrophysical Journal Letters*, 668(2), L163.
- Law, N. M., Hodgkin, S. and Mackay, C. (2006) 'Discovery of five very low mass close binaries, resolved in the visible with lucky imaging', *Monthly Notices of the Royal Astronomical Society*, 368(4), 1917-1924.
- Leggett, S., Allard, F., Geballe, T., Hauschildt, P. and Schweitzer, A. (2001) 'Infrared spectra and spectral energy distributions of late M and L dwarfs', *The Astrophysical Journal*, 548(2), 908.
- Lepine, S., Thorstensen, J. R., Shara, M. M. and Rich, R. M. (2009) 'New Neighbors: Parallaxes of 18 nearby stars selected from the LSPM-north catalog', *The Astronomical Journal*, 137(5), 4109.
- Liebert, J., Kirkpatrick, J. D., Cruz, K., Reid, I. N., Burgasser, A., Tinney, C. and Gizis, J. E. (2003) 'A flaring L5 dwarf: the nature of H α emission in very low mass (sub) stellar objects', *The Astronomical Journal*, 125(1), 343.
- Liebert, J., Kirkpatrick, J. D., Reid, I. N. and Fisher, M. (1999) 'A 2MASS ultracool M dwarf observed in a spectacular flare', *The Astrophysical Journal*, 519(1), 345.
- Linnell Nemec, A. and Nemec, J. M. (1985) 'A test of significance for periods derived using phase-dispersion-minimization techniques', *The Astronomical Journal*, 90, 2317-2320.

- Littlefair, S., Dhillon, V., Marsh, T., Shahbaz, T., Martín, E. and Copperwheat, C. (2008) 'Optical variability of the ultracool dwarf TVLM 513-46546: evidence for inhomogeneous dust clouds', *Monthly Notices of the Royal Astronomical Society: Letters*, 391(1), L88-L92.
- Liu, M. C., Dupuy, T. J. and Leggett, S. (2010) 'Discovery of a highly unequal-mass binary T dwarf with Keck laser Guide Star Adaptive Optics: A coevality test of substellar theoretical models and effective temperatures', *The Astrophysical Journal*, 722(1), 311.
- Lomb, N. R. (1976) 'Least-squares frequency analysis of unequally spaced data', *Astrophysics and space science*, 39(2), 447-462.
- Lynch, C., Mutel, R. and Güdel, M. (2015) 'Wideband dynamic radio spectra of two ultracool dwarfs', *The Astrophysical Journal*, 802(2), 106.
- Lynch, C. R. (2014) 'Studying the magnetic fields of cool stars'.
- MacKay, D.J. and Mac Kay, D.J., 2003. *Information theory, inference and learning algorithms*. Cambridge university press.
- Mackey, R., Thornton, D. and Dainty, C. (2005) *Towards a high-speed adaptive optics system for strong turbulence correction*, translated by International Society for Optics and Photonics, 59810L.
- Maiti, M. (2007) 'Observational evidence of optical variability in L dwarfs', *The Astronomical Journal*, 133(4), 1633.
- Mangenev, A. and Veltri, P. (1976) 'On the theory of type I solar radio bursts. I-Beam plasma instabilities in a turbulent magnetized plasma. II-A model for the source', *Astronomy and Astrophysics*, 47, 165-192.
- Marley, M., Saumon, D., Guillot, T., Freedman, R., Hubbard, W. B., Burrows, A. and Lunine, J. (1996) 'Atmospheric, evolutionary, and spectral models of the brown dwarf Gliese 229 B', *Science*, 272(5270), 1919-1921.
- Marley, M. S. and Robinson, T. D. (2015) 'On the cool side: Modeling the atmospheres of brown dwarfs and giant planets', *Annual Review of Astronomy and Astrophysics*, 53, 279-323.
- Martín, E. L., Delfosse, X., Basri, G., Goldman, B., Forveille, T. and Osorio, M. R. Z. (1999) 'Spectroscopic classification of late-M and L field dwarfs', *The Astronomical Journal*, 118(5), 2466.

- Martín, E. L., Osorio, M. R. Z. and Lehto, H. J. (2001) 'Photometric Variability in the Ultracool Dwarf BRI 0021–0214: Possible Evidence for Dust Clouds', *The Astrophysical Journal*, 557(2), 822.
- Ménard, F., Delfosse, X. and Monin, J.L., 2002. Optical linear polarimetry of ultra cool dwarfs. *Astronomy & Astrophysics*, 396(3), pp.L35-L38.
- McLean, M., Berger, E., Irwin, J., Forbrich, J. and Reiners, A. (2011) 'Periodic Radio Emission from the M7 Dwarf 2MASS J13142039+ 1320011: Implications for the Magnetic Field Topology', *The Astrophysical Journal*, 741(1), 27.
- McLean, M., Berger, E. and Reiners, A. (2012) 'The radio activity-rotation relation of ultracool dwarfs', *The Astrophysical Journal*, 746(1), 23.
- Melrose, D. (1976) 'An interpretation of Jupiter's decametric radiation and the terrestrial kilometric radiation as direct amplified gyroemission', *The Astrophysical Journal*, 207, 651-662.
- Meneses-Goytia S., Peletier, R.F., Trager, S.C., Falcón-Barroso, J., Koleva, M. and Vazdekis, A., 2015. Single stellar populations in the near-infrared-I. Preparation of the IRTF spectral stellar library. *Astronomy & Astrophysics*, 582, p.A96.
- Metchev, S. A., Heinze, A., Apai, D., F plateau, D., Radigan, J., Burgasser, A., Marley, M. S., Artigau, É., Plavchan, P. and Goldman, B. (2015) 'Weather on other worlds. II. Survey results: Spots are ubiquitous on L and T dwarfs', *The Astrophysical Journal*, 799(2), 154.
- Miles-Páez, P.A., Osorio, M.Z., Pallé, E. and Ramírez, K.P., 2013. Linear polarization of rapidly rotating ultracool dwarfs. *Astronomy & Astrophysics*, 556, p.A125.
- Mohanty, S. and Basri, G. (2003) 'Rotation and activity in mid-M to L field dwarfs', *The Astrophysical Journal*, 583(1), 451.
- Mohanty, S., Basri, G., Shu, F., Allard, F. and Chabrier, G. (2002) 'Activity in very cool stars: Magnetic dissipation in late M and L dwarf atmospheres', *The Astrophysical Journal*, 571(1), 469.
- Monin, J.-L., Ménard, F. and Duchêne, G. (1998) 'Using polarimetry to check rotation alignment in PMS binary stars. Principles of the method and first results', *Astronomy and Astrophysics*, 339, 113-122.
- Monin, J.-L., Ménard, F. and Peretto, N. (2006) 'Disc orientations in pre-main-sequence multiple systems-A study in southern star formation regions', *Astronomy & Astrophysics*, 446(1), 201-210.

- Morin, J., Donati, J.-F., Petit, P., Delfosse, X., Forveille, T., Albert, L., Auriere, M., Cabanac, R., Dintrans, B. and Fares, R. (2008) 'Large-scale magnetic topologies of mid M dwarfs', *Monthly Notices of the Royal Astronomical Society*, 390(2), 567-581.
- Morin, J., Donati, J.-F., Petit, P., Delfosse, X., Forveille, T. and Jardine, M. (2010) 'Large-scale magnetic topologies of late M dwarfs', *Monthly Notices of the Royal Astronomical Society*, 407(4), 2269-2286.
- Morin, J., Dormy, E., Schrunner, M. and Donati, J.F., 2011. Weak-and strong-field dynamos: from the Earth to the stars. *Monthly Notices of the Royal Astronomical Society: Letters*, 418(1), pp.L133-L137.
- Neuhäuser, R., Briceño, C., Cameron, F., Hearty, T., Martin, E. L., Schmitt, J. H., Stelzer, B., Supper, R., Voges, W. and Zinnecker, H. (1998) 'Search for X-ray emission from bona-fide and candidate brown dwarfs', arXiv preprint astro-ph/9812436.
- Nichols, J.D., Burleigh, M.R., Casewell, S.L., Cowley, S.W.H., Wynn, G.A., Clarke, J.T. and West, A.A., 2012. Origin of electron cyclotron maser induced radio emissions at ultracool dwarfs: magnetosphere-ionosphere coupling currents. *The Astrophysical Journal*, 760(1), p.59.
- Oppenheimer, B., Kulkarni, S., Matthews, K. and Nakajima, T. (1995) 'Infrared spectrum of the cool brown dwarf Gl 229B', *Science*, 270(5241), 1478-1479.
- Osborn, J., Föhring, D., Dhillon, V. and Wilson, R. (2015) 'Atmospheric scintillation in astronomical photometry', *Monthly Notices of the Royal Astronomical Society*, 452(2), 1707-1716.
- Osorio, M.Z., Caballero, J.A. and Béjar, V.J.S., 2005. Optical linear polarization of late M and L type dwarfs. *The Astrophysical Journal*, 621(1), p.445.
- Osorio, M. Z., Martín, E., Bouy, H., Tata, R., Deshpande, R. and Wainscoat, R. (2006) 'Spectroscopic rotational velocities of brown dwarfs', *The Astrophysical Journal*, 647(2), 1405.
- Ossendrijver, M. (2003) 'The solar dynamo', *The Astronomy and Astrophysics Review*, 11(4), 287-367.
- Osten, R. A., Hawley, S. L., Bastian, T. S. and Reid, I. N. (2006) 'The radio spectrum of TVLM 513-46546: Constraints on the coronal properties of a late M dwarf', *The Astrophysical Journal*, 637(1), 518.

- Pantell, R. H. (1959) 'Backward-wave oscillations in an unloaded waveguide', PROCEEDINGS OF THE INSTITUTE OF RADIO ENGINEERS, 47(6), 1146-1146.
- Parker, E. N. (1975) 'The generation of magnetic fields in astrophysical bodies. X-Magnetic buoyancy and the solar dynamo', The Astrophysical Journal, 198, 205-209.
- Pevtsov, A. A., Fisher, G. H., Acton, L. W., Longcope, D. W., Johns-Krull, C. M., Kankelborg, C. C. and Metcalf, T. R. (2003) 'The relationship between X-ray radiance and magnetic flux', The Astrophysical Journal, 598(2), 1387.
- Pineda, J. S., Hallinan, G., Kirkpatrick, J. D., Cotter, G., Kao, M. M. and Mooley, K. (2016) 'A Survey for H α Emission from Late L Dwarfs and T Dwarfs', The Astrophysical Journal, 826(1), 73.
- Pineda, J.S., Hallinan, G. and Kao, M.M., 2017. A panchromatic view of brown dwarf aurorae. The Astrophysical Journal, 846(1), p.75.
- Pols, O. R. (2011) Stellar structure and evolution, Astronomical Institute Utrecht.
- Pritchett, P. (1984a) 'Relativistic dispersion and the generation of auroral kilometric radiation', Geophysical research letters, 11(2), 143-146.
- Pritchett, P. (1984b) 'Relativistic dispersion, the cyclotron maser instability, and auroral kilometric radiation', Journal of Geophysical Research: Space Physics, 89(A10), 8957-8970.
- Pyper, D. M., Stevens, I. R. and Adelman, S. J. (2013) 'An update on the rotational period of the magnetic chemically peculiar star CU Virginis', Monthly Notices of the Royal Astronomical Society, 431(3), 2106-2110.
- Radigan, J., Jayawardhana, R., Lafreniere, D., Artigau, E., Marley, M. and Saumon, D. (2012) 'Large-amplitude variations of an L/T transition brown dwarf: multi-wavelength observations of patchy, high-contrast cloud features', The Astrophysical Journal, 750(2), 105.
- Radigan, J., Lafrenière, D., Jayawardhana, R. and Artigau, E. (2014) 'Strong brightness variations signal cloudy-to-clear transition of brown dwarfs', The Astrophysical Journal, 793(2), 75.
- Ravi, V., Hallinan, G., Hobbs, G. and Champion, D. J. (2011) 'The magnetosphere of the ultracool dwarf DENIS 1048–3956', The Astrophysical Journal Letters, 735(1), L2.

- Ravi, V., Hobbs, G., Wickramasinghe, D., Champion, D. J., Keith, M., Manchester, R. N., Norris, R. P., Bray, J. D., Ferrario, L. and Melrose, D. (2010) 'Observations of radio pulses from CU Virginis', *Monthly Notices of the Royal Astronomical Society: Letters*, 408(1), L99-L103.
- Redfern, R. (1991) 'High-resolution imaging in la palma', *Vistas in astronomy*, 34, 201-233.
- Reid, I. N., Burgasser, A., Cruz, K., Kirkpatrick, J. D. and Gizis, J. (2001) 'Near-infrared spectral classification of late M and L dwarfs', *The Astronomical Journal*, 121(3), 1710.
- Reid, I. N., Kirkpatrick, J. D., Gizis, J., Dahn, C., Monet, D., Williams, R. J., Liebert, J. and Burgasser, A. (2000) 'Four nearby L dwarfs', *The Astronomical Journal*, 119(1), 369.
- Reid, I. N., Kirkpatrick, J. D., Gizis, J. and Liebert, J. (1999) 'BRI 0021–0214: Another Surprise at the Bottom of the Main Sequence', *The Astrophysical Journal Letters*, 527(2), L105.
- Reiners, A. and Basri, G. (2007) 'The first direct measurements of surface magnetic fields on very low mass stars', *The Astrophysical Journal*, 656(2), 1121.
- Reiners, A. and Basri, G. (2009) 'On the magnetic topology of partially and fully convective stars', *Astronomy & Astrophysics*, 496(3), 787-790.
- Reiners, A., Bean, J., Huber, K., Dreizler, S., Seifahrt, A. and Czesla, S. (2010) 'Detecting planets around very low mass stars with the radial velocity method', *The Astrophysical Journal*, 710(1), 432.
- Reiners, A. and Basri, G., 2008. Chromospheric activity, rotation, and rotational braking in M and L dwarfs. *The Astrophysical Journal*, 684(2), p.1390.
- Reiners, A. and Basri, G., 2010. A volume-limited sample of 63 M7-M9. 5 dwarfs. II. Activity, magnetism, and the fade of the rotation-dominated dynamo. *The Astrophysical Journal*, 710(2), p.924.
- Robbins, M. S. and Hadwen, B. J. (2003) 'The noise performance of electron multiplying charge-coupled devices', *IEEE transactions on Electron Devices*, 50(5), 1227-1232.
- Robrade, J., Poppenhaeger, K., and Schmitt, J.H.M.M., "Quiescent and flaring X-ray emission from the nearby M/T dwarf binary SCR 1845-6357", *Astronomy & Astrophysics* 513 A12, 2010.

- Rockenfeller, B., Bailer-Jones, C. A., Mundt, R. and Ibrahimov, M. A. (2006) 'Multiband photometric detection of a huge flare on the M9 dwarf 2MASSW J1707183+643933', *Monthly Notices of the Royal Astronomical Society*, 367(1), 407-411.
- Romanishin, W. (2006) 'An Introduction to Astronomical Photometry Using CCDs', University of Oklahoma, 17.
- Route, M. and Wolszczan, A. (2012) 'The arecibo detection of the coolest radio-flaring brown dwarf', *The Astrophysical Journal Letters*, 747(2), L22.
- Route, M. and Wolszczan, A. (2016) 'Radio Flaring from the T6 Dwarf WISEPC J112254.73+ 255021.5 with a Possible Ultra-short Periodicity', *The Astrophysical Journal Letters*, 821(2), L21.
- Rutledge, R. E., Basri, G., Martín, E. L. and Bildsten, L. (2000) 'Chandra detection of an X-ray flare from the brown dwarf LP 944-20', *The Astrophysical Journal Letters*, 538(2), L141.
- Rybicki, G. B. and Lightman, A. P. (2008) *Radiative processes in astrophysics*, John Wiley & Sons.
- Rädler, K.-H., Wiedemann, E., Brandenburg, A., Meinel, R. and Tuominen, I. (1990) 'Nonlinear mean-field dynamo models-Stability and evolution of three-dimensional magnetic field configurations', *Astronomy and Astrophysics*, 239, 413-423.
- Saar, S. and Linsky, J. (1985) 'The photospheric magnetic field of the dM3.5e flare star AD Leonis', *The Astrophysical Journal*, 299, L47-L50.
- Saumon, D. and Marley, M.S., 2008. The evolution of L and T dwarfs in color-magnitude diagrams. *The Astrophysical Journal*, 689(2), p.1327.
- Saur, J., Neubauer, F.M., Connerney, J.E.P., Zarka, P. and Kivelson, M.G., 2004. Plasma interaction of Io with its plasma torus. *Jupiter: The Planet, Satellites and Magnetosphere*, 1, pp.537-560.
- Scargle, J. D. (1982) 'Studies in astronomical time series analysis. II-Statistical aspects of spectral analysis of unevenly spaced data', *The Astrophysical Journal*, 263, 835-853.
- Scargle, J. D. (1989) 'Studies in astronomical time series analysis. III-Fourier transforms, autocorrelation functions, and cross-correlation functions of unevenly spaced data', *The Astrophysical Journal*, 343, 874-887.

- Schlieder, J. E., Bonnefoy, M., Herbst, T., Lépine, S., Berger, E., Henning, T., Skemer, A., Chauvin, G., Rice, E. and Biller, B. (2014) 'Characterization of the benchmark binary NLTT 33370', *The Astrophysical Journal*, 783(1), 27.
- Schmidt, S. J., Hawley, S. L., West, A. A., Bochanski, J. J., Davenport, J. R., Ge, J. and Schneider, D. P. (2015) 'BOSS ultracool dwarfs. I. Colors and magnetic activity of M and L dwarfs', *The Astronomical Journal*, 149(5), 158.
- Schneider, J. (1959) 'Stimulated emission of radiation by relativistic electrons in a magnetic field', *Physical Review Letters*, 2(12), 504.
- Schrijver, C., Cote, J., Zwaan, C. and Saar, S. (1989) 'Relations between the photospheric magnetic field and the emission from the outer atmospheres of cool stars. I-The solar CA II K line core emission', *The Astrophysical Journal*, 337, 964-976.
- Schrijver, C.J., 2009. On a transition from solar-like coronae to rotation-dominated Jovian-like magnetospheres in ultracool main-sequence stars. *The Astrophysical Journal Letters*, 699(2), p.L148.
- Schwarzenberg-Czerny, A. (1989) 'On the advantage of using analysis of variance for period search', *Monthly Notices of the Royal Astronomical Society*, 241(2), 153-165.
- Schwarzenberg-Czerny, A. (1997) 'The correct probability distribution for the phase dispersion minimization periodogram', *The Astrophysical Journal*, 489(2), 941.
- Schweitzer, A., Gizis, J. E., Hauschildt, P. H., Allard, F. and Reid, I. N. (2001) 'Analysis of Keck HIRES spectra of early L-type dwarfs', *The Astrophysical Journal*, 555(1), 368.
- Seaquist, E. (1993) 'Radio emission from stars', *Reports on Progress in Physics*, 56(9), 1145.
- Sheehan, B. J. (2008) '<Brendan_Thesis_FINAL copy.pdf>', Ph.D thesis.
- Sheehan, B. J. and Butler, R. F. (2008) Development and use of an L3CCD high-cadence imaging system for Optical Astronomy, translated by AIP, 162-167.
- Sheehan, B. J., Lane, C. and Butler, R. F. (2006) Performance modeling and development of an L3-CCD camera system for high cadence imaging with maximum efficiency, translated by International Society for Optics and Photonics, 62654D.

- Shu, F. H. (1991) 'The physics of astrophysics. Volume 1: Radiation', The physics of astrophysics. Volume 1: Radiation., by Shu, FH. University Science Books, Mill Valley, CA (USA), 1991, 446 p., ISBN 0-935702-64-4.
- Shu, F. H., Adams, F. C. and Lizano, S. (1987) 'Star formation in molecular clouds: observation and theory', *Annual review of astronomy and astrophysics*, 25(1), 23-81.
- Shulyak, D., Reiners, A., Engeln, A., Malo, L., Yadav, R., Morin, J. and Kochukhov, O. (2017) 'Strong dipole magnetic fields in fast rotating fully convective stars', *Nature Astronomy*, 1(8), 1-7.
- Smith, G. E. (2010) 'Nobel Lecture: The invention and early history of the CCD', *Reviews of modern physics*, 82(3), 2307.
- Smith, N., Coates, C., Giltinan, A., Howard, J., O'Connor, A., O'Driscoll, S., Hauser, M. and Wagner, S. (2004) EMCCD technology and its impact on rapid low-light photometry, translated by International Society for Optics and Photonics, 162-172.
- Sorahana, S., Yamamura, I. and Murakami, H., 2013. On the Radii of Brown Dwarfs Measured with AKARI Near-infrared Spectroscopy. *The Astrophysical Journal*, 767(1), p.77.
- Stellingwerf, R. F. (1978) 'Period determination using phase dispersion minimization', *The Astrophysical Journal*, 224, 953-960.
- Tinney, C. and Reid, I. (1998) 'High-resolution spectra of very low-mass stars', *Monthly Notices of the Royal Astronomical Society*, 301(4), 1031-1048.
- Treumann, R. A. (2006) 'The electron-cyclotron maser for astrophysical application', *The Astronomy and Astrophysics Review*, 13(4), 229-315.
- Twiss, R. (1958) 'Radiation transfer and the possibility of negative absorption in radio astronomy', *Australian Journal of Physics*, 11(4), 564-579.
- Ushomirsky, G., Matzner, C. D., Brown, E. F., Bildsten, L., Hilliard, V. G. and Schroeder, P. C. (1998) 'Light element depletion in contracting brown dwarfs and pre-main-sequence stars', *The Astrophysical Journal*, 497(1), 253.
- Visscher, C., Lodders, K. and Fegley Jr, B. (2006) 'Atmospheric chemistry in giant planets, brown dwarfs, and low-mass dwarf stars. II. Sulfur and phosphorus', *The Astrophysical Journal*, 648(2), 1181.

- Vos, J.M.C., 2019. Characterising weather and rotation on substellar worlds (Doctoral dissertation, University of Edinburgh).
- Vos, J.M., Allers, K.N. and Biller, B.A., 2017. The Viewing Geometry of Brown Dwarfs Influences Their Observed Colors and Variability Amplitudes. *The Astrophysical Journal*, 842(2), p.78.
- Vrba, F. J., Henden, A., Luginbuhl, C., Guetter, H., Munn, J., Canzian, B., Burgasser, A., Kirkpatrick, J. D., Fan, X. and Geballe, T. (2004) 'Preliminary parallaxes of 40 L and T dwarfs from the US Naval Observatory Infrared Astrometry Program', *The Astronomical Journal*, 127(5), 2948.
- Wang, S., Zhou, X., Zhang, H., Zhou, J., Ma, J., Fan, Z., Zou, H., Meng, Z. and Yang, J. (2012) 'The Inhomogeneous Effect of Cloud on CSTAR Photometry and Its Correction', *Publications of the Astronomical Society of the Pacific*, 124(921), 1167.
- Weis, E. (1974) 'On the inclination of rotation axes in visual binaries', *The Astrophysical Journal*, 190, 331-337.
- West, A. A., Hawley, S. L., Walkowicz, L. M., Covey, K. R., Silvestri, N. M., Raymond, S. N., Harris, H. C., Munn, J. A., McGehee, P. M. and Ivezić, Ž. (2004) 'Spectroscopic properties of cool stars in the Sloan Digital Sky Survey: an analysis of magnetic activity and a search for subdwarfs', *The Astronomical Journal*, 128(1), 426.
- Williams, P. K., Berger, E. and Zauderer, B. A. (2013) 'Quasi-quiescent Radio Emission from the First Radio-emitting T Dwarf', *The Astrophysical Journal Letters*, 767(2), L30.
- Williams, P. K. G., Berger, E., Irwin, J., Berta-Thompson, Z. and Charbonneau, D. (2015) 'Simultaneous Multiwavelength Observations of Magnetic Activity in Ultracool Dwarfs. IV. The Active, Young Binary NLTT 33370 AB (= 2MASS J13142039+1320011)', *The Astrophysical Journal*, 799(2), 192.
- Williams, P.K.G. and Berger, E., 2015. The rotation period and magnetic field of the T dwarf 2MASSI J1047539+ 212423 measured from periodic radio bursts. *The Astrophysical Journal*, 808(2), p.189.
- Wolf, S., Stecklum, B. and Henning, T. (2001) *Pre-main sequence binaries with aligned disks?*, translated by Cambridge University Press, 295-304.
- Wright, N. J. and Drake, J. J. (2016) 'Solar-type dynamo behaviour in fully convective stars without a tachocline', *Nature*, 535(7613), 526.

- Wu, C. and Lee, L. (1979) 'A theory of the terrestrial kilometric radiation', *The Astrophysical Journal*, 230, 621-626.
- Wu, Z., Chen, Y., Ning, H., Kong, X. and Lee, J. (2019) 'Gyrosynchrotron Emission Generated by Nonthermal Electrons with the Energy Spectra of a Broken Power Law', *The Astrophysical Journal*, 871(1), 22.
- Yadav, R.K., Christensen, U.R., Morin, J., Gastine, T., Reiners, A., Poppenhaeger, K. and Wolk, S.J., 2015. Explaining the coexistence of large-scale and small-scale magnetic fields in fully convective stars. *The Astrophysical Journal Letters*, 813(2), p.L31.
- Young, A. T., Genet, R. M., Boyd, L. J., Borucki, W. J., Lockwood, G. W., Henry, G. W., Hall, D. S., Smith, D. P., Baliunas, S. and Donahue, R. (1991) 'Precise automatic differential stellar photometry', *Publications of the Astronomical Society of the Pacific*, 103(660), 221.
- Yu, S., Doyle, J., Kuznetsov, A., Hallinan, G., Antonova, A., MacKinnon, A. and Golden, A. (2012) 'Electron-beam-induced radio emission from ultracool dwarfs', *The Astrophysical Journal*, 752(1), 60.
- Zarka, P. (1998) 'Auroral radio emissions at the outer planets: Observations and theories', *Journal of Geophysical Research: Planets*, 103(E9), 20159-20194.
- Zarka, P., 2007. Plasma interactions of exoplanets with their parent star and associated radio emissions. *Planetary and Space Science*, 55(5), pp.598-617.
- Zhang, L., Neves, L., Lundeen, J. S. and Walmsley, I. A. (2009) 'A characterization of the single-photon sensitivity of an electron multiplying charge-coupled device', *Journal of Physics B: Atomic, Molecular and Optical Physics*, 42(11), 114011.
- Zhang, Q., Hallinan, G., Brisken, W., Bourke, S. and Golden, A., 2020. Multi-Epoch VLBI of L Dwarf Binary 2MASS J0746+ 2000AB: Precise Mass Measurements and Confirmation of Radio Emission from Both Components. arXiv preprint arXiv:2005.03657.
- Zic, A., Lynch, C., Murphy, T., Kaplan, D. L. and Chandra, P. (2018) 'Low-frequency GMRT observations of ultra-cool dwarfs', *Monthly Notices of the Royal Astronomical Society*, 483(1), 614-623.